DSE - Reconfigurable Unmanned Cargo Aircraft

L.F.J. Brink	4388992	M. van der Panne	4295714
L.J.M. Ceelen	1369113	T.R. Paulsen	4225589
K. Fines	4223934	T.H.H. Tran	4345371
J. Hampsink	4269500	B. Vlamings	4144228
L. van Litsenburg	4282345	T.M.J. van der Weide	4291824

Final Report

Design Synthesis Excercise

TU Delft Delft University of Technology

Aerospace Engineering

June 27, 2017

Preface

This document forms the final report of the Design Synthesis Exercise (DSE), part of the BSc Aerospace Engineering curriculum, on our subject, the Reconfigurable Unmanned Cargo Aircraft. The main objective behind this report is to give the reader a complete overview of the design process.

This report includes the detailed design of the concept that was chosen and presented in the mid-term report. The detailed design of the subsystems is split up into different departments. The final result is a detailed design of a large number of subsystems.

The final report is the complete overview of the design process of a reconfigurable unmanned cargo aircraft. Performing the DSE helped us understand the different aspects of a design project and the importance of integrating systems engineering for the successful completion of the project. Furthermore, working in a group of 10 students in a limited amount of time further improved our project management skills and emphasized the importance of good team work.

Group 20
DSE Spring 2017 Delft, June 2017

Contents

Nomenclature

Acronyms

ABSAA Airborne Sense and Avoid Radar

AC Alternating Current

ACARS Aircraft Communications Addressing and Reporting System

ACS Aerodynamics, Control and Stability

ADS-B Automatic Dependent Surveillance-Broadcast

APU GEN Auxiliary power unit generator

AR Aspect ratio

ATC Air Traffic Control

ATLC Automatic Takeoff and Landing Capability

ATN Aeronautical Telecommunication Network

ATO Air Transport and Operations

BEP Break-even point

BPC Bus Power Contactor

CB Circuit Breaker

CC Combustion chamber

CCOHS Canadian Centre for Occupational Health and Safety

CFD Computational Fluid Dynamics

CG Center of gravity

CPDLC Controller-Pilot Data-Link Communications

CS Certification Specifications

CSD Constant Speed Drive

DC Direct Current

DCL Departure Clearance Service

DSE Design Synthesis Exercise

EAN European Aviation Network

ECS Environmental Control System

EHSA Electro Hydrostatic Actuator

EMERG GEN Emergency Generator

EPNL Effective Perceived Noise Level

EXT PWR External Power

FAA Federal Aviation Administration

FADEC Full Authority Digital Engine Controller

FANS Future Air Navigation System

FBD Free Body Diagram

FBS Functional Breakdown Structure

FEM Finite Element Method

FFD Functional Flow Diagram

FPP Flight Performance and Propulsion

FTK Freight Tonne Kilometer

GCS Ground Control Station

GDP Gross Domestic Product

GPS Global Positioning System

HEVC High Efficiency Video Coding

HLD High lift device

HPT High pressure turbine

ILS Instrument Landing System

IMMC Integrated Mission Managemen tComputer

INM Integrated Noise Model

INS Inertial Navigation System

IP Internet Protocol

IPS Internet Protocol Suite

JIT Just-In-Time

LDACS L-band digital aeronautical communications system

LPT Low pressure turbine

LTE Long-Term Evolution

MAC Mean aerodynamic chord

MPD Maintenance Planning Document

MTOM Maximum Take-Off Mass

MTOW Maximum Take-Off Weight

NAV Navigation

OCC Operations Control Center

OEW Operational Empty Weight

OPS Operations

PD&D	Project Design and Development
PTF	Permits to Fly
RAMS	Reliability Availability Maintainability and Safety
RAT	Ram Air Turbine
RCofA	Restricted Certificates of Airworthiness
ROC	Certifications for Remote Operators
RPM	Rounds per minute
RTC	Restricted Type Certificates
RTK	Revenue Tonne Kilometer
S.M.	Safety margin
SEL	Sound Exposure Level
SESAR	Single European Sky ATM Research
SF	Similarity factor
STC	Supplemental Type Certificate
STR	Structure
TAT	Turn around time
TCAS	Traffic Collision Avoidance System
TCP	Transmission Control Protocol
TOLT	Take-off, landing and taxiing
TR	Transformer Rectifiers
TR ESS	Essential Transformer Rectifier
UAS	Unmanned Aerial System
UAV	Unmanned Aerial Vehicle
ULD	Unit Load Device
UMS	Unmanned system
URC	Ultra Reliable Communication
VDL	VHF data link
VHF	Very high frequency

Greek Symbols

α	Incidence angle of main wing	deg
α_h	Angle of attack horizontal tail	deg
α_{0L}	Zero lift angle of attack	deg
β	Prandtl-Glauert compressibility correction factor	-
δ_E	Elevator deflection	deg
ϵ	Downwash angle	deg
η	Airfoil efficiency factor	-
η_{cc}	Combustion chamber efficiency	-
η_{prop}	Propeller efficiency	-
$\frac{\delta\epsilon}{\delta\alpha}$	Downwash gradient	-
$\Lambda_{0.5C}$	Half chord sweep	deg
Λ_{LE}	Leading edge sweep	deg
ϕ_{req}	Required bank angle	deg
ϕ_{req}	Steady state bank angle	deg
ρ	Density	kg/m^3
ρ_{fuel}	Fuel density	kg/m^3
σ	Bending stress	N/m^2
σ_v	Von Mises stress	N/m^2
τ	Shear stress	N/m^2
τ_e	Elevator angle of attack effectiveness	-
τ_r	Rudder angle of attack effectiveness	-
τ_a	Aileron angle of attack effectiveness	-

Roman Symbols

$\bar{c}$	Mean aerodynamic chord	m
$\bar{x_{ac}}$	Location of aerodynamic centre with respect to MAC	m
$\bar{x_{cg}}$	Location of centre of gravity with respect to MAC	%
$\bar{z}$	Centroid along the z-axis	m
$\dot{m}$	Mass flow	kg/s
$\dot{m}_f$	Fuel mass flow	kg/s
$\dot{P}$	Time rate of change of the aircraft roll rate	deg /s^2
η_i	Inboard flap location	-
η_o	Outboard flap location	-
$\frac{t}{c}$	Thickness over chord	-
A	Aspect ratio	-
A	Cross sectional area	m^2
A_h	Aspect ratio horizontal tail	-
A_{disk}	Propeller blade area	m^2

b_f	Width of fuselage	m
b_w	Wing span	m
C	Wing chord	m
c	Climb rate	m/s
C_A	Aileron chord	m
C_C	Chord length of the control surface	m
C_D	Drag coefficient	-
C_e	Elevator chord	m
C_f	Flap chord	m
C_h	Horizontal tail chord	m
c_p	Specific fuel consumption	-
C_R	Rudder chord	m
C_V	Vertical tail chord	m
C_w	Wing chord	m
$C_{D,R}$	Aircraft drag coefficient in rolling moment	-
C_{D0}	Zero-lift drag coefficient	-
$C_{D_{cr}}$	Drag coefficient during cruise	-
$C_{L_{\alpha-h}}$	3D Lift gradient of aircraft less tail	1/rad
$C_{L_{\alpha_h}}$	3D Lift gradient of horizontal tail	1/rad
$C_{l_{\alpha_h}}$	2D Lift gradient of horizontal tail	1/rad
C_{L_α}	Lift gradient of main wing	1/rad
$C_{L_{cr}}$	Lift coefficient during cruise	-
$C_{l_{design}}$	Lift coefficient	-
C_{L_h}	Lift coefficient of the horizontal tail	-
$C_{L_{max}}$	Maximum lift coefficient	-
$C_{m0_{wf}}$	Moment coefficient of wing and fuselage	-
C_{m_α}	moment coefficient of the aircraft	-
$c_{p,g}$	Specific gas heat	kJ · K/kg
D	Bolt diameter	m
D	Drag	N
d	Moment arm	m
D^{hole}	Diameter of the rivet hole	m
d_c	Effective bolt diameter	m
D_{trim}	Trim drag due to incidence angle	N
e	Oswald factor	-
e_h	Oswald factor horizontal tail	-
EI_{CO_2}	Emission Index of CO_2	m
f	Landing weight over take-off weight	-
g_0	Gravitational constant	m/s^2
h_f	Fuselage height	m
I	Moment of Inertia	m^4
i_h	Incidence angle of horizontal tail	deg
I_{xx}	Moment of Inertia	kg · m^2
L	Lift	N
L_A	Rolling moment	N · m
l_f	Length of the fuselage	m
l_h	Distance between aerodynamic center tail and wing	m
LHV_f	Lower heating value	kJ/kg
M	Moment	N · m
m_{CO_2}	CO_2 emission mass	kg
M_{crit}	Critical mach number	-
$M_{engines}$	Engine mass	kg
$m_{f,res}$	Reserve fuel mass	kg
$m_{f,used}$	Fuel mass	kg
M_{gears}	Gear mass	kg
M_{OEW}	Operational empty weight mass	kg
$M_{payload}$	Payload mass	kg
m_{PL}	Payload mass	kg
M_{tail}	Tail mass	kg
M_{wings}	Wing mass	kg
$N_m w$	Number of main landing gear wheel	-
$N_n w$	Number of nose landing gear wheel	-
$N_{engines}$	Number of engines	-
N_{gear}	Number of engines	-
n_{ult}	Ultimate load factor	-
P	Steady-state role rate	deg /s
P_a	Available power	W
$P_m w$	Static load per main landing gear wheel	kg

P_nw	Static load per nose landing gear wheel	kg	t	Thickness	m
P_{ss}	Steady state roll rate	$\frac{\text{deg}}{\text{s}}$	$T_{0,3}$	Combustion inlet temperature	K
Q	Load per unit width	N/m	$T_{0,4}$	Turbine inlet temperature	K
q_s	Shear flow	N/m	t_ϕ	Time for bank angle	s
R	Range	m	t_{sheet}	Sheet thickness	m
S	Shear force	N	u_0^2	Free stream velocity	m/s
S	Surface area	m^2	V	Velocity	m/s
S_C	Surface of the control surface	m^2	V_C	Cruise velocity	m/s
S_h	Horizontal tail surface area	m^2	V_h	Horizontal tail velocity	m/s
S_v	Vertical tail surface area	m^2	V_S	Stall Speed	m/s
s_{Land}	Landing length	m	V_v	Vertical tail volume coefficient	-
S_{net}	Wing surface area less wing area inside fuselage	m^2	V_D	Dive velocity	m/s
s_{TO}	Take-off length	m	V_{LOF}	Lift-off velocity	m
T	Thrust	N	V_{stall}	Stall speed	m/s

Executive Summary

The air cargo market is a rapidly growing sector with a promising outlook, especially within the express freight category. This growth in the market size asks for more flexibility from air cargo operators to fulfill different range requirements with the use of smaller, lighter aircraft. The use of a reconfigurable aircraft addresses this opportunity by introducing the possibility of using one aircraft system for drastically different missions. Moreover, the UAV sector is evolving quickly and unmanned cargo operation of the aircraft would thus allows for the transportation of dangerous goods without endangering human operators during flight, less personnel, and cheaper operations. The reconfigurability in combination with the unmanned operation delivers a unique and innovative product to the growing cargo market.

To be able to fulfill the market need in a successful manner, four candidate concepts are developed. A trade-off based on sustainability, costs, risk & complexity, performance, and operations resulted in the concept called the ModuLR being further investigated upon.

The ModuLR concept, a multi-engine turboprop aircraft, consists of three different configurations, being the ModuLR-100, ModuLR-200, and ModuLR-300, which all have different range, payload, and runway length requirements. The ModuLR-100 requires a minimum range of 1000 nmi, a minimum payload of 1200 kg, and a take-off and landing distance of maximum 3000 ft. The ModuLR-200, on the other hand, has a minimum range requirement of 2000 nmi, a minimum payload requirement of 6000 kg, and a take-off and landing distance of maximum 8000 ft. Lastly, the ModuLR-300 requires a minimum range of 4000 nmi, a minimum payload of 12000 kg, and a take-off and landing distance of maximum 10000 ft. The ModuLR aircraft will therefore be highly flexible, able to operate from small to large airports, and travel short to very long range missions.

To make the ModuLR aircraft attractive to all players within the market, operators only purchase the fuselage, which remains constant throughout all configurations. The configuration dependent wing-tail-engine combination is leased through a service model.

After a preliminary design phase with resulting mass and power budgets for all design areas, the sizing of the constant fuselage is performed first and done so for the largest aircraft, the ModuLR-300. Then, the performance and propulsion characteristics of the aircraft are investigated upon, which is concluded with the design of a new turboprop engine. Afterwards, the aerodynamics, as well as the control & stability of the aircraft are treated with the design of the wing, nose, tail, and control surfaces. Moreover, the structural design of the wingbox, landing gear, and bolts for the reconfiguration is performed. Furthermore, the operations concerning the communication and control of the unmanned aircraft are treated. Then, the electrical system is designed. The report is concluded with a financial analysis, including development costs, production costs, and operational costs.

The ModuLR uses standardized half pallets (96x64x61.5 in), and has a fixed fuselage length of 21.8m, with a cargo door at the forward side of the fuselage. The mass budgets of the aircraft variants are presented in Tab. 1, and the total power budget is determined to be 27630 VA.

Table 1: Operational empty weight, fuel weight, and maximum take-off weight of the three ModuLR configurations

	ModuLR-100	**ModuLR-200**	**ModuLR-300**
Operational empty weight [kg]	17358	20578	32112
Fuel weight [kg]	2776	6631	20082
Maximum take-off weight [kg]	21441	33376	64517

In terms of runway requirements, the ModuLR-100 requires a take-off distance of 914.4m, the -200 variant requires 2120.3m, and the -300 requires 3048.0m. The propulsion systems are designed as turboprops,

producing a maximum available power of 2647.3W and having an overall pressure ratio of 16.6. In addition to this, a propeller with 6 blades and a tip radius of 2.2m is used. This setup enables the ModuLR-300 variant to achieve a carbon dioxide emission 0.213 $\frac{kg}{km \cdot 1000kg}$, -7% lower than the existing Boeing 747-400 aircraft. For the $\frac{NO_x}{FTK}$, the ModuLR-300 produces 42% less than the Boeing 747-400 aircraft.

The wing of all ModuLR variants is the GOE412 airfoil, has an aspect ratio of 12, and a taper ratio of 0.4, keeping the leading edge perpendicular to the fuselage structure. The surface area for the -100 variant is 53.5m^2, for the -200 is 72.6m^2, and for the -300 is 138m^2. The respective wingspans also increase with variant, being 25.3m for the -100, 29.5m for the -200 variant, and 40.7 for the -300 variant. Flaps are required for all variants, to meet the runway requirements, and the nose of the aircraft is the Haack series with C = 0.

Initially, three different tails were designed for the three variants. However, it was found that it was more beneficial to use only two. The ModuLR-100 and -200 variants use the same T-tail configuration, with a horizontal tail surface area of 27.66m^2, and a vertical tail area of 9.48m^2. The -300 variant requires a bigger T-tail, with a horizontal tail surface area of 47.58m^2, and a vertical tail surface area of 16.18m^2. All tails use the NACA 64012 airfoil.

The ailerons enable the -100 variant to achieve a 45° bank angle in 1.39s, and the -200 and -300 to achieve a 30° bank angle in 1.49s. The elevators enable longitudinal trim to be maintained in conditions from stall cruise speed to optimum cruise speed, requiring a range of deflection from approximately 6° to 29°. The rudder allows for directional trim to be maintained in an one engine inoperative scenario, in both the take-off and cruise conditions. All control surface deflections are not greater than 30°. The actuator stroke length does not exceed 0.4m, and the maximum actuator force is 32.9kN, required by the ModuLR-300 variant. The symmetric flight motions of all variants are damped, with the -100 variant having the highest damping ratio. The aperiodic roll and Dutch roll are damped for all variants, with the -200 variant having the highest damping ratio. The total drag coefficients for the -100, -200 and -300 variants are 0.0433, 0.0364, and 0.035 respectively.

Structurally, a tapered wingbox is included, using the 7178-T6 aluminum alloy. Near the wing root, the -100 requires a maximum of 4 stringers, the -200 variant 8, and the -300 requires a maximum of 18. For the landing gear, 2 nose wheels are required for the nose landing gear, and 4 wheels for the main landing gear (placed on 2 struts). The fuselage is also pressurized. Fig.1 presents an exploded view of on of the ModuLR variants.

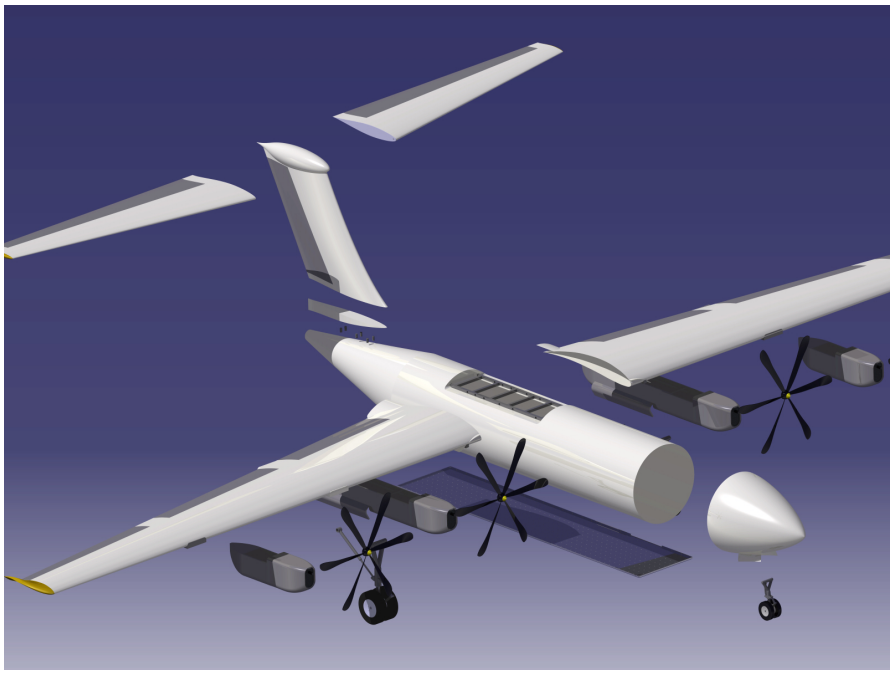

Figure 1: Exploded view of the ModuLR-300

In terms of communication, Fig. 8.2 presents an overview of the system design. All links are encrypted to ensure safety of the system. Additionally, 16 globally placed Operation Control Centers (OCCs) are designed, which will be use to monitor and control the operational aspects of the ModuLR aircraft. In the flight phase, a combination of onboard autonomous systems and the OCCs ensure an unmanned flight is possible. As previously discussed, a service model is designed, where a customer pays an upfront price of €20M for the fuselage, avionics, and the landing gear. After this, an annual €5M subscription fee is required, which allows the operator to lease any of the wing-tail-engine combinations to fulfill their mission needs. These can be reconfigured up to 12 times a year. Fig. 8.17 presents a possible setup for reconfiguring the aircraft.

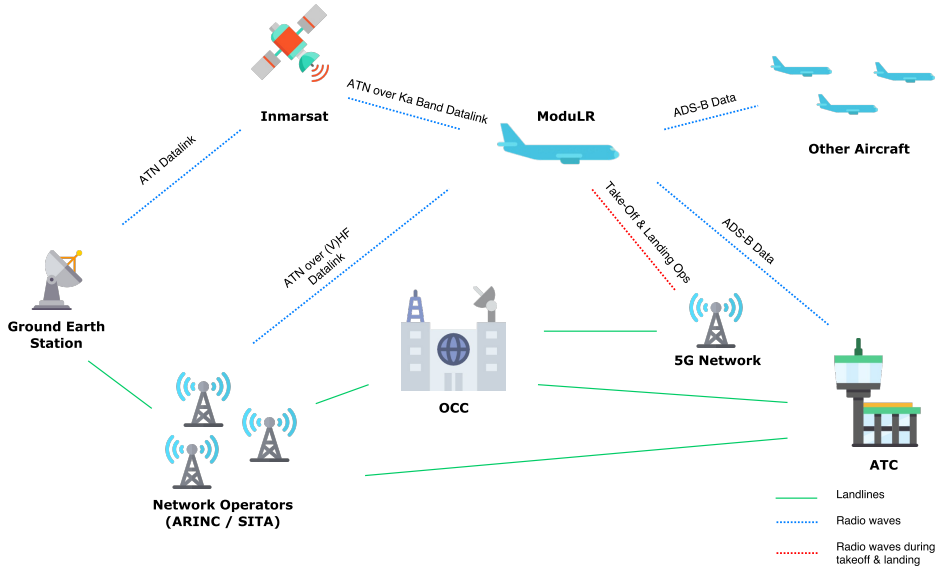

Figure 2: Communications system overview

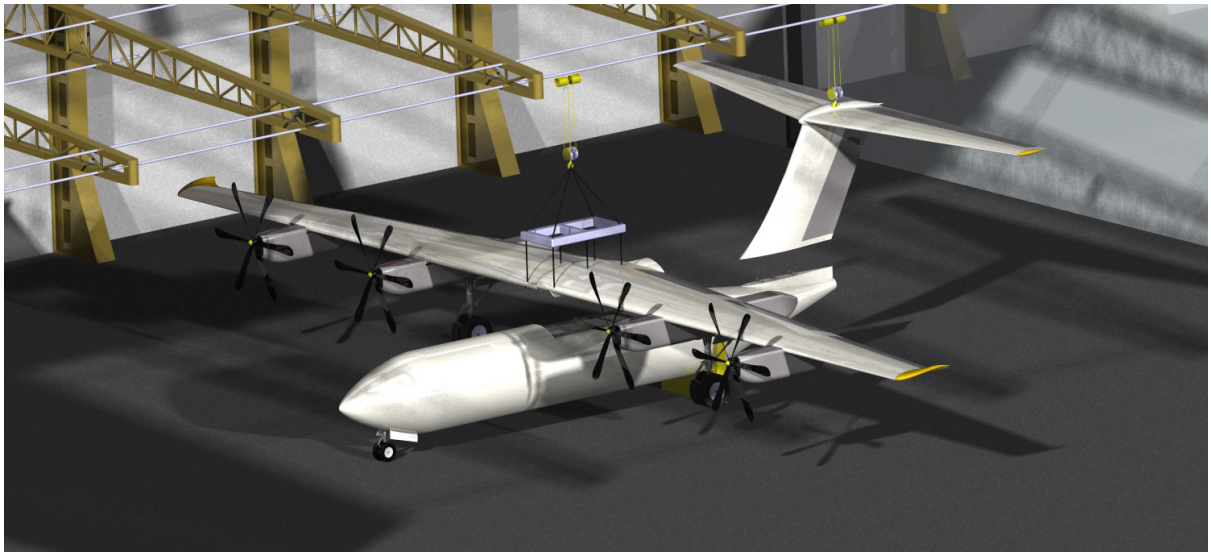

Figure 3: Reconfiguration of the ModuLR-300

Electrical systems are designed, which 2 generators, and 2 batteries. Additionally, wing contained hydraulic systems and fuel systems are designed, such that reconfiguration between wings can be achieved.

Financially, the total development costs are estimated to be at €1091M. The total cost for producing 180 aircraft, including 60 wings of each configuration, 100 engines and 60 tails of the -300 variant, and 30 tails for the -100 and -200 variants, results in total costs of €4.5B. The total production costs per

aircraft are €25M. When removing the costs for the extra reconfigurable parts, the production costs are €17.3M per aircraft. The yearly operational costs of the service model are estimated to be €1.6M. The break-even point is estimated to be achieved sometime in the year of 2043, 26 years after the development of the aircraft has begun.

To summarize, the ModuLR is a reconfigurable unmanned cargo aircraft, with versatile mission profiles, utilizing a service model. Fig. 4 presents a render of the three aircraft variants.

Figure 4: Overview of the three ModuLR configuration in flight

Chapter 1

Introduction

The growing air cargo market introduces the need for flexibility among air cargo operators. A reconfigurable cargo aircraft addresses this new opportunity in the market due to its usability for vastly different missions. Additionally, unmanned operation of the aircraft further allows for flexibility of cargo and operations. Reconfigurability in combination with unmanned operation delivers a unique and flexible product for the cargo market. In the mid-term report [1] a final concept for a reconfigurable unmanned cargo aircraft has been presented, the ModuLR. This concept is worked out in detail in order to move forward towards the production phase of the project.

The purpose of this report is to present, document, and justify the detailed choices and design of the ModuLR and its subsystems. The detailed design will adhere to the key and driving (sub)system requirements.

In chapter 2, a market analysis is performed in order to analyze the market possibilities and produce market requirements (Work Package 1212). Chapter 3 presents the mission analysis of the project, as well as a functional flow diagram (Work Package 1214) and a functional breakdown structure (Work Package 1215). The preliminary sizing of each concept, which is required to get the starting values for the detailed design, is presented in chapter 4. Afterwards, the chapters present the detailed design of the system (Work Package 1523). In chapter 5, the performance of the entire system is assessed (Work Package 1547), together with the detailed design of the propulsion system. In chapter 6, the detailed design of the wing, nose, tail, and control surfaces is presented, together with an analysis of the drag of the system and its dynamic stability. The detailed structural design of the wing and landing gear is presented in chapter 7. In chapter 8, the air and ground operation procedures and regulations are discussed, the connectors for reconfiguration are designed, and the RAMS characteristics of the system are assessed. The characteristics and layout of the electrical, hydraulic, fuel, and environmental control system can be found in chapter 9 (Work package 1545). Chapter 10 presents a risk assessment (Work Package 1514) of the design and a mitigation plan for the risks. A detailed cost analysis and financial forecast is performed in chapter 11 (Work Package 1542). Lastly the feasibility of the final design is checked by checking compliance with the requirements in chapter 12 (Work Package 1548).

Chapter 2

Market Analysis

The cargo transportation market is composed of many different transportation methods. The majority of these methods are interconnected to form vast modal transportation networks, resulting in cargo reaching destinations in a very timely fashion. Air transportation is considered to be one of the most time efficient transportation means and naturally forms the core market of this design project. This chapter presents the analysis of the air cargo transportation market and how a reconfigurable unmanned cargo aircraft would fit best in this market.

2.1 Market Size

The growth in the air cargo market is closely related to the GDP growth. The main drivers for the growth of the air cargo market are found to be the expansion of international trade and the increase in domestic trade [2][3].

Fig. 2.1 shows the expected growth of the air cargo market using RTKs (which incorporates both value and volumes). By 2035, the market is expected to have doubled in terms of RTK. According to a study conducted by Boeing [3], it is furthermore expected that the number of dedicated cargo aircraft will have increased to 3010 by 2030.

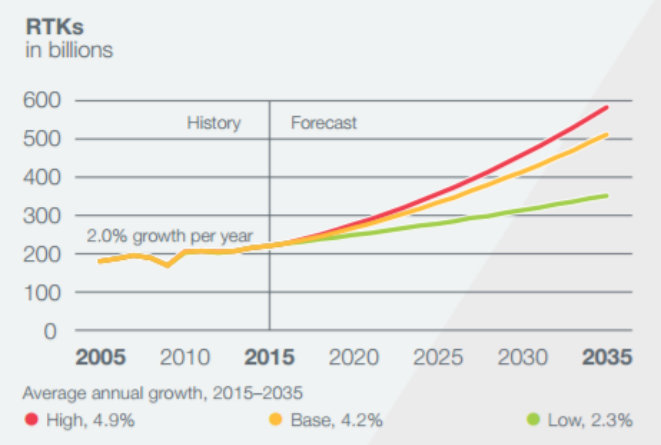

Figure 2.1: RTK Forecast for air cargo transport [2]

2.2 Technology and Operations

Currently, the market is primarily composed of three types of aircraft families, categorized by their payload capacity: small jet freighters, mid sized freighters, and large freighters. The number of regional (small and mid sized) freighters has decreased from 1240 in 2001 to 960 in 2011, whilst the number of intercontinental freighters has increased from about 450 to 620 [2]. The operational aspects of cargo transportation can be broken down into three categories: express, mail, and scheduled freighters. Currently more than half of the total air cargo is express freight, and it is expected that this will continue to be so [2]. Furthermore, it should be noted that the load factor of major air cargo operators is relatively low. For example, the cargo load factor of Air France - KLM is only 58.8% [4].

The short haul market category may experience the introduction of new small efficient aircraft. In the medium haul category, there may be conversions of aircraft or derivatives of existing aircraft. In the long haul category, derivatives of modern aircraft will continue to dominate the market [2].

2.3 Customer Demand

Although the air cargo market only accounts for less than 1% of the world cargo tonnage, 35% of world trade value is achieved via air cargo. This is explained by the most important advantage of air freight transport: it is faster than other transportation means such as boats and trains. Therefore, air transport is mainly focused on express, perishables, and emergency goods, such as mail, flowers, and human transplants respectively. A major disadvantage of air freight is the high cost involved. For expensive and luxury goods, the transport costs account for a lower percentage of the overall product value, thus air freight is used more often in these sectors. This causes the overall value of the transported goods to be high. It is expected that, from 2035 onwards, high tech goods and capital goods/spare parts will account for almost half of the transported goods [2].

In Fig. 2.2, four fields of competition in the air freight market are shown. The type of freight on the Y-axis, divided into special and standard freight, and the "distance" at the X-axis in continental and intercontinental.

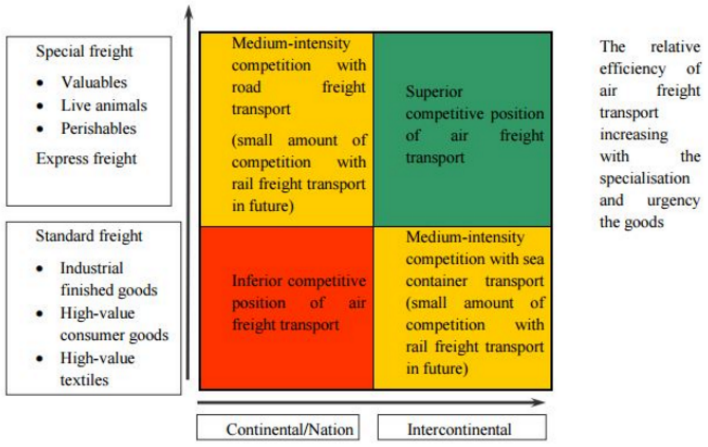

Figure 2.2: Competitive relationships between air freight transport and other transport modes [2]

2.4 Geography

As described in the section 2.1, the general air cargo market is expected to grow. Fig. 2.3 breaks down this growth in the different geographical locations. It can be concluded that the North America - Asia and Europe - Asia routes are expected to still be the two largest markets. The most important geographical trend is visible in the growth of the Chinese and Indian economies. Consequences of this are that the demand for local transport in Asia will increase. This is clearly visible in Fig. 2.3 as the largest growth rates are observed in the Domestic China and the Intra-Asia markets. Another consequence is that also the North America - Asia and Europe - Asia markets are growing. Their growth rate, however, is lower and more uncertain.

2.5 Competition

When comparing air freight to other forms of cargo transport, it can be seen that air freight is much faster, but also more expensive. Shipping costs per 1 m^3 for sea freight are somewhere between \$174 and \$280, and for air freight approximately \$650. From another perspective, sea, rail, road, and air freight costs are \$0.007, \$0.025, \$0.251, and \$0.588 per ton-mile (for short/medium range) respectively [2]. It is expected that these costs will remain lower than air transport and that competing on costs will not be possible.

When looking more specifically into the air cargo market, two forms of air cargo transport are identified. The first category is dedicated to freight flights and the second is belly freight. Globally, more than half of the air cargo is transported by dedicated air cargo aircraft [3]. Especially when both long-range and frequent service are required, dedicated air cargo aircraft are beneficial. A visible trend is that

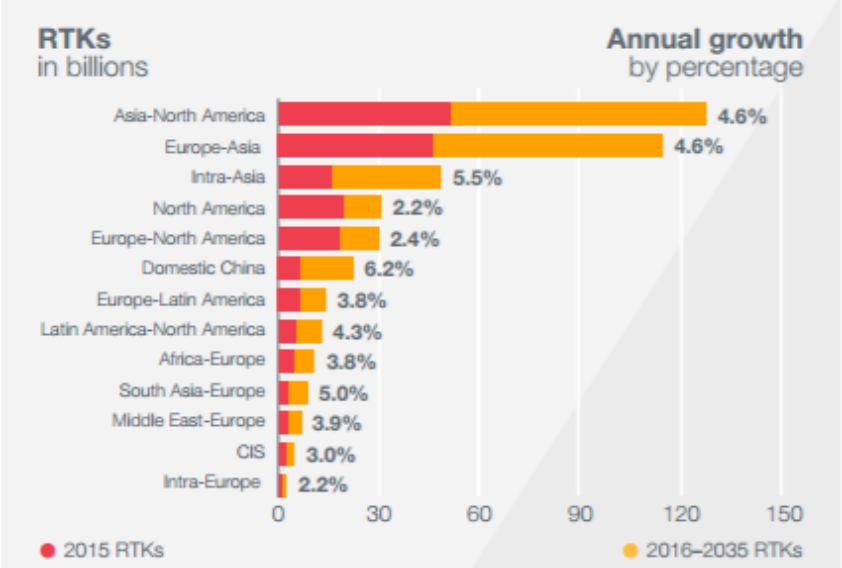

Figure 2.3: Forecast Air Cargo Growth [2]

the percentage of cargo transported with dedicated cargo aircraft instead of belly freight is increasing. This is due to the increasing demand for large volumes and high frequencies [3]. Furthermore trends of major companies such as Airbus and Boeing suggest that they will continue to focus on improving existing aircraft, such as the A320 NEO or B737 Max, into state of the art technologies [2]. This can be explained as the financial risks involved with developing completely new aircraft will still be a major limiting factor. In the short haul market category, there may be introductions of new aircraft models or new companies entering the market. Existing aircraft such as the Cessna Caravan, PC-12, and BN Islander may start to be replaced by more modern aircraft [2]. It is important to note that the rise of new carriers from China, the Middle East, and Turkey will set the price [2].

Although the UAV sector is rapidly evolving, there are no detailed plans for developing unmanned cargo aircraft yet. The main developments for large unmanned systems have mainly taken place in the military[1]. However, there are organizations and platforms like *Platform Unmanned Cargo Aircraft* [2] which provide platforms to exchange knowledge and ideas. Although predictions are not detailed, the UAV market is expected to grow rapidly the coming twenty to forty years. This indicates an increase in competition in the unmanned aircraft segment.

2.6 Conclusion

After performing the market analysis, many clear trends and needs are apparent. It can be concluded that the market will continue to grow steadily and express freight will be the bulk type of cargo transported. Still, load factors are relatively low for cargo transport. A future market opportunity therefore might be combining the required ranges with smaller aircraft, and hence lower OEW, to eventually lower the operating costs. More of these aircraft can operate more frequently and hence can cater better to the express freights. Since it is not expected that major companies will develop new cargo aircraft, and short to medium haul (Intra-Asia & Domestic China) transportation will grow significantly, a reconfigurable aircraft that can fly all these distances should be profitable. It is furthermore expected that unmanned operations will drive costs down as less piloting is needed, while they also allow for dangerous goods to be transported.

[1] http://www.aircargonews.net/news/single-view/news/is-the-air-cargo-industry-ready-for-an-unmanned-aircraft-revolution.html, visited on May 1, 2017

Chapter 3

Mission Analysis

From the market analysis described in chapter 2, an existing gap in the cargo market is apparent, and is used to design a freighter aircraft fulfilling multiple specific market needs. This need is described as the mission need statement, being:

"A flexible air cargo solution for varying operating conditions which is competitive with the current market is needed by 2035"

To fulfill this need, the mission is analyzed by firstly stating the flight profile of the to-be-designed aircraft in section 3.1. Then, the functions which the aircraft should be able to perform are stated in a functional breakdown structure and a functional flow diagram, presented in section 3.2. Lastly, the concept of the aircraft is discussed in section 3.3.

3.1 Flight Profile

The aircraft which will be designed in this report will fly according to a specific flight profile, as depicted in Fig. 3.1. However, no loiter is included in the profile as the reserve fuel is assumed to be higher than that for regular cargo flights.

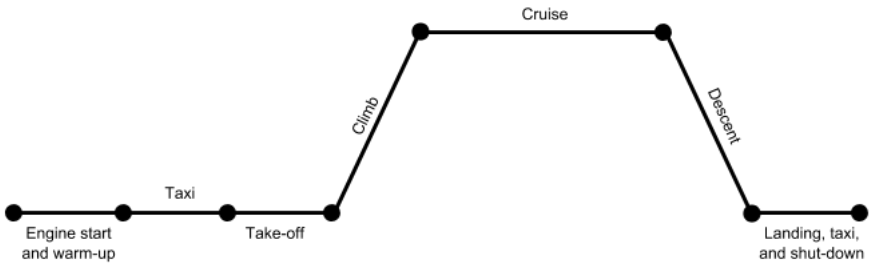

Figure 3.1: Flight profile diagram for the to-be-designed aircraft

3.2 Mission Functions

The functional flow diagram and the functional breakdown structure, shown in Fig. 3.2, 3.3, and 3.4, depict the functions which the aircraft has to fulfill. For a more detailed functional breakdown structure, please refer to App. B.

3.3 Aircraft Concept

To be able to fulfill both the mission need statement and the mission functions, a specific freighter aircraft will be designed which is not only unmanned, but also reconfigurable. From here on, the aircraft is named and referred to as the 'ModuLR', and will have three different wing-tail-engine combinations, based on the missions it needs to operate. The fuselage will thus remain constant for all different configurations. A service model will assure that operators are able to enjoy a low upfront cost, inasmuch as only the fuselage is bought. The wing-tail-engine combination, on the other hand, is leased and can be altered at any moment in time at designated hubs.

Three different configuration can be opted for, from now on, are referred to as the ModuLR-100, ModuLR-200, and ModuLR-300 versions.

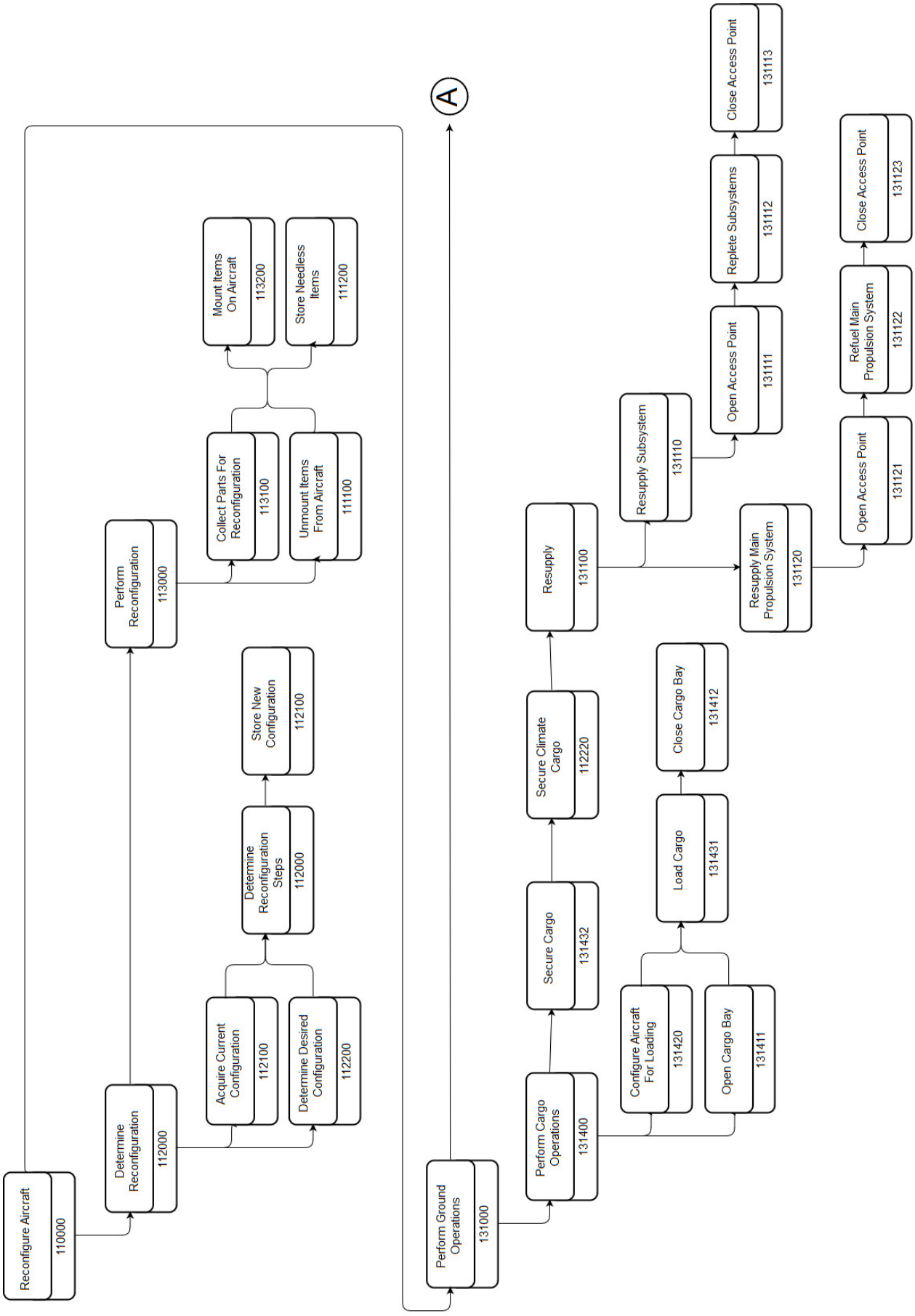

Figure 3.2: Functional Flow Diagram, part 1

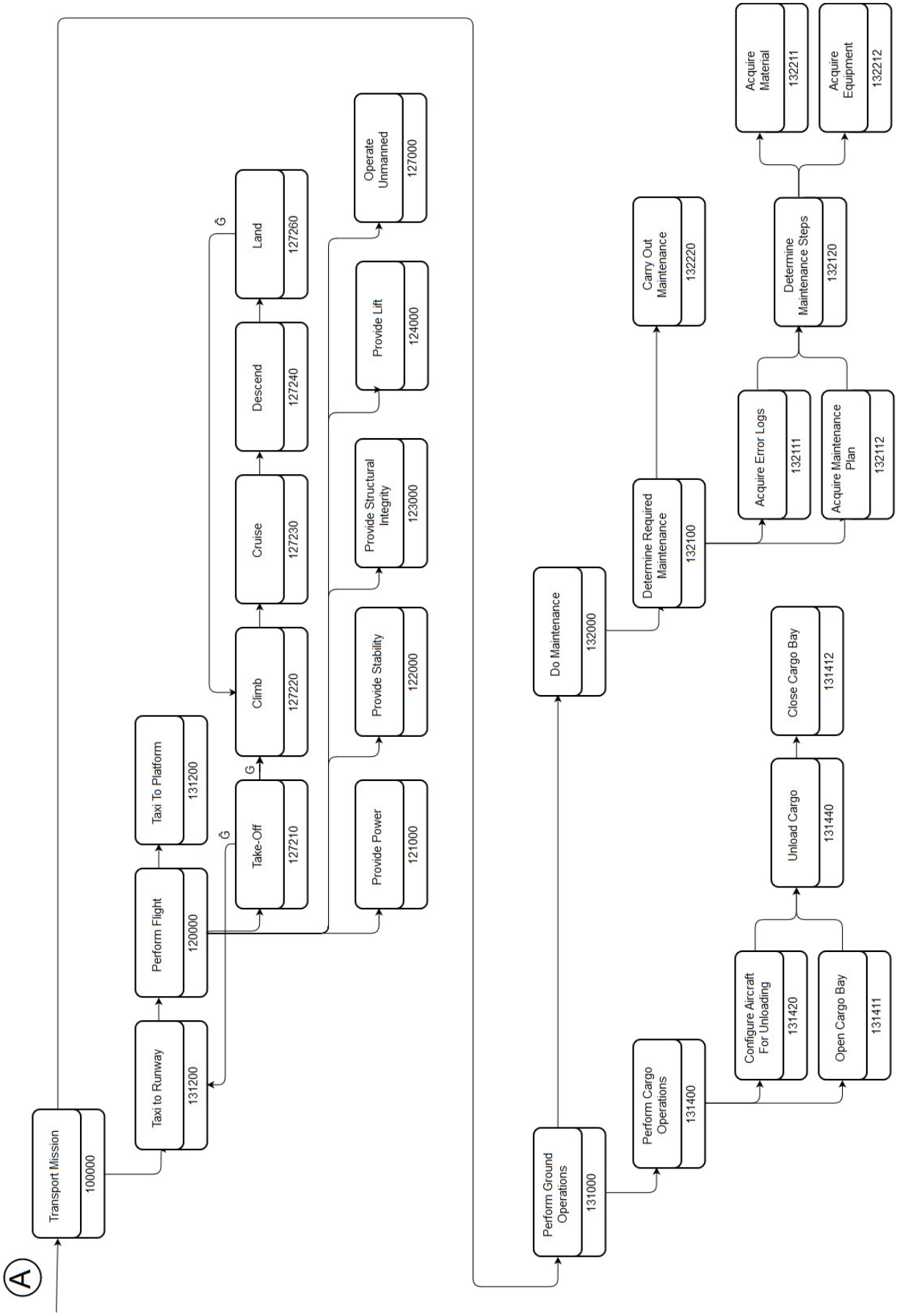

Figure 3.3: Functional Flow Diagram, part 2

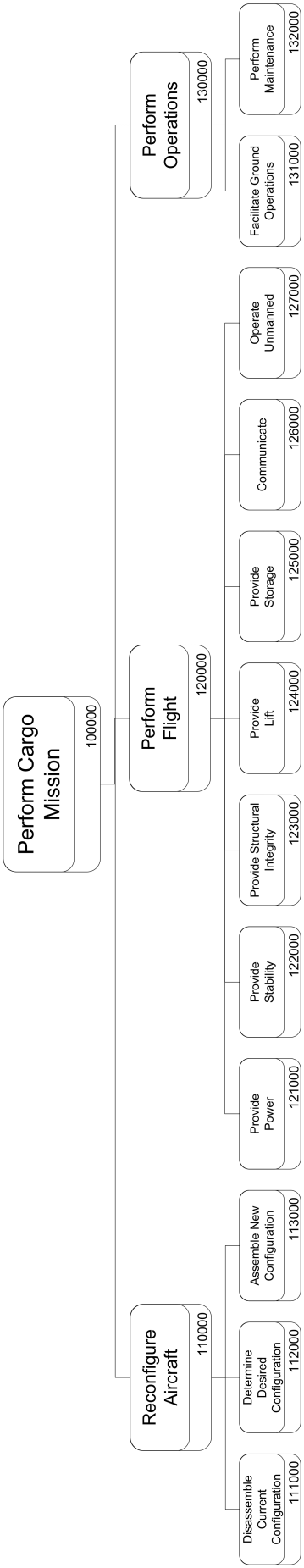

Figure 3.4: Functional Breakdown Structure, part 1

ModuLR-100

- Range: 1000 nmi;
- Payload: 1000 kg;
- Runway length: 3000ft.

ModuLR-200

- Range: 2000 nmi;
- Payload: 5000 kg;
- Runway length: 8000ft.

ModuLR-300

- Range: 4000 nmi;
- Payload: 10000 kg;
- Runway length: 10000 ft.

The detailed design of these configurations will be elaborated upon in the next chapters of this report. Starting off with the preliminary design in chapter 4, followed by the detailed design of all different design areas in chapters 5, 6, 7, and 8. Fig. 3.5 shows a sketch of how the aircraft could look like after detailed design.

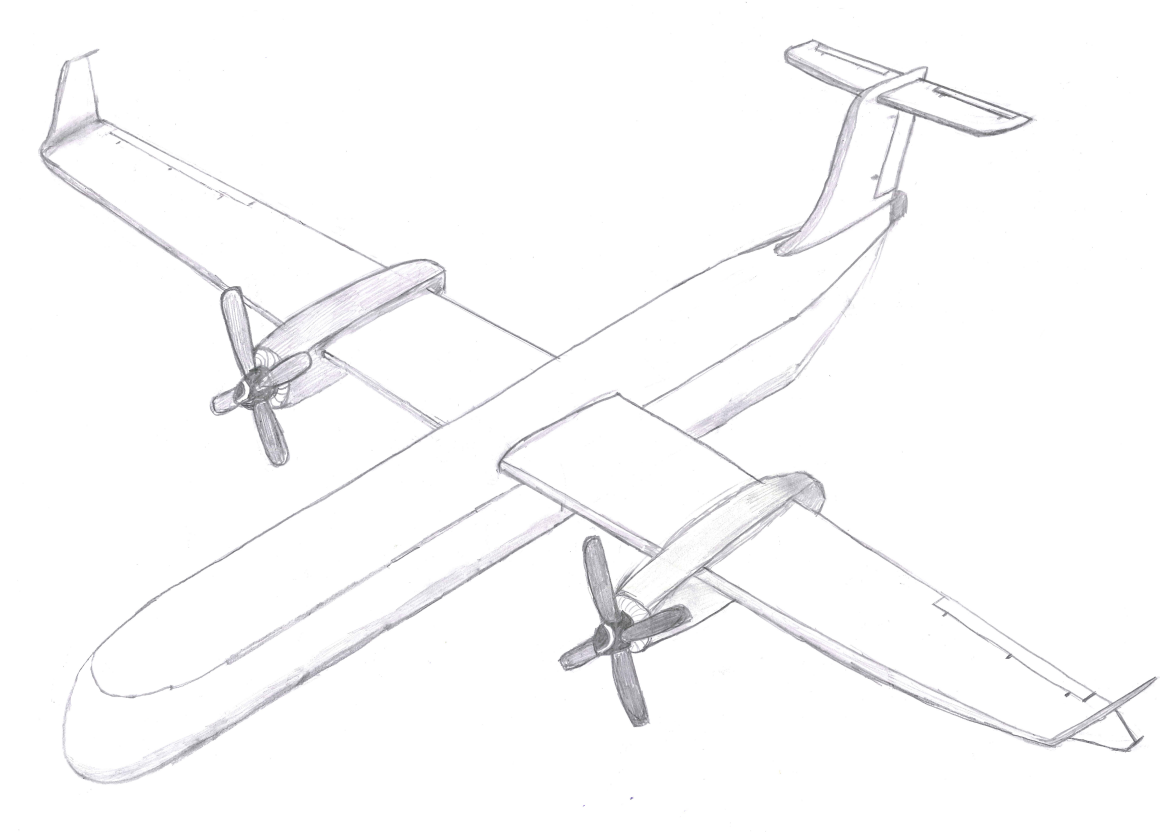

Figure 3.5: Sketch of the concept aircraft

Chapter 4

Preliminary Design

This section describes the method and results attained during the preliminary designing of the ModuLR. The preliminary design phase consists of a fully-automated Class I and Class II sizing, elaborated on in section 4.1 and section 4.2, respectively. From these, the mass and power budgets are allocated in section 4.4, to the respective subgroups.

4.1 Class I Sizing

The Class I sizing builds upon the preliminary weight estimation performed in the mid-term report [1]. In addition to this, wing loading diagrams are drawn, as can be seen by the designed and implemented graphical user interface in Fig. 4.1, where the take-off and stall speed requirements are limiting the design. From this, the wing surface area and take-off power are computed.

Moreover, a preliminary wing design is performed using the computed wing surface area. During this iterative design, the ailerons and flaps are checked to see whether they meet the $C_{L_{max}}$ requirements with the available space within the wing ($\frac{C_f}{C}$). Firstly, the $C_{L_{Max}}$ for the clean wing is estimated, after which statistical relations are used for $\Delta C_{L_{max}}$ during take-off and landing [5].

Furthermore, a preliminary sizing for the empennage, landing gear, and stability and control is implemented into the Class I sizing according to the methods described in Roskam [5].

Lastly, the drag polar is constructed according to the method by Roskam [5], resulting in a new L/D value. In case this new value differs more than 5% from the initial L/D value used as an input for the Class I sizing, the Class I sizing will be performed again. This iteration can be seen in the code flow chart in Fig. 4.6.

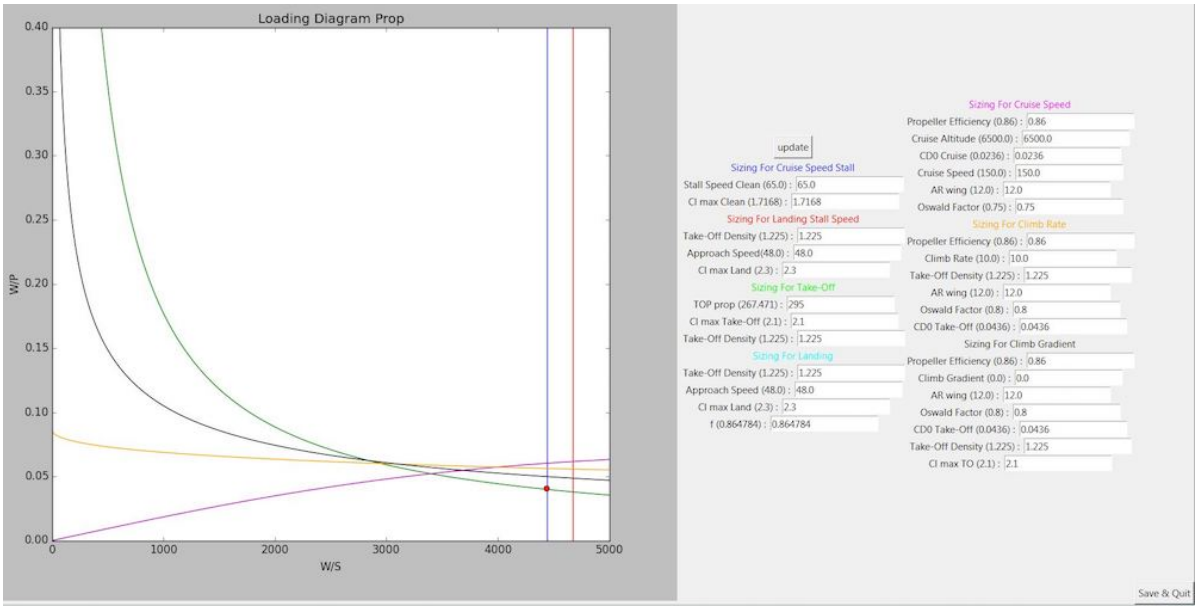

Figure 4.1: Graphical user interface for the wing loading diagrams

4.2 Class II Sizing

The Class II methods to construct the V-n diagram and to estimate airplane component weights are based on Roskam [6]. During the design of the different versions of the ModuLR, the Torenbeek method for commercial transport airplanes is employed, where all equations have a statistical basis.

4.2.1 V-n Diagrams

The V-n diagrams, which are shown in Fig. 4.2, are constructed for all ModuLR versions according to FAR25 regulations. The goal is to determine the design ultimate load factors as well as the speeds that the structure shall need to withstand. In particular, V_D and n_{ult} are used during the component weight estimation of subsection 4.2.3. It is important to note that this method only considers flap-up cases.

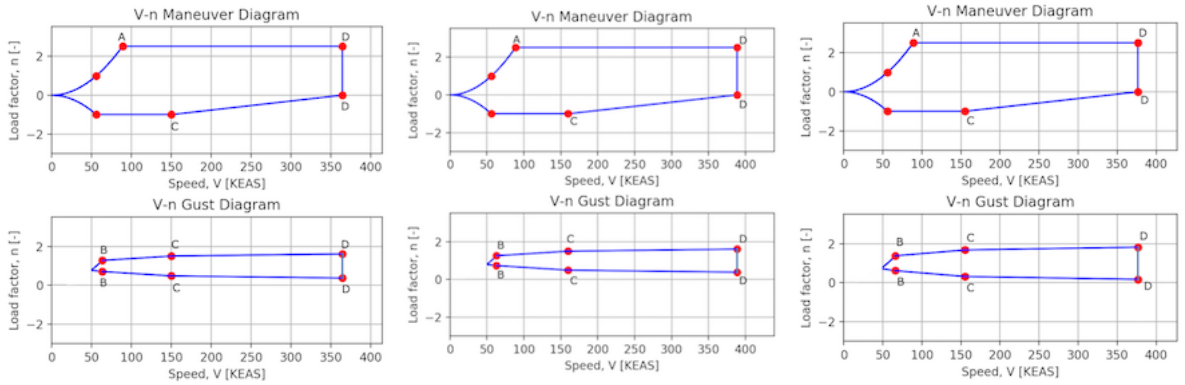

(a) ModuLR-100 (b) ModuLR-200 (c) ModuLR-300

Figure 4.2: V-n maneuver and gust diagrams

4.2.2 Fuselage Design

The ModuLR is designed to be reconfigurable, using the same fuselage for different missions, as discussed in section 3.3. The consequence of this design choice is that the smaller configurations will perform their mission with a fuselage which will be too large for the cargo it is designed for. Therefore, reducing the unused space in the fuselage of the largest configuration is the design objective for the fuselage design. Furthermore, to accommodate cargo that has to be pressurized (discussed in subsection 7.2.2), a circular shape for the fuselage is chosen. A circular shape is the most effective option for resisting the pressure loads. Subsection 7.2.2 discusses the choice for a pressurized fuselage in more detail.

Container management

Today, the aviation industry is based on many standardizations of equipment. This ensures that most aircraft do not need specialized equipment for ground handling, reducing the cost for operators and airports. Therefore, when designing a new product for this market, it is important to implement standardizations as much as possible, in order to increase the feasibility of the final design in terms of operational costs.

With respect to standardized containers, the aviation industry mostly makes use of the Unit Load Devices (ULD). According to IATA[1], around 900,000 ULDs are currently in service. ULDs are further distinguished between containers and pallets.

The smallest container is the LD2, which is shown in Fig. 4.3a[2]. Inside the fuselage, two LD2 containers or one LD8 container, which is the same size as two LD2[2] containers, will result in the smallest diameter for the fuselage when making use of containers. In Fig. 4.3b the fuselage with a LD8 is shown, resulting in a fuselage diameter of 3.5 m. However, a large 'empty' area at the top of the fuselage can be seen, producing a significant amount of unused space.

Another option is the use of ULD pallets upon which cargo is stacked and secured with a web net. Pallets are cheaper and lighter than containers, can accept different sizes of cargo, and empty pallets can also be stacked and returned by plane in case of an imbalance in the total network[3]. The result of using a half size pallet, shown in Fig. 4.3c, is shown in Fig. 4.3d from which a fuselage diameter of 2.9 m emanates. As can be seen, the option using the half pallet has less unused space and a smaller diameter which is also beneficial for reducing drag.

[1] http://www.iata.org/whatwedo/cargo/unit-load-devices/Pages/index.aspx, visited on June 9, 2017

[2] http://www.boeing.com/resources/boeingdotcom/company/about_bca/pdf/CargoPalletsContainers.pdf, visited on: June 9, 2017

[3] http://vrr-aviation.com/uld-info/whats-a-uld/, visited on: June 9, 2017

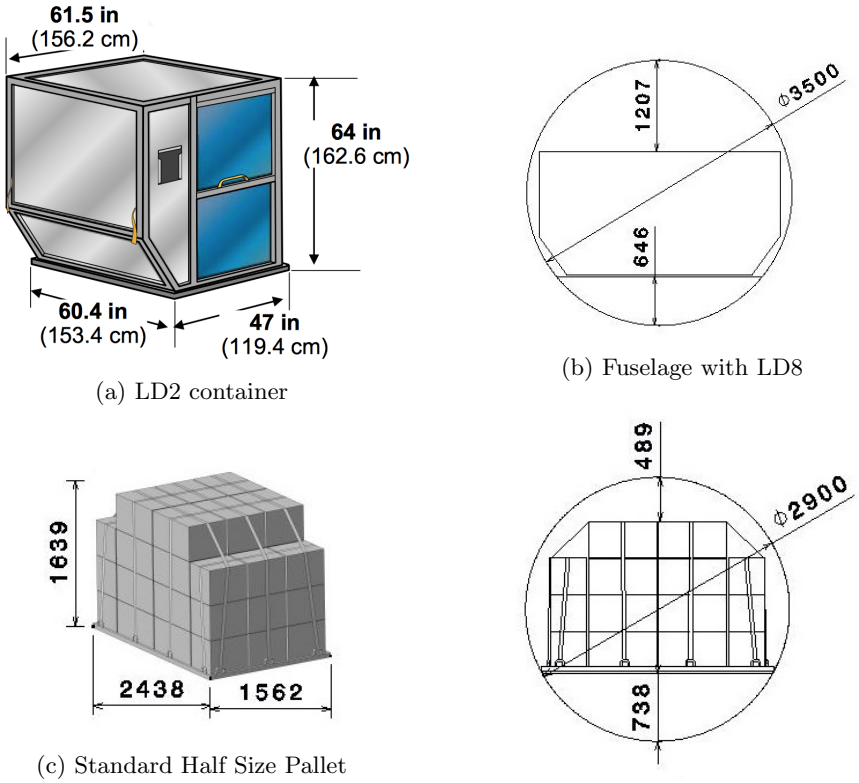

(a) LD2 container

(b) Fuselage with LD8

(c) Standard Half Size Pallet

(d) Fuselage with pallet

Figure 4.3: Figure showing the LD2 container on the top left (a) and the fuselage containing an LD8 container on the top right (b). The bottom left (c) shows a standard half size pallet. The bottom right (d) depicts the pallet from (c) inside the fuselage

Fuselage sizing

With the previous established fuselage diameter, the nose, tail, and total length of the fuselage can be designed. For aerodynamic considerations, the slenderness ratio (length over diameter) is best at 0.3 [7]. However, most aircraft have ratios around 0.1. Thus, to approach the ideal slenderness ratio of 0.3 with a fixed fuselage diameter, the length should be minimized.

The cargo hold length is limited by the amount of cargo that has to be transported. A half size pallet can carry a total of 2366 kg or 5.5 m^3 of cargo. As seen in Fig. 4.3c, the pallet is not completely loaded due to the curves on the top left and right, therefore a maximum of 2151 kg and 5 m^3 is considered. The RUCA-T-REC-AC-2 requirement states that 40 m^3 should be transported, resulting in a total of 8 half pallets. This amount of pallets is enough to carry the maximum cargo weight of 10000 kg defined in requirement RUCA-T-REC-AC-4. With this information, the total cargo hold length is found to be 12.50 m. Due to a constant fuselage requirement RUCA-T-REC-AC-1 and 3, and RUCA-T-NOM-CN-2 is also met.

The nose cone length can be approximated using the ratio for nose cone length over diameter. Typical values for this ratio are 1.2 – 2.5 [7] and, when considering the slenderness ratio, the lowest ratio is chosen resulting in a length of 3.48 m. The same procedure is used for the tail cone with typical values of 2 – 5, resulting in a length of 5.8 m using the lowest ratio.

The shape of the nose cone is not constraint by the presence of a cockpit, so it can be optimized for performance which will be done in section 6.2. The shape of the tail cone is constrained by two angles for the best performance. The first angle is the rotation angle, defining the bottom part of the tail cone, and the second angle is the divergence angle which should be 24 degrees or lower. The resulting shape of the fuselage and lengths can be seen in Fig. 4.4.

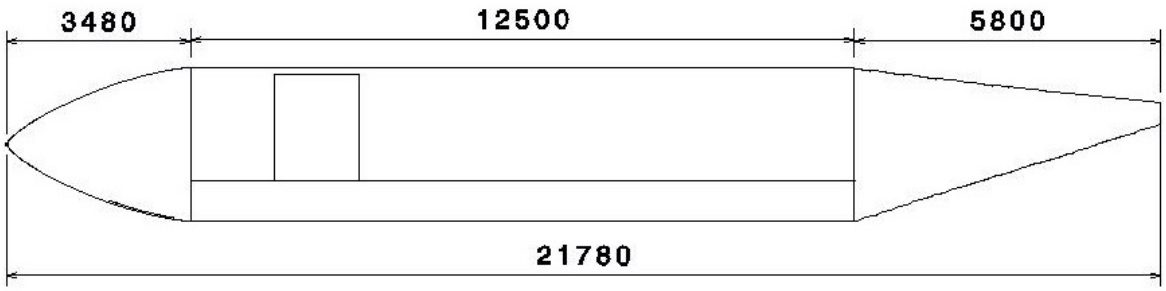

Figure 4.4: Fuselage dimensions

Cargo door
In the mid-term report [1], the ModuLR was proposed to both have a cargo door at the rear of the fuselage and a movable nose for nose loading. However, the nose of the ModuLR will be filled with the equipment necessary for unmanned flying, including the radar and antenna systems. Using the nose for loading will increase the structure weight and increase the difficulty of the system arrangements in the nose. Furthermore, the size and location of the largest wing would not allow for a cargo door behind the wing. Therefore, the choice has been made to only use a cargo door in the forward side of the fuselage. The cargo door also allows the cargo to be accessible for customs meeting requirement RUCA-T-OPS-GH-4. Considering the amounts of cargo pallets, the time decrease when using two doors will be minimal and the lower number of crew needed during cargo loading is an advantage. Also, locating the cargo door at the front is beneficial for the static stability during cargo loading and unloading. However, a downside of not having a nose loading door is the limitation on the size of the cargo.

4.2.3 Component Weight Estimation

As a start, the empty weight is split into three different groups: structure weight, powerplant weight, and fixed equipment weight. Within these groups a detailed division is made to determine the component weights. Furthermore, the fixed equipment weight, as well as the fuselage and landing gear weight remain constant for all three versions of the ModuLR, as described in section 3.3.

To be able to use this method, however, the MTOW and OEW values from the Class I sizing are used as a first input for the Class II sizing. When the OEW output value from this Class II sizing differs more than 10% from the Class I sizing, Class I sizing is performed again with the new Class II values. When the OEW output value from Class II sizing differs less than 10%, yet more than 1% from the input value, an iteration within Class II weight estimation is to be performed. Lastly, when the OEW output value differs less than 1% from the input value, the iteration is stopped. The entire iteration procedure can be found in Fig. 4.6. The Class II component weights, as shown in Tab. 4.1, are used during the mass budget allocation as will be explained in section 4.4.

4.3 Class-I and -II sensitivity analysis

The preliminary design method is the starting point of the detailed subsystem design. Since starting parameters can change during the design process it is important to know how sensitive the method is for changes in key system parameters. The influence of the key requirements: range, payload, and runway length are analyzed. The cruise speed parameter is also analyzed because of the influence it has on different subsystem designs. In Fig. 4.5, the influence of the change in these parameters on the MTOW can be seen. The range parameter has a large influence on the MTOW of the design, since a larger range results in a higher fuel weight and in turn a higher weight for the subsystems. It can also be seen that a reduction in runway length increases the MTOW, however an increase has almost no effect on the MTOW. This is because other factors are limiting for the design based on a longer runway length. A change in the payload parameter has a linear effect on the MTOW. It can be seen that decreasing the cruise speed has little effect on the MTOW, since other factors will have a limiting effect on the design.

From this, it can be seen that the method is most sensitive to a change in the range requirement and runway length.

Table 4.1: Class II component weight estimation according to Roskam [6]

Subgroup	Mass [kg]		
	ModuLR-100	ModuLR-200	ModuLR-300
Wing	3240	5800	13230
Empennage	540	864	1620
Engines	962	1434	3600
Nacelle	490	655	1013
Fuselage	2100	2100	2100
Landing gear	2972	2972	2972
Flight control system	1014	1014	1014
Fuel system	388	562	685
Hydraulic, pneumatic & electrical system	528	528	528
Instrumentation, avionics & electronics	355	355	355
Air-conditioning & pressurization	19	19	19
Oxygen system	304	304	304
Auxiliary power unit	3545	3545	3545
Furnishings	458	458	458
Cargo handling equipment	352	352	352
Auxiliary gear	341	341	341
Paint	549	945	1328
Propeller	200	253	358
Propulsion system	3240	5800	13229
Total	18357	22501	33822

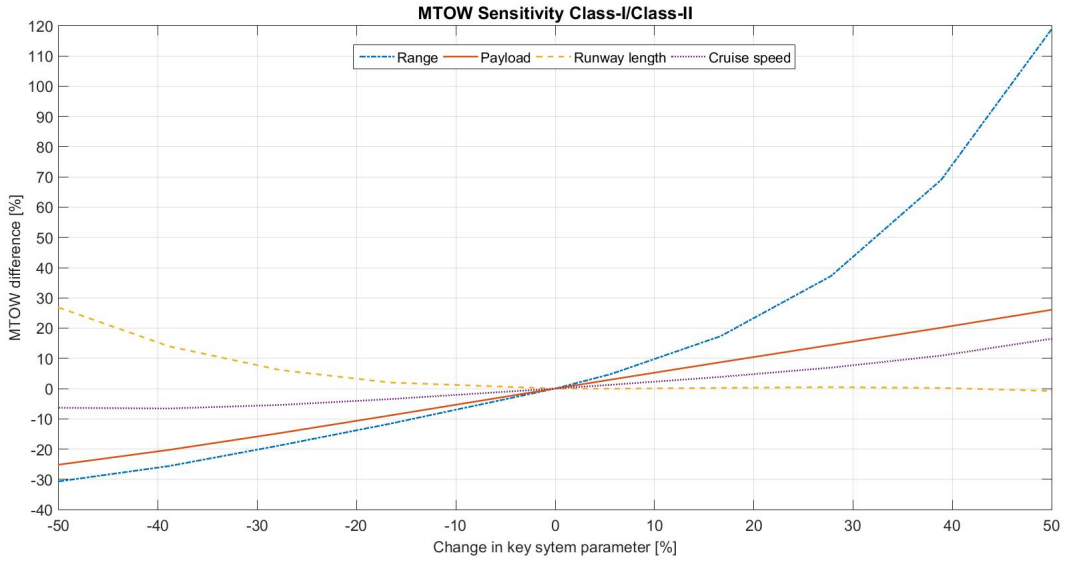

Figure 4.5: Sensitivity analysis on the Class I and Class II sizing

4.4 Budget Allocation

This section will elaborate on the power and mass budget allocation. For both, a contingency factor of 20% is taken into account for the uncertainty in the early stage of the design. All budgets are then used as a requirement for further design of the subsystems.

4.4.1 Mass

The weight budget allocation is done by means of the outcome of the Class II weight estimation from section 4.2.3. It is important to note that in Tab. 4.1, the contingency factor was not taken into account.

4.4.2 Power

The electrical power budget is analyzed during the most critical load case and is allocated with the use of the method described in Roskam [8]. Here, the McDonnell Douglas DC-10 is used as a reference aircraft. However, due to the age of the DC-10, also the electrical load analysis from [9] is used. Tab. 4.2 shows the power budget allocation, including the 20% contingency factor. The flight control and hydraulics were allocated more electrical power due to the fact that the ModuLR versions are unmanned and that electrohydrostatic pumps are used, respectively.

Further details concerning the electrical system are described in chapter 9.1.

Table 4.2: Power budget allocation

Subgroup	**Maximum Power [VA]**
Exterior lighting	570
Fuel	2280
Hydraulics	3000
Flight control	12000
Electrical power	9480
Miscellaneous	300
Total	27630

The flowchart in Fig. 4.6 depicts the entire flow during both the preliminary Class I and Class II sizings, as well as the detailed design. Every part within the flowchart has been programmed in either Python or Matlab and updates a single data matrix with all input and output variables. This matrix, consisting of over 1200 parameters, contains the complete aircraft design

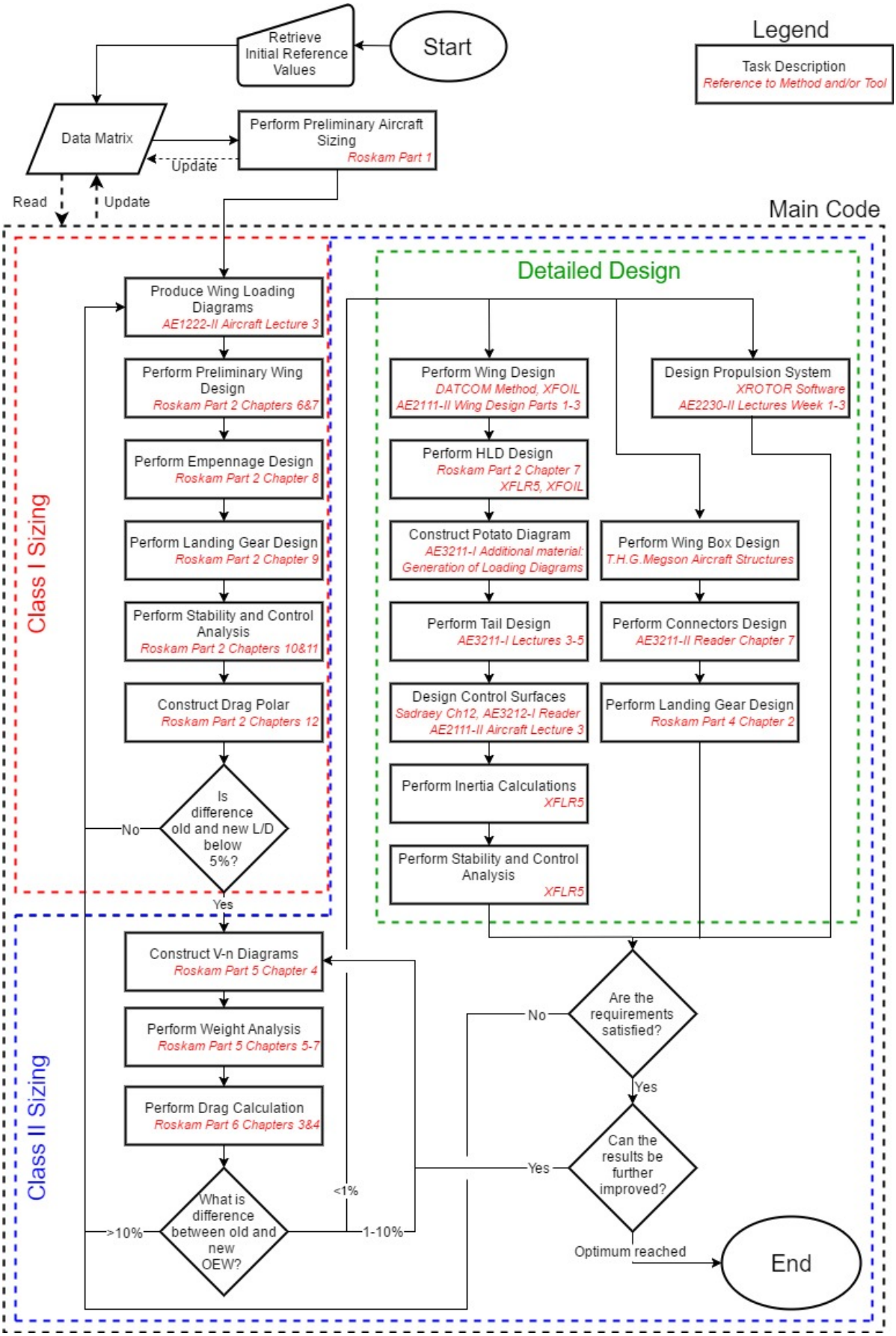

Figure 4.6: Code flow chart

Chapter 5

Performance and Propulsion

In this chapter, the performance characteristics and propulsion system of the ModuLR are presented. Even though variables are constantly exchanged between both areas, the aircraft performance is described first in section 5.1 followed by the propulsion system design in section 5.2. The design of the aircraft performance and the propulsion system is based on the FPP requirements from the compliance matrix in chapter 12. The adherence to these requirements is discussed in the combined conclusion section 5.3.

5.1 Performance

The aircraft's performance consists of various elements such as range, take-off and landing distances, and environmental considerations which includes noise and greenhouse gas emissions. The stability and controllability performance of the aircraft are however described in chapter 6.

5.1.1 Method

The calculation methods of the performance parameters are elaborated on in the subsequent sections.

Range Performance Calculation

A general, but essential performance indicator is the attainable range of the cargo aircraft while carrying a certain amount of payload and fuel. This section describes the method on how the payload-range and fuel-range relations are obtained, in the order that they are mentioned. The method is applicable to all three configurations.

Before proceeding with the formulas, the main code has been run and terminated successfully to ensure that all required parameters are available and have converged to optimum values. For the payload-range relation, the Breguet range formula for propeller aircraft [10] is used to obtain the range in Eq. 5.1. The fuel fraction in cruise is calculated according to the fuel fractions method [10] in Eq. 5.2.

$$R = \frac{\eta_{prop}}{g_0 \cdot c_p} \frac{C_{L_{cr}}}{C_{D_{cr}}} ln\left(\frac{W_4}{W_5}\right) \qquad (5.1)$$

$$\frac{W_5}{W_6} = \frac{\frac{W_2}{W_s}\frac{W_3}{W_2}\frac{W_4}{W_3}\frac{W_5}{W_4}\frac{W_7}{W_6}\frac{W_e}{W_7}}{1 - \frac{m_{f,used}}{MTOM}} \qquad (5.2)$$

Since reserve fuel is present, $m_{f,used}$ equals the total carried fuel mass divided by a factor of 1.1. The variables that remain constant for all the configurations are summarized in Tab. 5.1.

Table 5.1: Constants used for all configurations for range calculations [10]

Constant	Value	Unit	Constant	Value	Unit
$\frac{W_2}{W_s}$ (engine start-up)	0.992	-	g_0	9.8067	m/s^2
$\frac{W_3}{W_2}$ (taxi)	0.996	-	η_{prop}	0.86	-
$\frac{W_4}{W_3}$ (take-off)	0.996	-	c_p	$6.81{\cdot}10^{-8}$	kg/J
$\frac{W_5}{W_4}$ (climb)	0.990	-	ρ_{fuel} [a]	804	kg/m^3
$\frac{W_7}{W_6}$ (descent)	0.992	-			
$\frac{W_e}{W_7}$ (landing, taxi, shutdown)	0.992	-			

[a] https://web.archive.org/web/20110608075828/http://www.bp.com/liveassets/bp_internet/aviation/air_bp/STAGING/local_assets/downloads_pdfs/a/air_bp_products_handbook_04004_1.pdf, visited on: June 22, 2017

Different ranges can be obtained if the payload is exchanged for fuel, so there are three loading cases that are investigated:

1. Carry maximum payload for which the configuration is designed and the remaining mass is fuel;
2. The wing fuel tanks are completely filled and the remainder is payload. If the MTOW does not allow for full wing fuel tanks, then these are filled as much as is allowed and the payload mass will be zero;
3. Carry no payload and the remaining mass is fuel.

For the above cases it is assumed that the MTOW and OEW remain constant, and that additional fuel can be stored in the fuselage if the wing fuel tank capacity is exceeded. The application of Eq. 5.1 for each case yields a set of payload (and fuel) masses linked with specific range values. At this point the payload-range diagram can be plotted. Since the fuel masses have also been determined for the cases, the fuel-range diagram can be plotted as well. As a note, the fuel values used for the plot do not include reserve fuel. Per diagram, three curves are obtained, which represent the three configurations.

Take-off and Landing Performance Calculation

The take-off and landing performances are evaluated according to the lecture slides [11][12]. For the calculations, the assumptions made are as follows:

- The runway is horizontal and dry;
- There is no wind;
- The aircraft weight is constant;
- The thrust vector is parallel to the velocity;
- The ground effect is neglected;
- Climb is steady at screen height.

The take-off performance is analyzed is two ways. First, using the power available the take-off distance is calculated. Next, the required take-off distance and initial guess of power as input are used to calculate the power needed in an iterative process until the required take-off distance value is reached. Eq. 5.3 is used for this process [11].

$$s_{TO,total} = \frac{MTOW V_{LOF}^2}{2g_0(\frac{P\eta_{TO,roll}}{V\eta_{prop}} - \bar{D} - \bar{D}_g)} + \frac{\frac{1}{2g_0}(V_{scr}^2 - V_{LOF}^2) + h_{scr}}{\frac{P/V_{scr} - \bar{D}}{MTOW}} \tag{5.3}$$

In addition, the climb rate and climb gradient are calculated using Eq. 5.4 and 5.5 [13], respectively. Take-off conditions are used for both equations.

$$c = \frac{\eta_{prop} P_{br}}{MTOW} - \frac{\sqrt{\frac{2MTOW}{S\rho}}}{\frac{C_L^{3/2}}{C_D}} \tag{5.4}$$

$$\frac{c}{V} = \frac{\eta_{prop} P_{br}}{MTOW} \frac{1}{\sqrt{\frac{MTOW}{S\rho C_L}}} - \frac{C_D}{C_L} \tag{5.5}$$

The landing performance is evaluated using Eq. 5.6 [12].

$$s_{Land,total} = s_{airborne} + s_{ground} = \frac{\frac{W_{Land}}{2g_0}(V_T^2 - V_A^2) - W_{Land} h_{scr}}{\bar{T} - \bar{D}} + \frac{W_{Land}}{2g_0} \frac{V_T^2}{\bar{T_{rev}} + \bar{D} + \bar{D_g}} \tag{5.6}$$

Greenhouse Gas Emissions Calculation

There are two greenhouse gases that are of interest in this project, CO_2 and NO_x, as they are directly linked to the requirements. Additionally, the analysis of these gas emissions provides insight on how sustainable the design is.

Firstly, the aircraft's CO_2 emissions are calculated using Eq. 5.7, which are presented as the cruise CO_2 emissions divided by FTK (Freight Tonne Kilometer). The division by FTK enables the comparison of the gas emission performance with other aircraft and relates the gas emissions with cargo aircraft performance indicators.

$$\frac{m_{CO_2}}{FTK} = \frac{m_{f,used} \cdot EI_{CO_2}}{\frac{m_{PL}}{1000} \cdot \frac{R}{1000}} \tag{5.7}$$

It is assumed that all aircraft used for the CO_2 emissions calculations make use of the same jet fuel (A-1) that has an Emission Index (EI_{CO_2}) of 3.144 kg CO_2 per kg of fuel[1] given a fuel density[2] of 804 kg/m^3. The values of the other variables on the right hand side of the equation are results from the range performance calculations from section 5.1.1. The analysis is performed for all the aircraft configurations, Boeing 747-400, and few other reference aircraft.

Secondly, the aircraft's NO_x emissions calculations are done according to the DLR method [14], as suggested by the emissions research department of TU Delft's faculty of Aerospace Engineering. The method contains a step by step procedure, which is not presented in this report due to page limitations, although it only contains three steps. The method uses as input parameters the local atmospheric properties, the engine fuel flows with their corresponding power setting, and reference values for EI_{NO_x}. An estimation of the EI_{NO_x} is returned at the end. The used assumptions and conditions are listed below for the ModuLR and the Boeing 747-400, which are the only aircraft used for the NO_x emissions analysis:

- **ModuLR (applicable to all configurations)**: Since EI_{NO_x} data is not available for the engines, a comparable engine (T56-A-19 engine [15]) is used to obtain the EI_{NO_x} versus fuel flow curve. Furthermore, the cruise conditions are used and ISA is assumed for the calculation of atmospheric properties. The fuel flow value comes from the engine properties calculations, which is described in section 5.2. The fuel flow value of a single engine is used in the DLR method;
- **Boeing 747-400**: The assumptions are very similar to the ModuLR's. The reference EI_{NO_x} and fuel flow data are used from the General Electric CF6-80C2B1F engine data [16]. The cruise and ISA conditions are used. The total fuel mass flow during cruise is estimated by dividing the fuel mass by the range and then multiplying by the cruise velocity. For the analysis the fuel flow of a single engine must be used, so the fuel flow is divided by four. Information on the cruise conditions and other parameters of the Boeing 747-400 can be found in the information sheets[3]. The data for the basic Boeing 747-400 with General Electric CF6-80C2B1F engines are used.

Once EI_{NO_x} is obtained, Eq. 5.8 can be used to calculate the NO_x emission performance.

$$\frac{m_{NO_x}}{FTK} = \frac{m_{f,used} \cdot EI_{NO_x}}{\frac{m_{PL}}{1000} \cdot \frac{R}{1000}} \tag{5.8}$$

Noise Emissions Calculation

To investigate the noise emissions of the ModuLR, and to compare that with a Fokker 50 due to requirement RUCA-C-ENV-1, the Integrated Noise Model (INM) software is used. The software is provided by the Air Transport and Operations (ATO) section of the faculty of Aerospace Engineering of TU Delft.

The INM requires specific noise data from the engine to be able to model the noise or Sound Exposure Level (SEL) contour. The XROTOR software [17] does return the sound levels in dB of the engine, but gives no data on SEL nor Effective Perceived Noise Level (EPNL) which are required as input data for the INM. The use of XROTOR is further elaborated in section 5.2. Thorough analysis of the engine and airframe noise requires extensive research and cannot be performed within the given time of this project. Therefore a comparable but slightly more powerful engine is used, which already exists in the INM database. The chosen engine is the 501D13 turboprop which has similar properties as the ModuLR's, but delivers 2800 kW of power [18] compared to the ModuLR's 2645 kW. Inside the INM, various settings are changed to model the noise contour, ranging from runway specifications to aircraft data. The entire setup is changed with the help of the user manual [19]. Firstly, the airport location was set 0 for both lateral and longitudinal coordinates, and the elevation was also set to 0. The civil aircraft of interest are then included, which are the DHC830 and a modified copy of the C-130E that will represent the ModuLR. Due to requirement RUCA-C-ENV-1, the Fokker 50 SEL contour must be compared to the ModuLR's. However, the INM sees the DHC830 as a replacement of the Fokker 50. For certification purposes, three reference location points[4] are added afterwards. Next, one runway is defined with an

[1] https://www.eia.gov/environment/emissions/co2_vol_mass.php, visited on: June 22, 2017

[2] https://web.archive.org/web/20110608075828/http://www.bp.com/liveassets/bp_internet/aviation/air_bp/STAGING/local_assets/downloads_pdfs/a/air_bp_products_handbook_04004_1.pdf, visited on June 22, 2017

[3] http://www.boeing.com/resources/boeingdotcom/company/about_bca/startup/pdf/freighters/747−400f.pdf, visited on June 22, 2017

[4] https://www.icao.int/Meetings/EnvironmentalWorkshops/Documents/Noise-Certification-Workshop-2006/Depitre_4.pdf, visited on June 25, 2017

arbitrarily chosen length of 3.5 km and the tracks are straight extensions of the runways with each having a length of 100km. In the following step, the ModuLR data from Tab. 5.2 are inserted.

Table 5.2: ModuLR input data for the INM

Parameter	Value	Units
Max Gross Take-off Weight	64517	kg
Max Gross Landing Weight	64517	kg
Max Landing Distance	2036	m
Noise	501D13	-
Number of Engines	4	-
Static Thrust	5067	lbf

The flight profiles are left unmodified as well as the flap and general coefficients, since those require data that come from measurements [19]. Only after obtaining the required data, the coefficients can be calculated using a specific method [20]. There is one departure flight added, and run settings are adjusted such that SEL is calculated and that the lower and upper boundary values are set to 45 and 85dB respectively.

5.1.2 Results

In this section, the results of the analyses described in section 5.1.1 are described in the same structured way.

Range Performance Results

The payload-range and fuel-range diagrams are presented in Fig. 5.1a and 5.1b, respectively. Referring to the diagrams, there is no kink at the point where the fuel tanks in the wing are fully loaded because any additional fuel can be kept inside the fuselage.

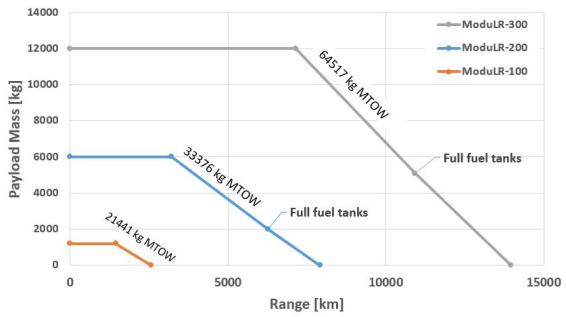

(a) The payload-range diagram of the ModuLR

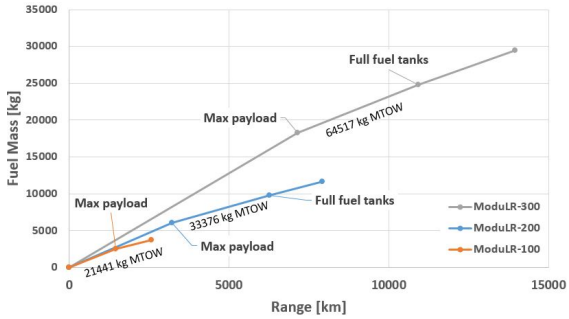

(b) The fuel-range diagram of the ModuLR

Figure 5.1: The payload-range and fuel-range diagram of all ModuLR configurations

Take-off and Landing Performance Results

The findings from the take-off, landing, and climb calculations are summarized in Tab. 5.3.

Table 5.3: Take-off, landing , and climb performance of all configurations

Parameter	ModuLR-100	ModuLR-200	ModuLR-300
Take-off distance [m]	914.4	2120.3	3048.0
Landing distance [m]	903.3	1511.3	2035.8
Climb rate [m/s]	12.9	7.06	7.23
Climb gradient [-]	0.233	0.119	0.112
Required power per engine [kW]	2645	2189	2111

Greenhouse Gas Emissions Results

In Tab. 5.4, the findings from the greenhouse gas emissions analysis are summarized. The variables correspond with the ones used in Eq. 5.7 and 5.8. In the gas emission per FTK columns the percentage in difference with respect to the Boeing 747-400 are indicated. It is assumed that the 747-400 carries 70% of its payload capacity for the chosen range.

Table 5.4: CO_2 and NO_x emissions performance using the Boeing 747-400 as reference (0%)

Aircraft Type	m_{fuel} [kg]	EI_{CO_2} [kg/kg]	EI_{NO_x} [kg/kg]	R [km]	m_{PL} [kg]	CO_2/FTK [kg/(km*1000kg)]	NO_x/FTK [kg/(km*1000kg)]
ModuLR-100	2524	3.144437	0.008228	1443	1200	4.583368 (+537%)	0.011993 (+293%)
ModuLR-200	6028	3.144437	0.008342	3215	6000	0.982616 (+37%)	0.002607 (-14%)
ModuLR-300	18256	3.144437	0.008342	7144	12000	0.669616 (-7%)	0.001777 (-41%)
Boeing 747-400[a]	119170	3.144437	0.013215	9300	56000	0.719513 (0%)	0.003055 (0%)
Aeritalia G.222[b]	8110	3.144437	-	4630	3800	1.449437 (+101%)	-
An-72A[c]	5450	3.144437	-	800	10000	2.142148 (+198%)	-
C-130[d]	20108	3.144437	-	4000	19355	0.816693 (-14%)	-

[a] http://www.boeing.com/resources/boeingdotcom/company/about_bca/startup/pdf/freighters/747−400f.pdf, visited on June 24, 2017
[b] http://www.flugzeuginfo.net/acdata_php/acdata_g222_en.php, visited on June 24, 2017
[c] http://www.aerospaceweb.org/aircraft/transport−m/an72/, visited on June 24, 2017
[d] http://www.aerospaceweb.org/aircraft/transport−m/c130/, visited on June 24, 2017

Noise Emissions Results

Only the largest configuration, the ModuLR-300, is used in the model since it is the noisiest of all three configurations by having 4 engines and the largest airframe. This implies that if this configuration meets the noise requirements, then the other configurations meet them as well. The SEL contour of the DCH830 is presented in Fig. 5.2 and the ModuLR's in Fig. 5.3. Notice that for each figure three circles are placed that represent the approach, lateral and flyover points respectively if seen from left to right. These refer to the points as indicated in the ICAO noise standards [21], which is used for certification.

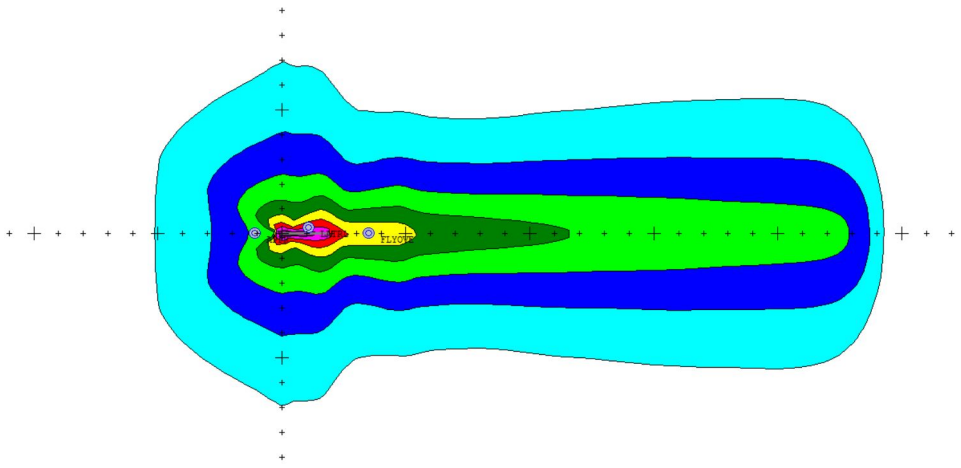

Figure 5.2: The DCH830 (the Fokker 50 substitute) SEL contour at departure, where the border between green and dark blue is 55 dB

5.1.3 Verification and Validation

The verification and validation (V&V) of the results and used tools are elaborated on in the following subsections.

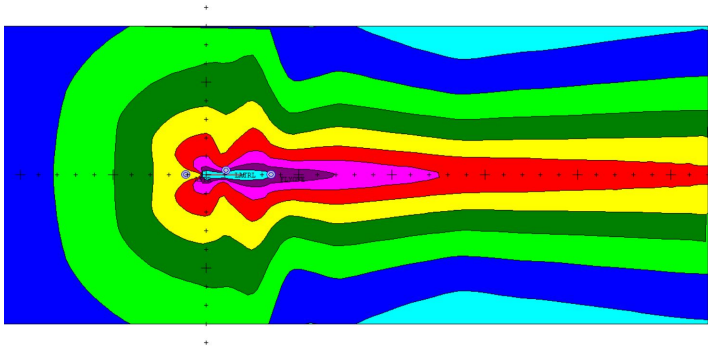

Figure 5.3: The modified C-130E (the ModuLR-300 substitute) SEL contour at departure, where the border between green and dark blue is 55 dB

Range Performance

Analysis of dimensions is done for Eq. 5.1 and 5.2 and are deemed correct. To check whether the formula are written correctly in the spreadsheet, each variable is substituted by 0, one at a time, to check if the outcome is logical. Furthermore, it is checked whether the input values make sense, e.g. the sum of OEW, m_{fuel}, and m_{PL} should return the value of MTOM minus trapped fuel. Additionally, it is checked that the wing fuel tank can hold enough fuel required at nominal payload for all configurations. Also, the units are checked whether the correct SI units are used and dimensionless if the variable is a coefficient. The calculations are considered verified after performing these checks. Validation is done by comparing the results with the performance[5] of a Fokker 50. The Fokker 50 flies 2300 km with 2500 kg of fuel and 3500 kg payload whereas the ModuLR-200 flies 3908 km with 5000 kg payload using 6937 kg fuel. So the ratio of fuel mass over FTK of the Fokker 50 and ModuLR-200 are 0.29 and 0.36 respectively, and validates the results as those numbers are of the same order.

Take-off and Landing Performance

The results of the equations used in the methodology, section 5.1.1, are calculated using Python. Therefore the syntax, input and output variables, and values of those variables are checked for inconsistencies and typing errors. Especially the units of variables have been converted to SI units when necessary. The equations have undergone the same procedure and by changing input values one-by-one, the outputs are checked whether they change as they should. For instance, by setting P_{br} to zero in Eq. 5.4 and 5.5 the outcome will be negative. The dimensional analysis is performed for all used equations from Eq. 5.3 to 5.6, and they are deemed correct at the end. The code solves the equations in the order that they are presented in the report and runs without giving any errors. It returns correct values using examples from lecture slides [13]. All in all, the code is then considered as verified. Due to the lack of available data and time constraints, only the ModuLR-300's take-off and landing performance is compared with the P-3 Orion, which has around the same MTOW and OEW. The P-3's take-off run and landing distance are 1297.3 m and 883.9 m respectively, which are significantly lower than ModuLR's as seen in Tab. 5.3. Data of the P-3 Orion are provided on the manufacturer's website[6]. To complete the validation analysis, for each configuration more reference aircraft must be identified and the missing data must be requested directly from the manufacturers instead of searching the internet for data.

Greenhouse Gas Emissions

Similar to how the range performance is verified, dimensional analysis is performed and the results' behavior is observed when variables are changed to 0 one at a time. Moreover, the conversion factors used to convert imperial units to metric units are checked. Intermediate results are displayed to check whether the values are in the correct magnitude, e.g. the range in km multiplied by payload mass in tonnes should not result in a value smaller than 1000 or yield a negative number. The calculations are thereby verified. For validation, the results are compared with values of reference aircraft, for example the CO_2 emissions are compared with three other comparable cargo aircraft as seen in the bottom rows

[5] http://www.flyfokker.com/sites/default/files/FLYFokker/FlyFokker_PDF_Fokker50_Performance.pdf, visited on June 24, 2017

[6] http://lockheedmartin.com/us/products/p3/p-3-specifications.html, visited on: June 26, 2017

of Tab. 5.4. All those CO_2/FTK values are of the same magnitude, so they indeed make sense. As for the validation of the DLR method which is used to calculate NO_x/FTK, it is described in reference [14].

Noise Emissions

The INM tool has already been verified and validated by FAA[7] and so is the INM database. Fig. 5.2 is therefore accurate enough to represent the Fokker 50 for this project, as only preset values are used for that aircraft and its engines. For the verification of ModuLR's noise emissions, it is assumed that the calculations done by the INM are correct since realistic input values are used and are within the bounds that the program can handle. Moreover, many parameters are kept at their preset values. The execution of the program does not return any error messages and no discretization errors are found in the output, i.e. the noise contour. Only near the borders of the grid irregularities can be found and a notification that the climb rate has slightly changed emerges, but they do not affect the analysis significantly. Therefore, the model of the ModuLR is considered as verified. For the validation part, it is required to perform real-life measurements of the noise that is emitted by the engine and propellers in order to compare it with the results from the model. In the model a comparable, but slightly overpowered turboprop is used which is part of the standard INM database, so the results from those measurements should return lower noise values. But as the ModuLR's noise contour is right now, it even produces significantly more noise than the comparable aircraft C-130E. Thus the modeled contour is not representative for the ModuLR-300.

5.1.4 Sensitivity

This section elaborates upon the sensitivity of the results of the performance indicators that are discussed in this chapter. Emissions sensitivity is left out since by inspection of Eq. 5.7 and 5.8 the relations between variables are straightforward. The noise sensitivity is omitted due to the incomplete validation of the results.

Range Performance Sensitivity

The range sensitivity is reflected in Tab. 5.5. The effects on range due to changes to most of the variables from Eq. 5.1 are obvious, so only the lift-over-drag ratio, MTOW, and the reserve fuel can be seen in the table. The velocity and altitude are initially variables of interest, but since these are closely related to many parameters such as the Reynolds number, angle of attack, component drag, propeller speed and efficiency etc., it takes a lot of time and resource to analyze the effects to the range. Thus it is decided to use the lift-over-drag instead. As for the increase in MTOW, the additional weight belongs to the OEW. The third parameter, $m_{f,res}$, represents the reserve fuel, which is originally 10% of the used fuel.

Table 5.5: Sensitivity of the range for all configurations, where the values represent range in km

ModuLR	R at max m_{PL}	MTOW + 10%	$m_{f,res} = 0.05\ m_{f,used}$	L/D +10%
-100	1444	1234	1555	1588
-200	3908	3425	4165	4298
-300	7144	6278	7611	7859

Take-off and Landing Performance Sensitivity

Tab. 5.6 contains results from the sensitivity analysis where the values are given in SI units. To save space, the original values are not present in the table. Those values can be found in Tab. 5.3.

5.1.5 Sustainability

Effort put into sustainability is partially reflected in Tab. 5.4 where especially the ModuLR-300 performs better in emissions than the Boeing 747-400 freighter. The performance decreases regarding the ModuLR-100 and -200 due to their FTK values, even though their EI_{NO_x} are lower than that of the 747.

5.2 Propulsion

All three configurations have different maximum power requirements as described in Tab. 5.3 in section 5.1.2. Selecting a different engine per configuration results in high production and maintenance cost.

[7] https://www.faa.gov/about/office_org/headquarters_offices/apl/research/models/inm_model/, visited on: June 26, 2017

Table 5.6: Take-off, landing , and climb performance sensitivity of all configurations

	MTOW +10%				V_{LOF} +10%	h_{scr} +10%		$C_{L,max,TO}$ +10%		
ModuLR	s_{TO}	s_L	c	$\frac{c}{V}$	s_{TO}	s_{TO}	s_L	s_{TO}	c	$\frac{c}{V}$
-100	1164	1002	10.5	0.181	957	919.7	917.8	808.0	14.05	0.248
-200	2781	1681	5.62	0.091	2286	2131	1526.8	1861.6	7.82	0.128
-300	4040	2308	6.98	0.088	3335	3061	2051.9	2663.8	7.80	0.118

Therefore, a new engine is designed that optimally combines the power requirements of the different configurations and can be used on all three of them. The maximum power of the engine is based on the maximum power requirement of the small configuration (2645 kW). This means that automatically a design margin is applied to the baseline and big configuration. This engine should have a high efficiency and low specific fuel consumption. The propeller of the engine should furthermore be designed for minimum noise based on the noise requirements from chapter 12.

5.2.1 Method

The design of the power subsystem consists of designing the gas turbine (engine) and the propeller itself. Firstly, the design method of the engine will be discussed, followed by the propeller design method.

Engine

The design of the engine is split into three phases. Firstly, general design decisions are made based on literature and reference engines with similar power requirements. Then, a tool is built in order to calculate the performance of the engine and to optimize this with respect to specific fuel consumption during cruise. Lastly, the engine design is finalized by calculating its dimensions and weight.

Based on the maximum power requirement during take-off as described in section 5.1.2, five reference engines are selected and analyzed. These are used throughout the design process to both get indication of values and configurations and to validate the design.

Four general design decisions are made before starting with the engine model. These include choosing between a radial and axial compressor, selecting the turbine type, choosing a type of combustion chamber, and lastly deciding about the type of nozzle to be used.

The engine model allows for calculating the engine parameters. Its two main goals are to minimize the specific fuel consumption during cruise and to provide a take-off power of 2645 kW. The model is split into two sections. The first section considers take-off performance whilst the second section represents cruise performance. The model calculates the temperature and pressure at each stage of the engine using thermodynamic formulas for real cycles [22]. Then, the total thrust and power are calculated using both the propeller thrust component and the airflow thrust component. Lastly, the specific fuel consumption is computed by dividing the fuel mass flow by the available power.

The engine model uses two kinds of variables, called fixed and free variables. The fixed variables are set throughout the calculations and cannot be changed whilst the free variables are changed to optimize the engine.

In setting up the model, eleven important assumptions about fixed variables are made. These are listed below:

- Jet A-1 fuel with a caloric value of 42.8 MJ/kg is used [23];
- The mechanical efficiency is equal to 0.99 [23][24];
- The turbine isentropic efficiency is equal to 0.89 [23][24];
- The combustion chamber pressure ratio is equal to 0.96 [23][24];
- The nozzle efficiency is equal to 0.95 [23][24];
- The combustion efficiency is equal to 0995 [23][24];
- The inlet isentropic efficiency is equal to 0.9 [23][24];
- The pressure ratio over a compressor stage is equal to 1.36 [25];

- The mass flow during take-off is equal to 30 kg/s [23][24][26][8][9];
- The mass flow during cruise is equal to 20 kg/s [23][24][26] [10][11];
- The compressor pressure ratio for cruise and take-off are equal [23].

The main free variable parameters to optimize the engine are the pressure ratio over the compressor and inlet (Π), the combination of compressors and turbines and their pressure ratios, and the turbine inlet temperature ($T_{0,4}$). Increasing $T_{0,4}$ models a higher throttle setting (more fuel). A higher Π increases the temperature at the inlet of the combustion chamber, resulting in a lower required fuel mass flow. The same holds for a $T_{0,4}$, which also decreases the ΔT required to be achieved in the combustion chamber. Eq. 5.9, where $T_{0,3}$ represents the combustor inlet temperature, $T_{0,4}$ the turbine inlet temperature, and $\dot{m}_f$ the fuel mass flow, illustrates these effects. The number of compressors and turbines, often varying between 1 and 3 [25], influences the efficiency of the engine as well.

$$\dot{m}_f = \frac{\dot{m} c_{p,g} (T_{0,4} - T_{0,3})}{LHV_f \eta_{cc}} \tag{5.9}$$

After calculating the engine performance, the engine is sized. This sizing consists of determining the engine diameter, length, and mass. The selected type of compressor, number of compressor stages, combustor type, maximum power, and the number of turbines are compared to the five reference engines. Based on the level of similarity between these components, the engine is sized. The similarity between a reference engine and the designed engine is quantified using a similarity factor (SF). Eq. 5.10 describes the computation of this similarity factor and Tab. 5.7 presents the SF per engine.

$$SF = \frac{\sum_{i=1}^{n} |1 - \frac{x_i}{x_{ref}}|}{n} \tag{5.10}$$

Table 5.7: Engine Sizing Overview

Engine Parameter	T56 Series	PW 150 Series	T64 Series	AE 2100D2	Ivchenko AI-20
SF	0.80	0.36	0.81	0.78	0.867

For the combustion chamber type and compressor type (not directly quantified), the score is adjusted by hand based on the similarity level. In order to calculate the engine length, for example, the similarity factors are multiplied with the respective reference engine lengths. These number are then summed up and divided by the sum of similarity factors. In this way, the engine length, diameter and mass are computed.

Propeller

As described in the section introduction, the propeller has to be designed for highest efficiency and low noise whilst being structurally feasible. The main design parameters in the propeller design are listed below:

- Material type;
- Constant speed or fixed pitch propeller;
- Number of blades;
- Blade radius;
- RPM;
- Airfoil.

[8] https://www.revolvy.com/main/index.php?s=General%20Electric%20T64
[9] https://en.wikipedia.org/wiki/Ivchenko_AI-20
[10] https://www.revolvy.com/main/index.php?s=General%20Electric%20T64
[11] https://en.wikipedia.org/wiki/Ivchenko_AI-20

Propellers are normally made out of metal (alloys) or composites[12]. The latter have a higher strength and have a better resistance against fatigue. However, they are more expensive and less robust[13]. Constant speed propellers can achieve higher efficiencies than fixed pitch propellers. However, they are heavier and more complex [27]. A higher number of blades positively influences the propeller efficiency as the power and thrust are distributed more evenly the propeller wake [28]. Increasing the blade radius also has a big positive impact on the propeller efficiency because a bigger volume of incoming air is caught which allows for distributing the power and thrust over a bigger volume [28]. However, a larger blade radius increases the moment created by the thrust at the root of the blade. A larger blade radius also increases to tip velocity and therefore the tip Mach number. This can lead to stall at the outer parts of the rotor blade which then leads to a decrease in lift and consequently of efficiency. The same principle is applicable to the RPM of the propeller. A higher RPM is, in principle, good for the efficiency of the propeller until the Mach number at the outer parts of the blades get too high and a drop in lift occurs. The airfoil selection is an important tool in maximizing the efficiency whilst preventing too high stresses at the blade root and stall at the blade tip.

In the design of the propeller blade, the blade section is split into three. The first section ends at 0.33 r/R, the second at 0.66 r/R, and the third section at 1. r/R. For the first section, an airfoil with a high t/c will be selected as a high moment of inertia is important close to the blade root. For the third section, an airfoil will be selected with a low t/c value as a high critical Mach number is more important than a high moment of inertia here. The second section will consist of an airfoil with intermediate performance parameters. The exact t/c values will be based on the maximum Mach numbers in the sections. Marte and Kurtz [29] divide propeller noise into two categories. These include ordered (rotational) noise and vortex noise. The disk loading (force per disk area) is an important parameter in this ordered noise. The lower this disk loading the lower the perceived rotational noise [29]. The disk loading can be decreased by increasing the number of blades or increasing the blade radius. However, increasing the tip radius also increases the tip velocity which leads to an increase in rotational noise [30]. Therefore a balance in the blade radius has to be found. The second noise category is vortex noise. According to Marte and Kurtz [29], increasing the blade velocity and the blade area both have a negative influence on the vortex noise. However, doubling the blade velocity leads to a six times as high dB increase than doubling the blade area [29]. A final consideration in designing the propeller for noise is that a too high number of blades can result in blades operating in each others disturbances, causing an increase in noise [31].

After deciding about the material type and between using a constant speed propeller or a fixed pitch propeller, the other parameters are changed simultaneously to obtain an efficient low-noise design. These simulations are performed using a modified written design model combining Matlab[14] and XROTOR [17]. Here Matlab is used to extract airfoil parameters and perform the structural analysis after wich the data is transferred to XROTOR for the blade design and vice versa. The propeller is designed for a maximum efficiency during cruise as this is the dominant flight phase. The structural analysis is performed using the following method.

From rotor geometry, the c/R ratio is obtained at the station closest to the propeller hub. Using the chord and the airfoil t/c, the blade thickness at the root can be determined. The bending moment at the blade root is calculated assuming that the total thrust is distributed evenly across the blades and can be represented by a single force acting at 0.75 r/R [32]. The moment of inertia and maximum normal stress (σ) at the root are then calculated using Eq. 5.11 and 5.12 respectively.

$$I_{xx} = \frac{1}{12} c(t)^3 \qquad (5.11) \qquad\qquad \sigma = \frac{My}{I_{xx}} \qquad (5.12)$$

The calculated stress value is compared to maximum tensile (yield) stresses of the selected material type in order to verify that the design is structurally feasible.

The propeller design procedure can be summarized as follows. After selecting a material and type of propeller, the preliminary Mach number distribution across the blade is determined and a Reynolds number is estimated. With this and a $C_{l_{design}}$, the airfoils can be selected and the propeller blades can be sized. Then, a noise analysis and structural check are performed. When the structure is not strong enough, the blade is redesigned. The formulas used to determine the Mach number distribution, size the blades, and perform the noise analysis are incorporated in the XROTOR software [17].

[12] http://www.experimentalaircraft.info/articles/aircraft-propeller-selection.php, visited on June 24, 2017
[13] http://www.fp-propeller.com/e_technology_con.html, visited on June 24, 2017
[14] https://nl.mathworks.com/products/matlab.html, visited on: https://nl.mathworks.com/products/matlab.html

5.2.2 Results

The resulting engine and propeller design are presented in this section.

Engine

The first general design decision considers the compressor type. As axial compressors are able to achieve higher pressure ratios than radial compressors, positively influencing the overall engine efficiency [33][34], an axial compressor will be used in the engine. It furthermore requires less frontal area which is convenient for reconfiguration purposes. The effects of its higher maintenance cost are minimized by only using one type of engine for the three configurations. The engineers therefore only have to perform maintenance on one type of engine.

Another general design decision is the use of a free turbine in a multiple shaft configuration. This allows the compressor(s) and propeller to operate at a different RPM, and for a lower overall noise and higher overall efficiency [15] [35]. A gearbox will furthermore be used between the turbine and the propeller to shift the RPM of the shaft. This is necessary as the turbine usually rotates at a RPM in the order of 10000 and the propeller at about 1000 RPM [36].

In selecting the type of combustion chamber, a can, annular, cannular and reverse flow type are considered [37]. The reverse flow combustion chamber is deemed unfavourable due to its high diameter and because it is normally used in combination with radial compressors [37]. The can combustion chamber is also considered less good of an option due its inferior performance characteristics. In the end, an annular combustor is selected based on its more uniform combustion, lower required surface area, low pressure drop, relatively simple design, and uniform exit temperatures. It also has a smaller size, which is especially important as the landing gear will fold into the the nacelle behind the engine [38][39].

Lastly, a convergent nozzle is selected to increase the thrust resulting from the engine exhaust [23].

Tab. 5.8 displays the final output of the engine optimization. The maximum available power (P_a) will be achieved in take-off whilst the engine is designed to be most efficient in cruise. It is furthermore observed that the engine performs best with one compressor instead of with both a low and high pressure compressor.

Table 5.8: Outcome of engine optimization

LR-Dash8NeXtGeN	**Units**	**Value**
Maximum available power	[W]	2647.26
Specific fuel consumption cruise	[kg/J]	6.81E-8
Number of compressors	[-]	1
Number of turbines	[-]	2
Compressor pressure ratio	[-]	15.1
Inlet pressure ratio	[-]	1.1
Overall pressure ratio	[-]	16.6
Number of compressor stages	[-]	9

Fig. 5.4 shows the schematic layout of the engine. Nine compressor stages are visible, connected to a shaft which is driven by the high pressure turbine (HPT). The low pressure turbine (LPT) drives the propeller via the gearbox, as indicated by the blue and green shafts. The combustion chamber blocks (CC) represent the annular combustion chamber.

Using the numbers in Fig. 5.4, representing the different stages of the engine, the T-S diagram is drawn. This is shown in Fig. 5.5.

The selected type of compressor, number of compressor stages, combustor type, maximum power, and the number of turbines are compared to the five reference engines. Based on the level of similarity between these components and the individual reference aircraft, the engine is sized. Tab. 5.9 gives an overview of the calculated engine length, diameter, and mass.

[15] https://www.airlinepilotforums.com/hangar-talk/9038-free-turbine-vs-direct-drive.html,visited on June 120, 2017

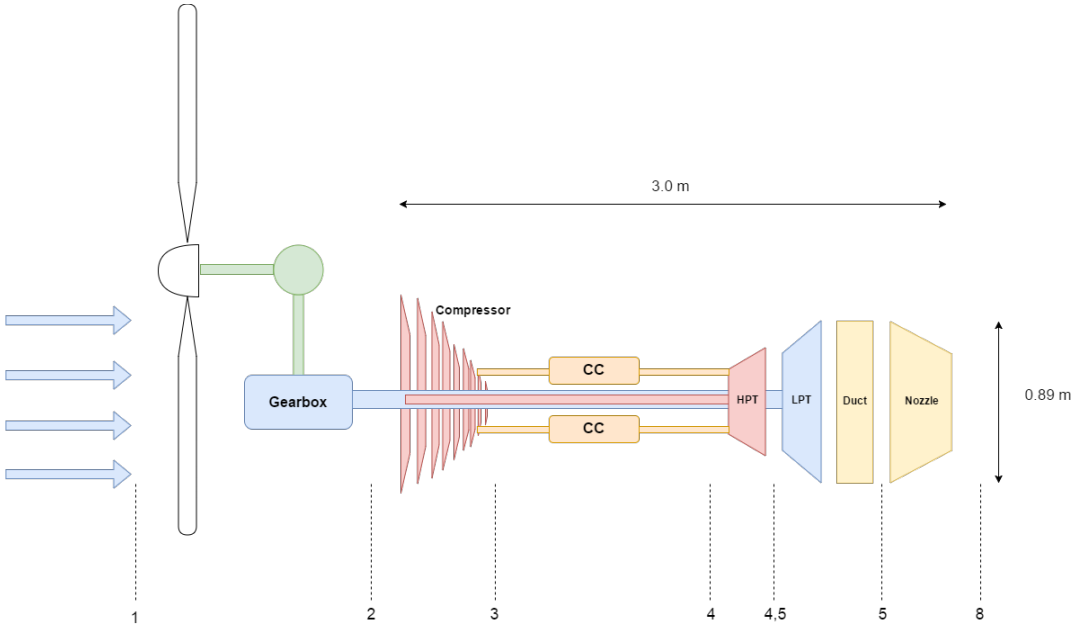

Figure 5.4: Schematic Engine Layout

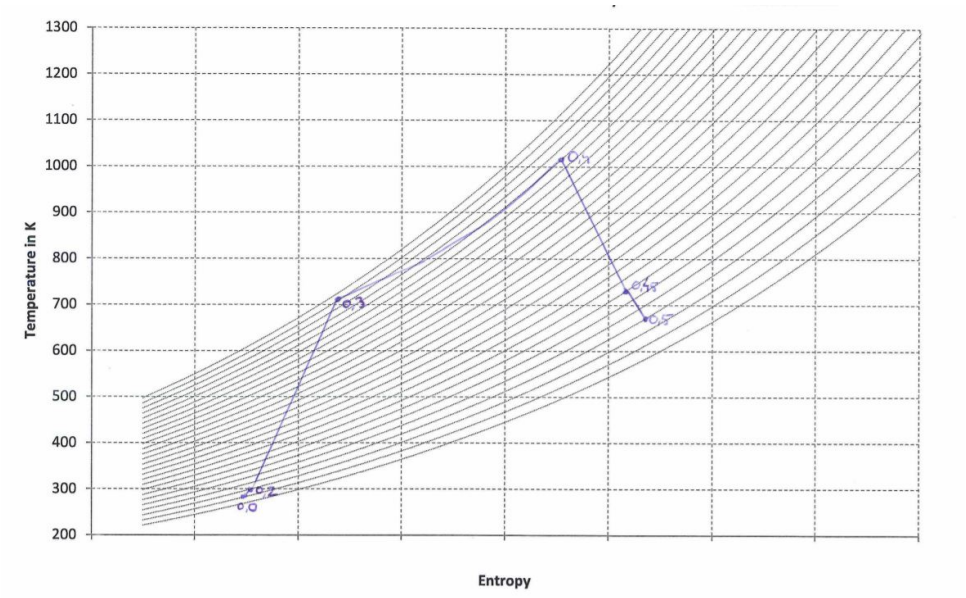

Figure 5.5: T-S Diagram Take-Off

Table 5.9: Engine Sizing Overview

Engine Parameter	Units	Value
Length	[m]	3.0
Diameter	[m]	0.89
Mass	[kg]	855

Propeller

As described in the method section, the first general design decisions in the propeller design consider the material type and the type of propeller. Composites are selected as material type because of their high

tensile strength and because of their good fatigue performance [16] [17]. A 'guide' maximum of stress of 360 MPa is used based on composite stress data[18]. Furthermore, a constant speed propeller is selected because of its high efficiency. It furthermore allows for a high efficiency in multiple thrust settings[19], which is beneficial when using the same propeller blades in the different aircraft configurations.

Tab. 5.10 gives an overview of the selected airfoils. The critical Mach numbers are evaluated at a $C_{l_{design}}$ of 0.6[20] and a Reynolds number of 2E5. Note that the first section starts at r/R=0.11 because of the propeller hub.

Table 5.10: Airfoil Selection

Section	**Airfoil**	**Mcrit**	C_{lmax}	**t/c**
0.11 - 0.33 r/R	NACA 63-630	0.52	2.4	0.30
0.33 - 0.66 r/R	NACA 2418	0.64	1.62	0.18
0.66 - 1.0 r/R	NACA 40006	0.8	0.71	0.065

Using these airfoils, the blade is designed for highest efficiency and low noise. The efficiency and the main design parameters are shown in Tab. 5.11.

Table 5.11: Initial Propeller Design

Efficiency	**Number of Blades**	**Tip Radius**	**Hub Radius**	**RPM**
0.90	6	2.2	0.1750	890

Fig. 5.6a presents this blade geometry. The local efficiency, Mach number, and C_l are visible in Fig. 5.6b. Fig. 5.6c presents a ground noise footprint for cruise altitude.
The yellow dotted line in Fig. 5.6b represents the Mach number along the blade length. Comparing this graph with the critical Mach numbers in Tab. 5.11, it is clear that the distribution along the blade nicely fits with the selected airfoils. The Mach number at the blade tip is equal to 0.8 whilst the maximum Mach number in section 1 and 2 are 0.52 and 0.63 respectively.

Looking at Fig. 5.6a, it seems that c/R at the blade root is very small. From the propeller data, it follows that c/R is equal to 0.0081. This small chord is most likely to be caused by a too high number of blades [28]. When performing the structural analysis as described in section 5.2.1, the bending stress is calculated to be 47.5 GPa. This is way above the 360 MPa that is being designed for and therefore this propeller design is deemed unfeasible.

The designed propeller blade is then adjusted in order to reduce the tip stress but to still keep the efficiency high and the noise low. The outcome of the design adjustment is shown in Tab. 5.12.

Table 5.12: Final Propeller Design

Efficiency	**Number of Blades**	**Tip Radius**	**Hub Radius**	**RPM**
0.86	4	2.2	0.24	795

Fig. 5.7a presents the final blade geometry and the local efficiency, Mach number, and C_l are shown in Fig. 5.7b. Fig. 5.7c presents the new ground noise footprint for cruise altitude.

Comparing the initial optimal design with the final design, it is observed that the efficiency has dropped from 0.90 to 0.86. The Mach numbers along the final blade are slightly lower than for the initial design as the RPM has decreased from 890 to 795. Although the RPM has decreased, the engine noise has slightly increased (about 5 dB at 10,000 ft). This is most likely caused by the decrease in the number of blades.

[16] http://www.compositesblog.com/2010/03/composites-vs-metal.html, visited on June 20, 2017
[17] http://www-mdp.eng.cam.ac.uk/web/library/enginfo/cueddatabooks/materials.pdf, visited on June 20, 2017
[18] http://advtechconsultants.com/CompositeMaterial.htm, visited on June 20, 2017
[19] http://www.flyingmag.com/technique/tip-week/constant-speed-prop-basics, visited on June 20, 2017
[20] http://www.dtic.mil/dtic/tr/fulltext/u2/a050593.pdf, visited on June 20, 2017

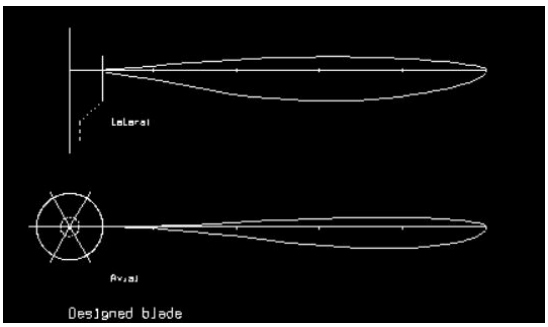

(a) Ideal Blade Geometry

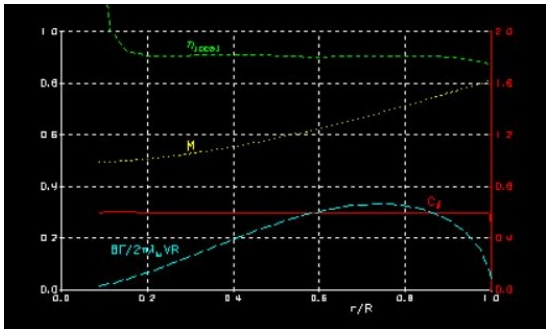

(b) Ideal Blade Performance Data

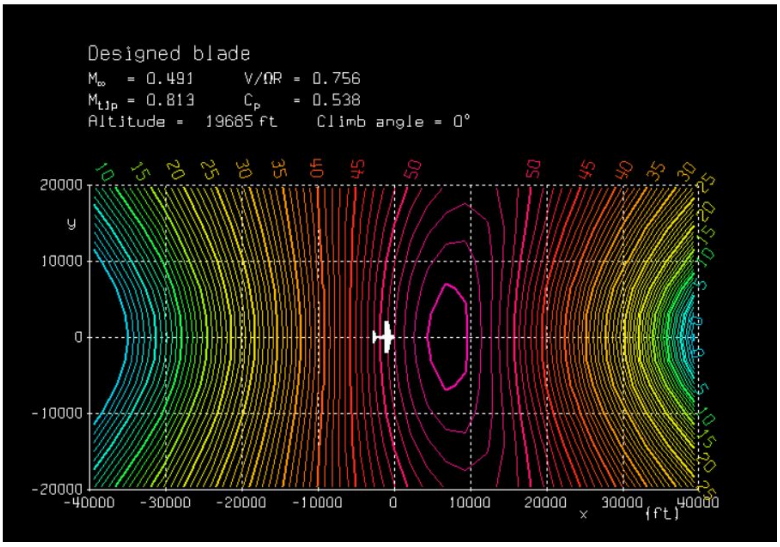

(c) Ideal Ground Noise Footprint

Figure 5.6: Blade geometry (a), parameters of the propeller (b), and ground noise footprint (c) of the initial run

The c/R ratio at the root of the final design is equal to 0.0415. Performing the structural analysis from section 5.2.1, a maximum bending stress of 338 MPa is calculated. With this, the structure is considered to be strong enough.

5.2.3 Verification & Validation

In this section, the verification and validation of the engine and propeller design is described. The verification and validation are performed conform to the plan as described in the Mid Term Report [1].

Engine

Code verification has been a constant process while setting up the model and solving (syntax) errors. Calculation verification of the engine model is performed by inserting data from Ir. Melkert [24] in the model and comparing the resulting values to the ones provided. As the results are the same, it is verified that all calculated temperatures and pressures, velocities, and thrust values in the model are correct.

Validation of the engine model is performed by comparing the outcomes to reference engines. More specifically, the combination of T-S diagram (or specific temperatures) and thrust of the designed engine is compared to the same combination for reference engines. When comparing the temperatures and powers, it is observed that the turbine inlet temperature of 1095 K is relatively low compared to the inlet temperature of the reference engines (1150-1200 K). This is explained by the lower required take-off power for the designed engine. As the general design decisions and the sizing of the engine are performed based on reference engines, these have already been validated.

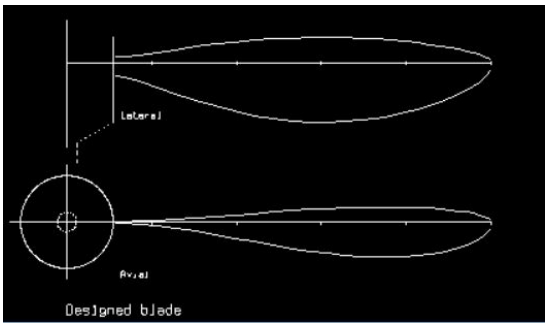

(a) Final Blade Geometry

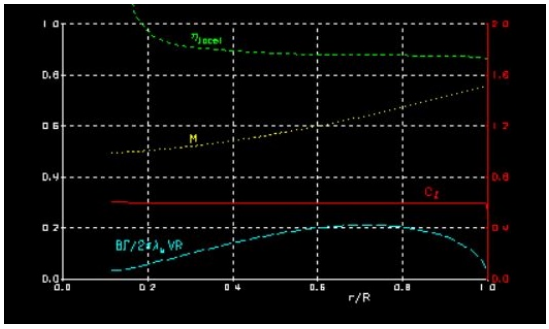

(b) Final Blade Performance Data

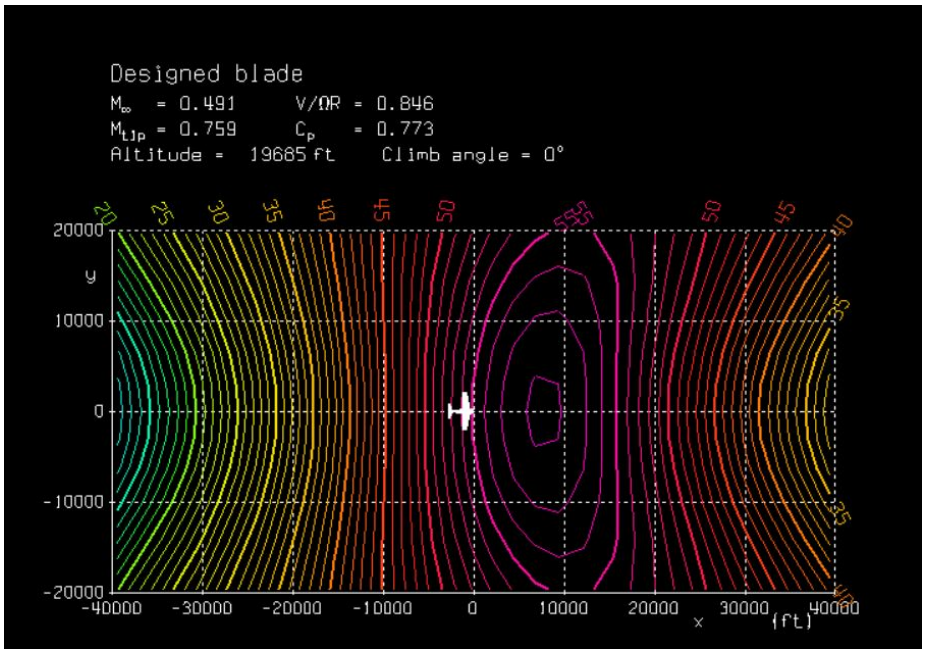

(c) Final Ground Noise Footprint

Figure 5.7: Final Blade geometry (a), parameters of the propeller (b), and ground noise footprint (c)

Propeller

As XROTOR was used to model the propeller dimensions, it is assumed that the model code and its calculations have already been verified.

Validation of the engine model is done in twofold. The first part consists of using a simplified formula to calculate the propeller efficiency and using existing noise data to validate the noise results. The second part concerns the feasibility and compares the rotor geometry with existing models.

Equation 5.13 [40] is used as alternative method for calculating the propeller efficiency. In order to compute the disk are (A_{disk}), an average c/R of 0.15 is assumed and the hub area is not taken into account. The calculated efficiency is 0.88, compared to 0.86 from the model. This 2% difference is acceptable, especially taking into the account the assumptions made.

$$\eta_{prop} = \frac{2}{1 + (\frac{T}{A_{disk} u_0^2 \frac{\rho}{2}} + 1)^2} \tag{5.13}$$

The ground noise level of an aircraft propeller flying at 1000 ft is normally around 88 dB [41][21]. When generating a noise map for the designed propeller at 1000 ft, the maximum perceived dB level is 82 dB. This value is considered feasible as the propeller is specifically designed for low noise.

[21] http://airportnoiselaw.org/dblevels.html, visited on: June 20, 2017

The feasibility of the design geometry is validated by looking at existing propellers and their radius and number of blades. Tab. 5.13 describes the basic geometry properties of three comparable propellers. From Tab. 5.13, it is concluded that a blade radius of 2.2 m is feasible. Although all three propellers have more than four blades, four blades is still considered to be a feasible amount considering the fact that many propellers with four blades exist[22] and based on information by Ir. Melkert [42].

Table 5.13: Propeller Geometry Basics Comparison

Propeller	Number of Blades	Tip Radius
ModuLR Propeller	4	2.2
Fokker 50 Propeller	6	1.83
Bombardier Q400 Propeller	6	2.05
TP400-D6 Propeller	8	2.67

5.2.4 Sensitivity

Engine

The sensitivity of the engine design is performed by analyzing how changing the turbine inlet temperature, pressure ratio, density and velocity change the power during take-off and the specific fuel consumption during cruise. Each of the four input parameters is both increased and decreases with 5, 10 and 20%. Higher percentages will lead to unfeasible input values. Fig. 5.8a and Fig. 5.8b present the results of the analysis. The most notable result is that increasing the pressure ratio initially seems to decrease the SFC. This is explained by the available power decreasing more rapidly than the fuel mass flow. Please note that not all turbine values and pressure ratios are possible, explaining the limited amount of blue points in Fig. 5.8b.

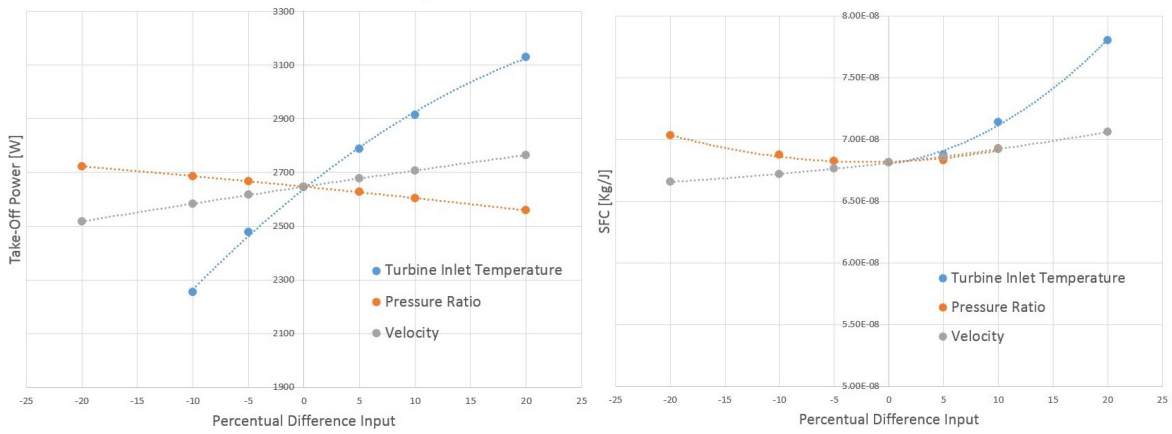

(a) Take-off power sensitivity

(b) Cruise SFC sensitivity

Figure 5.8: Sensitivity graphs on the take-off power (a) and cruise SFC (b)

Propeller

The propeller sensitivity analysis is performed by evaluating the effect of changing the input RPM, blade radius, and number of blades. The RPM and blade radius are both increased and decreased by 5, 10, and 20% whilst the number of blades is changed to five and six. The effect of these changes on the propeller efficiency and the ground noise level (dB) at 20,000 ft from the aircraft in cruise is analyzed. Note that the structural feasibility of the propeller after the input changes is not considered.

Figure 5.9a shows the results of the sensitivity analysis for the propeller efficiency. Both increasing the RPM and increasing the blade radius have a positive on the propeller efficiency. Comparing the two, increasing the blade radius has a bigger effect on the efficiency than increasing the RPM. It must be

[22] https://en.wikipedia.org/wiki/Category:Turboprop_aircraft, visited on: June 19, 2017

noted that increasing the blade radius (too far) will lead to tip stall and will cause the root stresses to be too high.

From the noise sensitivity results as presented in Fig. 5.9b, it can be seen that increasing the RPM increases the noise level. This is expected according to the theory as presented in section 5.2.1. In short, a higher tip speed causes the noise to be higher. Increasing the blade radius initially leads to an increase in noise but when increasing the blade radius with 20%, the noise decreases again. The increase in noise can be explained by the fact that the tip speed increases due to a longer blade. However, the blade area also increases which leads to a decrease in disk loading. The decrease in noise could be explained by the disk loading being more dominant.

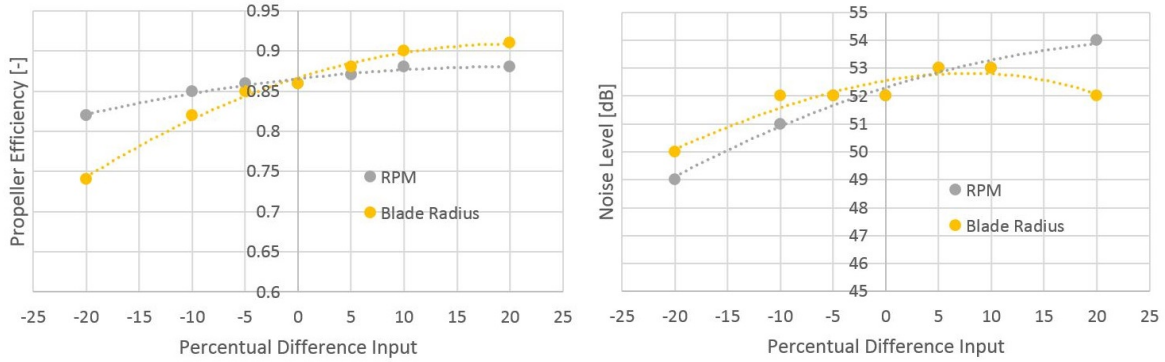

(a) Propeller efficiency sensitivity

(b) Noise sensitivity (20,000 ft ground, cruise)

Figure 5.9: Sensitivity graphs on the propeller efficiency (a) and noise level (b)

The sensitivity of changing the number of blades is summarized in Tab. 5.14. Increasing the number of blades positively influence both the efficiency and the noise. The big influence on noise is however striking. In practice, increasing the number of blades will lead to thinner blades, resulting in higher root stresses again.

Table 5.14: Number of Blades Sensitivity

Outcome Parameter	4 Blades	5 Blades	6 Blades
Efficiency [-]	0.86	0.88	0.88
Noise [dB]	52	47	42

5.2.5 Sustainability

Environmental, social, and economic sustainability aspects are all considered in the power system design. Minimizing the fuel consumption of the engine and maximizing the efficiency of the propeller contribute to reducing emissions and therefore positively influence the environmental sustainability. Selecting composite rotor blades might contribute negatively to environmental sustainability looking purely at the material itself. However, using composites also allows the propeller to be more efficient and therefore not only has a negative effect on environmental sustainability. The noise is reduced in order to positively influence the social sustainability. Lastly, designing one engine for three different aircraft improves the economic sustainability as the complexity of the design is reduced.

5.3 Conclusion and Recommendations

First, the conclusion of the performance and power analysis is described after which recommendations are made. The conclusion is structured using the requirements flowing from the requirements discovery tree and shown in the compliance matrix in chapter 12.

Conclusion

To conclude this chapter on performance and propulsion, an overview of requirements including compliance descriptions are presented from which conclusions about the design are drawn. Overall, it is concluded that the aircraft performs well given its inefficiencies induced by its reconfigurability.

Considering the range requirements, the ModuLR-300 loaded with 10000kg payload has a range of 8130km, which is higher than the specified range of 4000 nmi (7408 km) in RUCA-T-REC-AP-4. The ModuLR-200 also meets its range requirement (RUCA-T-NOM-PN-2) of 2000 nmi carrying a payload of 5000 kg. However, the ModuLR-100 loaded with 1000 kg payload has a range of 1611 km which is shorter than the required 1000 nmi (1852 km) as specified by RUCA-T-REC-AP-3. This difference is causes by a lower final L/D than specified by the Class II base code. Assuming that intercontinental routes exist and the aircraft is allowed to fly on those routes, the ferry range of 13965 km of the ModuLR-300 covers all destinations in the world when departing from Amsterdam Schiphol Airport. Only eastern Australia cannot be reached. Even its nominal range of 8130 km at 10000 kg payload allows for intercontinental coverage[23]. Thus, requirement RUCA-T-OPS-FO-2 is met. Since that requirement is met, it automatically implies that RUCA-T-OPS-FO-1 is met as well.

RUCA-T-REC-AP-1 specifies a maximum runway length of 914.4 m (3000 ft) which is met by the ModuLR-100 with the numbers from Tab. 5.3. The engine and propeller are specifically designed to meet this requirement, which has been explained in section 5.2 and is also formally stated by the RUCA-T-FPP-P-1 requirement. Similarly, RUCA-T-REC-AP-2 specifies a minimum runway length of 3048 m (10000 ft) which is met by the ModuLR-300 with the numbers from Tab. 5.3. Akin to the previous requirements, RUCA-T-NOM-PN-1 specifies a maximum runway length of 2438.4 m (8000 ft) which is met by the ModuLR-200 with its take-off distance value from Tab. 5.3. With the current MTOW values as seen in Tab. A.3, all configurations meet the take-off and landing distance requirements and therefore RUCA-T-NOM-PN-4 is met.

The aircraft at its best (ModuLR-300) is capable of reaching a m_{fuel}/FTK of 0.213 kg/(km*1000kg) when the numbers from Tab. 5.4 are used. That is a -7% difference with respect to the Boeing 747-400, which means that RUCA-T-NOM-PN-3 is not met since at least -50% is needed. Since a constant Emission Index for CO_2 is used for all aircraft, the difference percentage of the ModuLR-300 with respect to the Boeing 747-400 is also -7%. Therefore, RUCA-C-ENV-2 is not met. The ModuLR-300 reduces the NO_x/FTK by 42% compared to the Boeing 747-400 according to Tab. 5.4, whereas 50% is required. Thus, the ModuLR does not meet RUCA-C-ENV-3. The reason for not meeting this requirement is the inefficiency induced by carrying the same fuselage. The Boeing 747-400 does not have this issue and therefore the difference is smaller than 50% when normalizing the emissions to range and payload.

The ModuLR's contour is larger than the Fokker's according to Fig. 5.2 and 5.3 and therefore RUCA-C-ENV-1 is not satisfied. This is partially due to the use of some coefficients from reference aircraft rather than of the newly designed engine and especially the propeller, and partly because of the slightly overpowered engine. Certain coefficients, as mentioned in the method section, are not representative for the ModuLR but are used for the model nonetheless since real measurement data are not available. More recommendations can be found in the last part of this section. Even though the location points in Fig. 5.3 are placed according to ICAO chapter IV noise standards [21], the noise contour does not seem to represent the ModuLR correctly. This is discussed in the verification and validation section 5.1.3. RUCA-C-LEG-2 can therefore not be checked for compliance at this stage. Compliance with the CS-25 certification standard can also not completely be verified given the large amount of regulations and the limited time and data available for this project. It is recommended as an action point to walk through the complete CS-25 in future studies. In conclusion, RUCA-C-LEG-3 can not be checked for compliance.

Recommendations

There are several recommendations for improvement and further investigations for the performance analysis. Those are grouped in the four categories of range, take-off and landing, gas emissions, and noise.

- **Range**: As mentioned in the sensitivity analysis, the effects of cruise velocity and altitude on the range are suggested as further research. Furthermore, the effects on the fuel fractions due to unmanned operations are suggested to be investigated, since the values are now based on statistics of manned operations.
- **Take-off and landing**: In section 5.1.3 the lack of validation data is indicated, so for future studies it is recommended to contact manufacturers or data banks to minimize the risk of missing data. Take-off and landing distances are influenced by pilot technique, but if both procedures are automated and optimized, then those distances may change to better values. A topic for research

[23] http://gc.kls2.com, visited on June 23, 2017

can therefore be the take-off, approach, and landing flight paths optimization for unmanned aircraft systems.

- **Gas emissions**: The CO_2 can be done in more detail by investigating the constituents of certain types of aviation fuel used by certain aircraft and setting up chemical equations for (ideal if possible) combustion. Moreover, emissions during take-off and landing phases should be investigated in addition to the cruise.
- **Noise**: In order to obtain improved results for the noise contour of the ModuLR, it is recommended to investigate the noise effects of not only the engine, but also the airframe which is not modeled by the INM. Thereby it is suggested to use the method[24] published by NASA. Furthermore, detailed departure procedures specifically aimed at the ModuLR should be defined. That includes defining among others the power setting, thrust, control surfaces and high lift devices settings at any point in time during departure. When to climb, accelerate, or level are included as well. INM also uses airplane coefficients [19] that can only be obtained using a certain standard. If more time is made available for the project, then the noise analysis will be more accurate.

Although the propulsion system design has been detailed already, the following recommendations can be taken into account for further design. The individual engine components could be designed in more detail. Think for example of designing the compressor and turbine in detail for a higher efficiency. In this detailed compressor design, the pressure ratio over the stages could also be designed to be the exact value required for optimum engine performance. In the current design, the pressure ratio over the compressor is furthermore assumed to be the same during take-off and cruise while in reality they are different. A more thorough analysis into this is another recommendation.

The current propeller design is mainly focused on cruise flight. As a constant speed propeller is considered, the pitch would have to change for take-off. A more detailed analysis of the propeller efficiency during take-off and the take-off pitch angles is required. This is especially useful as tip speeds may increase significantly. The current design lift coefficient for the propeller blades of 0.6 might furthermore be a bit high and might be scaled down in future work. Another point to be researched is the possibility of designing a different set of rotor blades for each aircraft configuration. In this way, the noise and efficiency can be optimized. However, due to the increasing (high) propeller cost, the profitability of this measure must be researched as well. Using more than three airfoils could also improve the performance of the propeller. Again, the profitability is an issue here and must be thoroughly analyzed. In further design, a detailed material selection has to be performed as well. It turns out that the propeller performance is limited by the bending stress (and fatigue), so high-strength materials could lead to higher efficiencies and lower noise levels. Furthermore, also different software like Helicel could be used. Lastly, a detailed analysis of the power systems required for the engine and propeller would be a next step as well.

[24] https://ntrs.nasa.gov/archive/nasa/casi.ntrs.nasa.gov/19920001380.pdf, visited on June 26, 2017

Chapter 6

Aerodynamics, Stability & Control

This chapter presents the design methodologies and final outcomes of the aerodynamics, stability & control analyses for the ModuLR-100, -200, and -300 variants. Section 6.1 presents the wing designs, followed by the nose design in section 6.2. The determination of the center of gravity is performed in section 6.3. Section 6.4 presents the tail design, section 6.5 presents the control surface design, and section 6.6 presents the stability and control characteristics. Finally, the total drag of the aircraft is evaluated in section 6.7.

6.1 Wing design

In this section, the design of the wings and high lift devices (HLD) is discussed. Initially, the design requirements are stated, followed by the method for the wing design. After this, the results from the methods are presented. A sensitivity analysis is performed on the method.

The wings and high lift devices should adhere to the requirements RUCA-T-ACS-W-1 until RUCA-T-ACS-W-6, which are explained in chapter 12. The wings will also adhere to RUCA-T-LEG-1 which indicates the approach speed to be below 72 m/s which translates to a stall at landing of 56 m/s.

6.1.1 Method

Wings

In order to size the wing, an airfoil that fits within the aforementioned constraints has to be selected. Airfoils are chosen that meet the requirements and have a design lift coefficient which is slightly higher than the average lift coefficient during the cruise phase to allow for efficient flight. It is chosen slightly higher such that the lift coefficient for the 3D wing will be closer to the design lift coefficient.

For the selection of airfoils, the parameters of the 3D wing are calculated to provide a basis for evaluation. This is done using Eq. 6.1 and 6.2 from the the DATCOM method [43]. Using the new 3D lift coefficient slopes and Eq. 6.3 for the 3D drag, the polars of the wings can be created.

$$C_{L_\alpha} = \frac{2\pi A}{2 + \sqrt{4 + \frac{A\beta}{\eta} + (1 + \frac{tan^2 \Lambda_{0.5C}}{\beta^2})}} \quad (6.1) \qquad C_L = C_{L_\alpha}\alpha - C_{L_\alpha}\alpha_{0L} \quad (6.2)$$

$$C_D = C_{D0} + \frac{C_L^2}{\pi A e} \quad (6.3)$$

The 3D stall behavior and maximum lift coefficient of the wing are estimated using Eq. 6.4 and 6.5 from the DATCOM method [43] to complete the polars. The sharpness parameter of an airfoil is required, which is calculated using Eq. 6.6.

$$C_{L_{max}} = \left(\frac{C_{L_{max}}}{C_{l_{max}}}\right) C_{l_{max}} + \Delta C_{L_{max}} \quad (6.4) \qquad \alpha_s = \frac{C_{L_{max}}}{C_{L_\alpha}} + \alpha_{0L} + \Delta\alpha_{C_{L_{max}}} \quad (6.5)$$

$$\Delta Y = \frac{Y_{0.06c} - Y_{0.06c}}{c} \cdot 100 \quad (6.6)$$

All wings have a taper of 0.4 and a zero sweep at the leading edge, which together with the surface area and aspect ratio determine the planform of the wings. The zero sweep at the leading edge is chosen to increase the maximum lift coefficient of the wing. The taper of 0.4 is chosen to approach an elliptical lift distribution [43]. The drag coefficient at the beginning, middle and end of the cruise phase is checked to provide a proper basis for airfoil comparison. The total drag coefficient is calculated using equation 6.8. The drag coefficients at maximum lift are also evaluated. The drag coefficient instead of the wing drag can be used for evaluation as all wing designs will have the same wing surface area. Hereafter, a final check is done for the critical mach number, maximum lift coefficient, and corresponding drag coefficient.

The span efficiency number is calculated using Eq. 6.7 [44]. The Reynolds number is obtained from the XFLR5 software.

$$e = \frac{1}{1.05 + 0.007\pi AR} \tag{6.7}$$

$$C_D = C_{D0} + \frac{C_L^2}{\pi ARe} \tag{6.8}$$

This whole process is automated by integrating python and XFoil. The chosen designs are evaluated using the plane and wing design environment in XFLR5 to get more accurate final results for the clean configuration of the wings.

Flaps

In order to increase the lift, flaps are to be designed. The method from Roskam [5] together with the results from the clean configuration of the wings are used. A safety factor of 1.1 is taken for the clean maximum lift coefficient as depicted by Roskam. Fowler flaps are used and the required and obtained lift change in lift can now be computed using Eq. 6.9, 6.10, 6.11, and 6.12 together with Fig. 6.1

$$\Delta C_{l_{max}} = (\Delta C_{L_{max}})(S/S_{wf})/(k_\lambda) \tag{6.9}$$

$$K_\lambda = (1 - 0.08cos^2(\Lambda_{c/4}))cos^{3/4}(\Lambda_{c/4}) \tag{6.10}$$

$$S_{wf}/S = (\eta_o - \eta_i)(2 - (1-\lambda)(\eta_i - \eta_o))/(1+\lambda) \tag{6.11}$$

$$\Delta C_l = C_{l_\alpha}(1 + c_f/c)\alpha_{\delta_f}\delta_f \tag{6.12}$$

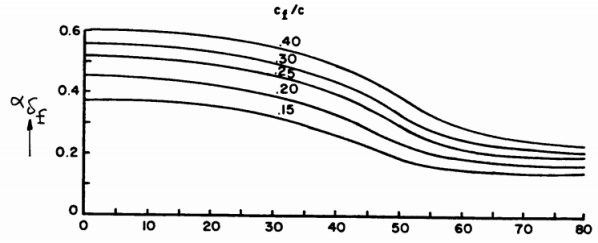

Figure 6.1: Section Lift Effectiveness Parameter [5]

6.1.2 Results

Wings

The main geometrical parameters and used parameters for the wing evaluation are presented in Tab. 6.1 and 6.2, respectively. The planform of the wing is presented in Fig. 6.2. The airfoils that is used for all three wings is the GOE412.

ModuLR	100	200	300
AR [-]	12.0	12.0	12.0
S [m^2]	53.5	72.6	138
b [m]	25.3	29.5	40.7
λ [-]	0.40	0.40	0.40
c_{root} [m]	2.84	3.31	4.56
c_{tip} [m]	1.14	1.32	1.83

Table 6.1: Geometrical data of the wings for all aircraft

ModuLR	100	200	300
e [-]	0.76	0.76	0.756
Mach [-]	0.5	0.5	0.5
N_{crit} [-]	9.0	9.0	9.0
Re_{tip} [-]	$11 \cdot 10^6$	$13 \cdot 10^6$	$18 \cdot 10^6$
Re_{root} [-]	$28 \cdot 10^6$	$33 \cdot 10^6$	$46 \cdot 10^6$

Table 6.2: Input parameters used for aerodynamic analysis

The drag, lift, and moment polars are presented in Fig. 6.3. All are obtained by using the wing and plane design environment of XFLR5 in combination with the 2D airfoil evaluation environment. The induced drag is calculated by hand and added to the profile drag. The wings are evaluated at Mach 0.5 and the Reynolds is applied variable by XFLR5 over the wing span using polars evaluated at different Reynolds numbers.

Aerodynamic properties during various flight phases resulting from the aerodynamic analysis are presented in Fig. 6.3. The values for the maximum lift coefficient of each configuration can now be used

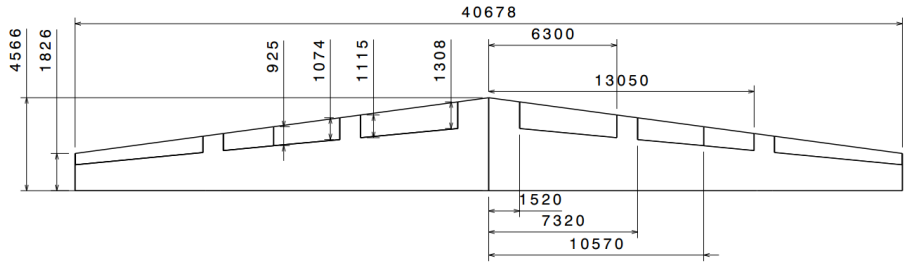

(a) Planform of the wing for the ModuLR-300

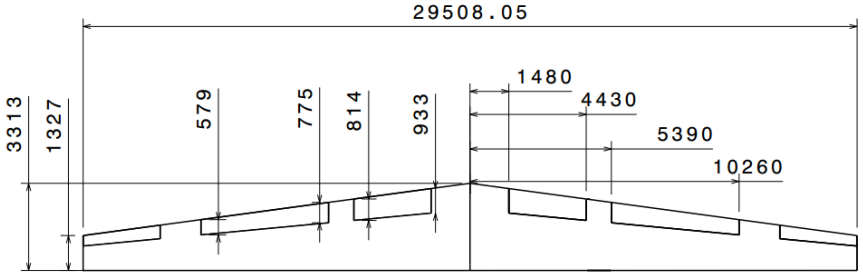

(b) Planform of the wing for the ModuLR-200

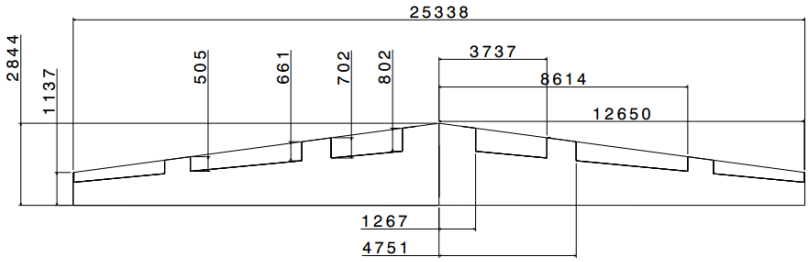

(c) Planform of the wing for the ModuLR-100

Figure 6.2: Planforms of the wings for each configuration

for the flap sizing.

Table 6.3: Wing Properties for each configuration

ModuLR	100	200	300
clcruise [-]	0.587	0.579	0.666
cdcruise [-]	0.019	0.018	0.022
cmcruise [-]	-0.47	-0.44	-0.44
alfacruise [deg]	-0.91	-0.89	-0.87
clmax [-]	1.83	1.85	1.87
alfastall [deg]	13.5	13.7	13.8

Flaps

Fowler flaps are chosen and the geometrical parameters as well as the related aerodynamic properties are presented in Tab. 6.4. The flaps are also presented in the planform of the wings in Fig. 6.2 and in Fig. 6.4. The flap chord over wing chord is 0.3 for all configurations.

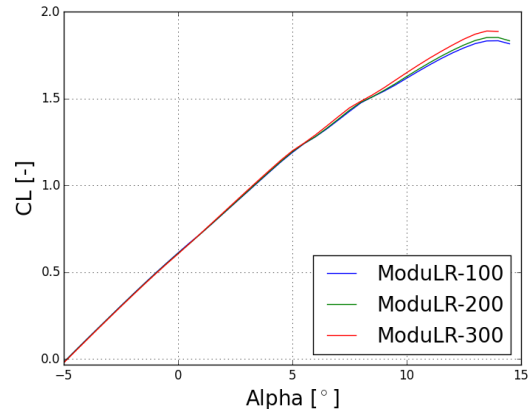

(a) Lift Coefficient to Angle of Attack

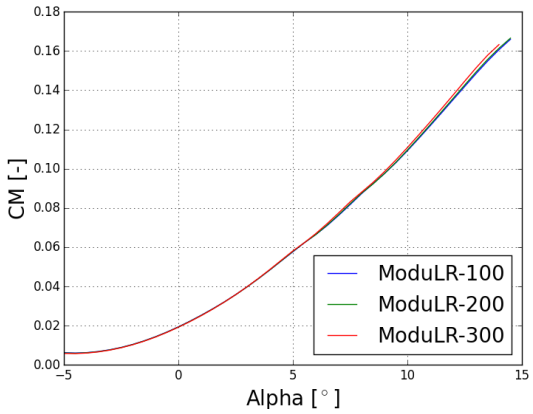

(b) Drag Coefficient to Angle of Attack

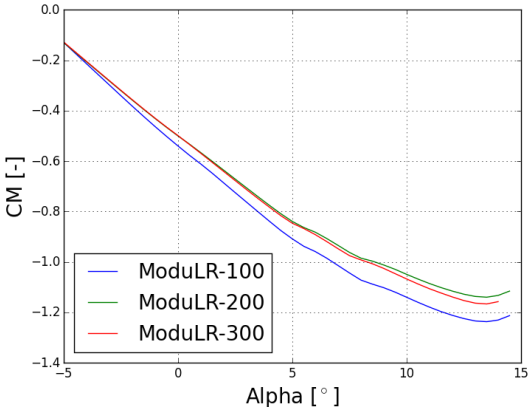

(c) Moment Coefficient to Angle of Attack

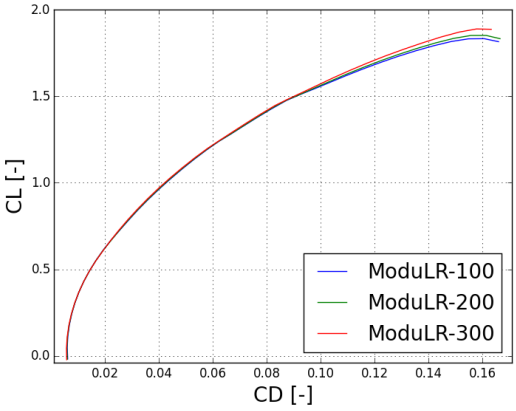

(d) Lift Coefficient to Drag Coefficient

Figure 6.3: Polars for all three wings with a GOE412 airfoil evaluated using XFLR5 at Mach = 0.5

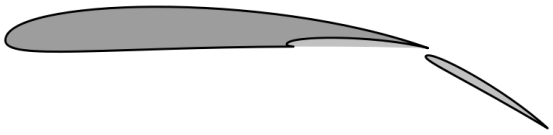

Figure 6.4: Visual representation of fowler flaps

Table 6.4: Input parameters used for aerodynamic analysis

ModuLR	100	200	300
$C_{L_{max_{clean}}}$ [-]	1.66	1.68	1.70
$C_{L_{TO}}$ [-]	2.80	2.63	2.22
$C_{L_{land}}$ [-]	2.07	3.22	1.7
dftakeoff [°]	14.6	12.1	6.5
dfland [°]	14.6	12.1	0.0
V_{TO} [m/s]	60.0	65.0	70.0
V_{land} [m/s]	62.0	65.0	70.0

6.1.3 Sensitivity

Wing

A sensitivity analysis on the wing method is performed to check the effect of selecting the minimum value for the maximum lift coefficient and the effect of changing the airfoil. The results are presented in Fig. 6.5a and 6.5b. It can be seen in Fig. 6.5a that increasing the threshold value for the maximum lift coefficient also increases the total drag of the wing. The threshold value for the maximum lift coefficient should therefore be carefully considered. The fact that the line is straight from the beginning follows from the fact that the airfoil with the lowest drag coefficient has a maximum lift coefficient which is around 1. The airfoil also has a big impact on the total drag , as can be seen in Fig. 6.5b, and obtainable maximum lift coefficient of the wing and the airfoil selection should therefore be treated with utmost

care.

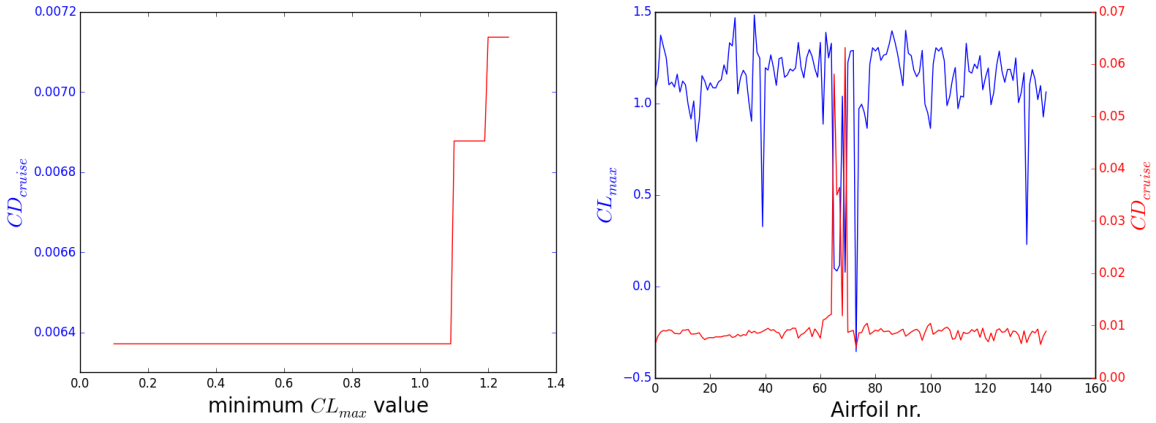

(a) maximum lift coefficient threshold value sensitivity

(b) Airfoil choice sensitivity

Figure 6.5: Loading diagram for all ModuLR configurations

Flaps

A sensitivity analysis is performed on the method to size the flaps to get a better understanding on the influence of variables on the method. The input variables used for the analysis are both the inboard and outboard location of the aileron positions, the taper ratio of the wing, and the flap chord over the wing chord.

It can be observed that both aileron positions show a sudden jump. This happens when the outboard aileron position passes the inboard aileron position and vice versa. It should therefore be carefully evaluated if both positions are defined correctly. It can also be observed that increasing the taper decreases the deflection angle required for the flap, and increasing the flap chord over wing chord increases the required deflection angle. The inboard and outboard locations have the largest influence, followed hereafter by the flap chord over wing chord. The flap chord over wing chord has a smaller influence but is still significant. All input parameters should therefore be carefully considered.

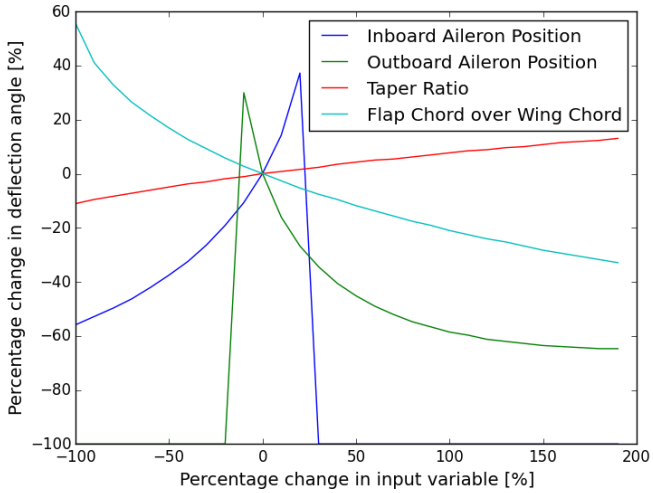

Figure 6.6: Sensitivity Analysis of the flap design method

6.1.4 Verification & Validation

Wings

Xfoil, XFLR5, and the DATCOM method have already been verified and validated [43][45][46]. It has been found, however, that the wing and plane design show drag results that are too optimistic in the three dimensional case. Therefore, the 2D results from XFoil are converted to the 3D results by means of the DATCOM method to get more accurate results. The section lifts can also be evaluated in a wind tunnel to validate the results more carefully or a scale model of the wing can be analyzed in the wind tunnel for more accurate results for the total wing aerodynamic behavior.

Flaps

The code has been verified by entering the input parameters from examples of Roskam in the program and checking if the same output is generated. The end results have also been compared to flap deflections of other aircraft as a final check. The method is derived from empirical data of other aircraft in combination with data of the wing itself, a way to validate this method more accurately for this specific aircraft is by comparing the results to the real performance of the aircraft to see if the method outcome resembles the performance of the flaps on the aircraft.

6.1.5 Sustainability

The wings are sized to attain a high maximum lift coefficient which allows for a higher climb gradient and therefore a smaller region of noise. The wings are also sized for a high lift over drag ratio which has a positive influence on the fuel consumption of the aircraft and thus a positive influence on sustainability. Optimizing for these two parameters leads to a sustainable design.

6.1.6 Conclusion & Recommendations

Wings

The wing does provide the required amount of lift and desired stall behavior. RUCA-T-ACS-W-1 until RUCA-T-ACS-W-6 have been met, except for RUCA-T-ACS-W-1 as the weight has changed during the design. RUCA-T-LEG-1 is also met. The wing is also optimized for the drag in the first iteration. Because many parts have changed during the design and designing an aircraft is rather complex, a new iteration has to be done for the airfoil of the wing. The weight has changed but the surface area has been assumed constant which requires the airfoil to operate at a lower cl and thus not at its most efficient point anymore. The wing loading has changed too due to this fact. Therefore, in the new iteration the surface area has to be changed and the airfoil re-evaluated. The drag of the wing in combination with other components should also be analyzed in the future to predict the changes in aerodynamic behavior due to interference between components. The maximum lift coefficients obtained from XFLR5 and the DATCOM method also showed some deviations and therefore a more careful analysis of the maximum lift coefficient for the wings is required. The airfoil has now remained constant due to the fact that it would have a too large impact on the other components as well, a redesign is highly recommended.

Flaps

The flaps have been sized and fulfill the requirements. They can provide the required increase in lift during landing and take-off. The flaps could be analyzed by more accurate methods to get a better prediction of their performance, which might lead between less deviation between experimental and theoretical results.

6.2 Nose design

This section describes the design of the aircraft nose. Firstly, the design method is explained in section 6.2.1 and then the results are presented in section 6.2.2. Sections 6.2.3 and 6.2.4 describe the verification and validation procedures and the sensitivity analysis. Lastly, the sustainability of the design is explained in section 6.2.5 and conclusions are drawn in section 6.2.6.

6.2.1 Method

From the requirement compliance matrix in chapter 12, it follows that the nose has to be designed for minimum drag in order to minimize emissions and increase the range. The nose design is split into three parts. Firstly, research is performed on the aerodynamic shape of the nose and seven shapes are selected for further analysis. Then, three fineness ratios are selected for the detailed analysis. Lastly, the combinations of shapes and fineness ratios are analyzed in detail with flow modeling software and the shape with the lowest drag coefficient is selected. The selection of nose shapes and fineness ratios for

the flow modeling are presented in this section and the results of the modeling are presented in section 6.2.2.

At Mach numbers below 0.8, pressure drag is very small compared to the friction drag [47]. The drag of the nose cone will therefore be mainly dependent on its wetted surface area, surface smoothness, and presence of discontinuities[1].

Based on Chin's [48] drag comparison of general nose shapes, seven nose shapes are selected. These shapes are displayed in Fig. 6.7. Using Chin [48], $x^{0.5}$ is selected for the power series and for the Haack Series the shapes for both C = 0. and C = 0.33 are selected. Except for the full parabola displayed on the middle left, also the half parabola is considered (different shaping factor K). Lastly, also a pure half circle is selected for the analysis due to its simplicity.

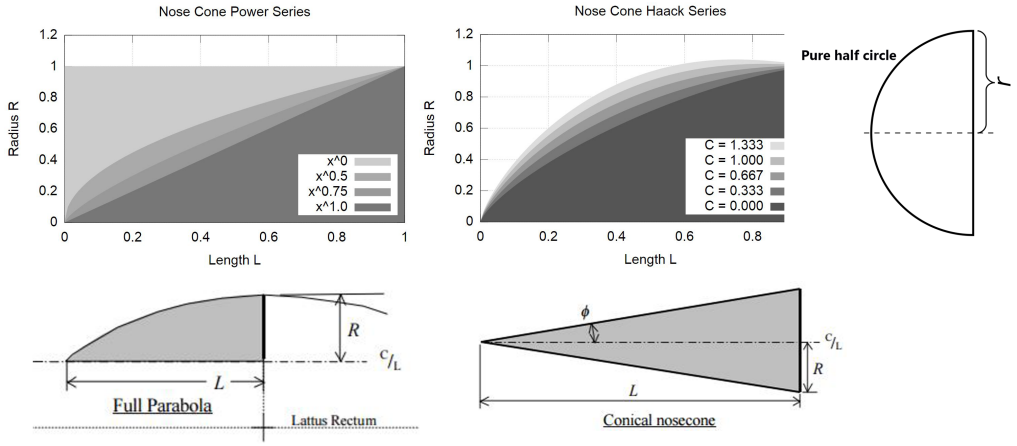

Figure 6.7: Selected general shapes for nose design [48][a]

[a]https://upload.wikimedia.org/wikipedia/commons/thumb/e/e9/Semicircle.svg/2000px-Semicircle.svg.png, visited on: June 18, 2017

The shapes displayed in Fig. 6.7 still have a variable length. The fineness ratio is used to determine the length of the shapes. Fig. 6.8 from Sforza [49] shows common fineness ratios for commercial aircraft noses. Based on this information and data from Torenbeek [50], fineness ratios of 1.2, 1.5, and 2.0 are chosen to be analyzed in the model.

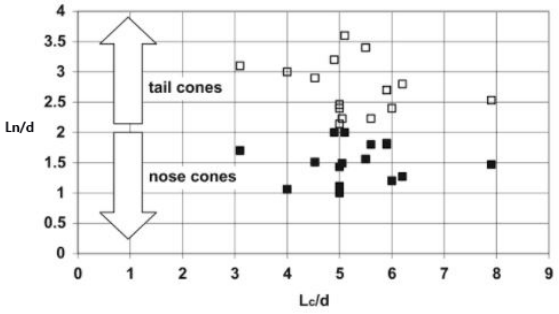

Figure 6.8: Common Fineness Ratios of Commercial Aircraft [49]

In order to decide which nose performs best according to the requirements described in chapter 12, the flow over the noses is modeled in a virtual wind tunnel using Autodesk Flow Design [51]. The speed in the wind tunnel is set equal to the average cruise speed of the three configurations (155 m/s). A 20-meter cylinder is placed behind each nose to be able to fairly compare them and to also take into account the way the nose 'guides' the flow over the fuselage instead of just testing the nose itself. The

[1]https://www.skybrary.aero/index.php/Friction_Drag, visited on: June 19, 2017

drag coefficient of each nose-cylinder combination is calculated, starting with the smallest fineness ratios. It is expected that their drag coefficient will be lower than for the other fineness ratios as the wetted surface area is smaller. The nose-cylinder combination is furthermore placed at the cruise angle of attack of the -200 version (0.41 deg), in order to compare the drag during the most fuel-intensive flight phase. Note that because of the absence of the real fuselage, the computed drag coefficients will solely be used to compare the different noses relatively an not to calculate accurate drag coefficient values.

6.2.2 Results

Tab. 6.5 presents the results of the flow analysis. As can be seen, the fineness ratio of 1.5 is not modeled for all shapes and the noses with a fineness ratio of 2 are not modeled at all. This is because it follows from the results that the drag coefficient increases with a higher fineness ratio (and therefore longer nose). As the computations are time-intensive, the analyses of noses with fineness ratios of 2.0 was considered unnecessary. From the results, it follows that the Haack series with C = 0 and a fineness ratio of 1.2 performs best.

Table 6.5: Drag Coefficients of Nose-Cylinder Combinations

Nose	Fineness	C_D
Pure cone	1.2	0.24
Pure cone	1.5	0.27
x$\hat{0}$.5 Power series	1.2	0.23
x$\hat{0}$.5 Power series	1.5	0.32
C=0 Haack series	1.2	0.22
C=0 Haack series	1.5	0.31
C=0.33 Haack series	1.2	0.28
Full parabola	1.2	0.23
Half parabola	1.2	0.26
Pure half circle	0.5	0.33

Fig. 6.9 shows the Haack series nose with C = 0 during the simulated wind tunnel test at the baseline cruise angle of attack (0.41°). A relatively small high-pressure region is visible at the tip of the nose, which transitions to lower pressure regions over the rest of the nose.

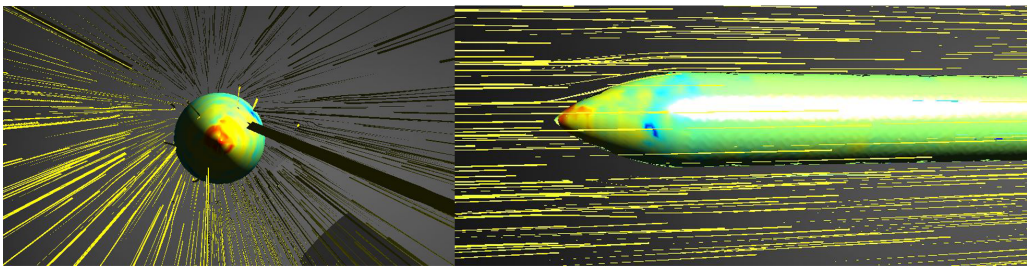

Figure 6.9: C=0 Haack Series Aerodynamic Analysis

The simulated noses with a fineness ratio of 1.2 are shown in Fig. 6.10. As expected, the highest pressure is observed at the front of the nose. This high pressure then gradually decreases and a relatively low pressure region is visible just behind the nose. The more the flow is 'diverted' from the cylindrical body by the nose, the lower the pressure in this region and the bigger the pressure difference between the cylindrical part just behind the nose and the cylindrical part further aft. A notable result is that for the shapes with the lowest drag coefficient (Haack C = 0, x^0.5 power series, and full parabola), the pressure differences between the area just behind the nose and the aft cylinder seem to be small, whilst for, for example, there is a big pressure difference visible when looking at the C = 0.33 Haack series.

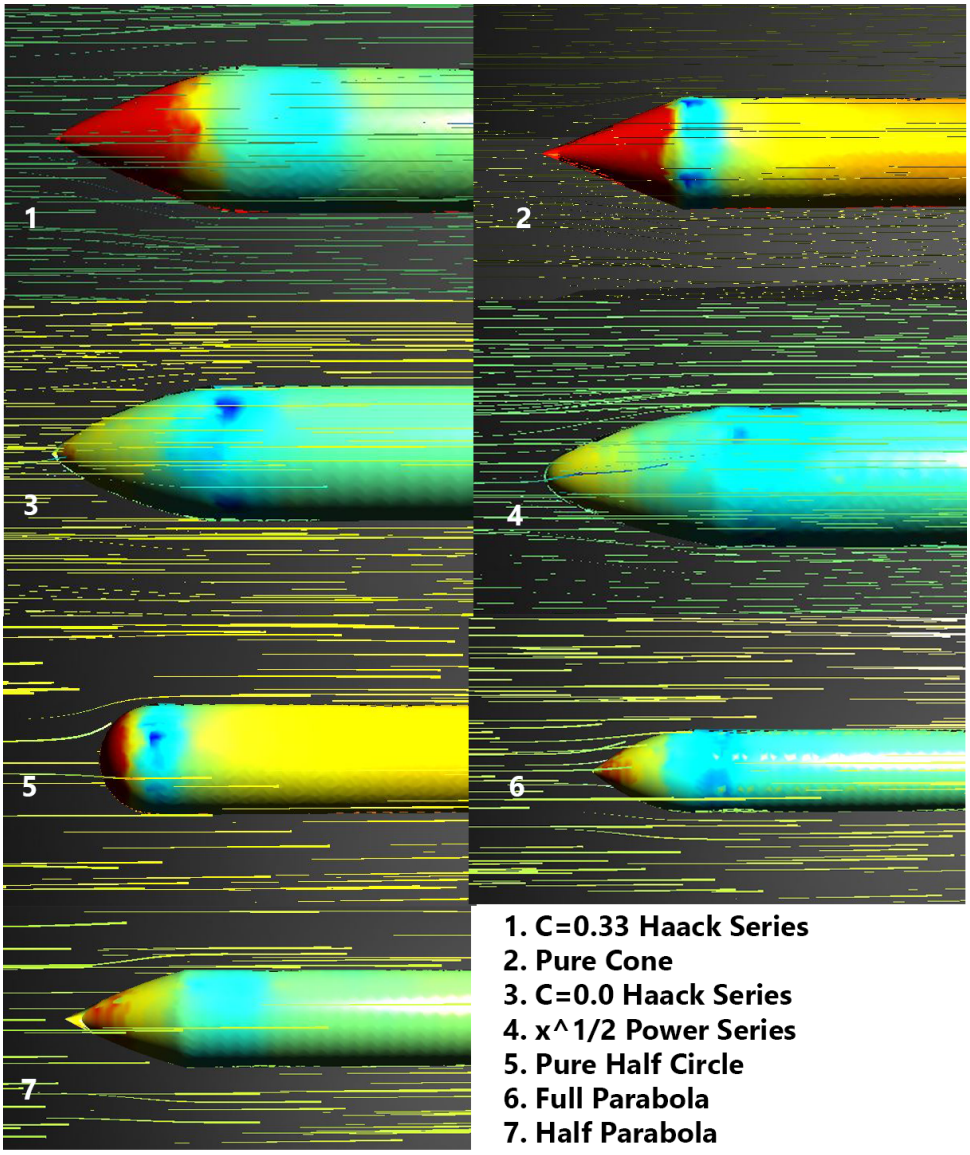

Figure 6.10: Overview of Nose Flow Analyses

6.2.3 Verification & Validation

In order to verify and validate the model, another drag analysis was performed using OpenRocket[2] at the same cruise Mach number (0.47). Tab. 6.6 shows the results of both methods next to each other.

From the verification and validation results, it follows that the C = 0 Haack Series still has the lowest drag coefficient (0.22). However, there are big differences in other drag coefficients. The big increase in drag coefficients for the pure cones is striking. OpenRocket shows that this increase is caused by the high pressure drag of the pure cone which is not present for the other shapes. OpenRocket furthermore calculates a similar friction drag for both 1.2 and 1.5 fineness ratios. This is questionable as the friction drag largely depends on the wetted surface area, which is larger for high fineness ratios. It is therefore useful to observe that the differences between the drag coefficients of the noses with a fineness ratio of 1.2 are all below 14% and the biggest changes occur for other fineness ratios. Recommendations to reduce the differences are made in section 6.2.6.

[2]http://openrocket.info/, visited on: June 23, 2017

Table 6.6: Nose Verification and Validation Results

Nose	Fineness	C_D initial	C_D OpenRocket	Percentual Difference
Pure cone	1.2	0.24	0.39	+63
Pure cone	1.5	0.27	0.36	+33
x$\hat{0}$.5 Power series	1.2	0.23	0.23	+/-0
x$\hat{0}$.5 Power series	1.5	0.32	0.23	-28
C=0 Haack series	1.2	0.22	0.22	+/-0
C=0 Haack series	1.5	0.31	0.23	-26
C=0.33 Haack series	1.2	0.28	0.24	-14
Full parabola	1.2	0.23	0.23	+/-0
Half parabola	1.2	0.26	0.23	-12
Pure half circle	0.5	0.33	0.23	-30

6.2.4 Sensitivity

The main input parameters of the wind tunnel analysis are the flow speed, angle of attack, and the wind tunnel dimensions. The latter are set large enough to not significantly influence the results according to the Autodesk wind tunnel configuration manual[3].

The sensitivity analysis is therefore performed by changing the values for the flow speed and the angle of attack. As computations are time-intensive, only the three best performing nose shapes are considered in the sensitivity analysis. These include the C=0 Haack series, the $x^{0.5}$ power series, and the full parabola. The models are tested with both a 10% higher and 10% lower speed than the 155 m/s average cruise speed. Furthermore, the model is run on a high angle of attack of 12.5 degrees in order to test its (close to) stall performance. The results of this analysis are shown in Tab. 6.7.

Table 6.7: Drag Coefficients of Nose-Cylinder Combinations

Nose	alpha [deg]	velocity [m/s]	New C_D	Initial C_D
C=0 Haack series	0.41	139.5	0.26	0.22
C=0 Haack series	0.41	170.5	0.22	0.22
C=0 Haack series	12.5	155	0.19	0.22
x$\hat{0}$.5 Power series	0. 41	139.5	0.26	0.23
x$\hat{0}$.5 Power series	0. 41	170.5	0.24	0.23
x$\hat{0}$.5 Power series	12.5	155	0.20	0.23
Full parabola	0.41	139.5	0.20	0.23
Full parabola	0.41	170.5	0.19	0.23
Full parabola	12.5	155	0.18	0.23

The results seem peculiar as the drag coefficients are highest for the lowest speed and highest for a high angle of attack whereas a reversed result would be expected. The explanation of this effect lies in the way the drag coefficient is computed. First, the total drag is calculated after which the drag coefficient is calculated using the frontal area and velocity. A higher flight velocity would therefore lead to a lower drag coefficient. The same holds for a high angle of attack, which increases the frontal area, and therefore reduces the drag coefficient. This hypothesis is confirmed when looking at the values for total drag. For the Full Parabola for example, the drag rises from 10677 N for the 10% lower velocity to 44939 for the 12.5 degrees angle of attack. This effect makes it hard to draw clear conclusions from the sensitivity analysis, rather than that the total drag increases for higher speed and angles of attack.

6.2.5 Sustainability

In designing the nose, environmental sustainability is the dominant form of sustainability considered. As described in section 6.2.1, designing the nose for the least amount of drag reduces the fuel consumption

[3]https://knowledge.autodesk.com/support/flow-design/learn-explore/caas/CloudHelp/cloudhelp/ENU/FlowDesign/files/GUID-7717625F-6388-4DAF-B893-989F1091938E-htm.html, visited on: June 22, 2017

and therefore positively contributes to environmental sustainability.

6.2.6 Conclusion & Recommendations

From the nose design, it is concluded that a Haack Series shape with C=0 is the best nose shape for the ModuLR as it has te lowest drag coefficient compared to the other shapes tested. This low drag coefficients contributes to fulfilling the emissions, range, and take-off requirements as described in chapter 12.

Recommendations are made for the further design of the nose. Using more accurate (CFD) software would increase the accuracy of the drag coefficient calculations. This is necessary as fluctuations are observed between different models and between different computations within a model. Another recommendation would be to analyze a greater variety of shapes and fineness ratios in order to come up with the design with the least drag possible. Lastly, the material of the nose could be considered. As skin friction is important at the speed range considered, the use of very smooth materials could improve the drag performance. A final consideration would be to look more at the total drag instead of mainly at the drag coefficients when comparing different conditions for a certain shape instead of comparing shapes with each other. This is necessary as the speed and areas to which the coefficients are normalized sometimes differ.

6.3 Center of gravity determination

In order to size the tail and determine other properties of the aircraft such as inertiae, the center of gravity is needed. In this section, the method for this determination as well as the results will be discussed. A sensitivity analysis on the method as well as verification and validation are performed. Finally, a conclusion is drawn and recommendations for center of gravity determination are proposed.

6.3.1 Method

There are several positions that the center of gravity can attain during flight as well as on the ground. A loading diagram has to be created to determine the locations of the center of gravity under various loading conditions. In order to do this, the weight of the aircraft is split up in several components and groups with corresponding locations.

The first step is to look at the center of gravity of the aircraft when it is not loaded with fuel and cargo. This will be the lowest point in the loading diagram. The aircraft then has to be loaded with fuel and cargo. The cargo can only be loaded from the front. The first container will be located closely to the nose, while the other containers are moved from the back to the nose. The fuel is located closely to the wing. The loading is done in two ways in the diagram. The first way is by loading the fuel first and then the cargo . The second by loading the cargo first and then the fuel.

From the diagram it can be seen that the most forward and most aft position for the center of gravity can be obtained. Several groups can be shifted to adjust these locations.

6.3.2 Results

The loading diagrams of all aircraft are presented in Fig. 6.11a, 6.11b, and 6.11c for the ModuLR-100, -200, and -300, respectively. The locations of the center of gravity can be found in Tab. 6.8 as well as the individual component weights and locations. A visual representation for the center of gravities is presented in Fig. 6.12.

Table 6.8: Input parameters used for aerodynamic analysis

	ModuLR-100	**ModuLR-200**	**ModuLR-300**
$c.g._{aft_{max}}$	0.481	0.449	0.422
$c.g._{aft_{min}}$	0.489	0.472	0.444

6.3.3 Sensitivity

A sensitivity analysis is performed on the method for the loading diagrams. The weights and locations of the wing group, fuselage group, and empennage group are relocated to look at the corresponding change in center of gravity. The most aft location of the c.g. is taken for this evaluation.

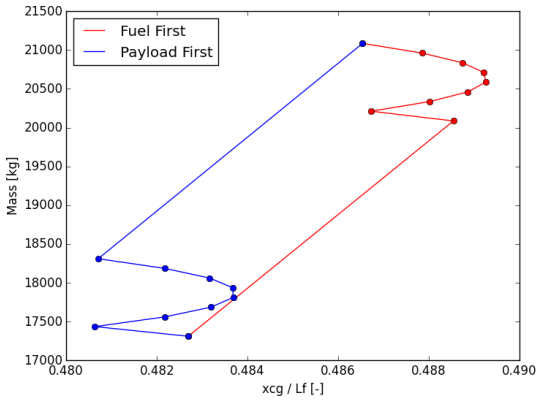

(a) ModuLR-100

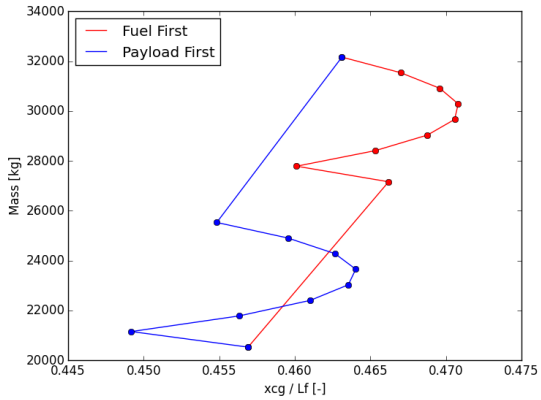

(b) ModuLR-200

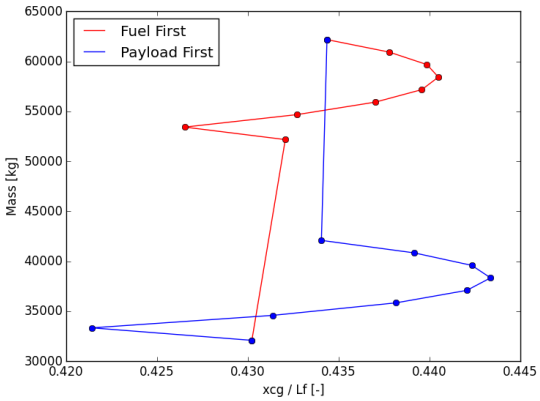

(c) ModuLR-300

Figure 6.11: Loading diagram for all ModuLR configurations

The sensitivity analysis for a change in mass is presented in Fig. 6.13a. All curves converge in an asymptotic matter towards the component location. The wing converges the fastest as it has the largest mass. The empennage in the slowest manner due to its low mass and big difference in location with respect to the original center of gravity. It can, however, be seen that the empennage does have the largest influence on the center of gravity when the mass is increased by a certain percentage, due to the fact that it is located far away from original center of gravity. Components with a large distance from the original center of gravity should therefore be carefully evaluated for their correct mass.

The sensitivity analysis for a change in location is presented in Fig. 6.13b. All curves increase in a almost linear matter. The larger that mass the bigger the change in location. Replacing components with a large mass thus has a large influence on the aircraft. The locations of components with large masses should therefore be carefully evaluated.

6.3.4 Verification & Validation

Code verification was performed by setting component weights and locations at a certain magnitude, resulting in center of gravity locations. These center of gravity locations were then also calculated by hand in order to verify the results.

Validation of the results can be performed by setting up a configuration where the weights and locations are simulated and the center of gravity determined in the setup. The results of the setup can than be determined by comparing the results to reality. Another option is to compare the results to the the CAD model when it is more complete to compare the c.g. of the script to the c.g. of this more accurate model.

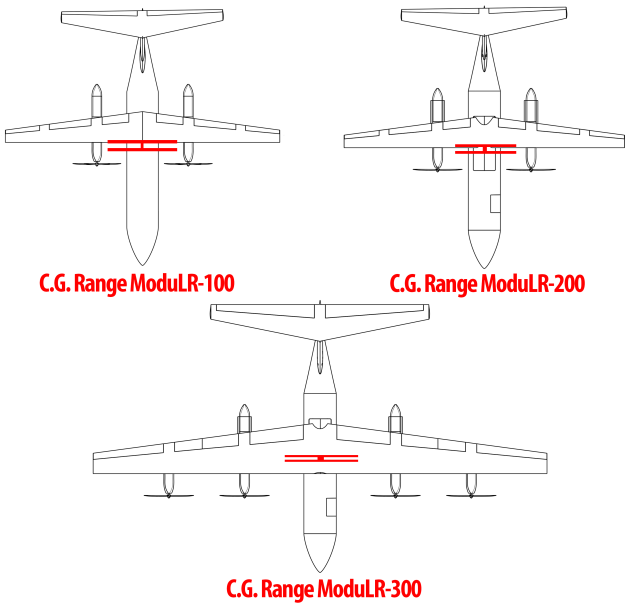

Figure 6.12: c.g. ranges of all ModuLR configurations

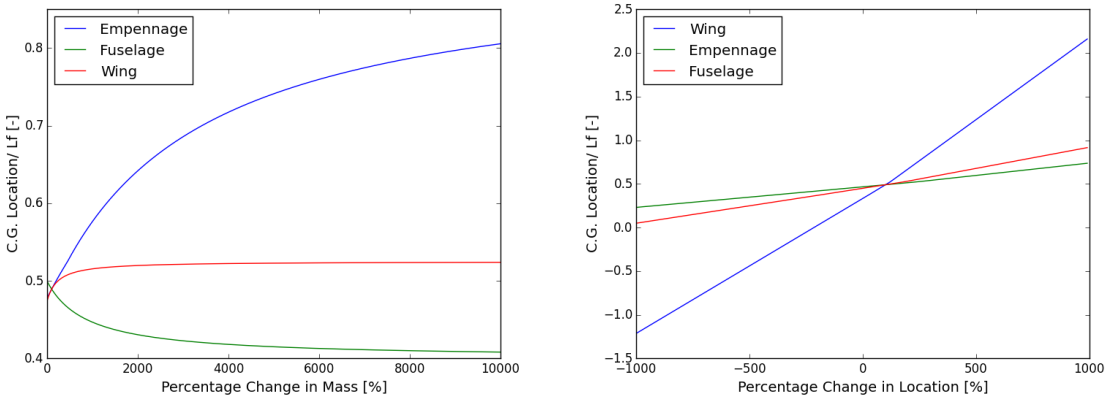

(a) Component mass

(b) Component location

Figure 6.13: Sensitivity analysis on component mass (a) and component location (b)

6.3.5 Conclusion & Recommendations

The center of gravity is now determined using the component weight estimation method and basic moment balance relations. In order to get a more accurate prediction, the weights and locations should be continuously updated as the design gets more detailed.

6.4 Tail design

In this section the empennage subsystem is designed. Firstly, the method for horizontal and vertical tail design, and an analysis of their aerodynamic characteristics is presented. Next, the results are presented together with verification and validation of the method. The tail subsystem has to fulfill requirements RUCA-T-ACS-T 1 - 3, RUCA-T-OPS-CT-2, and RUCA-T-REC from chapter 12. In the conclusion the requirements are checked and some recommendations are presented.

6.4.1 Method

For the tail design a T-tail configuration is chosen. This is mainly done because of the high wing configuration, where the T-tail ensures that the horizontal tail is out of the wake, downwash, and

vortices of the wing as well as the exit flow of the engines. Another reason for the choice is the fact that the fuselage remains the same length among all of the configurations. The T-tail allows for an increased distance between the aerodynamic center of the tail and that of the main wing due to the sweep of the vertical tail. However, the downsides of the configuration are a heavier structure of the vertical tail and the possibility of deep stall [52]. Both of them have to be monitored.

The design method of the T-tail is subdivided into the planform design of the horizontal tail, the planform design of the vertical tail, and the airfoil selection.

Horizontal tail

The first step of the horizontal tail design is looking into requirement RUCA-T-ACS-T-2, maintaining longitudinal trim. For this the stick-fixed static stability is assessed together with the neutral point which is checked with the most aft location of the c.g.. The horizontal tail area over the main wing area is the main parameter and is calculated according to Eq. 6.13, from [53] of c.g. values normalized with the MAC.

$$\frac{S_h}{S} = \frac{1}{\frac{C_{L\alpha_h}}{C_{L\alpha_{A-h}}}\left(1-\frac{\delta\epsilon}{\delta\alpha}\right)\frac{l_h}{\bar{c}}\left(\frac{V_h}{V}\right)^2}\bar{x_{cg}} - \frac{\bar{x_{ac}} - S.M.}{\frac{C_{L\alpha_h}}{C_{L\alpha_{A-h}}}\left(1-\frac{\delta\epsilon}{\delta\alpha}\right)\frac{l_h}{\bar{c}}\left(\frac{V_h}{V}\right)^2} \tag{6.13}$$

The lift rate coefficient of the aircraftless tail, $C_{L_{\alpha_{A-h}}}$, is determined using Eq. 6.14. The downwash gradient is estimated according to Eq. 6.15 using the DATCOM method from [53].

$$C_{L_{\alpha_{A-h}}} = C_{L_{\alpha_w}}\left(1+2.15\frac{b_f}{b}\right)\frac{S_{net}}{S} + \frac{\pi}{2}\frac{b_f^2}{S} \tag{6.14}$$

$$\frac{\delta\epsilon}{\delta\alpha} = \frac{2C_{L_{\alpha_w}}}{\pi A} \tag{6.15}$$

Next to stick-fixed static stability, the horizontal tail also has to fulfill requirement RUCA-T-OPS-CT-2, maintaining longitudinal control. Therefore, the tail is also checked for controllability for a range of c.g. values normalized with the MAC according to Eq. 6.16, from [54].

$$\frac{S_h}{S} = \frac{1}{\frac{C_{L_h}}{C_{L_{\alpha_{A-h}}}}\frac{l_h}{\bar{c}}\left(\frac{V_h}{V}\right)^2}\bar{x_{cg}} + \frac{\frac{C_{m_\alpha}}{C_{L_{A-h}}} - \bar{x_{ac}}}{\frac{C_{L_h}}{C_{L_{\alpha_{A-h}}}}\frac{l_h}{\bar{c}}\left(\frac{V_h}{V}\right)^2} \tag{6.16}$$

Eq. 6.13 and Eq. 6.16 result in two lines that, when plotted over each other, indicate stability and controllability for a range in c.g. locations. The horizontal tail area is chosen such that it fulfills both the controllability and stability requirement for the c.g. range, most forward and most aft, that the system will encounter.

The location of the most forward and aft c.g. is determined in section 6.3 with the use of a potato plot. However, the location of the wing along the fuselage influences the c.g. location. Therefore, the most forward and aft c.g. locations are determined for a range of wing locations. This range is plotted on the controllability and stability lines. From this final plot the location of the wing is chosen such that the tail area ratio is lowest, but still fulfills the stability and controllability requirements for the CG range at that wing location.

The planform of the horizontal tail is determined by setting the taper and aspect ratio and then solving for MAC, span, root chord, and tip chord simultaneously.

Vertical tail

The vertical tail needs to fulfill requirement RUCA-T-ACS-T-1 and RUCA-T-ACS-T-3, directional trim, and controllability in one engine inoperative situation. The vertical tail size is determined using the vertical tail volume coefficient. This coefficient is acquired from empirical data according to Eq. 6.17 from [55], relating the fuselage and wing dimensions to the vertical tail dimensions. Due to the T-tail configuration the horizontal tail affects the vertical tail trough the plate effect. Therefore, a reduction of 10% on the vertical tail volume coefficient is applied [56]. From the vertical tail volume coefficient the required surface area of the vertical tail is determined using Eq. 6.18.

$$V_v = 0.9\left(0.29\frac{h_f^2 l_f}{b_w S} + 0.0293\right) \tag{6.17}$$

$$S_v = \frac{b_w S V_v}{l_v} \tag{6.18}$$

The planform of the vertical tail is determined by setting the taper and aspect ratio and then solving for MAC, span, root chord, and tip chord simultaneously.

Aerodynamic characteristics

In order to meet the longitudinal trim requirement, RUCA-T-ACS-T-2, the required lift coefficient and incidence angle of the tail are analyzed. The required 2D lift coefficient for the horizontal tail is determined by using Eq. 6.19 from [52].

By using a MATLAB script a database of symmetric airfoils is checked in Xfoil [57] for this required design lift coefficient. The airfoil with the lowest drag coefficient at this lift coefficient is chosen for the horizontal tail. For the vertical tail an airfoil with a high lift gradient is chosen with the lowest possible drag at an zero angle of attack.

The 2D characteristics however need to be checked for 3D influences. The 3D lift rate coefficient for the horizontal tail is determined by Eq. 6.20. Using this value and iterating over different angle of attacks, a new angle of attack for the horizontal tail is determined in order for the 3D lift coefficient to meet the design lift coefficient.

$$C_{l_h} = \frac{\left(C_{m0_{wf}} + C_{L_{cr}}(\bar{x_{cg}} - \bar{x_{ac}})\right)}{\frac{l_h S_h}{\bar{C} S}} \quad (6.19) \qquad C_{L_{\alpha_h}} = \frac{C_{l_{\alpha_h}}}{1 + \frac{C_{l_{\alpha_h}}}{\pi A_h}} \quad (6.20)$$

The incidence angle of the horizontal tail is then determined by using Eq. 6.21. Where the downwash is determined by Eq. 6.22.

$$i_h = \alpha_h - \alpha_w + \epsilon \quad (6.21) \qquad \epsilon = \frac{2C_{L_w}}{\pi A} + \frac{\delta\epsilon}{\delta\alpha}\alpha_w \quad (6.22)$$

In order to evaluate the horizontal tail design the trim drag is evaluated following Eq. 6.23. Where the Oswald factor is calculated using Eq. 6.24 from [58].

$$D_{trim} = \frac{1}{2}\rho V^2 \left(\frac{V_h}{V}\right)^2 S_h \frac{C_{L_h}^2}{\pi A_h e_h} \quad (6.23) \qquad e_h = 4.61\left(1 - 0.045 A_h^{0.68}\right)\left(\cos\Lambda_{LE}\right)^{0.15} - 3.1 \quad (6.24)$$

The final check on the tail design is performed by checking the longitudinal stability by calculating C_{m_α} using Eq. 6.25 from [53]. Where C_{m_α} has to be negative in order for the system to be statically longitudinal stable.

$$C_{m_\alpha} = C_{L_{\alpha_w}}(\bar{x_{cg}} - \bar{x_{ac}})\frac{V_h}{V}^2 \frac{S_h}{S}\left(\frac{l_h}{\bar{C}} - \bar{x_{cg}}\right)\left(1 - \frac{\delta\epsilon}{\delta\alpha}\right) \quad (6.25)$$

6.4.2 Results

In this section the results of the tail sizing are presented. Firstly, the horizontal tail size is presented, secondly the vertical tail, and lastly their aerodynamic characteristics.

Horizontal tail

In Fig. 6.14 the scissor plots for all ModuLR configurations are presented. The wing location and following horizontal tail surface area ratio are chosen and indicated with a red dot in the figure. It has to be indicated that each configuration has a different wing location, since keeping the wing location the same for all the configurations would lead to horizontal tail surface area ratios of bigger than 1 as can be seen in the figure. As can be seen this results in a wing location of 0.53, 0.50, and 0.45 for the ModuLR -100, -200, and -300 respectively. The horizontal tail surface area ratios are 0.33, 0.38, and 0.35. The dimensions of the horizontal tail can be found in Fig. 6.15. Where the surface area of the horizontal tail is 17.82, 27.66, and 47.58 m^2.

The inputs for the method that led to this result can be found in App. A. Where the horizontal tail/wing speed ratio has been set to 1 because of the T-tail configuration. The l_h is determined with the location of the wing and the length of the fuselage by maximizing the distance and adding extra distance due to the sweep of the vertical tail. The safety margin on stability has been set to 5% from [53]. An aspect ratio of $\frac{2}{3}A_w$ has been chosen, and the taper ratio of the horizontal tail is the same as that of the main wing [52].

Vertical tail

The vertical tail sizing method results in a vertical tail volume coefficient of 0.06, 0.05, and 0.04 for the ModuLR -100,-200, and -300, respectively. The dimensions of the vertical tail can be found in Fig 6.15. Where the surface areas of the vertical tail are: 8.07, 9.48, and 16.18 m^2.

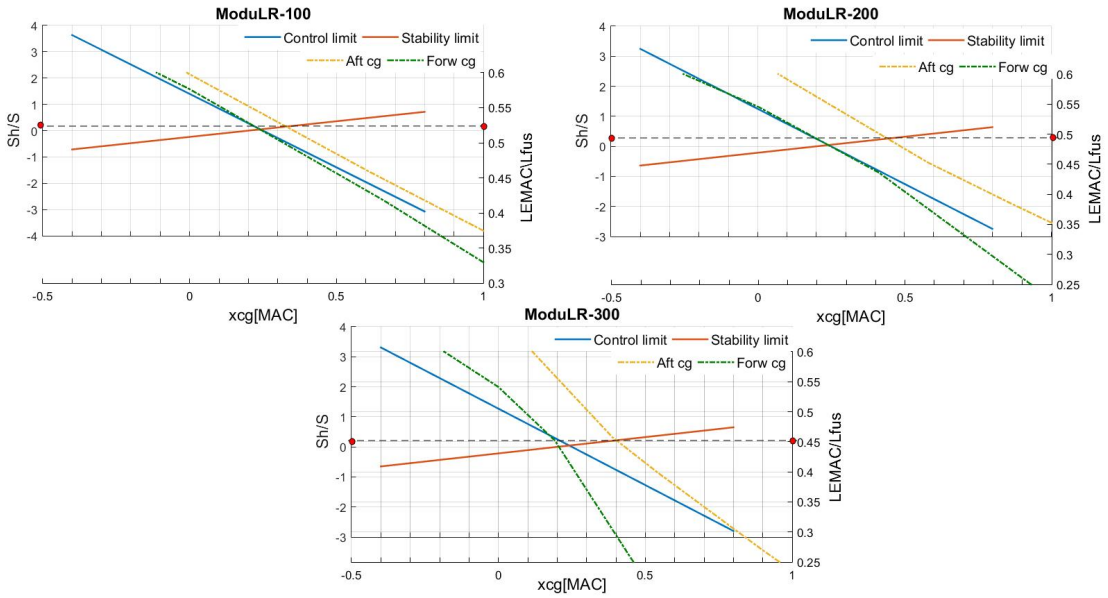

Figure 6.14: Scissorplots for all ModuLR configurations

These results are with the inputs from App A. The aspect ratio of the vertical tail is set at 1.2 with a taper ratio of 0.8 due to the T-tail configuration [52]. Next to that a leading edge sweep of 32 deg is calculated.

Aerodynamic characteristics

The result of the Xfoil analysis for a Reynolds number of 14e6 at a mach number of 0.5 can be found in Fig. 6.16. In the left graph the lift coefficient over the drag coefficient is plotted and in the right graph the lift coefficient over the angle of attack.

From the 2D airfoil selection and the dimensions of the tails the 3D results are displayed in Tab. 6.9.

Table 6.9: Aerodynamic characteristics horizontal and vertical tails.

	ModuLR-100	**ModuLR-200**	**ModuLR-300**
$Airfoil$	NACA 64012	NACA 64012	NACA 64012
$C_{L_h}[-]$	0.079	0.077	0.070
$C_{L_{\alpha_h}}[1/rad]$	5.17	5.17	5.17
$C_{L_{\alpha_v}}[1/rad]$	2.39	2.39	2.39
$a_h[\deg]$	0.87	0.85	0.77
$i_h[\deg]$	1.31	1.27	1.16
$a_{stall}[\deg]$	13.4	15.14	15.45
$e_h[-]$	0.65	0.65	0.65
$C_{D_0}[-]$	0.0057	0.0056	0.0054
$D_{trim}[N]$	47.57	84.02	112.23
$C_{m_\alpha}[-]$	-5.25	-5.45	-3.97

6.4.3 Verification & Validation

In order to verify the models created with the method, standard unit tests are performed. For the horizontal tail sizing the scissor plots are created with inputs following the example from [53] and [54] to check whether the model gives the same result. For the vertical tail the outcome of the vertical tail volume coefficient is checked with the example from [55].

In order to validate the design and check whether the tail design ensures stability, a stability analysis has been performed in XFLR5 [59]. The resulting non-dimensional stability coefficients that tell whether the aircraft is statically stable are C_{m_α} and C_{n_β}. If C_{m_α} is negative, the system has longitudinal static

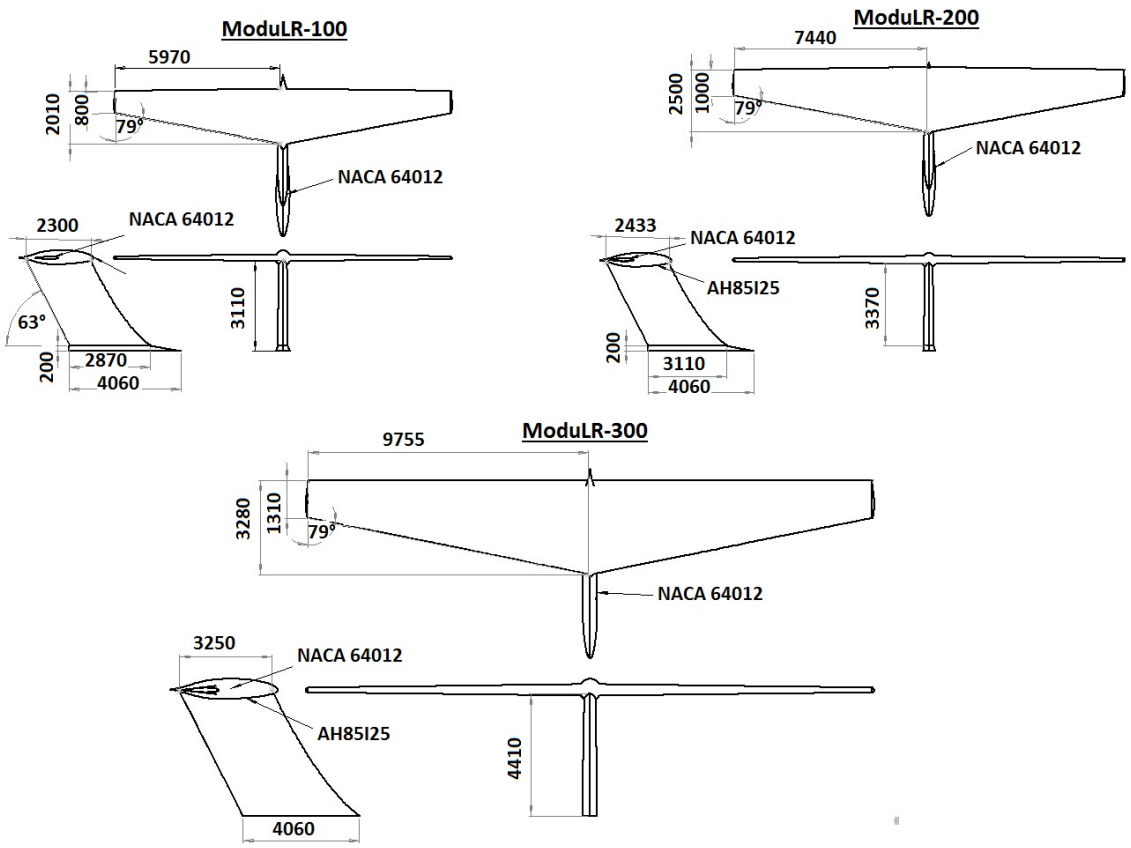

Figure 6.15: Planforms of the horizontal and vertical tail for ModuLR -100,-200, and -300

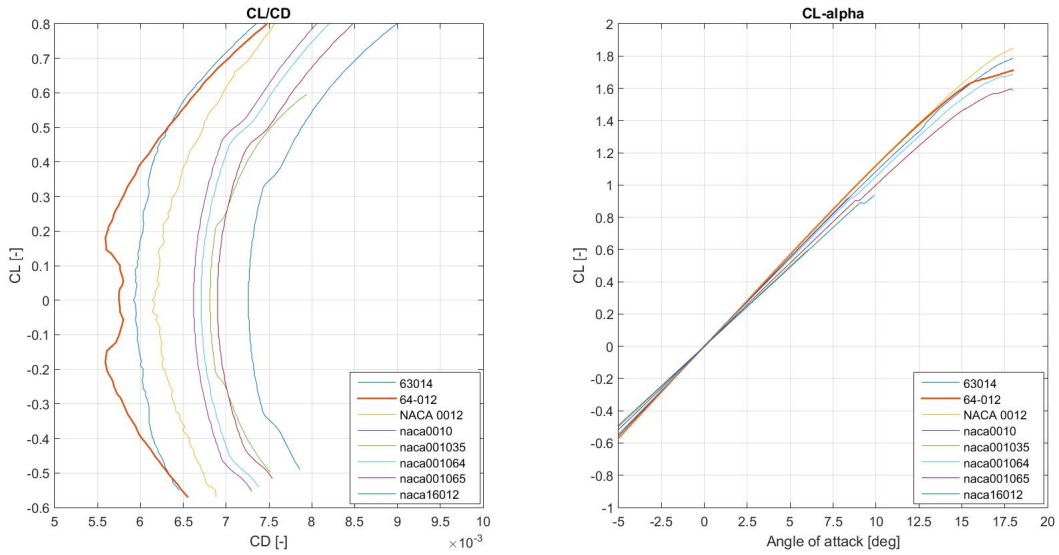

Figure 6.16: Symmetric airfoil analysis xfoil, Re=14e6, M=0.5, Ncrit=9.0

stability, and if C_{n_β} is positive, the system has directional static stability. Furthermore, the dynamic stability of the system is checked in section 6.6 by analyzing five eigenmotions. When the dynamic model is validated, it can be used to validate whether the tail design meets the requirements or should

be adjusted.

6.4.4 Sensitivity

The method for horizontal tail sizing is mostly dependent on the maximum aft and forward CG locations, which are directly linked to the wing location with respect to the fuselage. Therefore, the effect of changing the wing location on the horizontal tail surface area is analyzed. The result of this analysis is presented in Fig. 6.17. Here, it can be seen that the all configurations are extremely sensitive to the wing location, the effect on the -100 configuration is biggest since the c.g. is more influenced by the wing location than for the -300 configuration. From this, it is seen that close attention is necessary when choosing the wing location in order to optimize for the horizontal tail surface area. The vertical tail surface area is mainly dependent on the length of the fuselage. Therefore, the effect of changing the fuselage length on the vertical tail is analyzed. The results can be seen in Fig. 6.17.

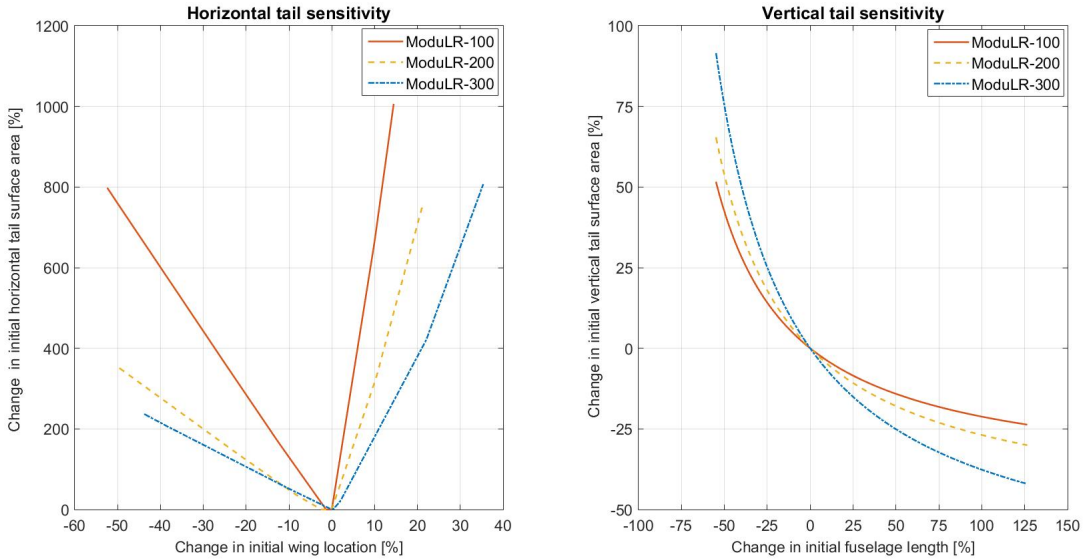

Figure 6.17: Sensitivity analysis for horizontal and vertical tail

6.4.5 Sustainability

Ensuring a sustainable design is in the first place achieved by designing the subsystem for lowest possible drag, in order to achieve a high lift over drag ratio for the aircraft and thus improve emissions. This ensures environmental sustainability and is taken into account for the design. Next to that, by using the same tail for the ModuLR -100 and -200, as is explained in subsection 6.4.6, a reduction in the complexity of the design is achieved together with a reduction of production costs and thus improving economic sustainability. The fact that the basic connector to attach the vertical tails to the fuselage stays the same for all configurations reduces the difficulty of reconfiguration and specialist equipment and personnel necessary. It however has to be noted that by keeping the connector the same, and thus the root chord, difficult geometries are introduced in the design. This in turn leads to a more difficult production process.

6.4.6 Conclusion & Recommendations

The results show that the size of the tails of the ModuLR-300 differs a lot from that of the ModuLR-200 and -100. However, the tails of the ModuLR-100 and -200 are quite similar. Therefore, the possibility is investigated whether the tail can stay the same for the -100 configuration compared to the ModuLR-200. When assuming the same thickness for all the tails it can be assumed that the weight ratio of the tails is equal to the tail ratio. By adding the surface areas the total empennage surface area becomes 25.89 and 37.14 for the ModuLR-100 and -200 respectively. This gives a weight ratio of 1.43. From Tab. 4.1 it can be seen that the empennage, however, is only 4% of the MTOW, so that weight ratio gives an increase on the MTOW of around 1.7%. By keeping the tail the same for the -100 and -200 configuration, it reduces reconfiguration time, production costs, and increases ease of certification. Therefore the decision

is made to keep the tail the same for the -100 and -200 configuration. The increase in size also improves stability characteristics of the -100 configuration.

The RUCA-T-ACS-T-2 requirement indicates that the aircraft shall have static longitudinal stability. Looking at the C_{m_α} values in Tab. 6.9 it can be seen that the value is negative and therefore indicates that this requirement is met.

The RUCA-T-ACS-T-1 requirement and RUCA-T-ACS-T-3 requirement, which indicates directional stability, is checked in section 6.6 by checking the C_{n_β} coefficient. Which, if positive, indicates that the requirement has been met. In the same section spiral stability is checked in order to determine whether the directional stability is not larger than the lateral stability. If necessary the vertical tail size should be adjusted to ensure spiral instability does not occur. It can be seen that the value is positive so it is met.

In order for all tails to be easily attached and detached from the fuselage, a fairing-like connector is designed on which the tails will be mounted, making them reconfigurable, meeting requirement RUCA-T-REC. Each vertical tail will have the same root chord for them to be mountable on the connector, however the tail for the -200 and -100 will reduce to their initial root chord within a span of 0.2 m.

It is recommended that the vertical tail is structurally checked, due to the T-tail configuration it needs to transfer the bending moment of the horizontal tail to the fuselage. Structural analysis has not been performed due to time constraints, however it should not be neglected since it could significantly increase the weight of the vertical tail and with it shift the range of center of gravity. Another recommendation is to ensure deep stall will not occur by employing a mechanism that enables the elevator angles to be full down if deep stall occurs. This to avoid being locked in deep stall, which is a potential fatal state. Next to this, a material selection needs to performed after the structural analysis to ensure the weight of the subsystem meets the mass budget. Finally, detailed connections need to be designed to attach the horizontal tail to the vertical tail.

6.5 Control Surfaces

In this section, the control surfaces which are used to direct and control the aircraft's trajectory are designed and presented. The ailerons, elevator, rudder, and actuation systems are considered, adhering to the RUCA-T-ACS-CS-1 until RUCA-T-ACS-CS-8 requirements, presented in section 12.

6.5.1 Design Method

This section describes the performed design methods, and is based on design procedures presented in the Aircraft Design and System Engineering Elements lecture series[60], the Aircraft Design: A system engineering approach book[52], and the TU Delft Flight Dynamics lecture notes [61]. The methods which will be discussed are all executed, optimized and iterated using the python programming language.

Ailerons

The ailerons are sized to meet the respective RUCA-T-ACS-CS-1 to RUCA-T-ACS-CS-3 requirements, for each ModuLR variant. The requirements are variant specific, as the classification[60] of each aircraft is different due to their different MTOWs.

The time taken to reach the required bank angles is given by Eq. 6.26, where ϕ_{req} is the required bank angle, and $\dot{P}$ is the time rate of change of the aircraft roll rate.

The time rate of change of the aircraft roll rate, $\dot{P}$, is calculated using Eq. 6.27, where P_{ss} is the steady-state roll rate, and ϕ_{ss} is the steady state bank angle.

$$t_\phi = \sqrt{\frac{2\phi_{req}}{\dot{P}}} \tag{6.26}$$

$$\dot{P} = \frac{P_{ss}^2}{2\phi_{ss}} \tag{6.27}$$

The steady-state roll rate is found using Eq. 6.28, where L_A is the aircraft rolling moment, S_w,S_h,S_vt are the surface areas of the wing, horizontal tail and vertical tail respectively, $C_{D,R}$ is the aircraft drag coefficient in rolling motion, and y_D is the average distance between the rolling drag center and aircraft centre of gravity. An average value of $C_{D,R} = 0.9$ is chosen based on existing aircraft [52], and it is assumed that the drag moment arm acts at 40% of the wing span, $y_D = 0.4\frac{b}{2}$ [52].

$$P_{ss} = \sqrt{\frac{2L_A}{\rho(S_w + S_h + S_{vt})C_{D,R}y_D^3}} \tag{6.28}$$

The aircraft rolling moment, L_A, is calculated using Eq. 6.29. The rolling moment coefficient, C_l, is calculated by $C_l = C_{l\delta A} \cdot \delta_A$, where δ_A is the aileron deflection, and $C_{l\delta A}$ is the rolling moment coefficient

due to the aileron deflection, calculated using Eq. 6.30. This equation includes the wing taper effects, evaluated between the inboard half wingspan aileron location y_i and the outboard half wingspan aileron location y_o. The aileron angle of attack effectiveness, τ_a, is approximated using the cubic expression[52] presented in Eq. 6.31, where $\frac{C_A}{C_w}$ is the ratio of the aileron chord to wing chord.

$$L_A = \frac{1}{2}\rho V_{app}^2 S C_l b \qquad (6.29) \qquad C_{l_{\delta_A}} = \frac{2C_{L_{\alpha_W}}\tau C_r}{Sb}\left(\frac{y^2}{2} + \frac{2}{3}\left[\frac{\lambda-1}{b}\right]y^3\right)\Bigg|_{y_i}^{y_o} \qquad (6.30)$$

$$\tau_a \simeq 3.1638\left(\frac{C_A}{C_w}\right)^3 - 4.6732\left(\frac{C_A}{C_w}\right)^2 + 2.8792\frac{C_A}{C_w} \qquad (6.31)$$

It is important to note that the additional 2 outboard engines drastically limit the aileron design space in the ModuLR-300 variant. It is found that the deflection requirement of RUCA-T-ACS-CS-3 requirement cannot be met with one outboard aileron in this variant, as it is not possible to further extend the aileron over the engine for aerodynamic and structural reasons. If the aileron were to span in this limited design space, from the outboard engine to wingtip, the deflection angle required becomes significantly greater than 30°. For this reason, Eq. 6.30 is augmented for the ModuLR-300 variant, to include the contribution of an inboard aileron. This will be discussed further in section 6.5.2. The augmented equation for the total $C_{l\delta A}$ is given in Eq. 6.32.

$$C_{l_{\delta A,total}} = \frac{2C_{L_{\alpha_W}}\tau C_r}{Sb}\left(\frac{y^2}{2} + \frac{2}{3}\left[\frac{\lambda-1}{b}\right]y^3\right)\Bigg|_{y_i}^{y_o} + \frac{2C_{L_{\alpha_W}}\tau C_r}{Sb}\left(\frac{y^2}{2} + \frac{2}{3}\left[\frac{\lambda-1}{b}\right]y^3\right)\Bigg|_{y_{i,inboard}}^{y_{o,inboard}} \qquad (6.32)$$

The bank angle achieved when the roll rate reaches the steady state value, P_{ss}, is calculated using Eq. 6.33.

$$\phi_{ss} = \frac{I_{xx}}{\rho y_D^3 (S_w + S_h + S_{vt}) C_{D,R}} ln(P_{ss}^2) \qquad (6.33)$$

Where I_{xx} is the moment of inertia about the longitudinal axis. This is conservatively approximated by modeling the three aircraft variants as[6]: a solid cylinder of the fuselage which includes the majority of systems and full payload, two solid cuboids for the wings which contain the fuel, and point masses for the vertical tail, engines and main landing gear. The solid cylinder mass is composed of the mass of the payload, systems, and structure of the fuselage, approximated as $M_{cylinder} = M_{OEW} + M_{payload} - M_{wings} - M_{engines} - M_{gears} - M_{tail}$. It is assumed that the wings contain all of the fuel mass, and the point masses are assumed to have the mass of the respective system group, as calculated in Tab. 4.1 in section 4.2. This inertia calculation is presented in Eq. 6.34.

$$\begin{aligned} I_{xx} = \frac{1}{2}M_{cylinder}r^2 + 2\Bigg(&\frac{\frac{M_{wings}+M_{fuel}}{2}}{12}\left(\left(\frac{b}{2}\right)^2 + t^2\right) + \frac{M_{wings}+M_{fuel}}{2}\left(\frac{b}{6}\right)^2\Bigg) \\ &+2\frac{M_{engines}}{N_{engines}}d_{engine}^2 + 2\frac{M_{gear}}{N_{gear}}d_{gear}^2 + M_{tail}d_t^2 \end{aligned} \qquad (6.34)$$

Where r is the radius of the fuselage, b is the wingspan, t is the maximum airfoil thickness, and all d variables are the perpendicular distances to the longitudinal axis. It is important to note that the ModuLR-300 variant has four engines, and thus the third from last term is included twice, but this time taking the outer engine distance for d_{engine}.

From the equations above, the influence of: δ_A on C_l, locations of y_i and y_o (and $y_{i,inboard}$ and $y_{o,outboard}$ for the ModuLR-300 variant) on $C_{l_{\delta A}}$, and $\frac{C_A}{C_w}$ on τ_a enable the ailerons to be sized. Therefore, δ_A, y_i, and y_o (as well as $y_{i,inboard}$ and $y_{o,outboard}$), and $\frac{C_A}{C_w}$ are optimized to meet the aforementioned requirements, and are used to yield the final aileron designs, presented in section 6.5.2. It is important to note that the maximum aileron deflection is designed such that it does not exceed the 30° requirement of RUCA-T-ACS-CS-3.

Elevator

The elevator is designed in order to allow a sufficient deflection to maintain longitudinal trim at flight speeds between V_S and V_C, complying with the RUCA-T-OPS-CT-4 requirements. The elevator deflection is ensured to be lower than 30°, in compliance with RUCA-T-ACS-CS-3. The elevator deflection required to maintain longitudinal trim is given by Eq. 6.35.

$$\delta_E = -\frac{\left(\frac{TZ_T}{\bar{q}S\bar{C}} + C_{m_0}\right)C_{L_\alpha} + (C_{L_{cr}} - C_{L_0})C_{m_\alpha}}{C_{L_\alpha}C_{m_{\delta_E}} - C_{m_\alpha}C_{L_{\delta_E}}} \tag{6.35}$$

Where T is the thrust during the cruise, and $Z_T = 0.5$ is assumed as the perpendicular distance between the thrust vector and the c.g. location. The elevator effectiveness coefficients, $C_{m_{\delta E}}$ and $C_{L_{\delta E}}$ are approximated using Eq. 6.36 and 6.37.

$$C_{m_{\delta E}} = -C_{L_{\alpha h}}\eta_h \bar{V}_H \frac{b_E}{b_h}\tau_e \tag{6.36}$$

$$C_{L_{\delta E}} = C_{L_{\alpha h}}\eta_h \frac{S_h}{S}\frac{b_E}{b_h}\tau_e \tag{6.37}$$

Where $\eta_h = 1$ is assumed for the horizontal tail dynamic pressure ratio as the T-tail elevator configuration is in the free stream, $\bar{V}_H$ is the horizontal tail volume, and $\frac{b_E}{b_h} = 0.9$ is used as the elevator is assumed to span over the whole usable length of the horizontal tail (therefore this accounts for the vertical tail structural interaction). The elevator angle of attack effectiveness, τ_e, is calculated using the cubic numerical approximation[52] presented in Eq. 6.38. This expression depends on $\frac{C_E}{C_h}$, which is the ratio of the elevator chord to the horizontal tail chord.

$$\tau_e \simeq 3.1638\left(\frac{C_E}{C_h}\right)^3 - 4.6732\left(\frac{C_E}{C_h}\right)^2 + 2.8792\frac{C_E}{C_h} \tag{6.38}$$

The value of $\frac{C_E}{C_h}$ must be lower than 0.5, as any value greater than this would require a horizontal tail that is completely movable[52], which is not desirable for structural reasons.

From these relations, the driving geometric parameter that the elevator is designed for is the $\frac{C_E}{C_h}$ ratio. The optimum value is found such that the aforementioned requirements are met.

Rudder

The rudder system is designed to meet the RUCA-T-ACS-CS-5 and RUCA-T-ACS-CS-6 requirements. Eq. 6.39 is used to determine the required rudder deflection in the asymmetric thrust condition.

$$\delta_R = \frac{T_L y_T}{-\bar{q}SbC_{n_{\delta R}}} \tag{6.39}$$

$$C_{n_{\delta R}} = -C_{L_{\alpha_V}}\bar{V}\eta_V\tau_r\frac{b_R}{b_V} \tag{6.40}$$

The asymmetric thrust, T_L, is considered in both the take-off/go-around and cruise condition, in accordance with the requirements. The variable y_T is the spanwise distance between the operating engine and centre of the fuselage, which is assumed to coincide with the c.g. location.

In order to comply with the different flight conditions stated in the requirement,, $\bar{q}$ is first considered at the landing conditions, with a minimum control speed of the $V = V_{MC} = V_S$, being significantly less than the RUCA-T-ACS-CS-6 requirement. This was done in order to account for safety reasons, such as a sudden gust drastically reducing the speed. For the cruise thrust conditions, $V = V_{MC} = V_{S,clean}$.

The rudder control derivative, $C_{n_{\delta R}}$ is given by Eq. 6.40. When calculating this variable, the tail volume coefficient is calculated by $\bar{V}_V = \frac{l_V S_V}{bS}$, and $\eta_V = 0.97$ [52] is assumed as the vertical tail dynamic pressure ratio. For ratio of the rudder span to vertical tail span, $\frac{b_R}{b_V} = 1$ is used as the rudder is assumed to span along the whole length of the vertical tail.

The rudder angle of attack effectiveness, τ_r, is determined using the same approximation method as in the previous control surface designs, as shown in Eq. 6.41[52].

$$\tau_r \simeq 3.1638\left(\frac{C_R}{C_V}\right)^3 - 4.6732\left(\frac{C_R}{C_V}\right)^2 + 2.8792\frac{C_R}{C_V} \tag{6.41}$$

From these relations, $\frac{C_R}{C_V}$ is iterated and optimized to meet the RUCA-T-ACS-CS-3 deflection requirements at speeds between V_S and V_C.

Actuator Control Force

The actuators must adhere to the stroke and force requirements stated in RUCA-T-ACS-CS-7 and RUCA-T-ACS-CS-8. The force required to move the control surface by the specified deflection angle of each control surface is calculated using Eq. 6.42. This equation is commonly known as the stick

force equation [61]. However, the ModuLR system is unmanned, and therefore will require an actuator to perform these movements, as there is no pilot on board of the aircraft. In this equation, δ_C is the deflection angle of the control surface, x_a is the distance the control actuator must move to achieve the require deflection, S_C is the surface area of the control surface, and C_C is the chord length of the control surface.

$$F_a = \frac{1}{2}\frac{\delta_C}{x_a}\rho V^2 S_C C_C C_h \qquad (6.42) \qquad\qquad C_h = C_{h_\alpha}\alpha + C_{h_{\delta_C}}\delta_C \qquad (6.43)$$

The hinge moment coefficient, C_h, is calculated using Eq. 6.43. For the hinge coefficients, $C_{h_\alpha} = -0.1$ and $C_{h_{\delta_C}} = -0.3$ are assumed, as these are average value from statistical aircraft [52].

In order to comply with the requirements, the Parker Fly-By-Wire Flight Control Actuator[4] is used as the typical aerospace actuator. This actuator has a maximum stroke length of 0.4m, and an operating force between approximately 6500 N and 533 kN. Therefore, the actuator distance of $x_a = 0.2$ is selected, as this means that the actuator is able to initially start from the "middle" extension of 0.2 m. It can then extend to 0.4 m, or shorten to 0 m, creating a 0.2 m change for the deflection of the control surfaces. The actuator is modeled as acting on the top side of the wing, therefore an extension of the actuator results in a downward control surface deflection, and a retraction in the actuator stroke results in a upwards deflection. Additionally, when calculating the forces for the ModuLR-300 variant, the aileron is assumed to be one surface, and is not split up into inboard and outboard ailerons.

6.5.2 Results

This section presents the results of the aforementioned methods. The input variables used to create these results are presented in Tab. A.4 in App. A.

Ailerons

Tab. 6.10 and 6.11 present the times required to achieve 30° and 45° bank angles, the dimensions of the aileron, and the required deflection angle, in both the landing and cruise configurations.

Table 6.10: Aileron system characteristics in landing configuration

ModuLR	**Units**	**-100**	**-200**	**-300**
Time to achieve a bank angle of 45°	[s]	1.39	1.82	1.83
Time to achieve a bank angle of 30°	[s]	1.13	1.49	1.49
Inboard aileron start	$[\frac{b}{2}]$	-	-	0.52
Inboard aileron end	$[\frac{b}{2}]$	-	-	0.64
Outboard aileron start	$[\frac{b}{2}]$	0.75	0.8	0.69
Outboard aileron end	$[\frac{b}{2}]$	1	1	1
Aileron chord to wing chord ratio	[-]	0.3	0.3	0.3
Deflection angle	[°]	29.7	29.6	29.4

Table 6.11: Aileron system characteristics in cruise configuration

ModuLR	**Units**	**-100**	**-200**	**-300**
Time to achieve a bank angle of 45°	[s]	1.39	1.83	1.83
Time to achieve a bank angle of 30°	[s]	1.14	1.49	1.49
Deflection angle	[°]	11.5	13.2	11.3

As can be seen in the tables, the ModuLR-100 achieves a 45° bank angle in 1.39 s, and the ModuLR-200 and -300 achieve a 30° in 1.49 s in both the landing and cruise configurations. The deflection required to make the bank angle in the cruise is almost one third for all variants. The ModuLR-300 variant, as previously mentioned, also contains an inboard aileron as the outboard engines interfere with the required size of the aileron. The dimensions of these are stated in the table.

[4] http://ph.parker.com/us/en/fly-by-wire-flight-control-actuators, visited on June 20, 2017

The maximum deflection occurs at the landing configuration, therefore Fig. 6.18 presents the required forces to deflect the control surface by the deflection angles presented in Tab. 6.11, for a range of typical angle of attacks. It is important to note that the force is positive for the downward deflection, as an actuator forward motion is required, and is negative for the upward deflection, as an actuator backward motion is required, as the actuator is assumed to act on the top side of the aileron.

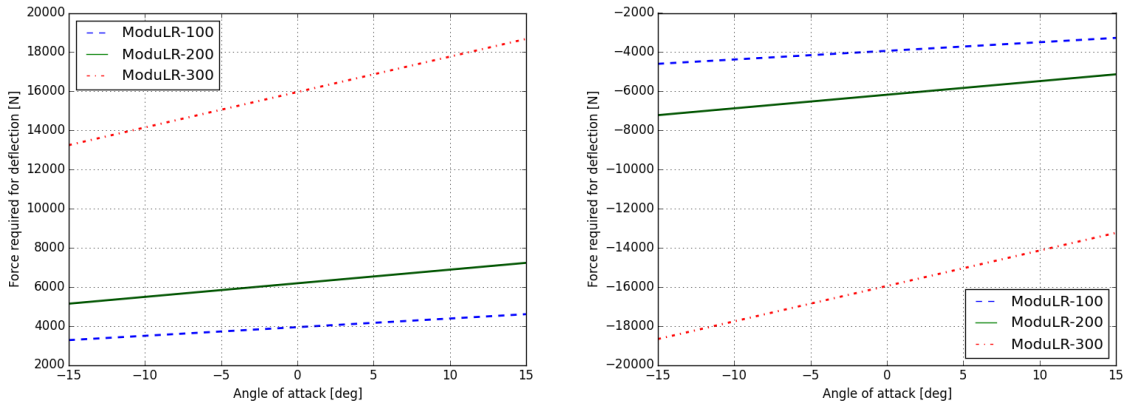

(a) Force for maximum downward aileron deflection (b) Force for maximum upward aileron deflection

Figure 6.18: Actuator force for aileron deflection

As can be seen, the maximum absolute force occurs at $\alpha = +15°$ for the downward aileron deflection, and at $\alpha = -15°$ for the upward deflection. For the ModuLR-100, the maximum absolute force is 4868.2 N, for the -200 variant, it is 7241.3 N, and for the -300 variant, it is 18927.9 N. The -300 experiences the largest forces, as the size of the aileron is significantly greater than the -100 and -200 variants.

Fig. 6.19a to 6.19c present the aileron position and dimensions on the wing. All numbers presented in the drawings are in mm.

Elevator

Tab. 6.12 presents the dimensions and deflections required to maintain longitudinal stability.

Table 6.12: Elevator system characteristics to maintain longitudinal trim at cruise

ModuLR	**Units**	**-100**	**-200**	**-300**
Elevator chord to horizontal tail chord ratio	[-]	0.22	0.2	0.38
Elevator span to horizontal tail span ratio	[-]	0.9	0.9	0.9
Elevator deflection	[°]	-7.4	-7.2	-6.4

All deflection angles are negative, meaning that an upward deflection of the elevator is required. The greatest elevator chord to horizontal tail chord ratio is required by the ModuLR-300, which requires an approximately 50% greater ratio than the -100 and -200 variants. However, the -300 exhibits the smallest required elevator deflection of -6.4°. The -200 and -100 variants have very similar elevator chord ratios, with the -100 variant requiring an approximately 10% greater elevator chord ratio than the -200.

Fig. 6.20 presents the elevator deflection angle for the range of speeds between the stall speed, V_S and the cruise speed V_C, for each ModuLR variant.

The maximum elevator deflection required to maintain longitudinal trim is -29.3° for the ModuLR-100 variant, and -29.2° for the -200 and -300. In the figure, the curves for the -200 and -300 overlap as they have the same stall speed of 70 m/s, where as the -100 has a stall speed of 65 m/s.

Fig. 6.21 presents the forces required for both the cruise condition, Fig. 6.21a, and at the aforementioned maximum elevator deflections required to maintain longitudinal trim, Fig. 6.21b.

For the longitudinal trim at cruise, the maximum force required is achieved at $\alpha = 15°$. For the ModuLR-100, the maximum absolute force is equal to 429.8 N, the -200 is equal to 737.2 N, and the -300 has a significantly larger force of 4456.2 N. As previously mentioned, the forces are negative as a

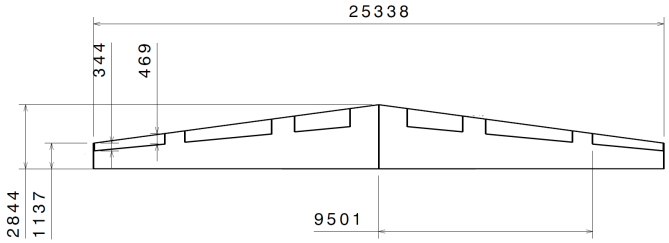

(a) ModuLR-100

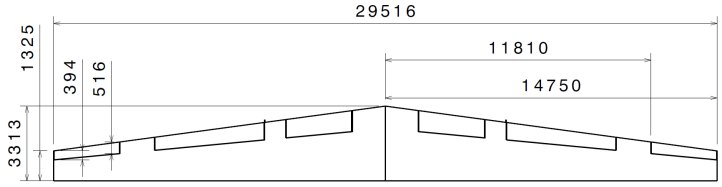

(b) ModuLR-200

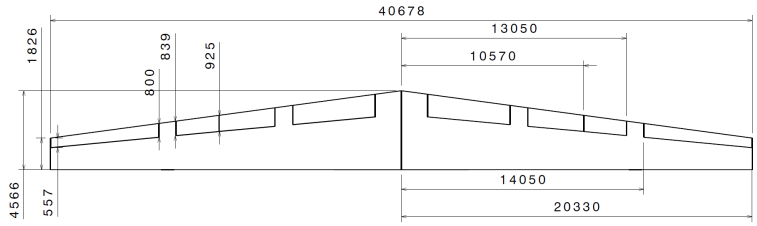

(c) ModuLR-300

Figure 6.19: Aileron positioning and dimensions of all ModuLR configurations

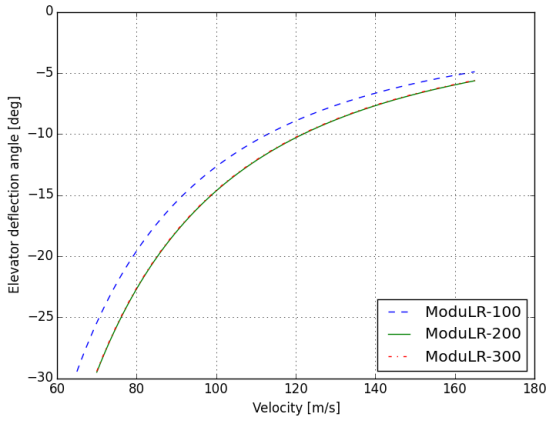

Figure 6.20: Elevator deflection for longitudinal trim for speeds between V_S and V_C

stick/actuator backward motion is required to deflect the elevator in the upwards direction. The greatest force at the maximum elevator deflection occurs at -15°. The absolute maximum elevator deflection force of the -100 variant is 2354.7 N, for the -200 variant is 4824.5 N and for the -300 variant is 32907.7 N.

Fig. 6.22a to 6.22c present the elevator position and dimensions on the horizontal tail. All numbers presented in the drawings are in mm.

Rudder

Tab. 6.13 and 6.14 present the rudder dimensions and required deflections to maintain directional trim in the landing and cruise conditions respectively.

In the landing conditions, the ModuLR-100 variant requires the biggest rudder chord to vertical tail

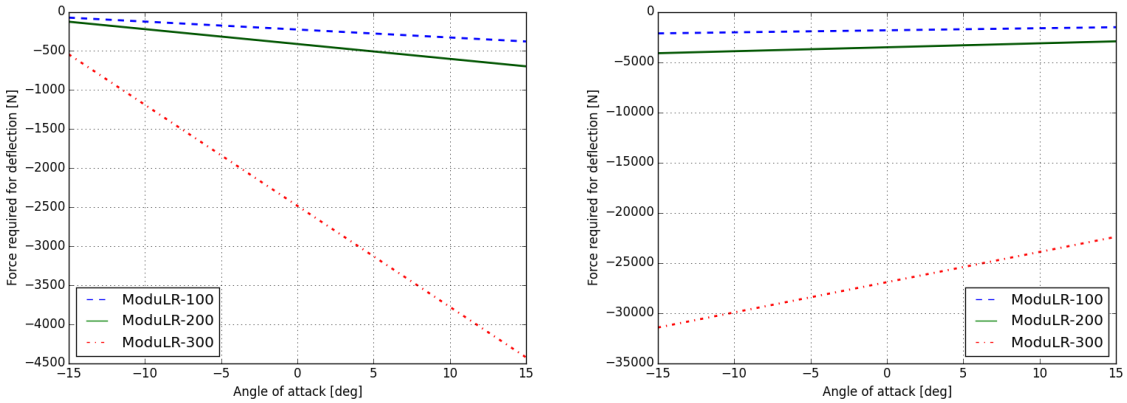

(a) Force for longitudinal trim at cruise

(b) Force at maximum elevator deflection

Figure 6.21: Actuator force for elevator deflection

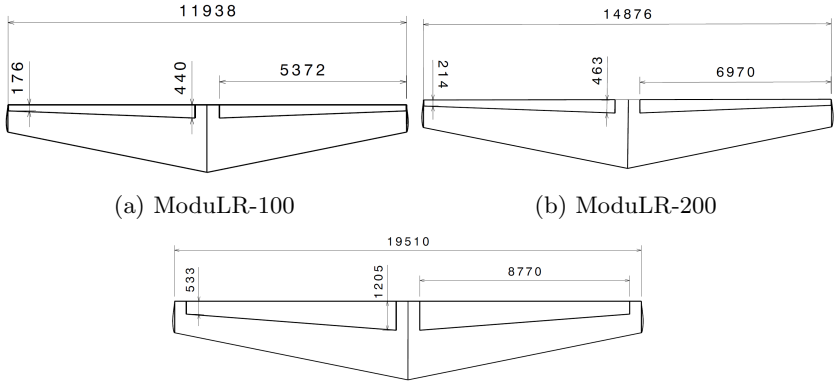

(a) ModuLR-100

(b) ModuLR-200

(c) ModuLR-300

Figure 6.22: Elevator positioning and dimensions

Table 6.13: Rudder system characteristics to maintain directional trim in an one engine inoperative landing/take-off condition

ModuLR	**Units**	**-100**	**-200**	**-300**
Rudder chord to vertical tail chord ratio	[-]	0.46	0.39	0.16
Rudder span to vertical tail span ratio	[-]	1	1	1
Rudder deflection	[°]	29.88	29.82	29.8

Table 6.14: Rudder system characteristics to maintain directional trim in an one engine inoperative cruise condition

ModuLR	**Units**	**-100**	**-200**	**-300**
Rudder chord to vertical tail chord ratio	[-]	0.46	0.39	0.16
Rudder span to vertical tail span ratio	[-]	1	1	1
Rudder deflection	[°]	1.84	1.97	7.21

chord ratio of 0.46, and also the greatest rudder deflection of any variant, at 29.88°. The -300 variant requires the smallest rudder chord ratio, at 0.16, and also the smallest rudder deflection of all variants at 29.8°. In the cruise conditions, the rudder deflection required by the -100 and -200 variants is almost

fifteen times smaller. This is also similar for the -300 variant, which requires a four times smaller rudder deflection.

The maximum rudder deflections are achieved in the landing/take-off conditions. Therefore, Fig. 6.23a and 6.23 presents the forces required for the maximum rudder deflections in this condition. It is important to note that the angle of attack in this situation is the sideslip angle of the aircraft, and not the longitudinal angle of attack.

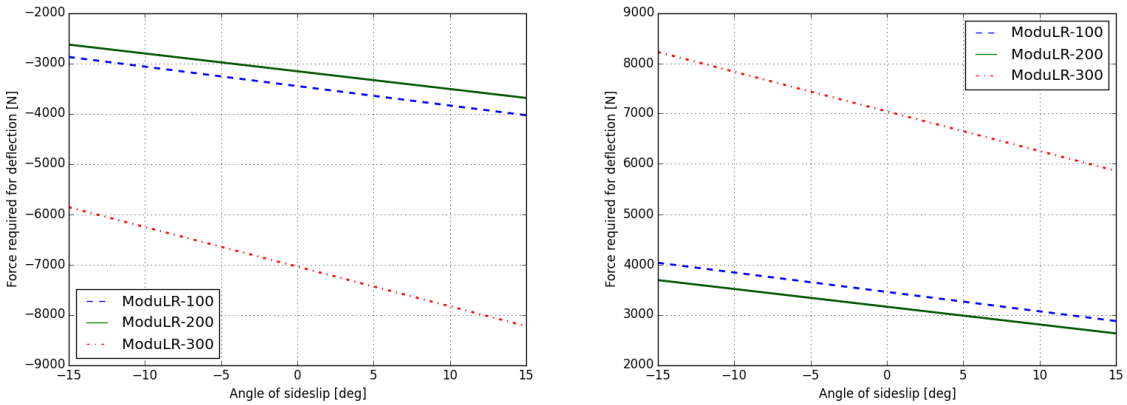

(a) Force for maximum right rudder deflection

(b) Force for maximum left rudder deflection

Figure 6.23: Actuator forces for rudder deflection

The absolute value of the maximum force required for the maximum rudder deflection is 8194.2 N for the ModuLR-300 variant, 4050.9 N for the -200, and 3591.3 N for the -100 variant.

Fig. 6.24a to 6.24c present the rudder position and dimensions of the vertical tail. All numbers presented in the drawings are in mm.

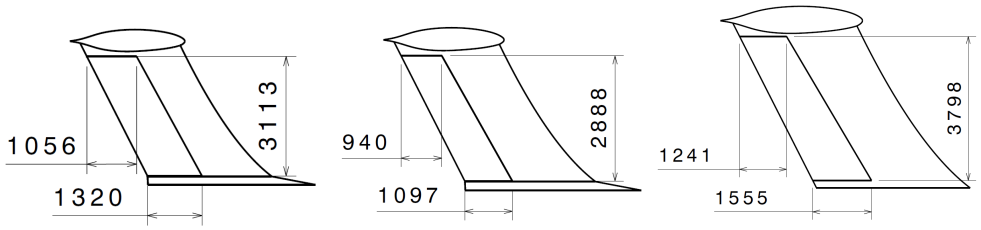

(a) ModuLR-100

(b) ModuLR-200

(c) ModuLR-300

Figure 6.24: Rudder positioning and dimensions

Actuators

Throughout all the previous control surface results, maximum forces required to move the control surface by the required deflection angle have been presented. Tab. 6.15 presents the summary of the forces required by the actuator.

Table 6.15: Actuator system characteristics

ModuLR	**Units**	**-100**	**-200**	**-300**
Maximum force for aileron deflection	[N]	4868.2	7241.3	18927.9
Maximum force for elevator deflection	[N]	2354.7	4824.5	32907.7
Maximum force for rudder deflection	[N]	3591.3	4050.9	8194.2

The largest forces required to deflect the control surfaces are experienced by the ModuLR-300 variant.

The -100 and -200 both experience their largest forces for the aileron deflections, of 4868.2 N and 7241.3 N, respectively. The -300 variant experiences its largest force of 32907.7 N for the elevator deflections.

6.5.3 Verification & Validation

Verification of the models used for all control surface design (aileron, elevator, rudder and actuator force) is achieved by selecting input values of aircraft that are described in examples from the Aircraft Design book [52]. When these values are chosen as inputs, the models are run and the final outcome is compared with the example solutions. The final outcomes of all methods differ between 5-7% of the solutions mentioned in the examples. After further investigation, it is deemed that the reason for this difference is due to rounding accuracy, as the methods used in this project use more decimal points for interim calculations. For example, the calculations of the density at an altitude contain many more decimal points than the constants presented in the book. In order to further investigate this, the values used in the methods were rounded to match the values of the examples. The outcome of this was that the difference between final outcomes was less than 1%, further justifying this explanation.

As with the tail design in section 6.4, validation is performed by modeling all three aircraft variants, including the control surfaces, in the XFLR5 aerodynamic analysis software [59]. A dynamic analysis is performed, the results of which must ensure longitudinal and directional stability. The validation results are presented and discussed in section 6.6.

6.5.4 Sensitivity

In this section, the sensitivity of the aforementioned control surface is assessed, where a variable is changed and the response in the design is observed.

Ailerons

Fig. 6.25 presents the aileron sensitivity of all variants. The inertia about the longitudinal axis, I_{xx} is increased and decreased by -40%.

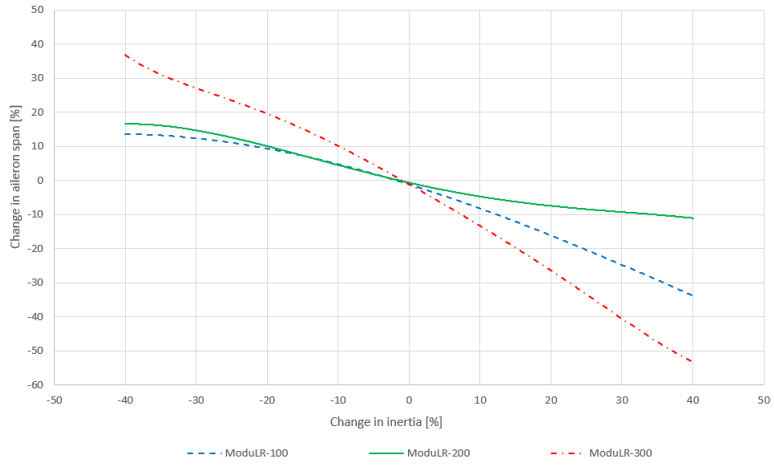

Figure 6.25: ModuLR aileron sensitivity analysis

The change in aileron span varies almost proportionally with a change in inertia, for all variants, as the sensitivity curves are almost linear. The -300 variant is the most sensitive, as the gradient of the curve is steepest. The -100 and -200 variants have similar gradients, both less than that of the -300. The -200 variant is the least sensitive as the gradient is the lowest.

Elevator

Fig. 6.26 presents the sensitivity analysis of the elevator chord. The C_{L_α} is increased and decrease by 60 % for the -100 and -200 variants. For the -300 variant, it is only decreased by 40%, as values greater than this result in an elevator that is greater than the horizontal tail.

As can be seen, the change in elevator chord is inversely proportional to the change in C_{L_α}. There is little difference between the sensitivity of the -100 and -200 variants, and slightly greater sensitivity for the -300 variant. However, the chord length of all variants is very sensitive to decreases of C_{L_α} from about -20% onwards.

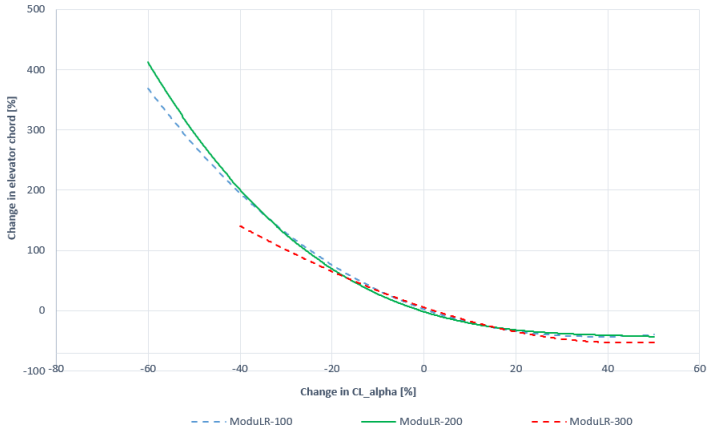

Figure 6.26: ModuLR elevator sensitivity analysis

Rudder

Fig. 6.27 presents the sensitivity analysis of the rudder. The take-off thrust is changed by +/- 50%.

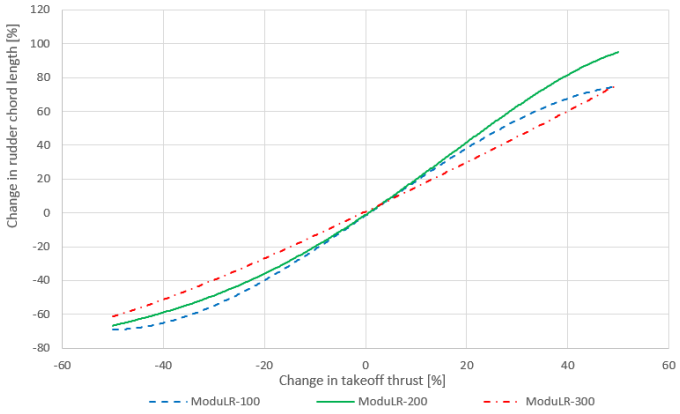

Figure 6.27: ModuLR rudder sensitivity analysis

As can be seen, the rudder chord length varies almost proportionally to changes in take-off thrust, as the sensitivity curves are almost linear. The -200 variant is the most sensitive, as it experiences the greatest gradient of all curves. The -300 is the least sensitive as it has the shallowest curve.

Sustainability

The control surface sustainability is primarily composed of ensuring environmental sustainability. This is achieved by designing the control surfaces for the minimum required size, thus minimizing the amount of parts required. This is done by meeting all requirements, and not over designing any control surface. The reason as to why this achieves environmental sustainability is that there will be fewer parts at the end of life of the control surfaces, therefore making an easier decommissioning procedure. Additionally, fewer parts are needed to be made, in order for the system to fulfill its mission. In terms of social and economic sustainability, the least amount of parts required means that it is easier to produce and maintain the system, thus promoting the sustainability.

6.5.5 Conclusion & Recommendations

The results show that there is a significant difference between the ModuLR-300 and other variants, in both the ailerons and elevators. The -300 requires significantly greater surfaces and actuator forces. However, the smallest rudder chord ratio is required by the -300 variant.

The RUCA-T-ACS-CS-1 and RUCA-T-ACS-CS-2 requirements are met as the ModuLR-100 system achieves a 45° bank angle in 1.39 s, the ModuLR-200 system achieves a 30° bank angle in 1.49 s, and the ModuLR-300 system also achieves 30° bank angle in 1.49 s.

The RUCA-T-ACS-CS-3 requirement is met, as the results show that no control surface requires a deflection greater than 30°. The maximum required deflection is 29.88°, required by the rudder of the ModuLR-100.

The RUCA-T-ACS-CS-4 requirement is met, as the elevator is operable within all the required flight speeds, as shown in Fig. 6.20 in the results.

RUCA-T-ACS-CS-5 is met as the rudder is able to deflect sufficiently to counter act the asymmetric thrust condition. RUCA-T-ACS-CS-6 is also met as the rudder control surface was conservatively designed for $V_{MC} = V_S$, and is demonstrated to achieve directional stability.

Finally, RUCA-T-ACS-CS-7 and RUCA-T-ACS-CS-8 requirements are met, as the the actuators were designed for a maximum stroke length of 0.4m, as was found from an existing actuator, and is within the operating limits of the existing actuator. The chosen actuator is the Parker Fly-By-Wire Flight Control Actuator[5], and the required maximum stroke length is 0.4m, under a maximum force of 32.9kN, clearly meeting the actuator operating limits.

By achieving the aforementioned requirements, the ModuLR system is additionally contributing to achieving the RUCA-C-LEG-4, RUCA-T-OPS-CT-2, and RUCA-T-OPS-CT-4 to RUCA-T-OPS-CT-6 requirements, as the aircraft is controllable and operable in both the cruise and landing conditions, whilst maintaining maneuverability and stability.

In the tail design section 6.4.2, it was determined that the ModuLR-200 tail could also be used for the -100 variant. After applying this situation to the model, it is found that a rudder deflection of only 27.4 ° is required in the take-off configuration (due to the larger vertical tail surface), and an elevator deflection of -4.6°. Therefore, using the bigger of the -200 for the -100 case is favorable in terms of controllability.

The following recommendations have been derived. Firstly, the inertia I_{xx} of the aircraft should be revised and calculated in a significantly more accurate way, such as finding the individual contribution of each sub system group. This will allow for a more accurate bank performance analysis, and a more accurate aileron sizing.

Secondly, investigations into sizing the elevator in order to achieve the required angle of attack in the take-off and landing phases should be undergone. This may change the size of the elevator, as this case is not investigated.

Thirdly, although the aircraft meets the deflection requirements, a greater margin for the deflection angle should be imposed, as the aircraft only adheres to the requirements at maximum deflection. It may be desirable to have even more maneuverability in terms of banking angle, instead of simply meeting the aforementioned requirements.

Fourthly, a sensitivity analysis could be performed on the actuator forces required, in case increasing the stroke length positively benefits the actuator system by requiring less actuator forces.

Finally, where possible, the assumptions of the constants, aerodynamic coefficients, dimensions (such as the value of z_T) should be revised and calculated through software tools, analytic methods, or by conducting experiments on scale models of the ModuLR aircraft. Using such values will increase the accuracy and reliability of the control elevator and rudder control surfaces, in particular.

6.6 Dynamic stability

In order to validate whether the current control surfaces and tail sizing meets the requirements an analysis on dynamic stability is performed.

6.6.1 Method & Results

All configurations of the system are analyzed on both symmetric an assymetric motions. For the cruise state of the aircraft both the symmetric motion and assymetric motion are written down into a space state system following the method from [61]. The state space systems are then modeled in MATLAB after a input on the system. The non-dimensional stability derivates used as input for the state space systems are obtained by performing a stability analysis in XFLR5 [62] for all the configurations. The stability derivatives obtained from XFLR5 [59], used as an input in the state space systems, can be found in App. A. The following motions are analyzed:

- **Short Period** The short period motion is a symmetric motion of the aircraft caused by an elevator step input. This temporarily elevator deflection causes the aircraft to pitch up and down, causing

[5] http://ph.parker.com/us/en/fly-by-wire-flight-control-actuators, visited on June 20, 2017

an oscillation. The short period motion response to a step elevator input of $\Delta - 0.005[rad]$ can be seen in Fig. 6.28.

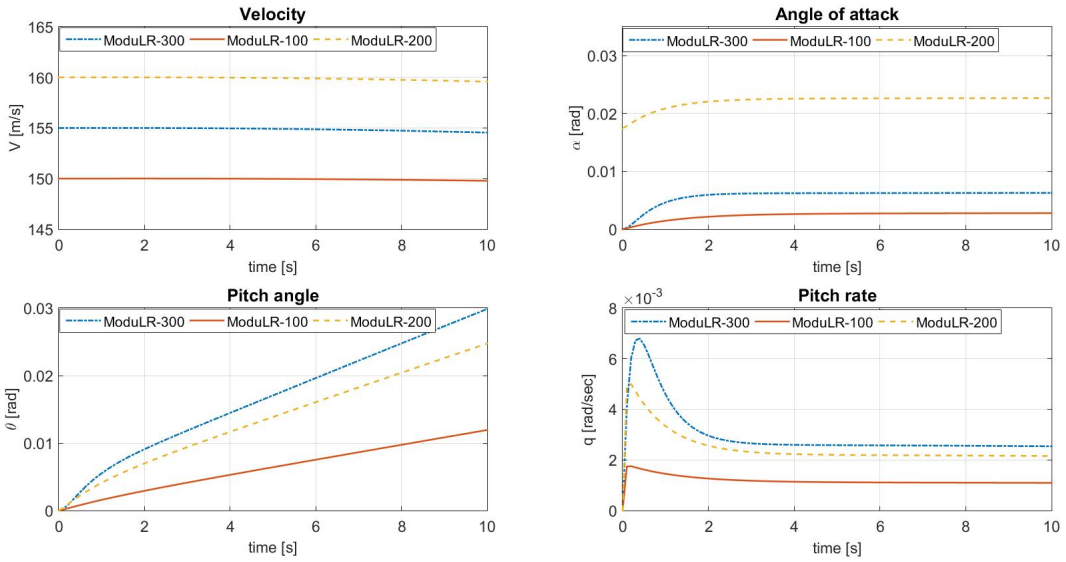

Figure 6.28: Short period response to a step elevator input, $\delta_e = -0.005[rad]$

- **Phugoid** The phugoid is just like the short period a symmetric motion of the aircraft. However, in contrast to the short period motion the phugoid is a long period oscillation. During the phugoid motion the aircraft starts to climb after a step input of the elevator. This climb results in a loss of lift, leading to a decrease in pitch angle, and increase in velocity. The described motion then repeats itself. The phugoid motion response to a step elevator input of $\Delta - 0.005[rad]$ can be seen in Fig. 6.29.

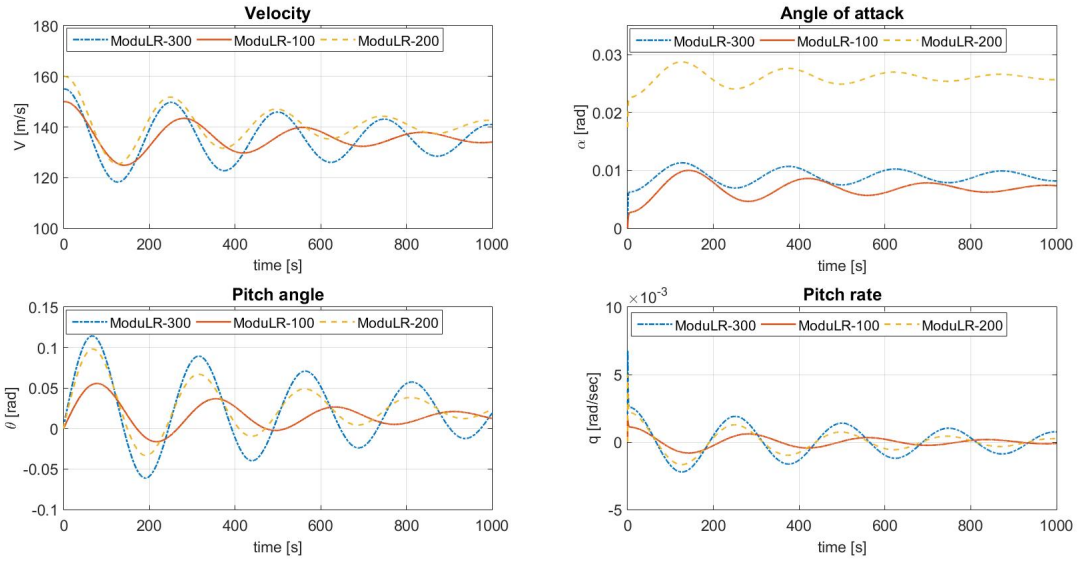

Figure 6.29: Phugoid response to a step elevator input, $\delta_e = -0.005[rad]$

- **Aperiodic Roll** This motion is initiated by a step input on the aileron, which induces a roll of the aircraft. During this roll, the lift of the lower wing increases, while it decreases on the upper wing, this then brings the airplane back in its initial condition.The aperiodic roll response to a

pulse aileron input of $\Delta + 0.025[rad]$ can be seen in Fig. 6.30.

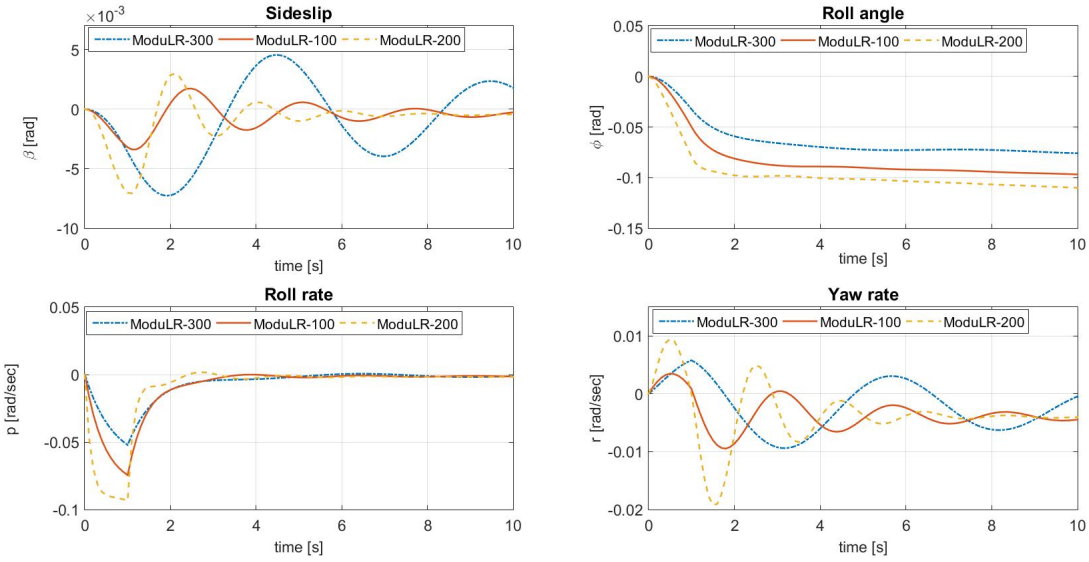

Figure 6.30: Aperiodic roll response to a pulse shaped aileron input, $\delta_a = +0.025[rad]$

- **Dutch Roll** The Dutch roll is triggered by a rudder input after which the aircraft starts to yaw, which causes a difference in airspeed over the wings. The difference in airspeed results in one wing that creates more lift, leading to a rolling motion. The dutch roll response to a pulse rudder input of $\Delta + 0.025[rad]$ can be seen in Fig. 6.31.

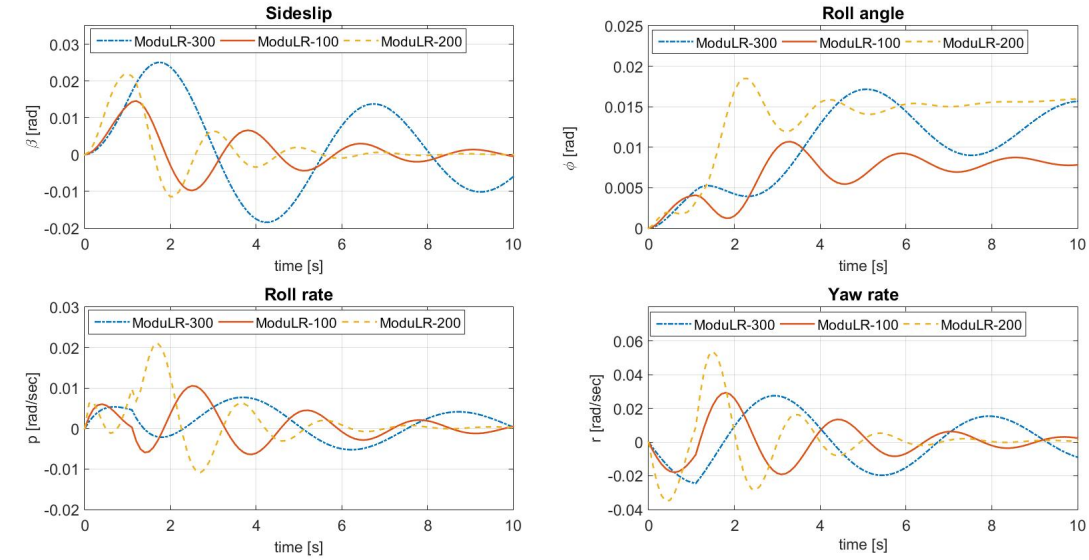

Figure 6.31: Dutch roll response to a pulse shaped rudder input, $\delta_r = +0.025[rad]$

- **Spiral motion** The spiral motion is an asymmetric motion, where the aircraft is disturbed into an initial roll angle, after which the horizontal component of the lift vector causes the aircraft to make a turn. Due to the tilting of the lift vector the vertical lift component decreases, causing the aircraft to lose altitude. The spiral response to a initial roll angle of $+0.175[rad]$ can be seen in Fig. 6.32.

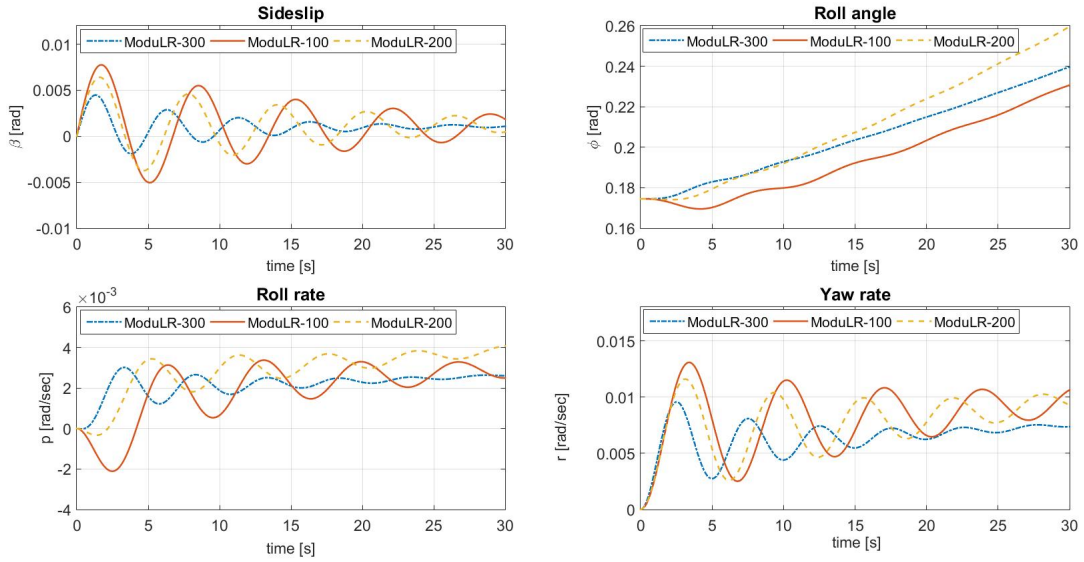

Figure 6.32: Spiral response to an initial disturbance of $\phi = +0.175[rad]$

6.6.2 Verification & Validation

The MATLAB model is verified by following the example from [61]. With the same inputs and coefficients to recreate the results. Validation of the model should be done by performing first wind tunnel test to get an initial estimate for the non dimensional stability derivatives and afterwards a flight test that records the flight data while performing all five eigenmotions. The model can then be compared to data from the flight test in order to evaluate and improve the accuracy of the model.

6.6.3 Conclusion & Recommendations

From the short period response and the phugoid response, Fig. 6.28 and 6.29 respectively, it can be seen that the symmetric motions are damped for all configurations. It can be seen that the period of the ModuLR-100 is longer but the damping ratio is highest. All motions for all configurations converge back to a steady state and therefore it can be said that the system fulfills the longitudinal stability requirement RUCA-T-ACS-T-2.

From the aperiodic roll response and the dutch roll response, Fig. 6.30 and 6.31 respectively, it can be seen that the asymmetric motions are damped for all configurations. It can be seen that the period of the ModuLR-200 is shortest and has the highest damping ratio for directional stability. All motions converge back to a steady state and therefore it can be said that the system fulfills the directional stability requirement RUCA-T-ACS-T-1. An analysis with one engine inoperative shows that a 0deg sideslip angle is still possible meeting requirement RUCA-T-ACS-T-3 and RUCA-T-ACS-CS-5

From the spiral motion response, Fig. 6.32, it can be seen that the system when disturbed into an initial roll angle does not return to a steady state. Instead the roll angle keeps increasing for all configurations. This indicates that the system for all configurations has spiral instability. Meaning that the static directional stability of the system is strong compared to the system maintaining lateral equilibrium.

It can be concluded that the aircraft has longitudinal and directional stability, but it has spiral instability. When designing the controller for the aircraft this has to be taken into account. Coming back from the spiral motion needs to happen gradually in order to avoid to high load factors due to elevator deflection, which could cause structural failure. When a failure of the control system occurs and the system will be disturbed into a roll angle, it can no longer return to a steady state due to the spiral instability. Therefore, as a recommendation, the controller should be designed in a fail safe way, with multiple feedback loops, in order for the system to be reliable.

As a recommendation, a redesign of the vertical tail should be performed. To work towards a combination of both, directional, and lateral stability. This can be done by decreasing C_{n_β} and making C_{l_β} more negative to get into the stable region as can be seen in Fig. 6.33 by an iterative process of

redesigning the vertical stabilizer. By achieving spiral stability the system will become more reliable, since it will always want to return to a steady state.

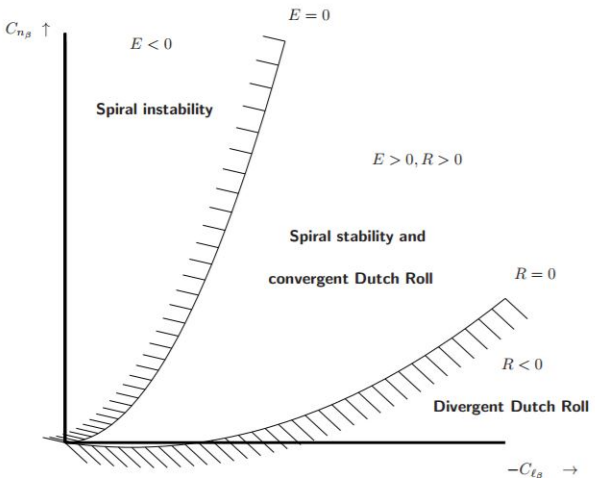

Figure 6.33: Lateral stability diagram [61]

6.7 Total Drag

In order to calculate the efficiency of the aircraft in terms of lift over drag the total drag needs to be known. In this section the drag forms will be evaluated and the efficiency of the aircraft will be presented.

6.7.1 Method

The drag of main components is estimated and added to get the total drag. A fudge factor of 1.06 is included to account for drag due to interference of many components. The components for which the drag is calculated are the wings, nacelles, nose, fuselage, vertical tail and horizontal tail. The drag contribution of the horizontal and vertical tail is explained in section 6.4. The drag due to the wing is explained in section 6.1. The other drag forms will be elaborated on in this section.

The drag of the nose and fuselage is calculated together using both the method from Roskam [63] and a program called Open Rocket. The two drag forms are compared and if the two don't deviate too much the drag form from Open Rocket if chosen as this resembles the aircraft fuselage and nose more closely. The drag of the nacelles is calculated using the method provided by Roskam [63]. The drag is then compared to reference values of other aircraft to provide a quick check.

All drag forms are known now and the total drag can be calculated. The total lift in cruise condition will be divided by the drag in cruise condition to get the Lift over Drag in cruise condition.

6.7.2 Results

The individual component drag coefficients and total drag coefficients for each of the configurations is presented in Tab. 6.16.

Table 6.16: Component and total drag coefficients of the aicraft in average cruise condition

	ModuLR-100	**ModuLR-200**	**ModuLR-300**
Wing	0.0191	0.0178	0.0216
Fuselage + Nose	0.0148	0.0109	0.00575
Nacelles + Pylons	0.00645	0.00475	0.00504
Horizontal Tail	0.00190	0.00217	0.00193
Vertical Tail	0.00102	0.000754	0.000657
Total	**0.0433**	**0.0364**	**0.0350**

6.7.3 Verification & Validation

The program that adds all the drag forms and calculates the total drag is verified by calculating the summation of the drag forms by hand and comparing it to the results of the program. Validation is by comparing results for each drag component. Each result is checked either by comparing it to other software or to reference aircraft. In this way a reference is provided to check the drags. For example the drag of the nose and fuselage is evaluated both with a program called OpenRocket and the methods depicted by Roskam. The Lift over Drag ratio of the aircraft are also compared to other aircraft to verify the end result.

The drag of the empennage is checked and seems to make sense when compared to other reference empennages. The fuselage drag is check by comparing the results of Open Rocket to Roskam [63]. The lift over drag values seem to deviate for the small and baseline version, but this can be explained by the fact that reference aircraft are not reconfigurable and therefore have components, such as the fuselage, which are sized to the rest of the aircraft. The penalty of not reconfiguring the fuselage results in the lower Lift over Drag value for these versions.

6.7.4 Sustainability

A balance had to be found between take-off performance and fuel efficiency. In this way sustainability in terms of noise and $C0_2$ emissions is to be traded off. The requirements with respect to noise are tried to be met and hereafter the fuel efficiency is tried to be minimized to achieve a good trade-off in sustainability.

6.7.5 Conclusion & Recommendations

The ModuLR-100 and ModuLR-200 meet the requirements and perform as expected with respect to efficiency in terms of lift over drag. The small configuration does not meet the lift over drag that was required during preliminary design. This is due to the fact that the keeping the fuselage constant amongst the different configurations has a bigger influence than expected. It might be convenient to re-evaluate this decision in a new iteration. The drag itself can also be evaluated more precisely by using more accurate CFD models or wind tunnel analyses. The drag due to interaction between components is difficult to simulate using the current methods and therefore this can be of great importance.

Chapter 7

Structures

This chapter analyses several aspects of the aircraft on a structural level. The wingbox, in section 7.1, is discussed in great detail. Several other aspects, such as the landing gear, the fuselage, and the reconfiguration of the ModuLR are analyzed more globally or only qualitatively in section 7.2. The variables needed to reproduces all methods are presented in Tab. A.1.

7.1 Wingbox

This section discusses the design of the wingbox. Firstly, in subsection 7.1.1 some assumptions are stated. Then, the method of the wingbox design is elaborated upon in subsection 7.1.2, after which its results are shown in subsection 7.1.3. In this subsection also the material analysis is performed. To verify and validate the results, unit tests are executed and a Catia model is generated in subsection 7.1.4. Moreover, subsection 7.1.5 analyzes the sensitivity of the numerical code model and evaluates the discretization error. Furthermore, the sustainability of the design is discussed in subsection 7.1.6. Lastly, some recommendations for further analysis and research are provided in subsection 7.1.7.

7.1.1 Assumptions

In order to get an appropriate estimation of the wingbox design, some assumptions are made. These assumptions are listed below:

- Lift is assumed to be elliptically distributed;
- The total drag is assumed to be equal to the lift drag;
- The wingbox is assumed to be symmetrical of rectangular shape;
- It is assumed that no deflections and no deformations take place in the wingbox;
- It is assumed that the wingbox has a single cell cross section;
- The fuel and wing weight are distributed according to area;
- The lift and drag act on the centroid of the wingbox;
- Centroid of the airfoil is at the same location as the centroid of the wingbox;
- Sweep is neglected for all calculations;
- The engines and landing gear are assumed to be point masses;
- The wing skin has a constant thickness of 3 mm.

7.1.2 Method

A wing is a complex structure on which several loads are acting. One of the most important loads is the lift, as discussed in chapter 6. Moreover, in chapter 5 the engines are designed, which leads to the thrust and weight of these point loads. Not only which engine, but also the number of engines for each configuration comes from this chapter. The location of the engines is both $\frac{1}{3}$ and $\frac{2}{3}$ (in case of four engines) of half the wingspan. Furthermore, the landing gear is positioned underneath the two engines closest to the fuselage, thus being at $\frac{1}{3}$ of half the wingspan.

As discussed in chapter 6, the wing has a taper ratio of 0.4: an elliptical wing is imitated. For simplification purposes, the lift is thus assumed to be elliptically distributed. This assumption, and more, are found in subsection 7.1.1.

The lift needed during take-off, however, cannot be generated only by the clean wing. So HLD's are included in the wing. These HLD's and ailerons, for manoeuvrability, require 30% of the chord and therefore take away area for the wingbox. Besides the discussed external loads, the wing structure itself, the fuel weight, the fuselage, and the payload do also contribute to the stresses in the wingbox.

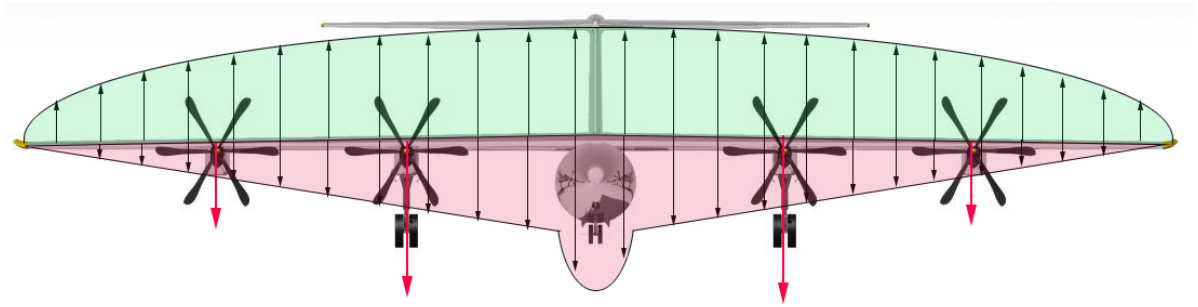

Figure 7.1: Front view of the ModuLR-300 with the applied loads

A visualization of all these loads is given in Fig. 7.1. In green the lift is shown, which is counteracting all the red forces and weights of the aircraft itself, composed of the structure itself and the engines with the landing gear included.
The loads as described above that are carried by the wingbox are analyzed by a numerical code model written in Python. Along the span of the wing is divided into small finite elements. For each cross section of these elements, firstly, the centroid is located. Secondly, the moment of inertia can be determined with the cross sectional dimensions in combination with the located centroid. Hereafter, the internal stresses can be calculated to finalize the wingbox design with the Von Mises stress.

Sections of the wingbox
When looking at the different configurations, the amount of engines varies, as is explained in chapter 5. The ModuLR-100 and ModuLR-200 versions both require two engines. The ModuLR-300, on the other hand, requires four engines. The position of the engines divides the wing into different sections. For an aircraft with two engines, a single wingbox has two sections. The version with four engines splits the wingbox into three sections. When going from one cross section to another, the acting loads differ. Tab. 7.3 presents the loads on each of these boxes. All ModuLR configurations, -100, -200, and -300, have box 3 connected to the fuselage, as can be seen in Fig. 7.2, i.e. the configurations -100 and -200 do not have box 2.

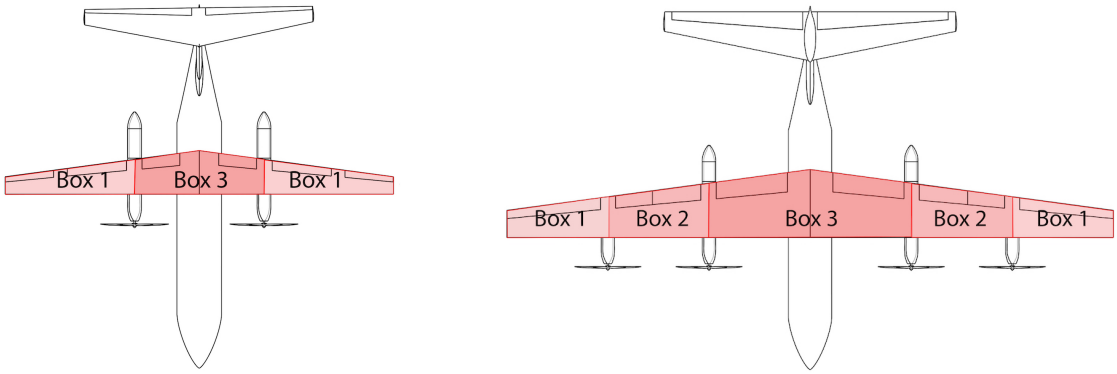

(a) ModuLR-100 (b) ModuLR-300

Figure 7.2: Top view of the ModuLR to indicate the different sections within the wingbox

Besides the engine, the wingbox is also influenced by control surfaces as mentioned earlier this section. With these control surfaces, which are designed for 30% of the chord, the wingbox has to be sized for the remaining approximately 60%. So the front spar and rear spar are located at $0.1c$ and $0.7c$, respectively. A sketch of the wingbox is presented in Fig. 7.3. As can be seen, the front and rear spar are connected with the top and bottom panel by four stiffeners. Furthermore, the wingbox contains stringers at the top and bottom to increase the moment of inertia, which will be discussed further down this section.

The dimensions of the cross section increase going from the tip towards the root. The thicknesses, however, only differs between the sections. Also the number of stringers differs between these section.

Table 7.1: Different sections within the wingbox with their respective loads

Box 1	Box 2	Box 3
Lift	Lift	Lift
Drag	Drag	Drag
Wing weight	Wing weight	Wing weight
Fuel weight	Fuel weight	Fuel weight
	Thrust	Thrust
	Engine weight	Engine weight
		Landing gear weight

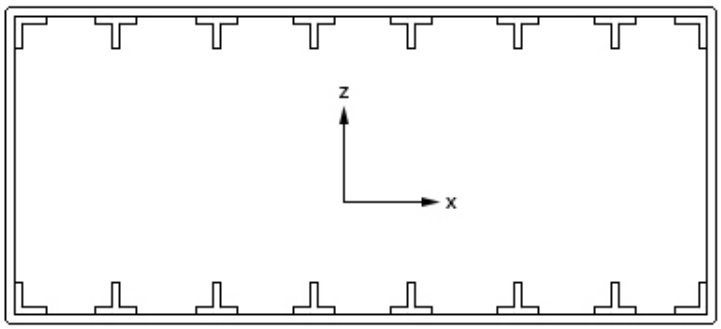

Figure 7.3: Front view of the wingbox, including the used axis system

Loading diagrams
The lift and all the weight contributions of Fig. 7.1 comes from the MTOW and the ultimate loading factor achieved from Fig. 4.2. With these loads, the shear and moment diagrams can be drawn, as seen in Fig. 7.4. Firstly, the shear diagrams for all different configurations are made. The value at the tip is equal to zero and increases towards the root. There are, however, jumps. At these positions the engines and landing gear are located. Between the root and the symmetry axis the shear force will decrease due to the fuselage and payload weight.

Secondly, the bending moments for all different configurations are determined with the shear force at each location along the span. As expected the lift distribution has the most influence on M_x, which results in a moment of quadratic shape. Furthermore, the influence of the engines and landing gear cause a change in slope for again the moment around the x-axis. In contrast to the M_x, M_z is only influenced by the engine thrust and the drag of the wing.

Centroid
The centroid of each cross section along the wingspan has to be determined. The centroid along the x-axis will always be in the middle due to symmetry, the centroid along the z-axis, however, should be determined according to Eq. 7.1.

$$\bar{z} = \frac{\sum A_i \cdot z_i}{\sum A_i} \tag{7.1}$$

Moment of Inertia
To define the moment of inertia of the aircraft, each cross section is separated into different elements, such as horizontal- and vertical parts of stringers and outer wingbox sheets. Every element is simplified as a rectangular shape. With that, the moment of inertia of each element is calculated with the use of Eq. 7.2. When every element is determined, they are summed to achieve I_{xx} and I_{zz} of every cross section. To complete the moment of inertia of each cross section the wing skin moment of inertia should be added. These moments of inertia are determined with the use of Catia V5.

$$I = \frac{b \cdot h^3}{12} + A \cdot d^2 \tag{7.2}$$

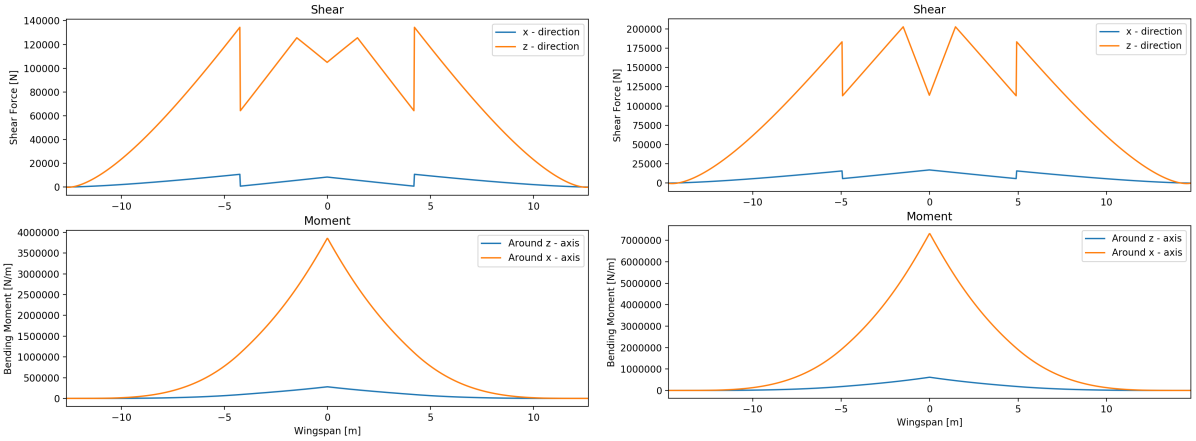

(a) ModuLR-100

(b) ModuLR-200

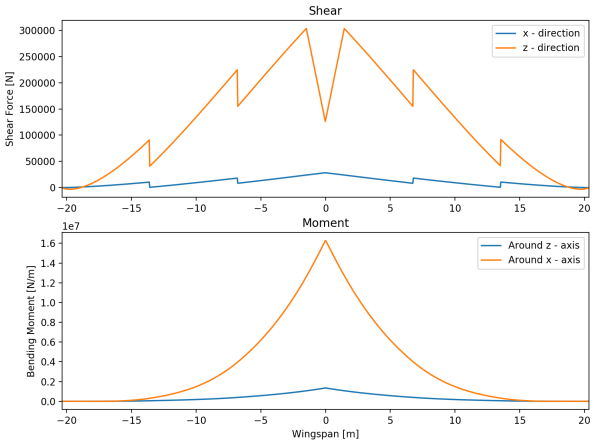

(c) ModuLR-300

Figure 7.4: Shear and bending moment diagrams of the different ModuLR versions during cruise

Bending

With the moment diagrams and the moments of inertia the bending stress, around y-axis, can be determined with Eq. 7.3. Since the lift is much higher in comparison with the drag, the first term is the main factor to this stress.

$$\sigma_y = \frac{M_z}{I_{zz}} x + \frac{M_x}{I_{xx}} z \tag{7.3}$$

Shear

The wingbox should, besides the bending stress, also be designed to carry shear stress. The shear stress arises from the forces parallel to the cross section i.e. shear force. With the shear forces and moments of inertia, the shear flow around the wingbox is determined with Eq. 7.4. By means of dividing the shear flow by the sheet thickness at the corresponding locating, the shear stress is obtained.

$$q_s = -(\frac{S_x}{I_{yy}}) \int_0^s txds - (\frac{S_y}{I_{xx}}) \int_0^s tyds + q_{s,0} \tag{7.4}$$

Von Mises

To predict the yielding of the wingbox the Von Mises stress is used. Based on the bending and shear stresses, the Von Mises stress is calculated using Eq. 7.5.

$$\sigma_v = \sqrt{\frac{1}{2}\sigma^2 + 3\tau^2} \tag{7.5}$$

Rivet spacing

Assemble all the part together can be done with all different kind of joints. Riveting is common in avionics, because rivets are reliable, readily applicable, and can be easily inspected and repaired, hence it is also used for the ModuLR. A riveted joint often has many rivets. These rivets are set out in rows at calculated distances and normalized to the nearest standard value. The optimum pitch to transfer the loads can be obtained according to Eq. 7.6 [64].

$$s = \frac{D^{hole}}{(1 - \frac{Q}{t_{sheet} \cdot \sigma_{failure}^{sheet}})} \tag{7.6}$$

7.1.3 Results

The results of the method described in section 7.1.2 will be discussed in this section. Import to note is that the ultimate load factor from Fig. 4.2 is multiplied with a safety factor to prevent the wingbox from failure due to unforeseen circumstances, such as risk 1 in the technical risk assessment in chapter 10.

For each ModuLR configuration, the maximum Von Mises stress is located at the root. A first run with the numerical code program with a random amount of stringers and sheet dimensions resulted in a Von Mises stress of 844 MPa on the ModuLR-300 configuration. Clearly too high, but as no material was yet chosen, an analysis on several types of aluminum was performed to choose exactly that alloy that has both a high yield stress and a relatively low density. The analysis can be seen in Fig. 7.5a[1] [65]. From this it is clear that the aluminum alloy 7178-T6 has the highest strength per $\frac{kg}{cm^3}$ and is therefore chosen as the material for the wingbox structure.

Even though this alloy has a yield strength of 538 MPa, the initial Von Mises stress is too high. A second run for the ModuLR-300 configuration with more stringers and different sheet thicknesses resulted in a Von Mises stress of 503 MPa as can be found in Fig. 7.5b. The maximum Von Mises stress of the ModuLR -200 and -100 are 390 MPa and 211 MPa respectively. The jumps in stress are due to a change in sheet thickness. This and more details on the wingbox dimensions of all configurations can be found in Tab. 7.2. Mind, however, that no ribs were placed along the wingspan.

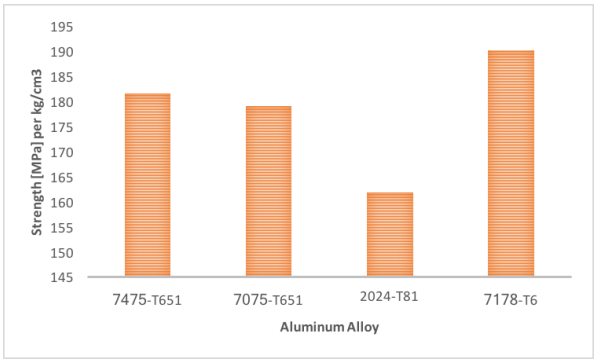

(a) Comparison between different aluminum alloys

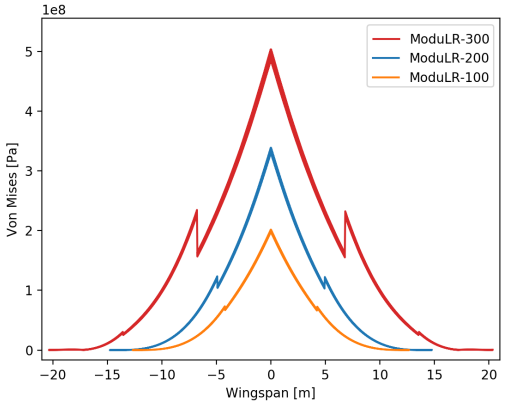

(b) Von Mises stresses in the top sheet of the wingbox for the ModuLR-100, -200, and -300

Figure 7.5: Comparison between different aluminum alloys and comparison of different Von Mises stresses between different configurations

The rivet spacing is designed for the maximum stress concentration. With Eq. 7.6 described in the method a joint with a single rivet row with a spacing of 1 cm is designed to withstand these maximum stress [64].

[1] http://www.aerospacemetals.com/aluminum-distributor.html, visited on June 24, 2017

Table 7.2: Dimensions and stresses of the wingbox of all configurations

Configuration	Section	Component	Value
ModuLR-100	Box 1	Sheet Thickness	1 mm
		# Stringers	2
		Stringer Dimensions	5 cm x 5 cm x 1 mm
	Box 3	Sheet Thickness	1 mm
		# Stringers	4
		Stringer Dimensions	5 cm x 5 cm x 1 mm
ModuLR-200	Box 1	Sheet Thickness	1 mm
		# Stringers	2
		Stringer Dimensions	5 cm x 5 cm x 1 mm
	Box 3	Sheet Thickness	2 mm
		# Stringers	8
		Stringer Dimensions	5 cm x 5 cm x 1 mm
ModuLR-300	Box 1	Sheet Thickness	1 mm
		# Stringers	4
		Stringer Dimensions	10 cm x 10 cm x 6 mm
	Box 2	Sheet Thickness	2 mm
		# Stringers	8
		Stringer Dimensions	10 cm x 10 cm x 6 mm
	Box 3	Sheet Thickness	6 mm
		# Stringers	18
		Stringer Dimensions	10 cm x 10 cm x 6 mm

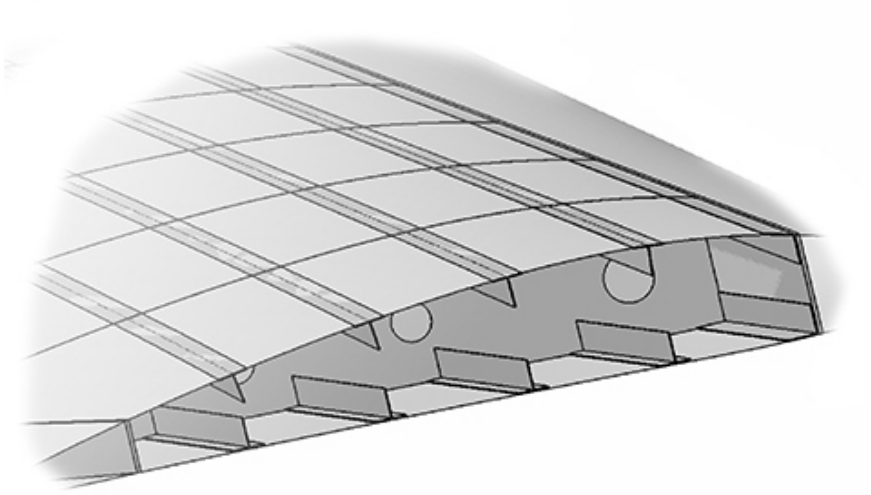

Figure 7.6: Catia V5 result of the wingbox at the tip of the wing of the ModuLR-300

7.1.4 Verification & Validation

To verify the code which has been written to compute the wingbox stresses, unit tests have been performed to assure correct results.

Firstly, it is checked whether the total lift during cruise equals the maximum take-off weight. With an error of 0.1% this is assumed verified.

Secondly, the total lift during cruise is checked against the sum of the weight components on the wing, including the fuel, engine, landing gear, fuselage, and payload weights. As certain components such as the tail, nacelle, and flight control systems are not included, the difference of 12000 kg can be rightly explained and thus be verified.

Then, the position of the engines and landing gear is checked. As can be seen in Fig. 7.4, the shifts in the shear diagram occur exactly at both $\frac{1}{3}$ and $\frac{2}{3}$ of half the wingspan. The shift at $\frac{1}{3}$ is slightly bigger due to the weight of the landing gear.

Lastly, both the shear and bending moment diagrams should start and end with zero shear force and bending moment, respectively. As again can be noticed in Fig. 7.4, this is indeed the case and can thus be verified.

Validation, on the other hand, is performed by comparing the numerical code model to a model of the ModuLR-300 constructed in Catia V5. The CAD model, however, used a different airfoil shape and different dimensions for the stringers and panel sheets as these were not yet known at the moment of constructing the Catia model. A front view as well as a side view of the CAD model can be seen in Fig. 7.7, where the highest stresses do indeed occur at the root section of the wing, as computed in subsection 7.1.3. The highest Von Mises stress for the ModuLR-300 is seen to be 480 MPa, which is only a 5% difference with the Von Mises stress computed in the numerical code model, the model thus having validated.

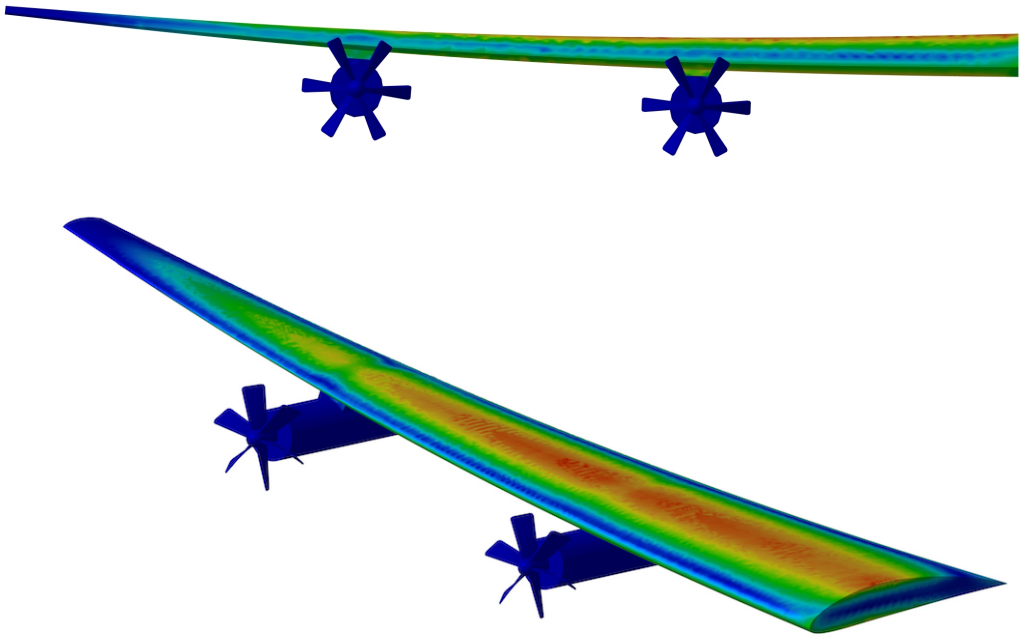

Figure 7.7: Side and top view of the Catia V5 stress analysis of the wing of the ModuLR-300

7.1.5 Sensitivity

To see how sensitive the computations within the numerical code model are, a sensitivity analysis is performed. Firstly, is it checked how the Von Mises stress changes when the position of the engines is altered. When positioning the engines more outboard, the Von Mises stress at the root of the wing should lower. Alternatively, when positioning the engines more inboard, the Von Mises stress should augment. It is, however, not taken into account that the engine cannot be placed at the root of the wing due to the clearance of the propeller blades or that an engine placement at the tip would be unfeasible. Fig. 7.8 shows the maximum Von Mises stress of the ModuLR-100 with different engine positions.

Finally, the discretization error within the numerical code model is analyzed. The amount of steps along the wingspan is altered to see its change on the shear in the z-direction at a distance of $5m$ from the root of the wing (of the ModuLR-300).

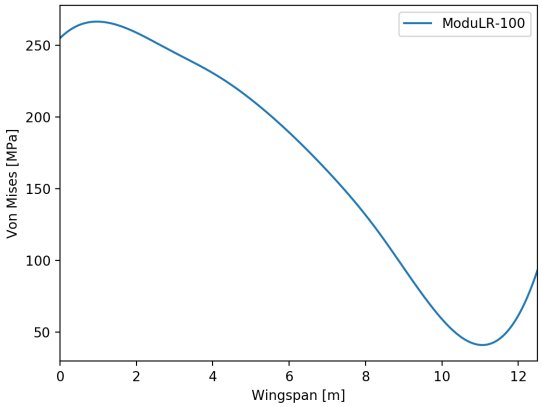

Figure 7.8: Sensitivity analysis of the engine position of the ModuLR-100 on the Von Mises stress occurring at the root

Table 7.3: Different sections within the ModuLR-300 wingbox with their respective loads

# Steps	Shear at 5m [N]	Error [%]
10	111587	45%
50	212146	4%
100	222872	9%
500	203194	0.3%
1000	202965	0.4%
5000	203925	0.04%
10000	203898	0.03%

7.1.6 Sustainability

To assure that the structure is as sustainable as possible, three different life-cycle factors will be looked at: production, use-phase, and end-of-life-phase.

The material choice of the structure is most important for sustainability. Subsection 7.1.3 discussed the material choice purely based on the strength to weight ratio. From this, the aluminum alloy 7178-T6 was chosen. Composites were not regarded during this analysis, even though the use-phase of composites is much more sustainable, inasmuch as it is lighter and thus results in a lower total fuel consumption. Composites, however, are much more expensive than aluminum and perform less well on sustainability during the production and end-of-life phase.

During the production, for example, of composites health issues might play parts. Firstly, an epoxy allergy can arise for some people[2]. Secondly, exposure to carbon fiber 'dust' is proven to lead to all kinds of lung complications[3].

Moreover, at the end-of-life-phase of aircraft, aluminum is intrinsically sustainable as the basic properties do not change with mechanical or physical processing. Recycling components of composite nature, however, is more difficult as it results in shorter fibers[4]. The needed strength in aerospace components can then not be reached anymore. Furthermore, the energy needed to recycle composites with the method called 'pyrolysis' is much higher than that of aluminum. It is, however, important to note that this method only uses about 5% of the energy needed for the original manufacturing process for carbon fiber[5].

[2]http://www.dermnetnz.org/topics/allergy-to-epoxy-resin/, visited on June 25, 2017
[3]http://www.carbonfiber.gr.jp/english/material/safety.html, visited on June 25, 2017
[4]https://recyclenation.com/2015/10/is-carbon-fiber-better-for-environment-than-steel/, visited on June 25, 2017
[5]http://www.compositesworld.com/articles/carbon-fiber-reclamation-going-commercial, visited on June 25, 2017

7.1.7 Conclusion & Recommendations

In this section the wingbox is designed based on the loads acting on the wing. The highest Von Mises stresses are seen to occur at the root of the wing for all ModuLR configurations. However, no optimization has been performed to accurately measure the ideal position of the engines in combination with the amount of stringers and the sheet thicknesses. Furthermore, an analysis should be performed on the addition of wing ribs along the wingspan.

Moreover, the stress analysis is now only performed during cruise with full fuel load in the wings, i.e. accounting for quite some bending relief. In further analysis the stress should also be computed at the end of cruise, i.e. when fuel does not account for bending relief anymore, and at the moment of touchdown, i.e. when extra point loads are introduced at the location of the landing gear.

A sensitivity analysis is performed in subsection 7.1.5. Here, the engine location is altered to see the effect on the Von Mises stress at the root of the wing. As discussed earlier, further optimization should be performed to analyze an ideal engine location. For the sensitivity analysis, also several other factors should be looked into and altered, such as: airfoil shape, number of stringers, sheet thicknesses, stringer dimensions, material, and rivet spacing. Furthermore, the discretization error is discussed. With 10000 steps the error is only 0.03%, but the computing power to do this for all computations is rather large. Further analysis should be performed with more computing power such that the results are as accurate as possible.

Also, an analysis is performed to choose an optimal aluminum alloy: 7178-T6. This analysis only regarded yield strength and density. In subsection 7.1.6 some sustainability aspects were discussed as well. However, more research should be conducted on the benefits of composite materials and whether it can be used on some parts or components of the ModuLR aircraft, as is done with the new Boeing 787 aircraft, which consist of 50% composite materials[6].

To validate the numerical code model, a Catia V5 model is made. Fig. 7.7 also shows the highest Von Mises stresses being at the root. However, the used version of Catia is not able to apply elliptical loads, only distributed loads of rectangular shape. As the highest stresses would occur at the root, the distributed load in Catia was assumed of the same magnitude as the highest load of the elliptical distribution. For a more precise stress analysis, another program should be used to be able to analyze the correct stresses along the entire wing and not only the root. What is more, the wing weight seemed not to give any correct results within Catia. To be able to also validate this result, the wing weight should be looked into further.

7.2 Miscellaneous

In this section the design of the landing gear, the decision on pressurizing the fuselage, and the bolts needed for the reconfiguration of the wings, tails, and engines is discussed. The landing gear is treated in subsection 7.2.1, the fuselage pressurization in subsection 7.2.2, and the structural reconfiguration in subsection 7.2.3.

7.2.1 Landing Gear

The landing gear is designed according to the methods proposed by Torenbeek [50]. Firstly, the number of wheels and struts on both the main and nose landing gear is analyzed with the use of Eq. 7.7, where N_{mw} is the number of wheels for the main landing gear, rounded to the nearest multiple of four. For large transport aircraft the nose landing gear has two wheels. As the landing gear will not be reconfigured, due to the fact that the drag penalty was deemed too small, the number of wheels for all configurations will be those designed for the ModuLR-300. The number of struts for any aircraft with less than twelve wheels is two.

$$N_{mw} = \frac{f \cdot MTOW}{210000} = \frac{0.66 \cdot 632912}{210000} \approx 1.99 \rightarrow 4 \tag{7.7}$$

Then, the tire pressure is estimated by using reference data based on the MTOW. Based on these reference data the tire pressure should be around 160 psi, or 11.2 $\frac{kg}{cm^2}$. Next, the static load per wheel is computed in Eq. 7.8, assuming that the main landing gear carries 92% of the total load.

$$P_{mw} = 0.92\frac{MTOW}{N_{mw}} = 14840 \text{ kg} \qquad P_{nw} = 0.08\frac{MTOW}{N_{nw}} = 2580 \text{ kg} \tag{7.8}$$

[6] http://www.boeing.com/commercial/aeromagazine/articles/qtr_4_06/article_04_2.html, visited on June 25, 2017

With the tire pressure and the static loads per wheel, reference data from Torenbeek [50] is used to see which tires meet the above requirements. From this, it is seen that a British tire with dimensions of 50 in x 15.75 in best fits the ModuLR aircraft. In Fig. 7.9 the landing gear wit according dimensions can be seen.

(a) Side view

(b) Front view

Figure 7.9: Front view and side view of the landing gear, including dimensions

The struts itself, especially the strength needed to withstand the static and dynamic loads, have not been analyzed and should be sized in further research. In further research the applicability of so-called ferrofluids should be analyzed [66].

7.2.2 Fuselage Pressurization

A qualitative approach on the question whether to pressurize the fuselage or not, is used to make the decision due to time and resource constraints. The procedure was to identify the effects of having pressurized containers instead of a pressurized fuselage, and vice versa. Afterwards, based on the findings and the time and resources allocated, the final decision is made.

- If pressurized containers would be used, the standardized containers may need to be reshaped to cope with the stress differences. This results in extra costs and effort in, among others: research of new pressurized containers, production, and also certification. Apart from reshaping, stronger or more materials could be used for manufacturing, but will still have the same consequences as mentioned before;
- If pressurized containers would be used, each container would have a air compressor or pressure regulator which adds weight and consumes additional power. It would also require more maintenance and thus cost;
- Even though the use of pressurized containers would enable differently shaped fuselage, the fuselage still needs to provide adequate space for the payload, while keeping the unused space at a minimum, and be aerodynamically shaped. Sharp-cornered fuselages and blended wing body are not the options for the design, so eventually the fuselage would look like as if it was pressurized;
- Having the fuselage unpressurized makes the skin vulnerable to the effect of dynamic pressure when flying at higher angles of attack.

In short, using pressurized containers would require more weight and costs, and call for more research which is not feasible within the project time allocated. A lot of uncertainties would then be introduced and numbers would not be justifiable partially due to lack of verification and validation. Having a pressurized fuselage is feasible, and numbers resulting from conventional pressurized fuselage sizing methods and modeling can be verified and validated.

7.2.3 Reconfiguration

The reconfiguration between the different aircraft parts is as easy as possible for a short operation time. The relative easy connection, turbofan engine to the wing, is used as example. In this section the bolts itself will be discussed in more detail. The reconfiguration operations, however, will be described later on.

The bolts should withstand the (shear) stresses in the structure and the total weight of the aircraft. First, the shear stress across the area of the bolt can be found in Eq. 7.9.

$$F_{ult} = \frac{\pi}{4} D^2 \tau_{fracture} \tag{7.9}$$

Furthermore, the maximum stress in the bolt from tensile load(s) is:

$$\sigma = \frac{F}{\frac{\pi}{4} d_c^2} \tag{7.10}$$

From the analysis in Fig. 7.5a, it is chosen to have the aluminum alloy 7178-T6 as material for the structure. With the specification of this material, the bolts dimensions can be sized. So are for the reconfiguration of the wing at least 4 aluminum (7178-T6) bolts of at least 15 cm diameter are needed [64].

In further research it is recommended to analyze the use of other material than the 7178-T6 aluminum alloy for the connection between the different aircraft parts. It can reduce the diameter and/or the amount of bolts and therefore (perhaps) the size of the connectors. Furthermore, the total connection shall have more critical components than just the bolts, hence, a closer look at all the components has to be done to make these connections more reliable.

Chapter 8

Air and Ground Operations

The operations heavily influence the feasibility of the design. The aircraft operations are split into nine parts in this chapter. Firstly, the regulations regarding unmanned flight and reconfiguration are discussed in sections 8.1 and 8.2. In section 8.3, the communications between the ground station and aircraft are designed, followed by the design of the unmanned control system in section 8.4. Section 8.5 will explain the proposed service model and its advantage for the ground and reconfiguration operations, presented in section 8.6 and 8.7. Section 8.8 will describe the RAMS characteristics followed by section 8.9 where the production plan is explained. Finally, the sustainability and conclusion are described in section 8.10 and 8.11, respectively.

8.1 Flight Operational Regulations

Aviation authorities both want to stimulate acceptance of unmanned systems into civil air traffic while maintaining a high safety standard. There are currently few regulations regarding unmanned flight. EASA released a policy statement highlighting considerations for future legislation in 2013 [67]. These served as early guidelines for future regulations with the main policy objectives being as follows:

- The primary Airworthiness Objective shall be to ensure the safety of people and property on the ground as the aircraft is unmanned. The risk posed by the unmanned operations should be equivalent to that of manned operations.
- The UAS shall adhere to the Environmental Protection Objectives in Basic Regulations Article 6 in addition to ICAO Annex 16, Volumes I and III, which make no distinction between manned and unmanned operation.

Furthermore, in 2015 EASA published a Technical Opinion, "Introduction to a Regulatory Framework for the operation of Unmanned Aircraft" [68], where the proposed framework would be proportionate with respect to the risk presented by a particular UAS. The ModuLR belongs in the Certified category as "International cargo transport operations with large unmanned aircraft" are specifically mentioned as belonging in this category. They rely on existing regulations for manned aircraft in the form of case by case issuing of Restricted Type Certificates (RTC) and Permits to Fly (PTF), in addition to Restricted Certificates of Airworthiness (RCofA) and Noise for individual UAS [68].

8.1.1 Certification Specification

Issuing of Certificates of Airworthiness are based on adhering to Certification Specifications (CS) and will be adopted from manned operations for the Certified Category. The policy statement presents a method for estimating the most applicable airworthiness code based on the kinetic energy hazard at impact calculated using equations 8.1 and 8.2 during loss of engine power and control respectively. Kinetic energy levels are given in Tab. 8.1 and their recommended Certification Specifications are then determined from Fig. 1 and 2 in App. 1 of the Policy Statement [67].

$$E_{k,unpremeditated} = \frac{m_{MTOW} 1.3 V_{stall}^2}{10^9} \quad (8.1) \qquad E_{k,loss-of-control} = \frac{m_{MTOW} 1.4 V_{op,max}^2}{10^9} \quad (8.2)$$

8.1.2 Special Conditions

Paragraph 21.A.16B Special Conditions in Part 21 states that "The Agency shall prescribe special detailed technical specifications, named special conditions" when an aircraft "has novel or unusual design features relative to the design practices on which the applicable certification specifications are based" [69]. This applies to both the unmanned operations and reconfigurability in the case of the ModuLR.

Table 8.1: Suggested Certification Specifications for each configuration based on impact kinetic energy levels during loss of power and control situations.

Configuration	E_k level, Unpremeditated	E_k level, Loss of control	Certification Specification
Small	0.43	5.58	CS-25
Baseline	0.67	9.89	CS-25
Large	1.30	17.93	CS-25

The Policy Statement gave some guiding Special Conditions to take into consideration with respect to unmanned operations as these are likely to affect future legislation [67].

Emergency Recovery Capability
A emergency recovery system can either be on the form of a flight termination or recovery system both aimed at minimizing danger to people on the ground. The former immediately terminates the flight and seeks to minimize the kinetic energy during impact on the ground, while the latter would initiate manual or pre-programmed recovery procedures guiding the aircraft to a safe emergency landing zone or runway.

Command and control link
For safe UAS operations, a reliable data link is required between the aircraft and command station. Type certification should include this aspect w.r.t. for example redundancy and electromagnetic interference.

Level of Autonomy
The achievable level of autonomy will mostly depend on the available technological for safely integrating UAS into non-segregated air space.

Human Machine Interface
The interface between the operator and aircraft should include requirements such as the needed level of situational awareness based on the level of autonomy.

Control station
Any functional aspect of the ground station that affects aircraft safety will be covered by the type certification, including equipment, uplink, backup systems and security measures.

8.1.3 Future UAS Regulatory Road Map

The Technical Opinion [68] presented a road map for the future legislative process where it was stated that work could start on amending Implementing Rules used for legislative guidance for the Certified category, and that initial CSs for unmanned aircraft were to be expected in Q2 of 2017.

8.2 Reconfigurability Operational Certification and Regulations

The regulations described in the previous section cover the unmanned control of the ModuLR. Another imported aspect with regard to regulation and certification is the reconfigurability of the ModuLR. Certification of a new aircraft involves many different tests on the aircraft to prove its compliance to the regulations concerned. After successful completion of the test phase, the aircraft will receive a Type Certification [70]. The Type Certification is valid for that specific design and is subject to continuous regulations regarding maintenance and different airworthiness tests.

When an alteration is made to the airframe, two different categories can be distinguished: minor and major alterations. When altering any component causes an appreciable change in its weight, balance, structural strength, performance, powerplant operation, flight characteristics, or other qualities affecting airworthiness, it is considered as a major alteration [71]. According to this definition, reconfiguration of the ModuLR can definitely be considered as a major alteration.

Next to the Type Certificate, another certificate can be used which is the Supplemental Type Certificate (STC) [72]. The STC is an additional certification when a major alteration is made to the original design. Since that major alteration is not part of the original Type Certificate, a STC can be used to certify the alteration. The advantage of using STCs is the reduction in the amount of certification procedures since only the alteration has to be certified and not the entire aircraft.

For the ModuLR, STCs can be used to certify the different wings and tail for other configurations. Then, when the reconfiguration is performed, the configuration type should be stored in a central database with the correct configuration and applicable STCs.

For large aircraft, reconfiguration is new and current regulations do not count on multiple major alterations in the lifetime of an aircraft. Therefore, there must be consultation with the concerned authorities for this concept. Perhaps an example can be taken from the world of gliders which are build in such way that they can easily be taken apart for transportation. Also, the DG-505 glider can fly in three different wing configurations based on the desired properties[1] without the need of extensive paper work.

8.3 Communications

Throughout the whole operating time of the ModuLR, reliable communication systems are needed that can provide enough bandwidth for different stages during operation. To reduce development costs and cooperate with international standards, the aim is to use current and future international standards as much as possible. This section is split up into two subsections: first communication systems during cruise will be handled, the second subsection is about communication during take-off and landing.

8.3.1 Cruise

During cruise, communication with the Operations Control Center (OCC) occurs mainly for monitoring the state of the aircraft and bandwidth-intense data streams such as video are not needed. Still, if necessary, the aircraft is perfectly controllable by updating waypoints, destinations, and other flight parameters. To allow for this, a service that is similar to the Controller-Pilot Data-Link Communications (CPDLC) service will be developed. Currently this service is implemented in two different architectures: FANS 1/A and ATN. It is expected that these architectures will merge into ATN B3 IPS [73][74]. Using the Internet Protocol Suite (IPS), the aircraft is able to use more bandwidth [75] and thus allows the broadband data connection that is required for an autonomous aircraft.

Multiple physical data links will be used. Primarily the Inmarsat Jet ConneX Ka-band network is used. This network provides a data downlink of 15 mbit/s and uplink of 1 mbit/s [76] and provides worldwide coverage as can be seen in Fig. 8.1.

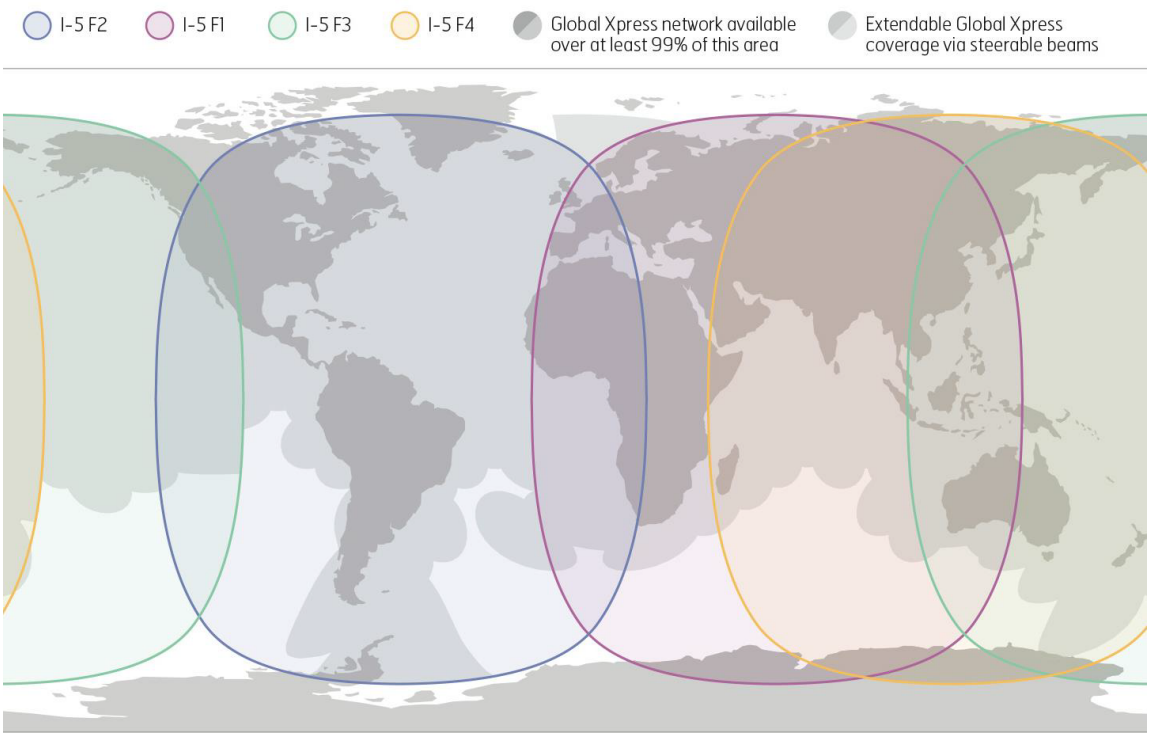

Figure 8.1: Inmarsat Jet ConneX Coverage map 2017[77]

It is expected that from 2020 onward, new satellites will be launched that provide an even higher capacity and better redundancy, promising higher data rates in the future. To allow for a reliable data connection over congested areas in Europe, the satellite infrastructure is complemented with the

[1] https://www.dg-flugzeugbau.de/en/library/dg-505-orion-short-description, visited on June 18, 2017

European Aviation Network (EAN) [77]. EAN combines an extra S-Band satellite infrastructure with a 4G LTE complementary ground component system, to allow for high throughput, high capacity, and a low latency up to 40 ms. Another advantage is the lower operational costs that are linked with this, making this the preferred connection when flying over Europe [77].

When a high data rate is not required, the aircraft can connect with the OCC using VHF frequencies. More specifically, an option is the ICAO VHF Data Link (VDL) Mode 2. This connection is currently available and provides a data rate of 31.5 kbit/s [78]. The ATN IPS system will also have backwards compatibility with the older ACARS architecture that uses the largest currently available VHF data link network [79]. This can be used as an extra redundancy in case the aircraft has to communicate with non compatible ATCs on the ground. In this case, a selection of transmitted data has to be chosen since data rate is limited to around 2.4 kbit/s [80].

Besides these three technologies that will be used during cruise, many new broadband communication systems such as LDACS [81] are currently being developed and might provide better performance in terms of bandwidth, latency and availability for a lower operating price than using a satellite connection. LDACS, for example, integrates communications, navigation and surveillance technology into one system.

Furthermore, the ModuLR uses Automatic Dependent Surveillance-Broadcast (ADS-B) to broadcast identification, position, altitude, velocity, and other status parameters to ATC and aircraft in its vicinity. ADS-B provides real-time high accuracy positioning for the ATC, enabling more efficient routing, improved take-off and landing accuracy. In general, the flow management is also better [82]. Another aspect of the integrated ADS-B system is ADS-B In; a feature which allows the aircraft to receive traffic information about surrounding aircraft that are also equipped with ADS-B Out. For most aircraft, it is already mandatory to have ADS-B Out equipment in Australian and European airspace [83]. In 2020 this will be mandatory in US airspace as well [84]. Using this ADS-B data from other aircraft and data from ATC, the aircraft can optimize its distinct route. This results in a lower chance of a mid air collision. Should a situation still occur where this system fails and a collision is about to happen, TCAS will ensure that the collision is avoided as final safety feature.

In Fig. 8.2, a graphical overview of the communication system is shown.

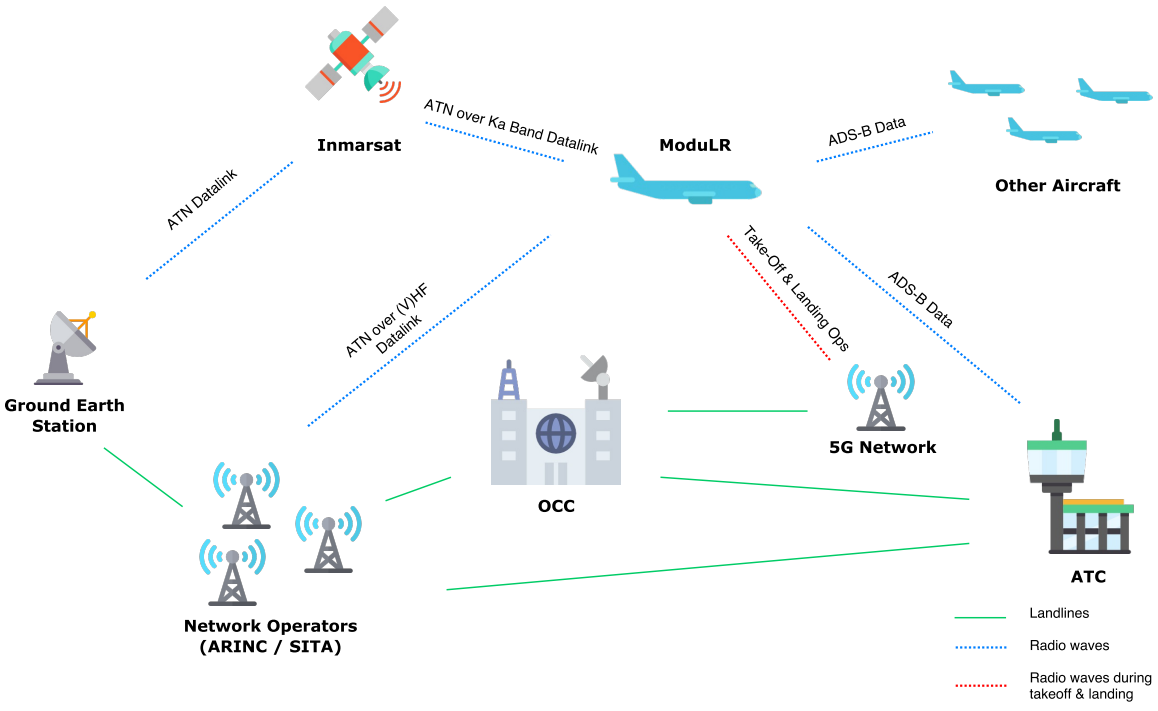

Figure 8.2: Communications system overview

8.3.2 Take-off & Landing

Different requirements arise during time-critical operations, such as landing and take-off. Latency during these operations can have catastrophic results. For this, a reliable low latency communication system

must be set up.

The challenge in this case is to always have a low latency and a respectable data rate, irrespective of whether communication channels are congested. Latencies starting at 100 ms may already deteriorate the ability of steering the aircraft, while higher latencies in the range of 250 ms - 300 ms [85] may provide unacceptable steering capabilities. The communication methods proposed in the previous section do not meet these requirements as communication with geostationary satellites like the Inmarsat will have a latency of at least 238 ms [85], while a VDL connection can only handle a data rate of 31.5 kbit/s. Although this is enough to send control parameters, sending images, video, haptic communications, and a higher range of parameters might pose a challenge. To achieve an optimal communications system, a latency budget is set up consisting of all steps that occur during communications.

Aside from the data connection itself, other aspects of the connection introduce latency as well. Since the data between the ModuLR and OCC requires a secure connection to prevent a malicious user of interacting with the aircraft, data needs to be encrypted and decrypted. It is estimated that this takes an extra 1-2 ms latency per operation. Since every round trip requires two times an encryption and decryption this adds up to about 4-8 ms latency [85].

Another aspect is error correction. Error correction is necessary when sending data that needs to arrive without small errors (on bit level). Using TCP/IP, verification of the data is performed. This however requires a slightly higher data rate for checksums and retransmitted data and produces extra latency. An extra delay of 1 ms is accounted for [85].

Furthermore, there will be a delay resulting from the difference in time of the moment that parameters to be send are calculated and gathered, and the actual moment of transmitting these. This latency largely depends on the computational power of the aircraft, still the computational power can be considered sufficiently enough to have a maximum of 10 ms latency.

Transmitting live video footage is bandwidth expensive and may congest the network or slow down other operations. For this reason, the video footage is encoded before it is sent to the OCC. Several encodings can be used and are currently being developed. It is expected that in 2035 even more optimal techniques exists. Still, using current techniques, a good prediction can be made for the highest latencies possible. Using the latest HEVC/H.265 encoding, an encoding speed of 392 fps can be achieved for videos with a resolution of 1920 by 1080 pixels (1080p) [86]. Assuming a video frame rate of 50 fps, 5 frames have to be encoded during the 100ms latency, resulting in an extra latency of 13 ms. On the ground, the video feed has to be decoded. This decoding happens with 720 frames per second [87], resulting in an extra latency of 7 ms. The total extra latency, consisting of both encoding and decoding, is 20 ms.

To make sure the ModuLR is able to land without extra workload or degradation in effectiveness, the maximum latency is aimed to be 100 ms. With this latency, the aircraft is still able to be operated safely. Combining all previous parts of the latency budgets in Tab. 8.2, it can be seen that from the 100 ms allowed latency, 61 ms latency is left for transportation of the signals.

Table 8.2: Latency budget

Aspect	**Latency**
Encryption & Decryption	8 ms
Error correction	1 ms
Computational time	10 ms
Encoding & Decoding	20 ms
Transportation	61 ms
Allowed nominal latency	100 ms

To allow for a high bandwidth and low latency during landing and take-off operations, 5G is considered as the primary mode of connection during these phases. It is to support a round trip latency of 1-4 ms [88]. Using the Ultra Reliable Communication (URC) mode, these low latencies can even be achieved while the 5G antenna handles a larger amount of users. Instead of suddenly unavailability of the service, performance gradually declines as more users are connected with the 5G antenna [89]. In these cases, it might prove advantageous to stream video footage using another data link as video footage requires the highest bandwidth. The 5G URC mode is also compatible with the ability to transport haptic data to the OCC [88] in case of a manual landing. Using this haptic data, the pilot will be able to perform the

landing better as the operation is better simulated.

After removing the 4 ms latency required by 5G, 57 ms remain to be used for landline transportation of signals between OCCs and 5G antenna's nearby airports. Of this 57 ms, 22 ms can be accounted for routing and switching latencies, queuing and buffering latencies and serialization delay. Data can travel with a velocity factor of about 40% to 80% of the speed of light through copper wire and a velocity factor of about 70% through fiber optic cables [90]. When a velocity factor of 60% is assumed and the remaining 35 ms propagation delay is allowed, a round trip distance of 3150 km can be achieved. Since most of the time the data lines are not in a straight line, the actual distance that needs to be traveled is longer. When using a safety factor of 25%, the round trip distance is reduced to 2350 km. This distance defines the number of OCCs required for worldwide coverage. In Fig. 8.3 all sixteen OCCs including their 2350 km range are displayed on the world map.

Figure 8.3: Locations of the 16 Operation Control Centers (OCCs), each having a range of 2350 km.

8.4 Unmanned Control System

A robust and reliable control system is required for safe autonomous air travel in unsegregated airspace. The unmanned aspect is mainly desired for possible cost reduction with respect to required personnel and streamlined operations. Although, this might be offset by higher system complexity which is highly dependent on near future technological advancements. For the ModuLR, four levels of autonomy to be used at various stages are proposed is sub-section 8.4.1.

8.4.1 Level of autonomy

Four levels of autonomy are considered in accordance with terminology set by the US National Institute of Standards and Technology [91].

- Fully Autonomous: No human interaction is involved in the unmanned system (UMS) performing its assigned mission while also being able to adapt to changing environmental conditions;
- Semi-autonomous: Some level of human interaction is required although the UMS operates autonomously in between these interactions;
- Teleoperation: A human operator controls the UMS from a remote location either directly or with intermittent inputs based on continuous sensory feedback;
- Remote Control: The UMS relies on continuous control input form a human operator in direct observation.

Based on the flight phases, presented in section 8.4.2, fully autonomous operation is desired during the departure and cruise phase, with the possibility of multiple aircraft per operator further into the future. Although this might prove to be a challenge. Taking Global Hawk UAV operations used to gather meteorological data of hurricanes[2] as an example, the workload was described as being close to that of manned operations, presumably in part due to the UAV not having sufficient collision avoidance and sense and detect systems. This is often said to be less of a burden for high altitude cruising UAVs where air traffic is sparser, something which will not be the case for the ModuLR with a lower cruise altitude at around 20000 feet. Therefore, the allowable level of autonomy will depend on requirements set by aviation authorities and available command and control, sense and avoid technologies along with independent decision making.

8.4.2 Flight Phase

A typical mission is assumed to comprise of the following eight flight phases, each with their own requirements. Common for most of these are three safety layers of collision avoidance ash shown in Fig. 8.4. ATC control for overall traffic management, Traffic Advisory and Resolution equipment for both situational awareness and coordination. And finally, Sense and Avoid equipment at close-in encounters.

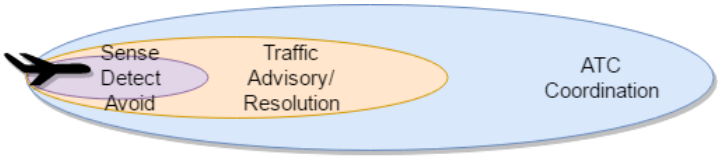

Figure 8.4: Simplified depiction of three layers of collision avoidance aspects.

Pre-flight, taxi and post-flight

- Pre-flight and Post-flight phases are primarily handled by the responsible technician, with the addition of the remote operator when closer to start-up/shutdown according to requirement RUCA-T-OPS-CT-1. A Portable Maintenance Aide (rugged laptop connected to the aircraft) will be used by the responsible technician for system test and diagnostics, task scheduling and maintenance manual library. Some time before take-off, the connection is handed over to the remote operator, which then initiates the start-up in coordination with the technician;
- Taxiing between the parking area and runway threshold will either be handled in a semi-autonomous or teleoperated manner. The former being with the use of ATC clearance and GPS coordinates and/or image recognition software building on today's advancements in autonomously driving vehicles. Currently, ATC clearance is gained verbally over radio, which would add to the workload of the remote operator. The ModuLR will seek to make use of future ATC data link functionality such as D-Taxi which is one of the FANS & ATN-B2 CPDLC functions under the Single European Sky ATM Research (SESAR) [92] program aimed at reducing required ATC voice interactions. In the case of unreliable GPS coordinates or high-risk ground traffic or weather conditions, the operator will take direct control using several cameras and ATC communications for situational awareness, augmented by ADS-B [93]. The cameras will be nightvison capable to provide equivalent vision during night time in accordance with requirement RUCA-T-OPS-FO-4 and RUCA-T-OPS-FO-3.

Take-off and Departure

- Automatic Take-off and Landing Capability (ATLC) software[3] will be utilized by the ModuLR together with autopilot flight director input and a Full Authority Digital Engine Controller (FADEC) autothrottle function. The Position will be provided by INS/Differential GPS and airport coordinate data. As the latency is acceptable, as explained in section 8.3, take-off can also be done manually by the remote operator. Especially since he was also already in control a moment earlier when initiating the mission;

[2] https://www.nasa.gov/mission_pages/hurricanes/missions/hs3/news/pilot-challenges.html, visited on June 18, 2017
[3] http://www.ga.com/dhs-fields-new-automatic-takeoff-and-landing-capability-for-predator-b-fleet, visited on June 18, 2017

- Departure clearance from the ATC according to the flight plan will be handled by future Controller Pilot Data Link Communication Departure Clearance Service (CPDLC DCL). Here, clearance and revising of departure plans are streamlined without the need for voice communication with ATC [94];
- ADS-B, TCAS-II and Airborne Sense and Avoid Radar (ABSAA) Radar provide situational awareness and collision avoidance.

Cruise

- The cruise phase will be handled by the aircraft's fully autonomous mode, which will follow the pre-uploaded flight plan. Amendments can made based on OCC, ATC, weather reporting, or safety systems input. Fully autonomous, in this case, includes freedom to independently adjust the flight path within certain limits without notifying the OCC. The limits will be optimized over time with respect to operational efficiency and safety. The operator will be notified if any required decision, action or situation will exceed these limits;
- ATC coordination will be automatic through either FANS 1/A or ATN CPDLC, depending on operating area, for traffic advisory and flight plan adjustments;
- ADS-B IN/OUT will provide situational awareness;
- ABSAA will provide Sense and Detect capability equivalent to that of a pilot's see and detect ability. ABSAA Radar will work in tandem with TCAS-II in suggesting vertical and horizontal separation maneuvers to the control system.

Approach and Landing

- Approach and pattern hold will be done semi-autonomously in cooperation with ATC. A future ADS-B Ground based Interval Spacing Management function will be implemented where ATC can define a spacing to be achieved and maintained by the flight control system with respect to a target aircraft[4];
- Landing will be done using ATLC software for autonomous control and ILS CAT II/III, Differential GPS, and radar altimeter for guidance in accordance with requirement RUCA-T-OPS-CT-6.

8.4.3 UAS Control Architecture

This section presents the proposed architecture of the unmanned control system residing within the aircraft in order to comply with requirement RUCA-T-OPS-CT-2. The architecture is in part influenced by the reports "Multi-Layer Control Architecture for Unmanned Aerial Vehicles" by J.D. Boskovic [95] and "Multiple-Scenario Unmanned Aerial System Control" by C.M. Eaton [96]. Fig. 8.5 presents a block diagram with the four main system management blocks which are further detailed in this sub-section. During semi-autonomous and teleoperated control modes, the decision module has less authority and the OCC must manually issue certain commands to the ModuLR. Remote control is always available as a manual override in accordance with requirement RUCA-T-OPS-CT-3. Maintenance personnel have full authority during maintenance.

Mission management block

The mission management block handles and distributes all pre-planned data such as flight plans, mission statements, priorities and optimal trajectories for varying parameters such as fuel efficiency or travel time. These can be uploaded either wireless or through a data cartridge inserted by a technician during pre-flight.

- The flight plan block receives and stores all the waypoints for the coming mission and transfers these to the path determination block as needed. These can also be updated mid-fight by either the OCC, ATC or the system itself depending on the situation. Pre-planned trajectories might be calculated beforehand and stored providing a database for optimized performance with respect to fuel consumption, flight time or sentimental risk, which can be followed if no alterations are needed.

[4] https://www.faa.gov/nextgen/programs/adsb/pilot/ima/, visited on June 19, 2017

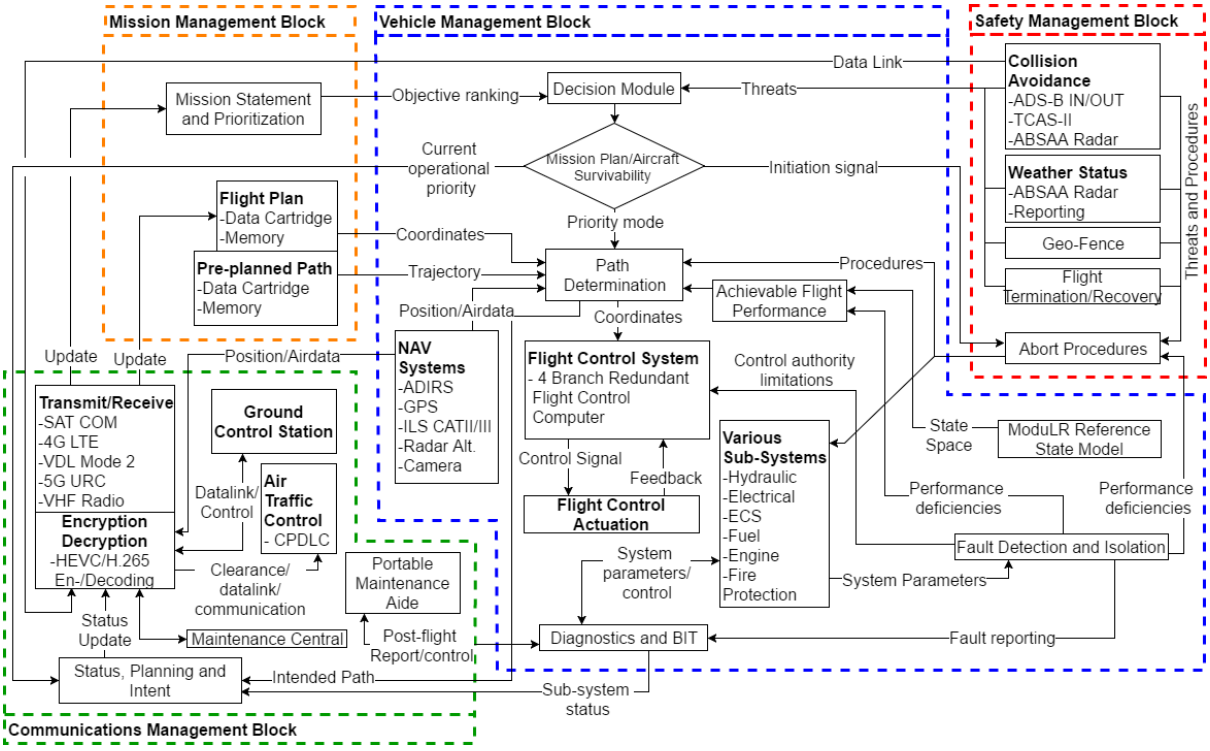

Figure 8.5: Simplified block diagram of the unmanned control system architecture with four main management blocks. Interconnection are shown as arrows along with what type of data is sent.

Communication management block

The communications management block consists of all subsystems used to establish a secure communications link with either ATC or OCC and the gathering and transmission of system status and current intent. This block, together with systems detailed in section 8.3, is in accordance with requirements RUCA-T-OPS-CM-2 and -3. Additionally, together with various proposed CPDLC functions mentioned in sub-section 8.4.2, this also complies with requirement RUCA-C-LEG-4.

- The status, planning and intent Block gathers all relevant data that is required for OCC and ATC to get a clear understanding of the current status and position along with intended future actions of the aircraft, also assuring compliance with requirement RUCA-T-OPS-CM-1. This will allow operators to plan ahead and prepare changes to the flight plan or mission objectives;
- The transmit/receive subsystem contains all systems required to reliably and securely transfer encrypted commands and control signals along with status updates between the aircraft, OCC and ATC. Essential components are redundant.

Safety management block

The safety management system includes collision and weather avoidance, geo-fence mapping, flight termination/recovery and automatic fault procedures. Flight termination/recovery modes are described in further detail in subsection 8.4.4. By including safety management the design meets requirement RUCA-T-NOM-RL-1.

- The collision avoidance is an essential block in integrating the ModuLR into non-segregated airspace and complying with requirement RUCA-T-OPS-CT-5. Collision avoidance through ATC coordination, traffic advisory technology and sense and detect ability must be equivalent to a manned aircraft pilot's see and detect ability. According to a FAA Advisory Circular, "Pilot's Role in Collision Avoidance", it is stated that "when weather conditions permit, regardless of whether the operation is conducted under instrument flight rules or visual flight rules, each person operating an aircraft shall maintain vigilance so as to see and avoid other aircraft", along with "Maintaining Vigilance: Traffic information equipment does not relieve a pilot's responsibility to see and avoid

other aircraft" [97]. Three systems are proposed and used as explained in subsection 8.4.2, ADS-B, TCAS-II and ABSAA radar. The latter especially useful as it provides detection of non-cooperating general aviation aircraft. And using Actively Scanned Array technology, such as customizable certified radar module can be as light as 30 kg [98]. The Collision avoidance block also continuously evaluates the risk of air or ground impact and forwards this to the decision module;

- Geo-fence and weather status functions can modify the boundary conditions in the path determination block. Geo-fencing would be a database defining restricted airspace, such as military airspace or areas with population densities higher than what the ModuLR at the time might be certified to operate over. The weather block would evaluate whether conditions are within safe limits, both current and en-route, in compliance with requirement RUCA-T-OPS-CT-4.

Vehicle management block

Vehicle management is the most comprehensive segment handling the operation and monitoring of the aircraft. It is interconnected with the three other segments through an Integrated Mission Management Computer (IMMC) [99]. The vehicle segment includes function blocks for flight path determination, system health monitoring, decision making and subsystem control.

- The path determination function calculates the flight trajectory with primary input from the pre-uploaded flight plan and optimized trajectories. The calculated optimum trajectory in between these waypoints is limited by achievable performance, which is both based on subsystem status (remaining fuel or potential faults) and addition operational limits set by the manufacturer and operator. Additional inputs come from the decision module and flight termination/recovery functions (safe recovery zones).

  Path determination might be one of the functions more susceptible to slow technological advancements. Creating efficient and deterministic algorithms for optimal trajectory calculation between coordinates, including the option of avoiding certain areas and moving objects, has been an ongoing process. However, it has been a difficult problem to solve mathematically due to a high number of feasible solutions, dimensions and constraints [100]. It must be noted that the field has seen more activity in recent years due to increased interest in autonomous control [96]. Another shortcoming is that much of the UAS path determination research up until now did not accurately take into consideration actual vehicle dynamics, but point-mass simplifications were for example used.

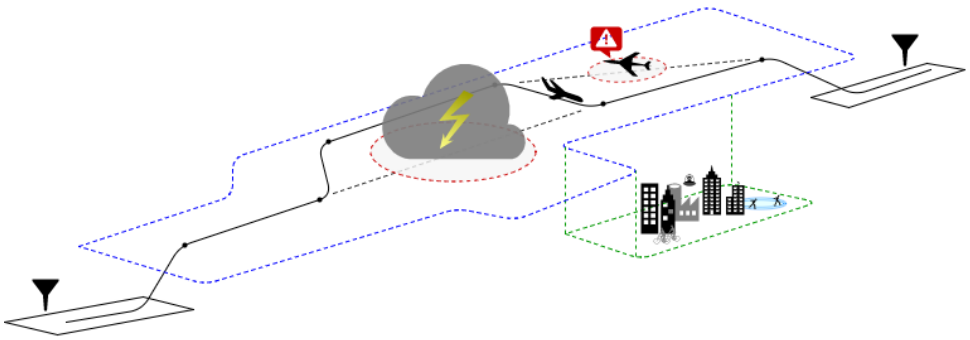

Figure 8.6: Simplified outline of path determination and decision making. The largest sector(blue) defines available envelope for trajectory determination (black line with waitpoints). Restricted sector from Geo-fencing (green) is depicted around a populated area. High risk areas (red) are made around threats and weather, circumvented by path rerouting (dashed black line original path).

  In case proper path determination algorithms are not sufficiently developed, this function can instead be handled manually by the operator and/or ATC. This process is similar to current unmanned operations. Although, still with some reduced workload as the safety management block can handle unexpected situations while at the same time notifying the operator. Which means he does not have to sit at the ready most of the flight with the system assuring enough time to assess the situation;

- Prioritization of mission success or vehicle safety and survivability (also accounting for external actors) is continuously evaluated by the decision module. This evaluation is performed based on

inputs from the safety management system, mission priorities, and the vehicle status (from a fault detection and identification function). If continued normal operation is decided against, either evasive maneuvers are activated in the path determination module or the termination/recovery function is initiated. The operator is notified through the status, planning and intent block;

- The fault detection and isolation block continuously monitors a wide variety of system parameters such as fluid levels and temperatures, electric generator power output and frequency, engine gas temperatures and pressure ratios, and downlink quality with the OCC. These are then used as limits on the available performance. These limits are used for path determination and as part of the evaluation don'ts in the decision module. Here, it is decided whether to continue or abort the mission. Any detected system faults are transmitted to the OCC and the operator is notified. This block also stores and submits any occurrences during flight and transfers them to the maintenance and operations center post-flight.

8.4.4 Flight Termination and Recovery modes

In order to mitigate potential damage due to loss of control link, emergency modes can be initiated by the decision module. Four main emergency modes, described in Tab. 8.3. The emergency modes presuppose connection loss with both OCC and ATC, because either should be able to oversee a safe recovery by themselves. Whether it is a lost connection with OCC, in which case ATC is granted increased control authority. Or a broken CPDLC link, in which case OCC can manually coordinate with ATC over an alternate communication line. In both cases, an alternate connection path is always attempted to rule out any faults in ground hardware and control can always be restored in case of a recovered link. Up-to-date emergency landing zones along any pre-planned route will be stored in a database within the aircraft and ATC is responsible for separating other traffic from an unresponsive ModuLR.

The selection of a suitable runway is based on last known air and ground traffic density, less is preferable, if within range. When an emergency landing is initiated, ADS-B provides separation from aircraft which are at a later stage of landing while other en-route aircraft are rerouted by ATC, similar to normal emergency situations. A decision will have to be made on whether it is preferable to stay in some holding pattern, in case the link might be reestablished and to provide more time for response crew, or to immediately initiate the emergency landing. The former might be preferable in areas of very low traffic, while the latter might be preferable to minimize disruption of normal traffic by a non-cooperating holding aircraft.

8.5 Service Model

A disadvantage of a reconfigurable aircraft is the need of having all the reconfigurable parts. This can get cost expensive, especially if the operator does not require a large number of aircraft. Would that be the case, then the operator would be able to mix the reconfigurable parts amongst the aircraft it owns, which lowers the total reconfigurable parts (per aircraft) required and therefore lowers the costs. Another significant downside reconfigurable aircraft is that the operator needs to invest in multiple hubs around the world where they would reconfigure the aircraft. If the operator once again does not have a large number of aircraft or a large number of reconfigurable parts, the parts might get swapped around different hubs and the required parts might not be available.

To overcome these problems, especially for operators requiring a low number of reconfigurable aircraft, a service model has been developed. In this model, the ModuLR Group takes over several operations that in the conventional case are handled or subcontracted by the operator.

The first operations the ModuLR Group takes over are the aforementioned reconfigurational operations. This is implemented by creating several hubs across the world, where every operator has the possibility to have their aircraft reconfigured. The ModuLR Group sets up these hubs and provides the required personnel and reconfigurable parts. Since there is now only one party that reconfigures all the ModuLR aircraft at limited locations, not every aircraft has to come with all reconfigurable parts as a pool is created where all operators can use reconfigurable parts from. However, a number of fixed parts, mainly the fuselage, avionics, and landing gear, remain to be bought by the customer. This has the advantage that the fuselage can be branded (paint etc.) according to the customers need.

The second part of the operations that the ModuLR Group takes over are the maintenance operations. Since the ModuLR Group takes care and owns all the reconfigurable parts, it will also provide maintenance for these parts. As this can be done easily while they are stored at the hubs, it significantly

Table 8.3: Table detailing the conditions for entering a certain flight termination/recovery mode along with the overall procedure the ModuLR will attempt to follow. Degraded powered flight capability means altitude can not be sustained, including both high and low sink rates.

Mode	Condition	Procedure
Immediate Flight Termination	- Lost OCC and ATC link and no suitable runway available, vehicle subsystem compromised. - Degraded Powered flight capability.	1. Asses severity of performance degradation. 2. Determine most suitable emergency landing zone from NAV and map data. 3. Initiate emergency landing procedure minimizing kinetic energy on impact as much as possible. The highest priority is avoiding populated areas.
Urgent Flight Termination	- Lost OCC and ATC link and no suitable runway available. - Powered/Controlled flight capable.	1. Determine suitable emergency landing zone from NAV and map data. 2. Initiate holding pattern within range for set time or link reestablished. 3. Initiate emergency landing.
Urgent Flight Recovery	- Lost OCC and ATC link, vehicle subsystem compromised - Degraded Powered flight capability	1. Asses severity of performance degradation. 2. Determine suitable runway based on achievable flight performance and type of fault. 3a. If within range, Initiate emergency landing. 3b. If not within range, initiate Immediate Flight Termination Mode.
Safe Flight Recovery	- Lost OCC and ATC link, vehicle systems functional - Powered/Controlled flight capable	1. Determine suitable runway based on last known traffic conditions and achievable flight performance. 2a. If low traffic, initiate pattern hold within range until set time or link is reestablished. 2b. If high traffic, initiate emergency landing. 2c. If no suitable runway, initiate Urgent Flight Termination Mode.

saves costs and maintenance burden as the operator can continue flying their aircraft with other parts. When the aircraft is being reconfigured, the ModuLR Group will also take care of maintenance for the fixed parts of the aircraft. In this way, overall costs are reduced since maintenance will occur in bulk and the maintenance crew only has to be trained for the ModuLR as one aircraft type. With this, the RUCA-T-OPS-MT-1, and the RUCA-T-OPS-MT-2 requirements have been complied with. Operators would not need to train personnel themselves or invest in capital to allow this maintenance.

The third and last operations part that the ModuLR Group takes over are the flight operations. Since there are no pilots on board, the aircraft has to be monitored and in some cases directly controlled from the ground. This requires specially trained personnel, a unique architecture set-up, and a great number of OCCs around the world as can be read more about in subsection 8.3.2. These reasons, together with the cost saving potential of providing bulk flight operations to all airliners, make it feasible and attractive for the ModuLR Group to also perform flight operations.

A graphical overview of how the service model is implemented is shown in Fig. 8.7.

To be able to offer these services, a yearly service subscription fee has to be paid by the customer. Apart from the service fee, customers pay a one-time purchase fee to obtain the fixed parts. Chapter 11 will go more in depth about the financial aspect of the service model and presents the costs for the fixed parts and the price of the service fee.

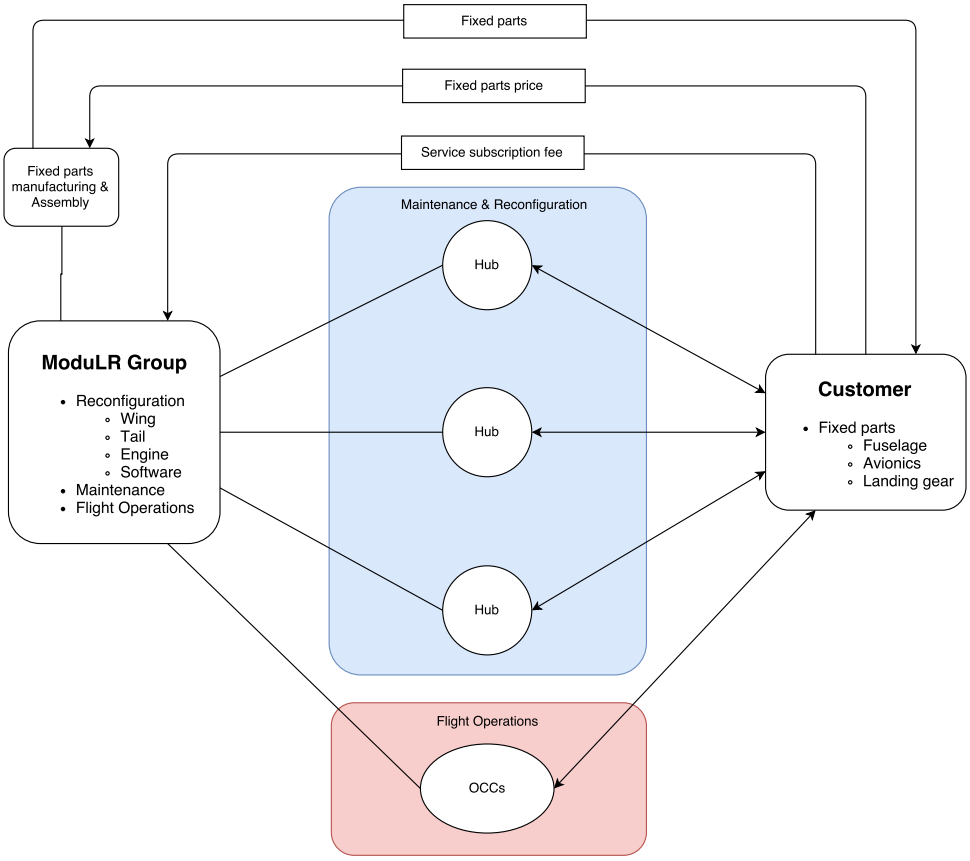

Figure 8.7: ModuLR service model

8.6 Ground Operations and Logistics

The transport of cargo by the ModuLR is only a part of the entire chain from sender to consignee. To prevent delays in this entire chain, each part of the chain should be optimized to decrease time delays. In this section, the handling of cargo with respect to the ModuLR is designed. Then, the turnaround time, the time needed for the aircraft from arrival till departure from the platform, is calculated for the three different configurations.

8.6.1 Cargo handling

As mentioned in section 4.2.2, the ModuLR will be designed to be used with ULDs. The benefit with respect to cargo handling is that the equipment needed for loading and unloading is already present at airports, meeting requirement RUCA-T-OPS-GH-2. The cargo floor of the ModuLR also has to be designed for easy cargo handling. As in most aircraft, the cargo floor will be covered with ball transfer rollers.

To find the total cargo handling equipment weight, the amount and total weight of the system of ball transfer rollers, the spacing, and weight per roller has to be determined. The spacing is important to prevent pallets from getting stuck. Since the ModuLR is not limited to the use of half size pallets, also ULDs with a smaller width or length are considered. The ULD with the smallest width, namely 1.19 m, is the LD2[2]. Considering the possibility of weight imbalance of a ULD and two different directions in which the ULD can be loaded, a spacing of 0.25 m is chosen in both directions. In that way, always 16 rollers per m^2 will support the pallets. With the maximum weight per m^2 of the applicable ULDs[2], rounded to 650 kg/m^2, the weight per roller is 40.63 kg.

For the ball transfer roller design, the weight per roller is multiplied by a load factor of 1.25 to ensure that there is no overloading of individual rollers when there is a weight imbalance in the ULD. With a gravitational acceleration of 9.81 m/s^2, the load capacity of an individual roller should be higher than $40.63 * 1.25 * 9.81 = 498$ Newtons. From Rexroth [101], the ball transfer unit with a load capacity of 500

Newtons, ball diameter of 15 mm, and weight of 0.038 kg is chosen and shown in Fig. 8.8. Next to the rollers on the floor, also rollers on the sides are placed for smooth transfer of the pallet in the length of the fuselage. This results in a total of 548 rollers placed in the floor and on the sides, with a combined weight of 548 * 0.038 kg = 21 kg.

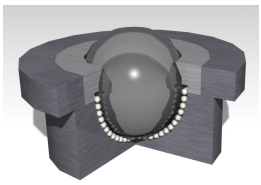

Figure 8.8: Ball transfer unit

It is important to safeguard the cargo and weight balance of the aircraft. For securing the cargo, standard quick lock clamps are used when the half pallets are loaded. In case of other cargo sizes, securing the cargo can also be done using straps that can be attached on different points in the floor, using rails embedded in the floor. When using four clamps per pallet and assuming a weight of 5 kg per clamp, the total weight of the cargo handling equipment is $21 + 8 * 4 * 5 = 181$ kg.

Currently, most (cargo) aircraft also use automatic rollers that transfer the ULDs inside the fuselage. However, installing such systems will increase the weight and cost of the aircraft. Since only 8 half pallets can be loaded, manual transferring inside the aircraft is considered favorable. From Rexroth [101], the friction coefficient is found to be 0.0034 using the load factor of the roller. Using the dimensions of the half pallet combined with the number of rollers per m^2 calculated earlier, a total of 60 rollers are supporting the half pallet. Combined with a maximum load of 2366 kg per half pallet[2], the total friction force is 78.9 N. According to CCOHS[5], horizontal pushing force with whole body involved should not exceed 225 N per person. Although the static friction will be higher, two cargo handlers should be able to transfer the pallet inside the aircraft.

Finally, the equipment needed on the airport will consist of a container loader or K loader and a truck with a sufficient amount of dollies to load the ULDs.

8.6.2 Turnaround time

The turnaround time is the time needed between the arrival of an aircraft on the platform and the moment the aircraft departs again. A short turnaround process can increase the amount of flights that can be flown within a certain amount of time, and at the same time decrease the cost for occupying the platform on airports. The turnaround process is shown in Fig. 8.9. It can be seen that the turnaround time is defined as the time between chocks on and chocks off. In contrast to passenger aircraft, simultaneously refueling and cargo handling is less of a (risk) problem. Therefore, the total turnaround time of the aircraft depends on either the time needed for refueling (blue chain) or time needed for cargo unloading and loading (red chain). Here it is assumed that miscellaneous tasks like paperwork are not the critical factor.

To calculate the time needed for refueling (RUCA-T-OPS-GH-7), the fuel masses for each configuration as calculated in chapter 5 are used. The time needed for attaching, detaching, and transferring fuel, is based on the Boeing 747-8 turntime analysis [102]. From this document, it is determined that the time needed for attaching and detaching the refueling system is 4.5 minutes. Then, using the amount of fuel and time needed for refueling the 747-8, the refueling rate is determined at 5.1x102 liters per minute. Since the fuel needed by the configurations is expressed in kilograms, the density for jet fuel A1, 0.804 kilogram per liter [103], is used.

The time needed for cargo handling per configuration is based on the amount of cargo and pallets needed by each configuration. Since the fuselage does not change between ModuLR configuration, the cargo handling process is similar. Therefore, a standard time is determined for opening cargo doors and other preparations. After analyzing cargo operations, the time needed for unloading and loading one half pallet is established at 1.25 minutes. This short period is deemed to be possible as, since the cargo does not have to travel fast inside the fuselage, multiple half pallets can be lifted simultaneously by a cargo loader, and the fastening of half pallets is standardized. The resulting turnaround processes for each configuration are shown in the Gannt charts in Fig. 8.10. The longest turnaround time, the one for the

[5]https://www.ccohs.ca/oshanswers/ergonomics/push1.html, visited on June 23, 2017

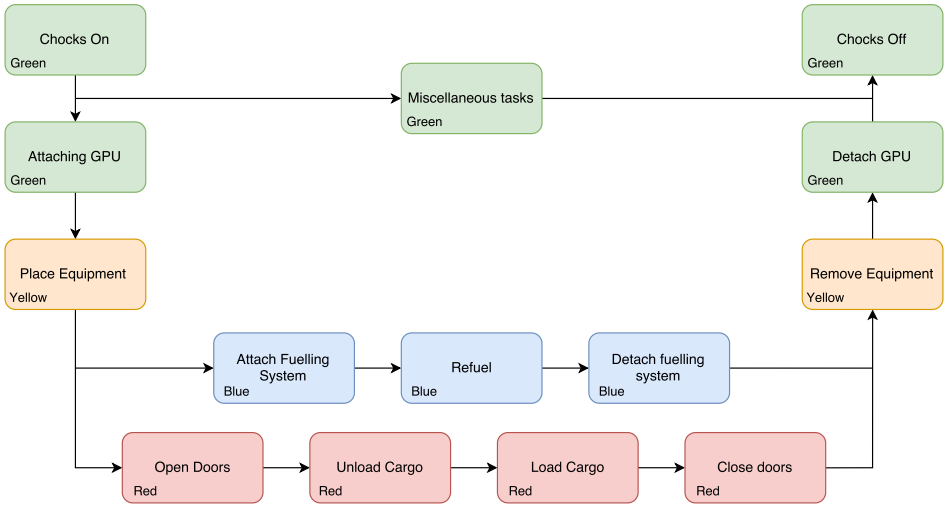

Figure 8.9: Turnaround flow diagram

largest configuration, is calculated to be 27 minutes, which is enough to meet the RUCA-T-OPS-GH-6 requirement as well as RUCA-T-OPS-GH-1.

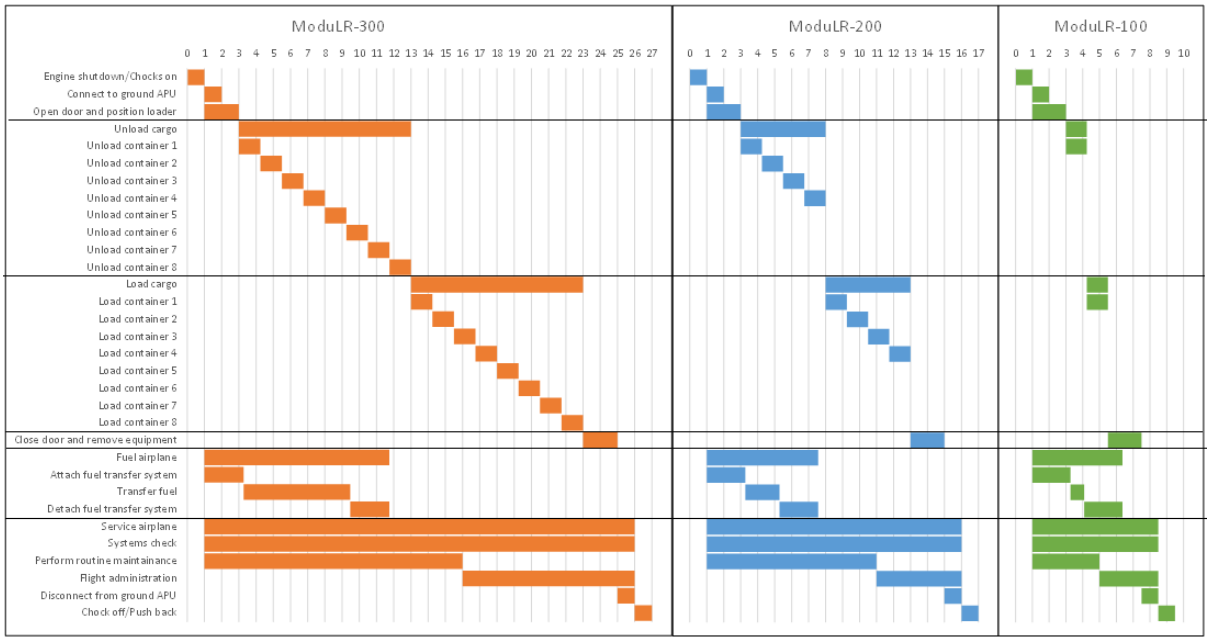

Figure 8.10: Turnaroung time Gannt chart

8.7 Reconfiguration Operations

The most driving requirement of the ModuLR is the ability of being reconfigurable. Currently, aircraft manufacturers already use a certain way of configuration in the sense of aircraft families. For example, the different versions of the A380 use additional fuselage parts that are located in front and back of the wing, as shown in Fig. 8.11a. Also, with the use of Supplemental Type Certificates, as mentioned earlier in section 8.2, manufacturers are changing the aircraft types by adapting parts and fit them on the original. However, this changing of parts commonly does not take place during the service life of the aircraft.

For the ModuLR, the changing of parts has to be optimized since it is a main feature and cannot take too much time. To make the reconfiguration of the tail, wing, and engine possible, the current

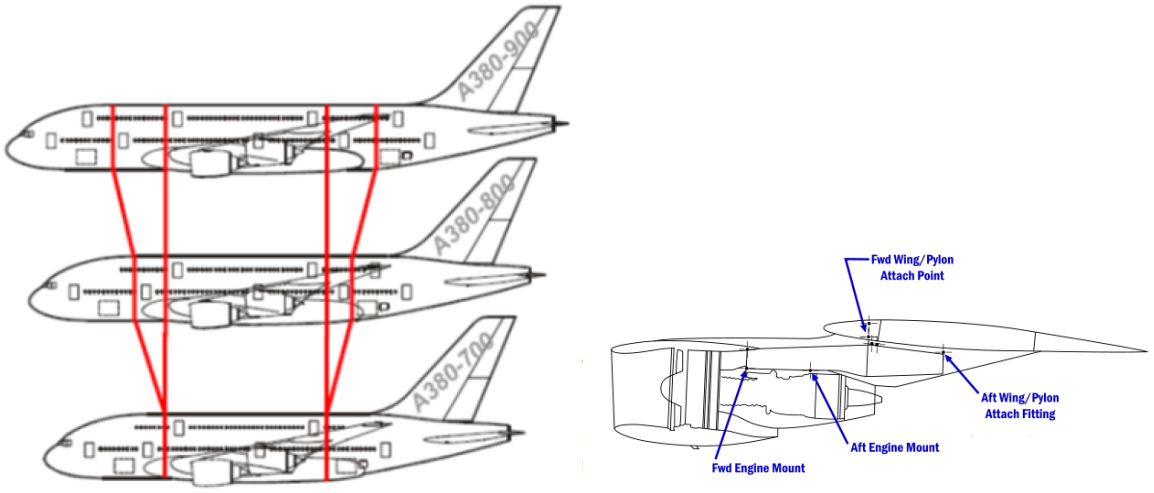

(a) Different A380 versions

(b) Turbofan engine attachment

Figure 8.11: View on the different A380 versions in (a) and the current engine attachment in (b)

connection of a turbofan engine to the wing is used as example because this engine is actually relatively easy to change. The engine is namely structurally attached to the wing by only a few bolts, depending on the type of aircraft, as shown in Fig. 8.11b. Next to the relatively fast engine swapping possibilities, the bolts are also designed to shear when the engine is damaged and causing too high (vibrational) stresses on the wing to prevent the wing from fatal damage. To conclude, this technique of connecting parts in the aviation industry using bolts is proven and the amount and size of the bolts can be adapted for the use in the ModuLR. Another advantage of this technique is that on airports, most of the equipment necessary for reconfiguration is available as mentioned in RUCA-T-OPS-GH-5

In section 8.5, a service model is be explained. For this section it is important to know that, since the reconfiguration will be performed in a hangar on one of the hubs of the service provider, the use of an overhead crane is necessary to lift the different reconfigurable parts up.

8.7.1 Tail reconfiguration operations

The ModuLR concept includes two different tails for its configurations. To ease the operations, the base of the fuselage and the base of the tail that is connected, including the connection points, are designed to be of equal shape and size. In other words: on the tail of the fuselage, a so called tail connector is placed where both the ModuLR-200 and ModuLR-300 tail can be attached to. The base of the -200 and -300 tail are therefore the same. On the tail connector, multiple bolts are placed for attachment on the tails.

In Fig. 8.12a, the fuselage with tail connector and the ModuLR-300 tail is shown. In Fig. 8.12b, the same fuselage with tail connector is shown with the ModuLR-200 tail. The tails are lowered on the connector and then the bolts are tightened in tension to pull the tail onto the fuselage. In the tail, small hatches will be placed for accessing these bolts. Depending on the stresses and forces in the connections, the size and number of bolts should be adapted. The skin is also connected using a small overlap and quick lock screws. However, this is only an aerodynamic measure, hence no forces and stresses have to be carried by this connection.

The tail also contains the elevator and rudder which should be connected as well. The first option is to mount electrical motors driving the control surfaces inside the tail, connected to the fuselage by a power and signal cable. The second option is to locate the motors in the tail of the fuselage and connect the rods from the control surfaces in the tail to those motors. A good example is the assembly of gliders where the control surface rods in the wing can be disconnected when the wings are disassembled for transport. Another option is to use hydraulic motors in the tail that are connected to the hydraulic system of the aircraft in the fuselage. During reconfiguration, the tail is lifted by the overhead crane from the fuselage when the connections are removed. Because the tail basis is the same, the tail can then be placed on a frame such that it can be moved on ground to the storage facility.

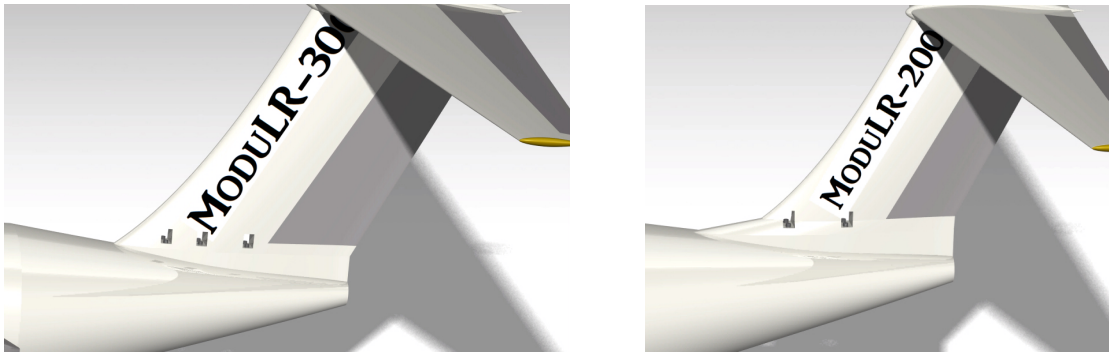

(a) ModuLR-300 (b) ModuLR-200

Figure 8.12: Reconfiguration of the tail of both the ModuLR-300 (a) and ModuLR-200 (b)

8.7.2 Wing reconfiguration operations

Each configuration of the ModuLR uses a different wing, therefore the entire wing has to be changed. In contrast to the tail, the different wings are located on different locations on the fuselage and can therefore not use the same connections. Since the fuselage remains the same, it should be able to be connected to each of the different wing configurations. Therefore, multiple connection points in the top of the fuselage have to be made. The length on the fuselage of this connection area is determined by the most forward and most aft wing position. These fuselage connection points are shown in Fig. 8.13. On these four connections points per wing (again depending on the stresses and forces in the connections, the size and number of bolts should be adapted), the center wingbox is connected. Finally, to cover the entire wing – fuselage connection area, a skin structure which is part of the wing is designed. This skin structure, or sleeve, covers the area and is connected to the skin using a small overlap and quick lock screws. The three different center wing structures are shown in Fig. 8.14a, 8.14b, and 8.14c. As mentioned earlier, each wing will have a part that will cover the connection area of the fuselage. This can be be seen in Fig. 8.15.

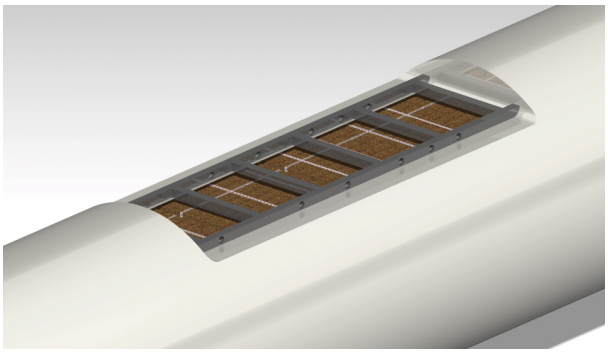

Figure 8.13: Wing connection points on the fuselage

Apart from the tail, more aircraft systems (like control surfaces) have to be connected between the wing and fuselage. The same connection possibilities mentioned for the tail connection are applicable to the wing – fuselage connection. These connections are all concentrated on the same location to ease the reconfiguration. Also, since the distance from the floor to the top of the fuselage is around 2 m, workers can easily reach all the connections from the inside of the fuselage. This limits the necessity for additional equipment to reach the connections.

8.7.3 Engine and landing gear reconfiguration operations

The same engines are used for all configurations, only the number of engines differs. The landing gear is placed underneath the wing and will retract inside the engine nacelle behind the engine.

In section 5.2, the engine was sized to be 3 m long. Furthermore, the landing gear is located at 0.6% of the local chord. Thus, starting with locating the landing gear of the ModuLR-100, the engine will

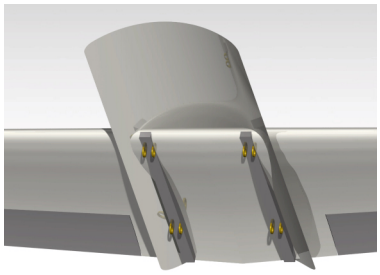

(a) ModuLR-100 wing and fuselage connection

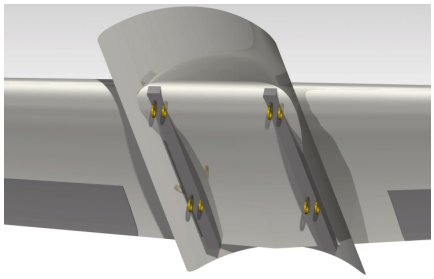

(b) ModuLR-200 wing and fuselage connection

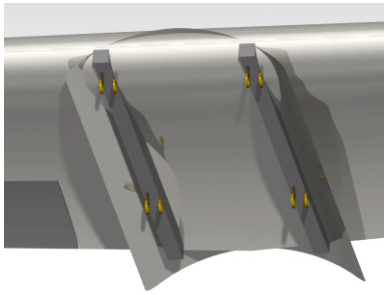

(c) ModuLR-300 wing and fuselage connection

Figure 8.14: Wing and fuselage connection for all ModuLR configurations

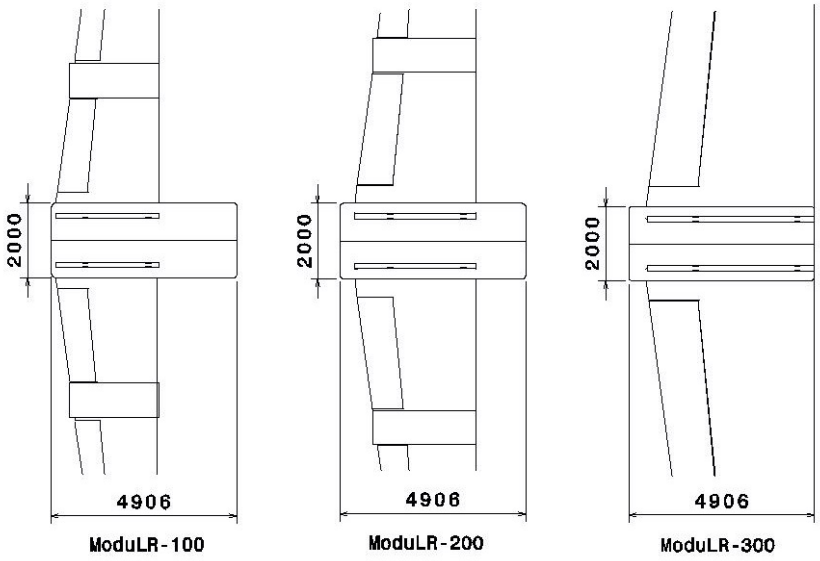

Figure 8.15: Wing fuselage connections of all wings

extent 1.75 m from the leading edge. To reduce the amount of different parts for each configuration, this is set as the standard for all configuration so that the engine mounts are universal on all wings.

The results of the three different configurations can be found in Fig. 8.16.

8.7.4 Total reconfiguration operations

As mentioned before, the reconfiguration operations will take place in a hangar of the service provider (section 8.5) and therefore overhead cranes are used.

The tail will have an attachment point located in the top of the vertical tail above the horizontal center of gravity to ensure horizontal transport of the tail section. When the crane is connected, the bolts can be loosened after which the tail can be lifted. For the attachment of the new tail, the reverse

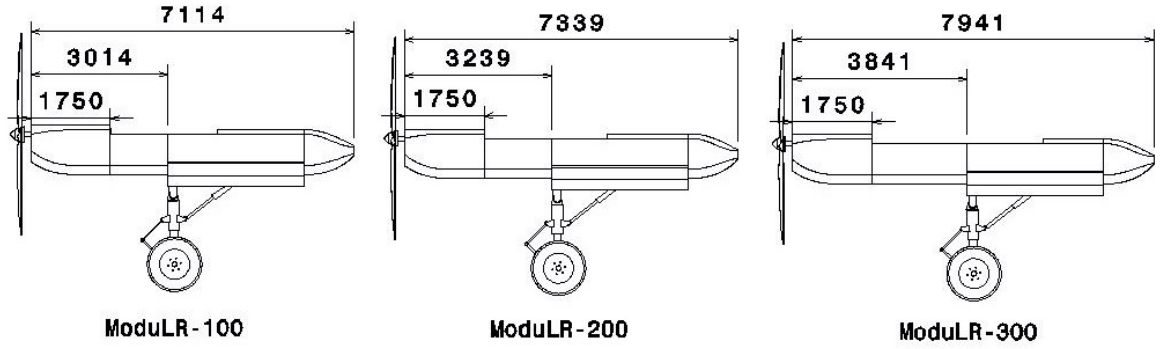

Figure 8.16: Engine nacelles for ModuLR-100, -200, and -300

procedure is used.

For the quickest operation, the wing including engines is lifted using a frame above the centre wingbox. Since this also includes the landing gear, the fuselage is temporarily supported at the end of the fuselage. After the decoupling of the wing and engines, the new wing with other engines is connected to the fuselage. It is possible to first detach the engines and landing gear if necessary, however it has some advantages not to do so. Firstly, the reconfiguration will take less time, reducing the aircraft's downtime. Secondly, parts that are not used can be maintained while the new parts are in operation so that the customer loses less time on maintenance. Lastly, the attachment and detachment of the engine and landing gear is not under time pressure. This results in a more evenly spread workload for the service provider and avoidance of peaks in the amount of workers. Avoiding a peak in the amount of workers reduces the number of people a company has to hire, both in costs and experience.

A typical reconfiguration described in this section is visualized in Fig. 8.17.

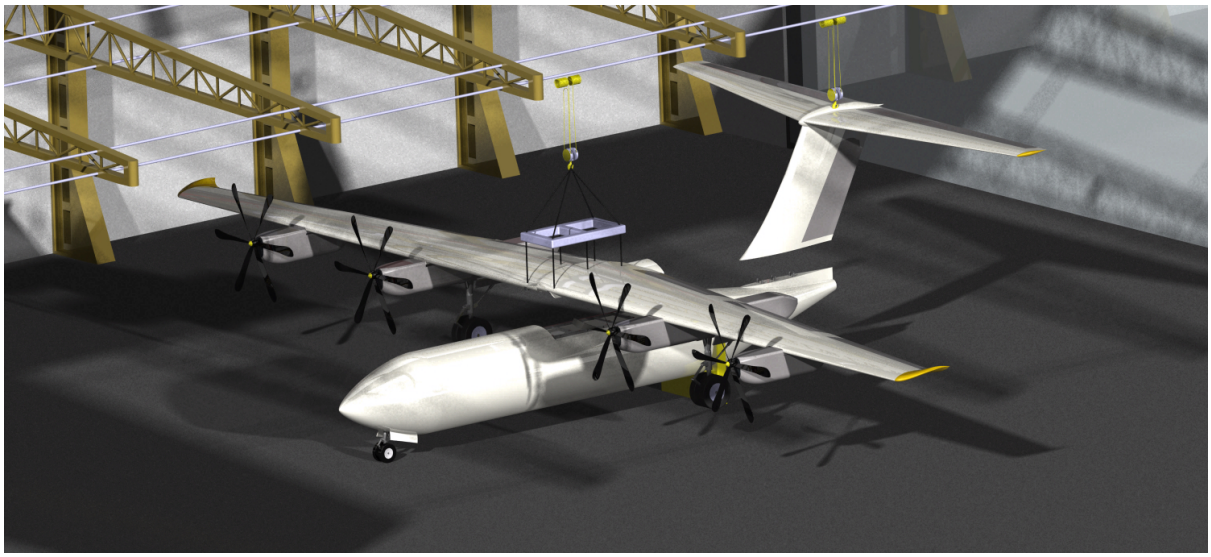

Figure 8.17: Reconfiguration of the ModuLR-300

8.8 Reliability, Availability, Maintainability, and Safety Characteristics

In this section the reliability, availability, maintainability and safety characteristics of the ModuLR project are presented.

8.8.1 Reliability, Availability and Maintainability

For an operator it is desirable that the aircraft has a high availability, or mission readiness, along with a high reliability for better predictability on future maintenance and number of available aircraft. Therefore requirements RUCA-T-OPS-MT-1 and 2 are stated to ensure the maintainability of the ModuLR.

Reliability should always be as high possible as it also relates to safety. Availability on the other hand has more of a financial influence and might be more difficult to predict in part due to reconfigurability being a relatively untested characteristic. Availability can be improved as wing and engine maintenance can be done separate from the aircraft, although this depends on the availability of spare parts. In addition, with the unmanned operations requiring a very software heavy design, both internal aircraft systems and external support system, can leave it susceptible to program bugs and instabilities. But then again it can still be better than many current aircraft who's design is based on several decades old system architectures which were later added to electronic maintenance management programs, rather than having been designed around it from the start.

Certain provisions can be made during design to improve the expected reliability and availability of the ModuLR. A focus can be on keeping the number of parts as low as possible, this reduces complexity both for maintenance tasks and parts to be keep track of. Analogue mechanisms or sensors can be switched out for newer electrical or digital components which interface better with diagnostics equipment, reducing troubleshooting time. Accessibility to line replaceable units should be kept in mind during further design, when possible for example use quick disconnect fittings.

A reliable electronic logistics management program will be developed which keeps track of the condition and location of all ModuLR aircraft including all associated parts. A post-flight report is uploaded to the system after each flight, automatically updating the number of flight hours and cycles allowing for easier scheduling of maintenance and replacement of parts. Keeps track of all past, current and future maintenance tasks.

As stated in section 8.5, hangar and base maintenance will be done by the ModuLR Group. This includes heavier maintenance, which although it happens at longer intervals, requires a higher amount of man-hours and longer times on the ground. It furthermore typically involves opening up the aircraft for scheduled inspections of internal components, inspecting for crack throughout the whole structure or micro cracks in susceptible areas, and replacement of harder to access components past their flight time/cycles.

Commonly, the operator devises a maintenance schedule which conforms both with aviation authorities and a Maintenance Planning Document (MPD) outlined by the manufacturer. Maintainability and availability are assumed to improve by having the same organization both defining and conduction the required maintenance. Allowing flexibility in the grouping of maintenance tasks has shown to improve availability in the case of the 737NG where airliners were allowed to determine the task composition of scheduled checks, rather than having to fully conform with the groupings given by a separate manufacturer in a Maintenance Planning Document. In this way they could optimize the checks with respect to their own organizational structure and availability of personnel and resources [104]. The maintenance program still has to be approved by the appropriate aviation authority.

Line maintenance, including inspections, servicing of fluids/lubricants or lighter maintenance like switching line replaceable units and system tests, which happen in a per flight, day or weekly basis will be done by the operators on site. Specialists on the unmanned and reconfigurable aspects will be stationed at airports where the ModuLR will operate.

8.8.2 Safety Characteristics

Along the chain of designing, manufacturing, testing, and using the ModuLR, safety should be of paramount importance. Because of this, safety is already discussed in several sections. This subsection however will globally present the safety characteristics of the ModuLR along all its phases.

Starting out with the design of the ModuLR, it can be seen as a double-edged sword with regard to safety. On one hand it is safer as there is no pilot on board. A ModuLR crash might damage or completely destroy cargo, however nobody on board will be killed, as the aircraft does not have any pilots or passengers aboard. On the other hand however, since the aircraft is remotely controlled it will be susceptible to hacking. Should the ModuLR get hacked, catastrophic consequences might occur as in the worst case the aircraft could be used as a guided bomb, potentially causing substantial harm. During the design phase, this has to be taken into account. Software has to be designed as resistant to hacking as possible. Extra software features might be implemented to keep the encryption software up to date.

During manufacturing of the aircraft, much attention has to be paid to safety as well. No manufacturing workers should be exposed to dangerous or toxic substances without protection. Manufacturing and assembly should also adhere to common industry-wide rules and laws. Specially assigned safety officers must make sure that these rules are being complied with. Should this not be the case, corrective measures must occur as safety is the number one priority. This also holds for the reconfiguration and maintenance operations.

During the testing phase, safety principles remain similar. Workers should not get injured and must adhere to the rules all the time. Furthermore aircraft testing should be done over non populated areas as much as possible to reduce the chance of lethal hazards.

During flight operations, several safety systems should safeguard the aircraft. Fire detection and suppression systems are to be installed in accordance with CS-25 and always provided power via the hot battery bus. Furthermore, all critical systems and functions shall be redundant. As stated in chapter 9 electrical power generation and distribution hardware is made redundant with critical systems having several power sources. Regarding the fuel system, fuel can be transferred in between tanks in case of boost pump failure. And for the hydraulic system, although consisting of two separated systems, can be connected in case of pump or engine failure on one side, still functioning with reduced actuating speed. The landing gear can be extended without hydraulic power by the use of gravity and over-center down-lock mechanisms. Additionally, the flight controls all have redundant power supply and control computers.

In case of signal loss with the OCC and/or ATC, the ModuLR will engage the appropriate flight termination/recovery mode detailed in subsection 8.4.4. In case the altitude can not be maintained, harm to people on the ground will be minimized by selecting an emergency landing zone with minimal population based on a stored database and navigational data.

8.9 Manufacturing, Assembly, and Integration Plan

This chapter will go into more detail on how the aircraft parts are manufactured, assembled, and integrated. Since the aircraft is reconfigurable, several different wings, tails, and engines have to be developed. To ensure an efficient use of reconfigurable parts, this plan integrates the production of the reconfigurable parts with the service model, which has been introduced in section 8.5.

To allow for an optimal production strategy, the aircraft parts are split up in several sections. In this way, the to-be-assembled parts can be produced in parallel, which increases the production efficiency. Divisions also enable an easier maintainability, better accessibility during production, and an easier breakdown for subcontractors [64]. The to be assembled parts will be created in batches by different subcontractors or, in a few cases, by the ModuLR design group.

The assembly process of the ModuLR is visualized in Fig. 8.18 and consists of one main assembly line and several subassembly lines. The main assembly line starts out with the assembly of the fuselage, after which several other parts from the sub assembly lines are added. Three of these subassembly lines are the lines to make the reconfigurable parts. Depending on the market and customer demands, independently of the main assembly line, reconfigurable parts as tails, wings and engines can be produced and transported to hubs to meet customer demands.

To make sure the assembly is performed as optimally as possible, assembly tasks are split up in several stations that do the same tasks every cycle. The cycle time for every station is the same, therefore the tasks will be of equal workload [64]. Another aspect of how the entire manufacturing process is optimized is by embracing the lean manufacturing principle. Using this principle waste is to be eliminated as much as possible while the process itself is knowledge driven and customer focused. Many methods and tools are used for this, including but not limited to:

- Production is customer focused and anticipated on the rapidly changing market requirements as can be seen in Fig. 8.18. An example of this is that the design of reconfigurable parts might change over time as market demands change;
- Waiting times are reduced by monitoring the workload and by equally balancing this for all stations on the production line. By using complex models, the usage of the reconfigurable parts by the customers is estimated as accurately as possible to minimize overproduction and the area required to store these parts at the reconfiguration hubs;
- The distance to possible subcontractors is seriously taken into account when choosing these subcontractors as transportation does not add value to the ModuLR and its reconfigurable parts;

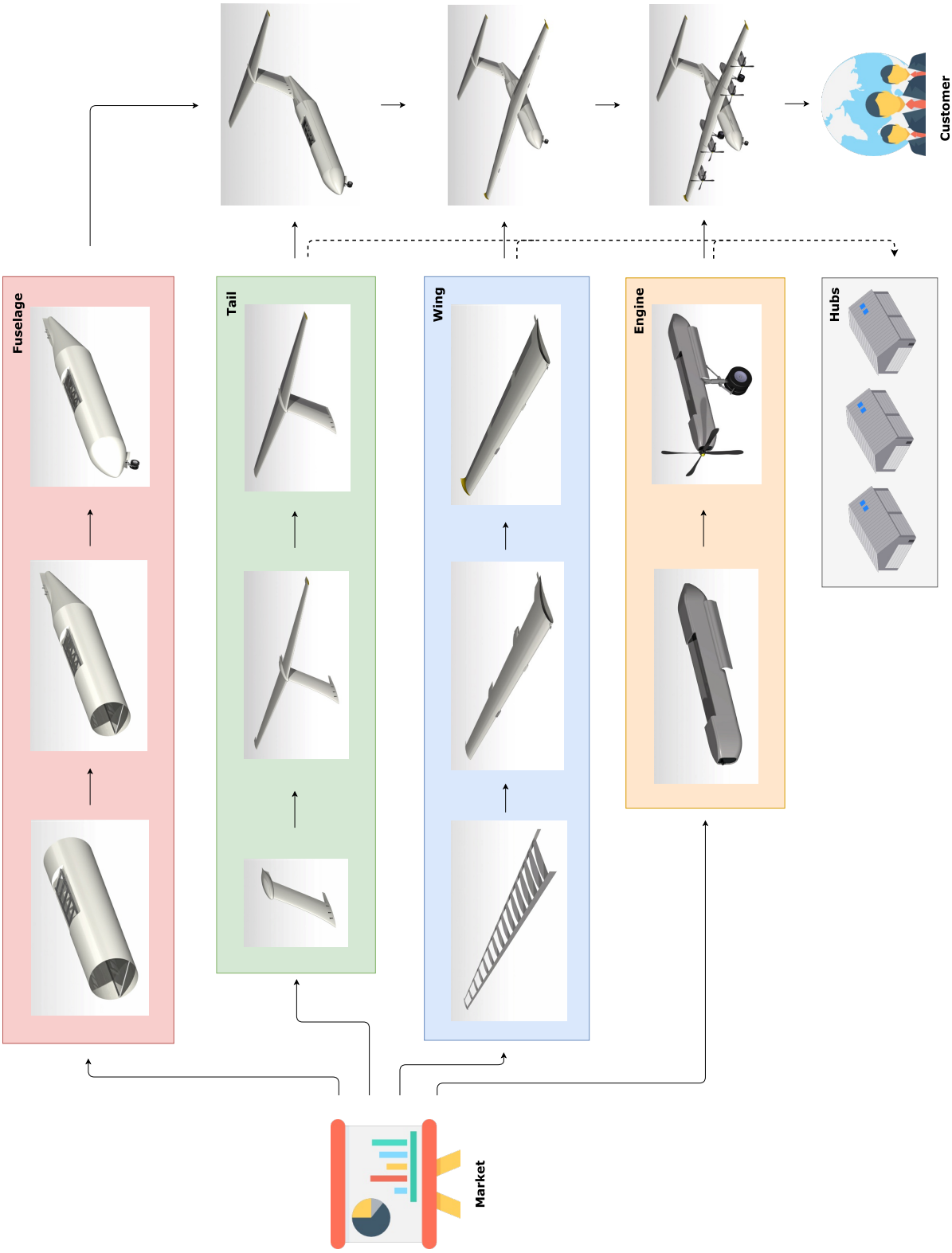

Figure 8.18: ModuLR assembly process

- For the aircraft parts, the Just-In-Time method (JIT) is applied. This way the parts required for assembly arrive exactly in time and no buffer is needed. This, however, is close to impossible to achieve, however substantial effort will be put into reducing the stocks and buffers required.

8.10 Sustainability

All operations have to be as sustainable as possible. Several methods like lean manufacturing, are already mentioned in this chapter that support sustainable operations. Moreover, the aircraft will use In-Trail Procedures, a part of ADS-B, to significantly save fuel. This technique enables reduced separations between aircraft. Since the aircraft is unmanned, more efficient route planning is also possible, as the aircraft will be able to plot optimal routes using live weather and traffic information.

For reconfiguration, an advanced model is used for production of reconfigurable parts. In this way overproduction and spillage of resources is prevented. In general offering bulk maintenance and reconfiguration will reduce resources needed, promoting overall sustainability. When hubs are established, they are placed as close to the customers as possible to reduce emissions. Should the ModuLR be sold to a great amount of extra customers, extra hubs can be opened, to reduce emissions further.

8.11 Conclusion and Recommendations

The architecture of a unmanned control system was proposed in subsection 8.4.3 that conceptually provides all higher order functions required for unmanned autonomous flight in unsegregated airspace, including enough flexibility to adapt to future regulations in accordance with requirement RUCA-C-LEG-5. Although it was discovered that aspects that would make such a system more autonomous that current UAV control systems, which are often functionally similar to the autopilots of manned aircraft, would rely on many technologies at various stages of development. Some distance from actual integration with commercial airspace. The closest innovation is within sensor fusion of several currently available traffic advisory and Sense and avoid functions to increase the situational awareness of remote operators, facilitating a slow gradual integration with national airspace through restricted operations. The feasibility of the proposed control system is heavily reliant on numerous advancements in the near future related to intelligent path optimization, decision making, fault detection, air traffic management and future aviation legislature.

For further research, the more promising projects within these fields of study can be identified to give an estimate on when such technology would be ready, at the very least on a prototype level. Specific technologies that augment situational awareness would be a starting point for further research, as these could provide more tangible results. Furthermore, innovations within air traffic control associated with SESAR can be investigated in further detail to determine exactly what kind of signal they provide and whether current hardware can utilize these correctly as control inputs. Additionally, research can also be done on the concept of adaptable flight control systems that are able to update control system parameters/gains on the fly to compensate for system faults or damage. This would be to compensate for the lack of feedback a pilot would usually feel being located in the aircraft.

For the reconfigurability of the ModuLR, it is important to reduce the number of different parts and connections. Therefore, a tail connector was designed such that the different tails are mounted in the same way to the fuselage. The benefits of this system will arise during the ground operations, training of the personnel, and reconfiguration operations. The chances on mistakes will be less preventing unnecessary damage or injuries under workers.

It is recommended for the further design to investigate the different universal connection options on operational effectiveness but also on structural forces and stresses. Furthermore, since the subsystems have to be connected through the tail - fuselage and wing - fuselage connection, also these connections should be further designed to find the best option for fast connection. These connection then should also be investigated on forces, stresses and vibrations.

Chapter 9

System Characteristics and Layout

This section provides a general description of the electric, hydraulic, fuel and environmental control subsystems of the ModuLR. Fig. 9.2 provides a simplified top view (not to scale) of the layout and connections between most of the components mentioned in this section.

9.1 Electrical System

Large scale aircraft require reliable power generation and distribution systems and can have several layers of redundancy depending on the size. Although the total amount of power handled by the electrical system depends on the aircraft type, most are made up of similar essential components required for alternating current (AC) and direct current (DC) power generation, distribution, regulation, indication, and safety. Additionally, it is assumed that the electrical characteristics of systems on the ModuLR are similar to what is used on most large aircraft: 115V 400Hz AC and 28V DC.

9.1.1 Requirements

Electrical system requirements are given in Certification Specification 25 [70], with some of the high order general requirements being as follows.

CS25.1351 General

(1)(b) Generating system. The generating system includes electrical power sources, main power buses, transmission cables, and associated control, regulation, and protective devices. It must be designed so that (1) Power sources function properly when independent and when connected in combination and (2) no failure or malfunction of any power source can create a hazard or impair the ability of remaining sources to supply essential loads;

(d) Operation without normal electrical power, [...] The services to be powered must include (i) Those required for immediate safety [...], without the need for flight crew action; (ii) Those required for continued controlled flight; and (iii) Those required for descent, approach and landing.

CS 25.1357 Circuit protective devices

(b) The protective and control devices in the generating system must be designed to de-energize [...] buses with sufficient rapidity to provide protection from hazardous over-voltage [...].

9.1.2 Power Generation

The general composition of the ModuLR electrical power system is shown in Fig. 9.1 and consists of the following main components.

AC Power generation

- Generators (GEN 1/2) which provide primary AC power are attached to the accessory drive gearbox of each main engine (inner mounted) via a constant speed drive (CSD). The generator provides a 115V, 3 phase AC regulated to a frequency of 400 Hz by the CSD. During engine startup, both main generators instead function as engine starter motors powered by the auxiliary power unit generator (APU GEN);
- The APU generator can provide power to both AC buses when the engines are not running, whether it being pre-start up or due to generator faults. Output is a 115V 400Hz AC;
- External Power (EXT PWR) is provided by a Ground Power Unit generating a 115V/200V 400Hz AC connected through the external power receptacle and monitored by an external power monitor. This is primarily used during maintenance;
- Emergency Generator (EMERG GEN) is less powerful and powered by a ram air turbine (RAT) which is extended in the case of AC BUS 1 and 2 failure. Power is provided to both AC and DC essential buses which power critical systems. Both emergency AC and DC transfer relays (EMERG AC/DC XFER RELAY) are controlled by a emergency power control unit;

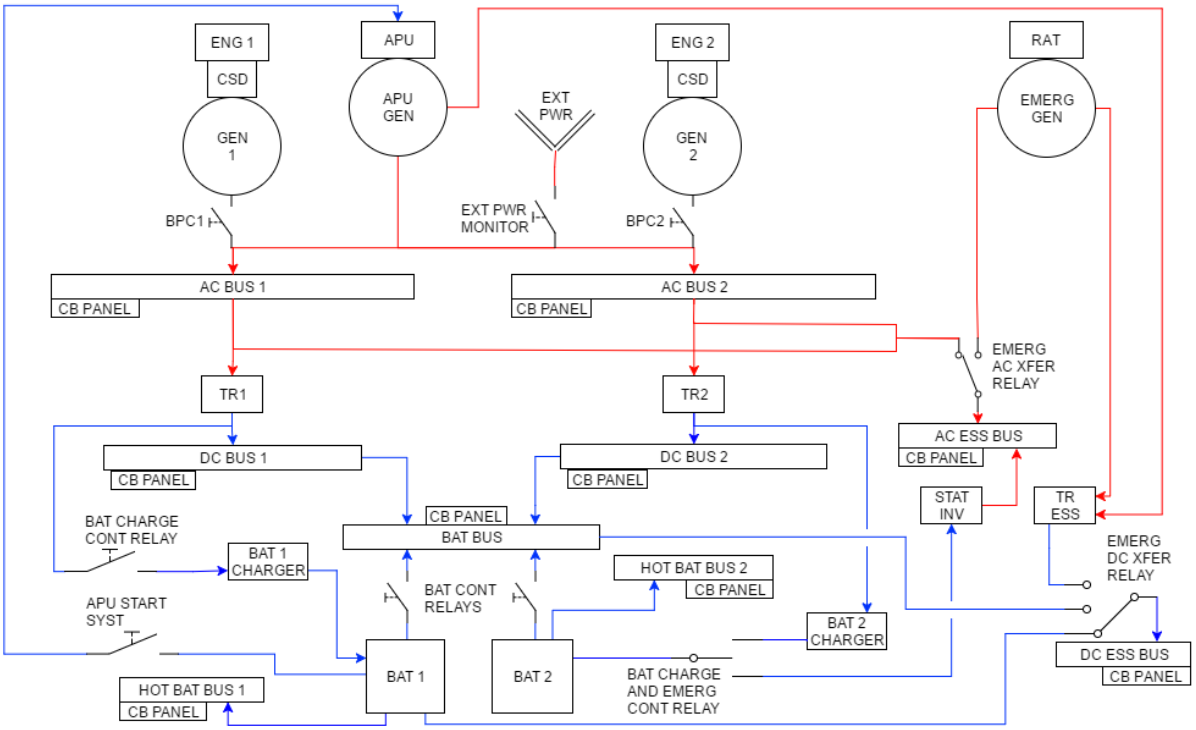

Figure 9.1: Simplified schematic of the electrical subsystem of the ModuLR. Red connections (in between generators and TR modules) transfer AC power while blue transfer DC power (remaining system).

- Static Inverter converts the DC output of battery 2 into a 115V 400Hz AC powering the AC essential bus in the case of AC bus 1 and 2 and emergency generator failures.

DC Power generation

- Transformer Rectifiers (TR 1/2) provide primary DC power by stepping down and rectifying the 115V AC to a 28V DC for the DC buses and battery chargers (BAT 1/2 Charger);
- Main batteries (BAT 1/2) provide 24 V DC for both ground and air start of the APU by powering the APU GEN which would then work as a starter motor. Additionally, the batteries provide backup power for the AC and DC essential buses with limited supply. Both batteries are continuously charged during normal operations. In the case of either primary AC power fault, the appropriate battery charge control relay will switch and battery control relay will close providing DC power to the battery bus;
- A Essential Transformer Rectifier (TR ESS) can power the DC essential bus with 28V DC from either the APU or RAT generators in the case of battery 2 and bus fault.

Power supply redundancy for essential and non-essential systems is assured by all distributing buses having several power sources. AC buses 1 and 2 are powered by either main generators or the APU GEN. DC buses 1 and 2 are powered by several generators via the AC buses and TR units. The Battery bus can be powered by either DC buses or batteries. And finally, both AC and DC essential buses have 4 and 3 power sources respectively.

9.1.3 Circuit Protection

Compliance with the requirements in subsection 9.1.1 will be through the use of various circuit control units (not shown directly in the block diagram), relays and circuit breakers.

9.1.4 Control Units

- The Generator Control Unit (GCU) regulates and monitors the output of both main generators. Regulation is done by the GCU adjusting a voltage produced by a permanent magnet section within the generator before it is fed back, dictating the amount of power generated by exciting

the main output section of the same generator. The GCU also monitors for under/over voltage and overcurrent, in which case it will shut the generator down and disconnect it form the AC BUS by tripping the relevant Bus Power Contactor (BPC 1/2), which is a powerful solenoid actuated relay. If under/over frequency is detected in the CSD, it will only tip the BPC until the frequency is within limits again. In both cases a caution is issued to the operators;

- Emergency Generator Control Unit regulated and monitors the output of both the APU generator and RAT Emergency Generator and controls the APU BPC and emergency AC and DC transfer relays (EMERG AC/DC XFER RELAY);
- External power monitor only tracks the power provided by a connected Ground Power Unit and controls its own disconnecting relay. It is automatically disconnected once either of the IDGs come online.

9.1.5 Circuit Breakers

- Circuit breaker panels (CB PANEL) will be located at each bus, which act as the interface between the electrical power generating subsystem and any other subsystem utilizing that power, protecting each connection from excess current caused by faulty regulation or a short circuit due to damage. Electrical flow to the vulnerable system is immediately discontinued. These can be reset by the appropriate control unit depending on the system, although it is advised a manual reset is required only after the cause is determined.

9.1.6 BUS System Distribution

Referring to the requirements in subsection 9.1.1, loss of normal electrical power is assumed to be a loss of power provided by main generators 1 and 2. If engine power is still available, services mentioned in the same regulations shall be made possible by assigning each flight critical system a minimum of two buses. AC and/or DC depending on the nature of the system. Switching to the next available source will happen automatically (with notification) when a fault is detected, although the operator will have the option of reverting said switch after having assessed the situation.

9.2 Hydraulic System

The hydraulic system is essential in most larger aircraft providing actuating power for flight control, landing gear extend/retract and miscellaneous other functions. A hydraulic systems commonly contain fluid storage, power supply, distribution, indication and actuation functions. Due to reconfigurability, ModuLR will use a combination of centralized and distributed systems as shown in Fig. 9.2. The centralized powered system is confined to the wing and associated removable fuselage segment, while distributed local systems will be used in the nose and tail sections. These only require electrical power and control connections.

9.2.1 Wing section

Due to reconfigurability it was desired for the wing to house its own conventional centralized system, dual redundant to assure actuating to power main flight controls. Major components follow the wing assembly by being located in compartments fore and aft of the main wingbox as shown in Fig. 9.2. Each system is made up of the following major components including associated piping:

- Pressurized reservoir for fluid storage. Functions include surge dampening from return line pressure spikes, storing fluid displaced by actuation and thermal expansion and the capture air that might have entered the system;
- Engine driven high pressure hydraulic pump mounted on the accessory drive gearbox of each engine. Variable delivery type pumps so as to keep the operating pressure constant irrespective of demand;
- Flight control accumulators for high demand compensation, pressure surge dampening and emergence actuation while the APU comes online to provide limited power via an electric motor driving the pump of one system;
- Ground servicing and test manifold providing connections for refill and pressurization during maintenance;
- Integrated servo actuators for aileron control containing all necessary function such as flight control system electrical interface, hydraulic system connections for both power and control fluid supply and a center-and-lock safety mode which improves continued control in case of failure;

- Main landing gear and compartment door extend/retract actuators along with break assemblies;
- Trailing edge flap actuating hydraulic rotary motor;

9.2.2 Nose and tail sections

These sections will utilize their own self-contained electro hydrostatic actuator (EHSA) systems. These packages contain all required functions with redundancy. The following functions will be assigned their own shared EHSA:

- Nose landing gear and compartment extend/retract and nose wheel steering;
- Elevator control and trim;
- Rudder control and trim.

9.3 Fuel subsystem

The primary functions of the fuel system are to store and provide sufficient fuel to all the engines at all times. The general layout of the fuel system of the ModuLR is shown in Fig. 9.2 consisting of separated Left and Right systems. Five integral tanks will be used for storage, connected by standpipes and transfer valves. The inner wing tanks will be drained first, then outer tanks and finally the center tank. Outer tanks are only drained second as to provide a longer lasting reduction of bending moment and dampening of flutter. Center of gravity control is not a function as all fuel is located close to it. Major components are as follows:

- Redundant electrically driven boost pumps for feed, sized for large configuration. Two are sufficient and left/right fuel systems can be unified by opening x-feed valve if required;
- Inner, outer wing tanks and Center tank all contain baffle plates, to reduce fuel sloshing, and capacitor based fuel probes indicating the amount of fuel mass left, rather than volume, as this is a better indication of remaining energy;
- The vent tank compensates for thermal expansion and manages the fuel tank pressurization provided by the environmental control system (ECS). Contains a tank pressure regulator to all wing tanks, overpressure vent and negative pressure relief valve. Facilitates fuel feed but also provides pressure transfer from outer tanks and inwards through transfer valves in case of inner wing tank pump failures;
- Refueling is done through the Ground Refuel Receptacle. Sequence is center, inner wing then outer wing tanks though the connecting standpipes. Both outer wing tanks contain float valves that automatically close the Ground Refuel Receptacle when full;
- Oil to fuel heat exchanger for cooling of hydraulic oil and fuel pre-heating for improved combustion.

9.4 Environmental Control System

The main functions of the Environmental Control System (ECS) is to provide for fuselage and fuel tank pressurization and cooling of electronic equipment which is necessary to meet requirement RUCA-T-NOM-CN-3. A simplified layout is shown in Fig. 9.2 with main components being:

- High and low stage compressor bleed air check valves and variable pressure regulator valve extract and regulate the input air to the ECS system from the compressors of the inner two engines;
- Bootstrap cooling assembly for better capacity and stability [105] over varied flight conditions, consisting of air cooling compressor/turbine setup and ram air-to-air heat exchangers supplying the cargo hold with temperature controlled pressurized air and avionic compartments with cooling air;
- Hot air control valve together with a temperature sensor sets the cooling air temperature by reintroducing an adjustable amount of hot air into the cooled air provided by the cooling assembly;
- Fuel system pressurization air is extracted after the first heat exchanger and lead to the vent tank;
- Hot air leak detection loops are installed along the hot air ducts from engines to cooling assembly as this air can reach temperatures up to 600 degrees [105];
- Ground service and test connectors allow for pressurization and cooling for example during fuel or prolonged avionic system testing.

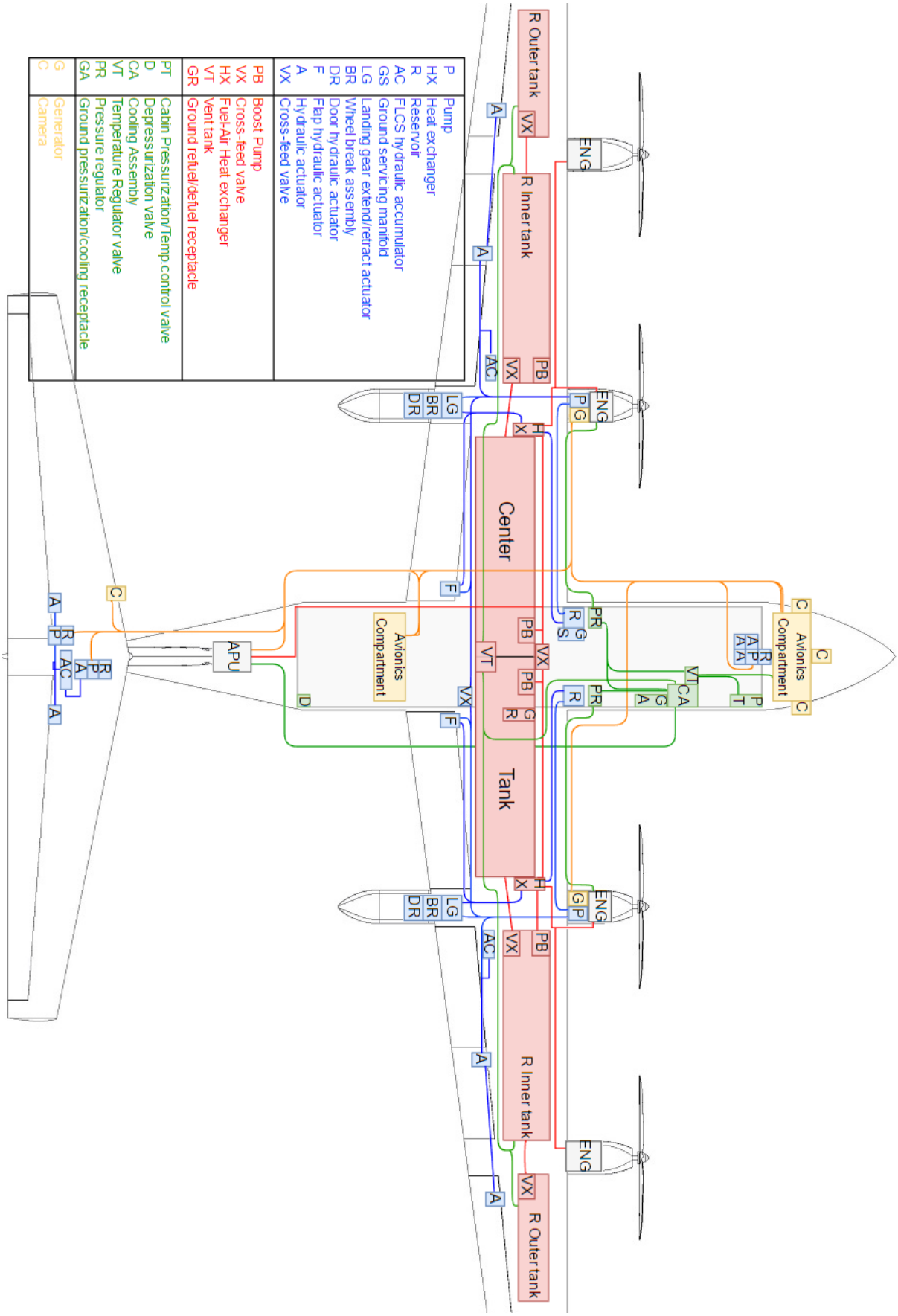

Figure 9.2: Simplified layout of hydraulic(blue), fuel(red), ECS(green) and electrical(yellow) sub-systems of the large configuration of the ModuLR. Systems are listed in the same sequence, from top till bottom, in the nomenclature table. Fuel tank and component block sizes are not to scale. Some routing is done outside of the fuselage for clarity. Only fuel, electrical and ECS connections are required between the fuselage and interchangeable main wing segment.

Chapter 10

Risk Assessment

This chapter provides an updated assessment on the technical risks involved with the detailed design, along with a rating on their probability and potential severity. Additionally, a plan mitigating the identified risks is included in section 10.2.

10.1 Risk Analysis

This section presents an overview of potential risks for the ModuLR. For the analysis of the risk, a table is generated with the identified risks and their corresponding severity and probability ratings, shown in Tab. 10.1. Each of these risks belongs to a certain design aspect. Risks 1 to 3 are related to structures, risks 4 to 7 relate to flight performance, risks 8 to 9 belong to aerodynamics, risk 10 to 17 apply to control and stability, risks 18 to 25 relate to operations and the remaining are general risks.

The severity is arranged from "1", negligible, up to "5", which represents a catastrophic event leading to a big performance degradation. Furthermore, the least likely case is rated as "1" and the most probable as "5". These numbers are explained in more detail in Tab. 10.2. All the risks are plotted in a risk map, Fig. 10.1, which shows on one hand the probability of occurrence and on the other, the consequence. The most critical risks are shown in the top right corner.

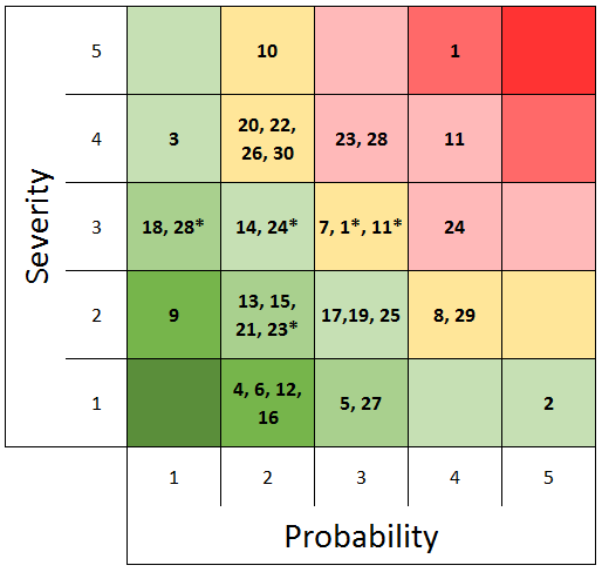

Figure 10.1: Technical risk map, including the risk after mitigation (*)

Table 10.1: Severity and probability for different risk cases

#	Case	Probability (1-5)	Severity (1-5)
1	The structure/wingbox is not designed for crack propagation	4	5
2	The vibrations of the engine match the system's natural frequency	1	5
3	The HLD are too large for having a proper wingbox	2	4
4	The engine is not as powerful as determined	2	1
5	The engine is not as fuel efficient as determined	3	1
6	Too much pressure drop in the flow	2	1
7	Noise is higher than expected	3	3
8	The tail generates too much drag	4	2
9	The landing gear pods increases the drag too much	1	2
10	Center of gravity is too much aft and will cause tipover	2	5
11	The connection for the different wings on the fuselage would have to shift too much along the longitudinal axis to achieve a stable aircraft	4	4
12	The onboard computer is unfamiliar with the phugoid eigenmotion	2	1
13	The onboard computer is unfamiliar with the aperiodic roll eigenmotion	2	2
14	The onboard computer is unfamiliar with the dutch roll eigenmotion	2	3
15	The onboard computer is unfamiliar with the spiral eigenmotion	2	2
16	The onboard computer is unfamiliar with the short period eigenmotion	2	1
17	The ailerons are too sensitive for cruise speeds	3	2
18	Too many customers will reconfigure their aircraft at the same time	2	4
19	Reconfiguration requires too many resources	3	2
20	Reconfiguration requires too specialized ground personnel	2	4
21	Regulations do not allow for fully autonomous take-off	2	3
22	Regulations do not allow for fully autonomous landing	2	4
23	The aircraft cannot fly at desired level of autonomy due to technical limitations	3	4
24	Maintenance is more expensive than expected	4	3
25	The aircraft requires more bandwidth than available	3	2
26	Production of aircraft impossible due to manufacturing constraints	2	4
27	Technological advancements progress slower than predicted	3	1
28	Theory of promising technology fails to deliver in practice	3	4
29	Manufacturing is not as sustainable as defined	4	2
30	Big design change have to be made due to unnoticed regulatory needs	2	4

Table 10.2: Explanation of the severity and probability ratings

Rate	Severity	Probability
1	Negligible	<10% occurrence
2	Minor performance degradation	10% - 36%
3	Moderate performance degradation	36% - 66%
4	Significant performance degradation, which may result in project failure	66% - 90%
5	Severe performance degradation, which results in project failure	>90% occurrence

10.2 Mitigation Plan

A mitigation plan is set up in this section for the highest-ranking risks, $severity \cdot probability$ of 12 or higher, located in the red area in the risk map in Fig. 10.1. Preventive measures and contingency plans are stated underneath for clarification. The following risks are mitigated starting with the most important one, risk 1 followed by risk 11, risk 23, risk 24, and risk 28. When sticking to these plans, the

risk map will change. The mitigation results can be seen by the numbers marked with a '*' in the risk map.

Risk 1: The structure/wingbox is not designed for crack propagation.

The structure/wingbox should be made out of (different) separated parts, so the crack could not propagate any further. Furthermore, a safety factor should be included to minimize the likelihood of occurrence.

Risk 11: The connection for the different wings on the fuselage shouldn't shift too much along the longitudinal axis to achieve a stable aircraft.

For each configuration, a scissor plot should be made and combined, making sure all different wings are approximately at the same location on the fuselage. Introducing movable loads in the cargo hold or having a tail, which is adjustable in position, could also provide a stable aircraft.

Risk 23: The aircraft cannot fly at the desired level of autonomy due to technical limitations.

The technical and legal challenges associated with autonomous flight should be investigated, listed, and analyzed in order to ensure the appropriate choice for the level of autonomous flight. The system should allow for a varying level of autonomous flight, such that it can be decided to switch to a lower or higher level of autonomy if necessary.

Risk 24: Maintenance is more expensive than expected.

The maintenance costs should be evaluated not only once, but continuously during the design process. This should be done using several methods to avoid outliers in costs and to reduce the probability of unexpected costs. The profitability should be evaluated including these risks to safely estimate the economic viability.

Risk 28: Theory of promising technology fails to deliver in practice.

No technologies should be used that have not been tested in practice yet. Technologies which have only been shown to be working in the laboratory should be avoided or investigated with great care to prevent big differences in expected and true performance. An alternative solution should be worked out and investigated, in parallel to promising high-risk technologies, such that the problem can be solved by using the alternative solution if needed.

Chapter 11

Financial Analysis

In this section, the ModuLR project is analyzed with respect to finances. This analysis starts out with the costs which are split into several cost subgroups for the ModuLR group and customer. In the subsequent sections, the revenues are calculated, a financial forecast is portrayed, and the break-even point is calculated.

11.1 Cost Analysis

In order to achieve a clear overview of the costs, they are split up into three subgroups: development costs, production costs, and operational costs. The latter is taken into account for both the customer and ModuLR Group, and is split up again into reconfiguration costs, flight operations costs and maintenance costs. An overview of the ModuLR Group cost breakdown can be found in Fig. 11.1.

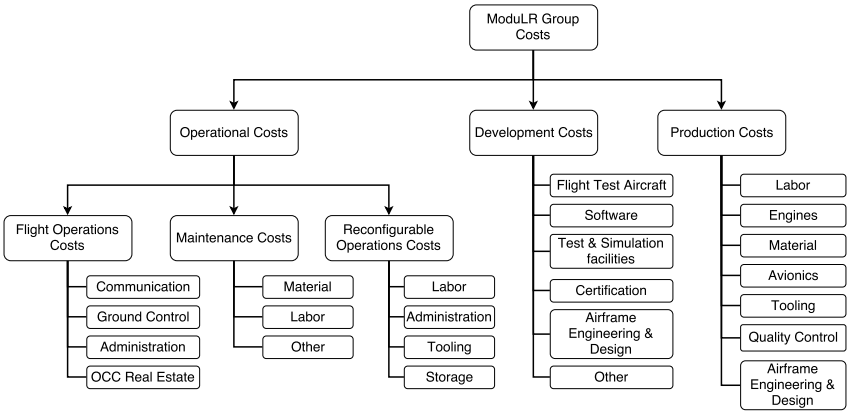

Figure 11.1: Cost breakdown structure

11.1.1 Development Costs

The development costs are calculated for both the baseline aircraft and all reconfigurable parts using Roskam [106]. The total development costs are estimated to be €1091M. An overview of the breakdown of the development costs can be found in Fig. 11.2a.

11.1.2 Production Costs

Using Roskam [106] the production costs are calculated for a batch of 180 aircraft that will be produced and sold during 10 years . It is assumed that for these 180 aircraft, each of the three configurations is equally used. Furthermore, to allow for reconfiguration, an extra 60 wings of each reconfiguration, 100 engines, 60 tails of the ModuLR-300 version, and 30 tails of the -200 and -100 variants are produced. However, when the customers are known, better predictions can be made resulting in a lower required inventory for the reconfigurable parts and hence a lower production costs. Fig. 11.2b gives an overview of the production costs components.

The total costs for the 180 aircraft, including the extra reconfigurational parts, is estimated to be €4.5B. The total production costs per aircraft are €25M. When looking at the baseline version and removing the costs for the extra reconfigurable parts, the costs are €17.3M. Since this is lower than the required €25M, the RUCA-C-ECO-1 requirement is met.

11.1.3 Operational Costs

The operational costs are split into two parts: the ModuLR Group operational costs and customer operational costs. The ModuLR Group acts not only as the aircraft developer, but also as the service

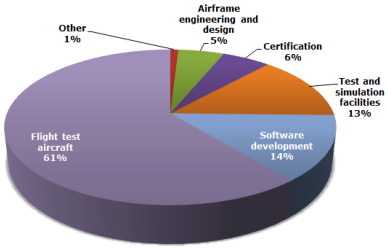

(a) Development costs

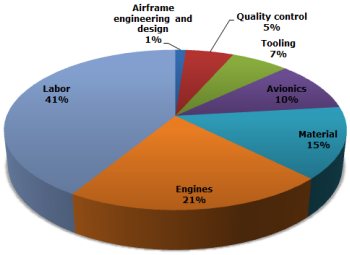

(b) Production costs

Figure 11.2: Development and production cost, respectively

provider. This has been further elaborated on in section 8.5.

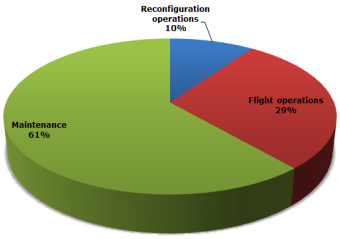

(a) ModuLR Group operational costs

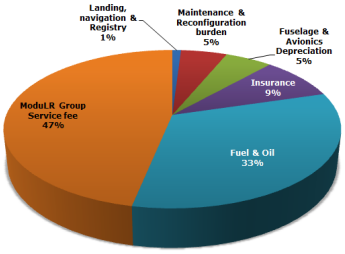

(b) Customer operational costs

Figure 11.3: Operational costs

ModuLR Group operational costs

In Fig. 11.3a, an overview is given for the ModuLR Group operational costs. These are split into three parts: operational costs for reconfiguration, flight operations costs, and maintenance costs. When all these costs are combined, the yearly operating cost per aircraft is estimated to be about €1.6M. In Fig. 11.4, these three cost parts are specified in more detail.

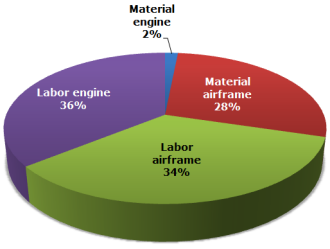

(a) Maintenance costs

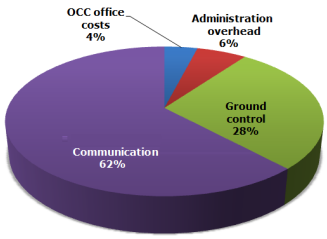

(b) Flight operations costs

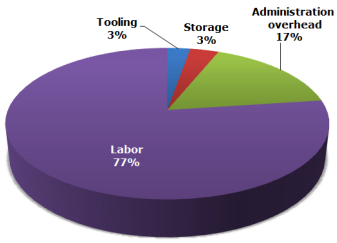

(c) Reconfigurable operations costs

Figure 11.4: Specifications operational costs ModuLR Group

Looking at the flight operations costs, displayed in Fig. 11.4b, the main contributor is communications. It is assumed that during the cruise, a minimum bitrate of 10 kilobytes per second is required and that the aircraft uses a satellite connection during half the operating time. Using the current price per MB for satellite internet connections [107], the communications costs can be calculated for this connection. Ground control costs have been estimated mainly using pilot costs. It is assumed that during cruise, each pilot can monitor 20 aircraft and during take-off, landing, and taxiing (TOLT) each pilot can handle only one aircraft. Combining these numbers with average pilot salaries, 1000 flight hours per pilot per year [108] and the average cruise hours and number of TOLT operations, the ground control costs are estimated.

The operations costs for reconfiguration contain all the costs needed to reconfigure the ModuLR. These include, but are not limited to, labor costs needed to remove and add configurable parts, hub storage costs to store the reconfigurable items, and hangar renting prices to accommodate these operations. It is assumed that on average, every ModuLR aircraft will be reconfigured once a month. Furthermore, the average aircraft maintenance technician wages, airport ground prices and hangar renting prices have been used to estimate the reconfigurable operations costs.

Customer operational costs

Despite the fact that the ModuLR Group takes care for several parts of operational costs, a large sum is still left for the customer. In Fig. 11.3b, the cost breakdown for customer operational costs is shown. The use of the ModuLR requires a yearly service fee to be paid to the ModuLR Group. This subscription fee covers the operational, reconfiguration and maintenance costs and also includes an extra margin to account for development and production costs. This service fee is the largest part of the customer operational costs and amounts €5M per year per aircraft. Another big part of the customer operational costs is of course the fuel and oil costs. Depreciation is only taken into account for the fuselage, avionics and landing gear since the rest of the aircraft consists of reconfigurable parts that are being rented. The maintenance costs have been included in the operational costs for the ModuLR group since they take care of this. When the total costs are normalized with respect to payload and range, the operational cost per ton-mile is \$0.57. This is 8% lower than the current cost per ton-mile for air cargo which is estimated to be \$0.618 [2] corrected for inflation. Making the system compatible with the market meeting requirement RUCA-C-ECO-2

11.2 Financial Forecast

To be able to make the ModuLR a better market compatible aircraft, the operational costs per ton mile should be equal or lower than the current market average costs per ton mile. To achieve this, the subscription service fee and one-time fixed parts price are optimized since they directly influence the customer operational costs as can be seen in Fig. 11.3b. Aside of the market compatibility, the ModuLR should also prove to be profitable with a break-even point (BEP) not too late.

It has been found that using a one-time fixed parts price of €20M and a service fee of €5M per year, the ModuLR is, in terms of operational costs, market compatible, as described in subsection 11.1.3. To have an estimation whether the ModuLR will be profitable (RUCA-C-ECO-3), a financial forecast is created using the estimated costs and prices. This forecast is illustrated in Fig. 11.5.

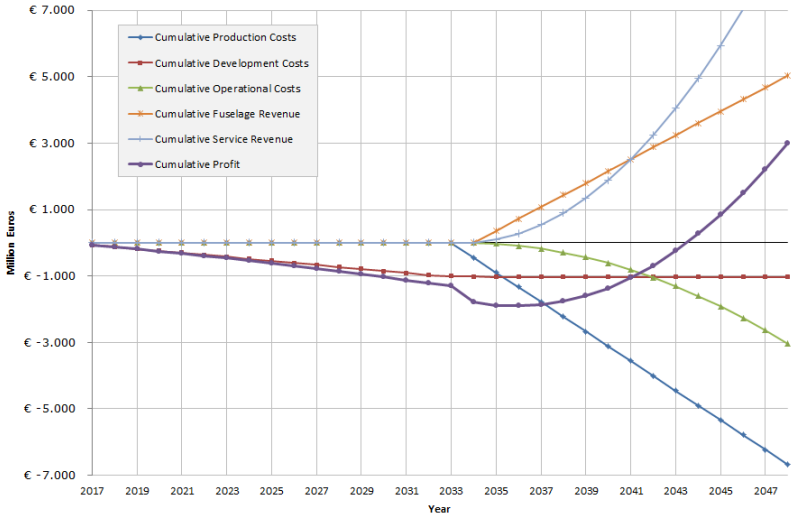

Figure 11.5: Financial forecast

From this figure it can be estimated that the ModuLR project will break-even around 2043. This will be 26 years after the development of the aircraft has begun. Depending on market demand, production rate might differ which will impact break-even time and return on investment. A proper price elasticity analysis will have to be done to find the optimum subscription service fee and fuselage & avionics price.

Chapter 12

Compliance

Throughout the design process, all subsystems and the final design need to adhere to the requirements. This chapter presents an overview of all the system and subsystem requirements used during the design process. The requirements can be found in Tab. 12.1, where the requirements are written down with their unique identifiers. In the section column, the sections of the report where the requirement is treated are described. In their corresponding sections an explanation is provided of how the requirement is met by the design, or when not met a reason is provided.

Table 12.1: Requirement compliance matrix

Identifier	**Requirement**	**Section**	**Compliance**
RUCA-T-REC	The system shall be reconfigurable	8.7	✓
RUCA-T-REC-AC-1	A reconfigured version of the system shall have a cargo volume of 10 m^3	4.2.2	✓
RUCA-T-REC-AC-2	A reconfigured version of the system shall have a cargo volume of 40 m^3	4.2.2	✓
RUCA-T-REC-AC-3	A reconfigured version of the system shall have a payload of 1000 kg	4.2.2	✓
RUCA-T-REC-AC-4	A reconfigured version of the system shall have a payload of 10000 kg	4.2.2	✓
RUCA-T-REC-AP-1	A reconfigured version of the system shall have a maximum runway length of 3000 ft	5.3	✓
RUCA-T-REC-AP-2	A reconfigured version of the system shall have a maximum runway length of 10000 ft	5.3	✓
RUCA-T-REC-AP-3	A reconfigured version of the system shall have a minimum range of 1000 nautical miles	5.3	✓
RUCA-T-REC-AP-4	A reconfigured version of the system shall have a minimum range of 4000 nautical miles	5.3	✓
RUCA-T-OPS-MT-1	The system shall be maintained as one aircraft type	8.5	✓
RUCA-T-OPS-MT-2	All critical components shall be accessible for maintenance	8.5	✓
RUCA-T-OPS-GH-1	The system shall have a loading time per unit volume at least equally fast as a Boeing 747-400 F	8.6.2	✓
RUCA-T-OPS-GH-2	Cargo shall be loaded with equipment currently available at airports	8.6.1	✓
RUCA-T-OPS-GH-3	Cargo shall be unloaded with equipment currently available at airports	8.6.1	✓
RUCA-T-OPS-GH-4	Cargo hold shall be accessible for customs	4.2.2	✓

Identifier	Requirement	Section	Compliance
RUCA-T-OPS-GH-5	The system shall be reconfigurable using typical available aviation equipment	8.7	✓
RUCA-T-OPS-GH-6	The system shall have a turn around time of less than 2 hours	8.6.2	✓
RUCA-T-OPS-GH-7	The system shall allow for refueling operations	8.6.2	✓
RUCA-T-OPS-CT-1	The system shall be directly controlled on the ground	8.4.2	✓
RUCA-T-OPS-CT-2	The system shall be autonomously controllable in air	6.4, 6.5, 8.4.3	✓
RUCA-T-OPS-CT-3	The system shall have a manual override	8.4.3	✓
RUCA-T-OPS-CT-4	The system shall be able to react to bad weather	6.5, 8.4.3	✓
RUCA-T-OPS-CT-5	The system shall be able to react to other air traffic	6.5, 8.4.3	✓
RUCA-T-OPS-CT-6	The system shall be able to land using existing landing system infrastructure	6.5, 8.4.2	✓
RUCA-T-OPS-CM-1	The system shall be allow the location of the cargo to be monitorable during all mission phases	8.4.3	✓
RUCA-T-OPS-CM-2	The system shall allow data communication	8.4.3	✓
RUCA-T-OPS-CM-3	The system shall allow the monitoring of flight performance	8.4.3	✓
RUCA-T-OPS-FO-1	The system shall be able to operate on continental routes	5.3	✓
RUCA-T-OPS-FO-2	The system shall be able to operate on intercontinental routes	5.3	✓
RUCA-T-OPS-FO-3	The system shall be able to operate during day time	8.4.2	✓
RUCA-T-OPS-FO-4	The system shall be able to operate during night time	8.4.2	✓
RUCA-T-NOM-CN-1	The baseline version of the system shall have a payload of min 5000 kg	5.3	✓
RUCA-T-NOM-CN-2	The baseline version of the system shall have a cargo volume of min 25 m^3	4.2.2	✓
RUCA-T-NOM-CN-3	The system shall include a climate controlled environment	9.4	✓
RUCA-T-NOM-PN-1	The baseline version of the system shall have a runway length of maximum 8000ft	5.3	✓

Identifier	Requirement	Section	Compliance
RUCA-T-NOM-PN-2	The baseline version of the system shall have a range of at least 2000 nautical miles	5.3	✓
RUCA-T-NOM-PN-3	The system shall have a fuel consumption per FTK which is 50% less than that of a Boeing 747-400F	5.3	X
RUCA-T-NOM-PN-4	The MTOW of the system shall be compliant with runway characteristics	5.3	✓
RUCA-T-NOM-RL-1	The system shall contain emergency systems	8.4.3	✓
RUCA-C-ECO-1	The production costs of the baseline version shall not exceed 25 million euro	11.1.2	✓
RUCA-C-ECO-2	The purchase price shall be compatible with the market	11.1.3	✓
RUCA-C-ECO-3	The system shall have a profitable return on investment	11.2	✓
RUCA-C-SDL-1	The system shall be operable by 2035	13	✓
RUCA-C-LEG-1	The system shall comply with ICAO aircraft approach category C	6.1	
RUCA-C-LEG-2	The system shall comply with ICAO chapter IV noise standards	5.3	X
RUCA-C-LEG-3	The system shall comply with EASA CS-25 certification standards	5.3	X
RUCA-C-LEG-4	The system shall adhere to air traffic control commands	6.5, 8.4.2	✓
RUCA-C-LEG-5	The system shall be adaptable to future regulatory changes with respect to autonomous flight	8.11	✓
RUCA-C-ENV-1	The 55dB SEL contour shall be 25% smaller than that of a Fokker 50	5.3	X
RUCA-C-ENV-2	The CO_2 emission per FTK shall be reduced by 50% compared to that of a Boeing 747-400F	5.3	X
RUCA-C-ENV-3	The NO_x emission per FTK shall be reduced by 50% compared to that of a Boeing 747-400F	5.3	X
RUCA-T-FPP-P-1	The power subsystem shall have a maximum power of 2745kW	5.3	✓
RUCA-T-ACS-W-1	The wings shall have a wing loading of 3931, 4511, 4587 $\frac{N}{m^2}$ for the ModuLR -100,-200, and -300 respectively	6.1	X
RUCA-T-ACS-W-2	The wings shall be able to provide 210, 327, and 633 kN of lift during nominal flight operation for the ModuLR -100, -200, and -300 respectively	6.1	✓
RUCA-T-ACS-W-3	The wings shall be reconfigurable	6.1	✓
RUCA-T-ACS-W-4	The wings shall be able to provide a lift coefficient of at least 1.2 in clean configuration	6.1	✓
RUCA-T-ACS-W-5	The wings shall have a stall speed of max 65, 70 and 70 m/s in clean configuration for the ModuLR -100, -200, -300 respectively	6.1	✓
RUCA-T-ACS-W-6	No transonic/supersonic speeds shall occur on any point of the wings during nominal flight	6.1	✓

Identifier	Requirement	Section	Compliance
RUCA-T-ACS-T-1	The system shall maintain directional trim in level flight with the landing gear and flaps retracted	6.4	✓
RUCA-T-ACS-T-2	The system shall maintain longitudinal trim in level flight with the landing gear and flaps retracted	6.4, 6.6	✓
RUCA-T-ACS-T-3	The system shall be controllable in one engine inoperative situation	6.4, 6.6	✓
RUCA-T-ACS-CS-1	The ModuLR-100 system variant shall be able to achieve a bank angle of 45° in 1.4s during all flight phases [60]	6.5	✓
RUCA-T-ACS-CS-2	The ModuLR-200 and -300 system variant shall be able to achieve a bank angle of 30° in 1.5s during all flight phases [60]	6.5	✓
RUCA-T-ACS-CS-3	All ModuLR system variants shall not exceed 30° control surface deflections [52]	6.5	✓
RUCA-T-ACS-CS-4	All ModuLR system variants shall be able to maintain longitudinal trim during cruise for flight speeds between at least V_S and V_C [52]	6.5	✓
RUCA-T-ACS-CS-5	All ModuLR systems shall be able to maintain a sideslip angle of 0° in a one engine inoperative situation, in the cruise and landing/take-off flight phases [52] [61]	6.5	✓
RUCA-T-ACS-CS-6	All ModuLR systems shall be directionally controllable in a one engine inoperative situation, at a minumum control speed not greater than ($V_{MC} = 1.13V_S$)[a]	6.5	✓
RUCA-T-ACS-CS-7	All actuator systems shall have a stroke length of existing actuators	6.5	✓
RUCA-T-ACS-CS-8	All actuator systems shall be operable within existing actuator force limits	6.5	✓

[a] https://www.law.cornell.edu/cfr/text/14/25.149, visited on June 14, 2017

Chapter 13

Project Design & Development Logic

The ModuLR is scheduled to be in production starting in 2035, according to the requirement RUCA-C-SDL-1. In this chapter, the procedures starting from the current point until the production phase will be described in the Project Design and Development logic (PD&D). The phases that will follow are the detailed design, development, and the post development phase [109].

At this stage, the detailed design phase of the ModuLR has started with the first design of subsystems described in this report. The next step will be a more thorough design of all subsystems and components and their interrelations. The design can be modeled such that Computational Fluid Dynamics (CFD) and Finite Element Method (FEM) can be performed. Also, scaled models of the design will be tested in, for example, wing tunnels. The final result will be a complete detailed design of the ModuLR.

The next step is called the development phase, in which the design will be produced and full scale testing for certification will take place. In this development phase, the manufacturing process will be assessed and improved if and where necessary. The testing shall start with ground tests, followed by the maiden flight. The maiden flight will be a milestone in the development process after which more intense flights tests will commence for the final certification. The ModuLR will undertake a high number of test flights, since it is an unmanned aircraft, and it consists of reconfigurable parts which have to be tested individually for the STCs, as described in section 8.2. The development phase will conclude with the complete certification of the ModuLR.

The post development phase includes the marketing and sales of the ModuLR. Also, training of personnel for ground handling, flight operations, reconfiguration operations, and maintenance will start. This phase will already start during the previously mentioned development phase. After certification, the production phase will start and therefore marketing, sales and training already have to be up and running. Also, since the development phase will cost €1.1B, as calculated in subsection 11.1.1, it is important to know if the aircraft is actually sold in sufficient numbers, in order to cover the final expenses.

In Fig. 13.1, the phases described above are visualized with blocks connected with arrows accordingly. Finally, in Fig. 13.2 the Gannt chart of the post-DSE is presented.

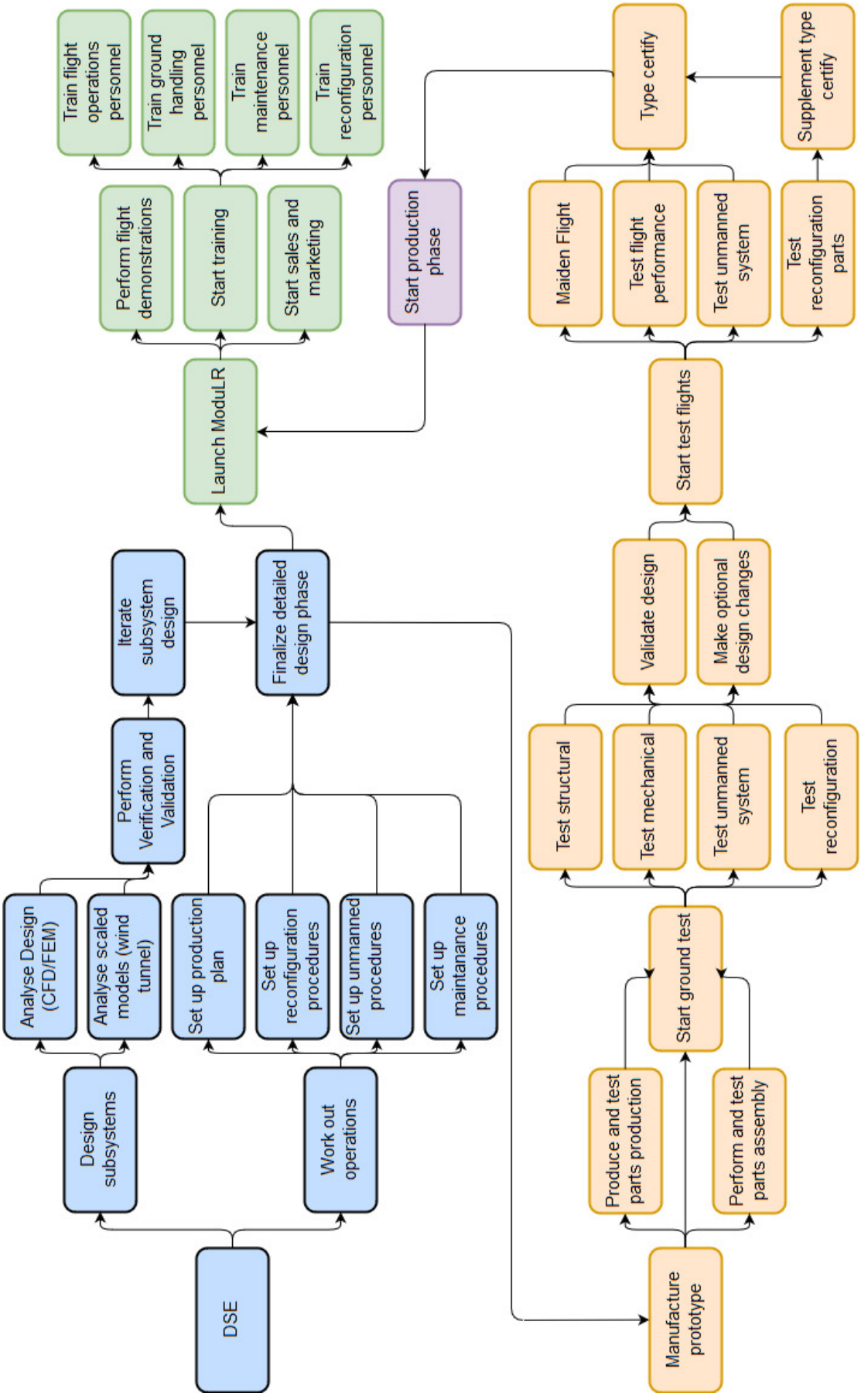

Figure 13.1: Project design & development logic

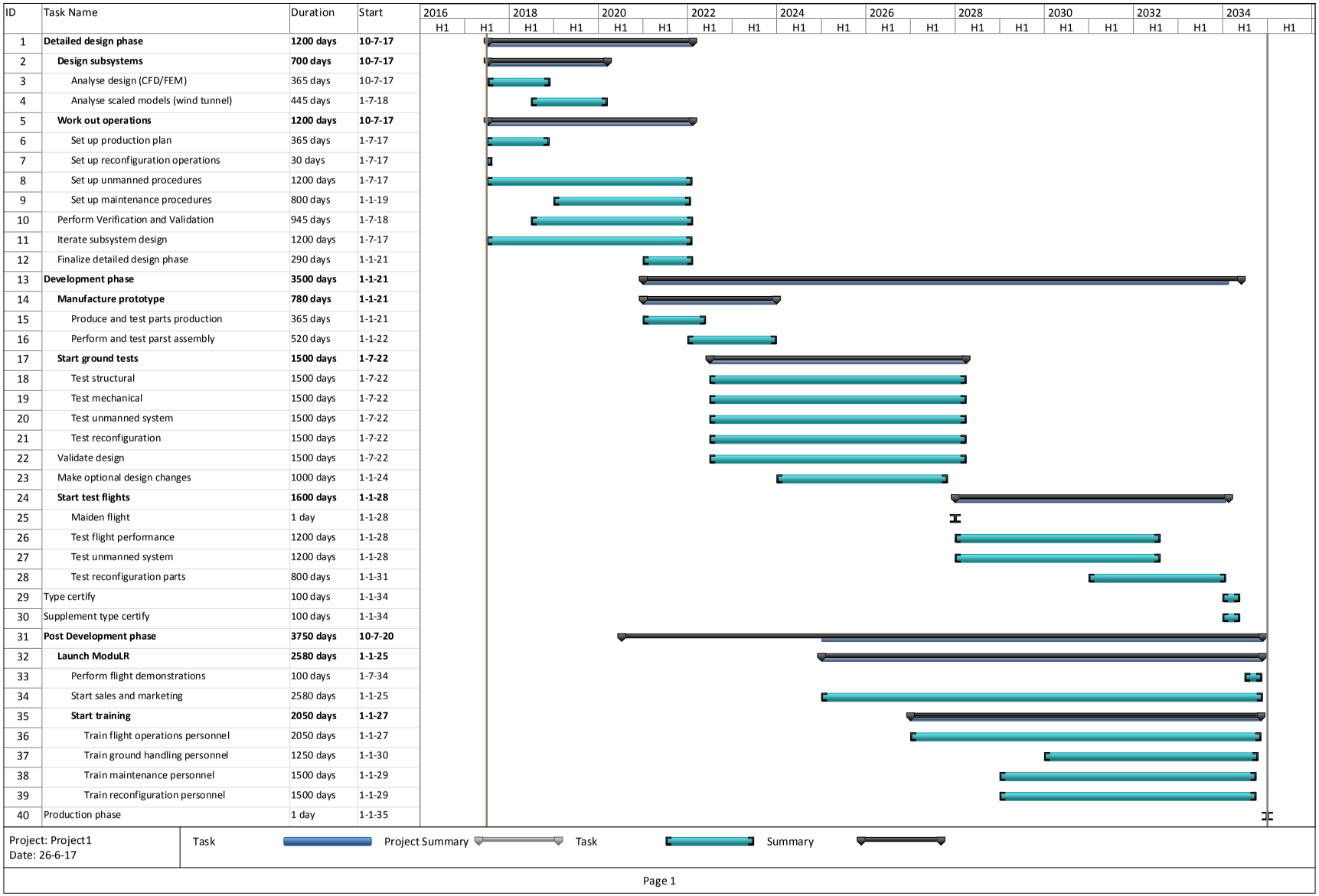

ID	Task Name	Duration	Start
1	**Detailed design phase**	**1200 days**	**10-7-17**
2	**Design subsystems**	**700 days**	**10-7-17**
3	Analyse design (CFD/FEM)	365 days	10-7-17
4	Analyse scaled models (wind tunnel)	445 days	1-7-18
5	**Work out operations**	**1200 days**	**10-7-17**
6	Set up production plan	365 days	1-7-17
7	Set up reconfiguration operations	30 days	1-7-17
8	Set up unmanned procedures	1200 days	1-7-17
9	Set up maintenance procedures	800 days	1-1-19
10	Perform Verification and Validation	945 days	1-7-18
11	Iterate subsystem design	1200 days	1-7-17
12	Finalize detailed design phase	290 days	1-1-21
13	**Development phase**	**3500 days**	**1-1-21**
14	**Manufacture prototype**	**780 days**	**1-1-21**
15	Produce and test parts production	365 days	1-1-21
16	Perform and test parst assembly	520 days	1-1-22
17	**Start ground tests**	**1500 days**	**1-7-22**
18	Test structural	1500 days	1-7-22
19	Test mechanical	1500 days	1-7-22
20	Test unmanned system	1500 days	1-7-22
21	Test reconfiguration	1500 days	1-7-22
22	Validate design	1500 days	1-7-22
23	Make optional design changes	1000 days	1-1-24
24	**Start test flights**	**1600 days**	**1-1-28**
25	Maiden flight	1 day	1-1-28
26	Test flight performance	1200 days	1-1-28
27	Test unmanned system	1200 days	1-1-28
28	Test reconfiguration parts	800 days	1-1-31
29	Type certify	100 days	1-1-34
30	Supplement type certify	100 days	1-1-34
31	**Post Development phase**	**3750 days**	**10-7-20**
32	**Launch ModuLR**	**2580 days**	**1-1-25**
33	Perform flight demonstrations	100 days	1-7-34
34	Start sales and marketing	2580 days	1-1-25
35	**Start training**	**2050 days**	**1-1-27**
36	Train flight operations personnel	2050 days	1-1-27
37	Train ground handling personnel	1250 days	1-1-30
38	Train maintenance personnel	1500 days	1-1-29
39	Train reconfiguration personnel	1500 days	1-1-29
40	Production phase	1 day	1-1-35

Figure 13.2: Post DSE Gannt chart

Chapter 14

Conclusion & Recommendations

The purpose of this report was to present, document, and justify the detailed choices and design of the ModuLR and its subsystems. The detailed design has to adhere to the key and driving (sub)system requirements. The overall conclusion is that with the current design, satisfying almost all requirements , a detailed design for innovating the air cargo market is established.

The following general design choices were best in order to comply with the requirements:

- The reconfigurable parts consist of the wing, tail, and engines;
- The fuselage and landing gear are designed for the -300 configuration;
- Turboprop engines are used.

The main conclusions from the detailed design are listed below:

- An engine providing a take-off power 2.6 MW was designed in order to comply with the take-off and emissions requirements. It is concluded that the take-off requirements of 3000, 8000, and 10000 ft respectively are met. The emissions requirement of <50% per metric tonne than the Boeing 747-400 freighter is met for the -300 version, but not for the -200 and -100 version. This is caused by the fuselage being not optimal for these versions;
- The noise requirement stated that the SEL contour has to be 25% smaller compared to the Fokker 50. It was concluded that this requirement is not met without a specially designed propeller. Therefore, the propeller was designed for low noise and high efficiency in order to comply with the noise requirement. The propeller consists of four blades with a 4.4 m diameter and has a cruise efficiency of 0.86;
- The wing was designed for the maximum L/D in the average cruise condition, in order to comply with the range requirements of 1000, 2000, and 4000 nm. With L/D values of 13.5, 15.9, 19.1, it is concluded that the range requirements are met for the -200 and -300 version. For the -100 version, requirement is not met yet. A reiteration has to be done using the new obtained Lift over Drag ratio to meet the requirement;
- The tails and control surfaces were successfully sized to ensure controllability and static and dynamic stability;
- The wingbox was designed for a maximum Von Mises stress of 503 MPa, belonging to the selected Al7178-T6 material. The skin thicknesses and stringer dimensions were selected for the lowest overall wing weight;
- It was concluded that a service model is the best way of introducing the aircraft to the market. Customers pay an annual subscription fee of €5MM per year and a €20MM purchase fee for the fuselage, avionics, and landing gear. For the annual fee, the customer can request twelve configurations per year. In this way, the break-even point is reached in 2043;
- The production cost of the baseline version (-200) are €18MM. With this the baseline cost requirement of €25MM is met;
- For reconfiguration operations, it is concluded that universal connections are best to use. These connections allow for easy mounting to the fuselage of the reconfiguration parts;
- It was concluded that an unmanned control architecture made up of four main parts, Mission, Vehicle, Communication and Safety Management blocks, is to be developed in order for the ModuLR to operate at four levels of autonomy. Fully and Semi-autonomous along with Teleoperated and Remote-controlled depending on the flight phase. The safety management module includes traffic management and sense and avoid provisions for future integration of the ModuLR into non-segregated airspace when further regulatory work is done.

Recommendations for further design were made. These are split up in general recommendations and detailed recommendations, belonging to specific subsystems. For both categories, the recommendations with the highest predicted impact are discussed here.

Automating the design process allows for quickly iterating the design in order to achieve the best performance. In future work, more iterations could be performed. These include both the iterations of the base code as well as iterations for the specific subsystem designs. A second general recommendation would be to build a scale model of the aircraft, and perform wind tunnel tests, in order to determine more accurate aerodynamic and control derivatives and coefficients. Furthermore, interviews with potential customers could be conducted in order to collect more recent and accurate market analysis data, gauging the feasibility of the aircraft. A more thorough study about the materials used on the ModuLR would also be required in further design. Some materials were selected but as materials are such a fundamental part of aircraft design, a more thorough material analysis is recommended. An opportunity that was briefly touched upon in the report is the transport of dangerous goods. This specific form of air cargo needs to be researched in more detail, both in an economical and technical level. A final general recommendation is to verify a greater amount of aircraft and parts with CS 25 requirements.

In the report, a wide variety of specific assumptions for the subsystem design were made. The most relevant ones to the reader are presented here. For performance, a more detailed noise analysis is required as the current analysis is mainly based on reference aircraft and engines instead of the new engine. With respect to the designed engine, the compressor and turbine could be designed in more detail. The available power during cruise could also be further optimized, according to the power needs in cruise. However, to not decrease the efficiency, a more thorough analysis of the pressure ratio during cruise is needed. A second recommendation concerning the engine is to set up a large engine database and update the selection of reference engines after each iteration. This is useful as, because of the iterative process, the power requirement of the engine changes. The propeller is currently designed for cruise conditions and could be designed for take-off more, in order to avoid high blade pitch angles.

Although the wing design has almost been completely analyzed, a full automation could be implemented. This would result in the selection of a new airfoil leading to a higher L/D during cruise. The code for this is already written, but was not included in its totality due to time and resource constraints. Even though the tails are already designed in detail, a thorough structural analysis is recommended for further work. This is especially relevant as the tails are detachable. The main structures part recommended to be designed in more detail is the fuselage, as this report focused on the reconfigurable wing structure. The main recommendations of the operations part of the report are to perform market research focused on the service model. In this way, it could be verified that customers want the product. A second recommendation for the operations part is to integrate the unmanned flying concepts in the design more in detail.

Overall, the design has been performed in great detail in the areas considered most relevant and critical in fulfilling the purpose of the mission. A good overview of what is to be done exists and is sincerely hoped to be performed.

Bibliography

[1] Group 20. DSE - Reconfigurable Unmanned Cargo Aircraft: Mid-Term Report, June 2017.

[2] Marcello Amato. Air cargo technology road map, 2013.

[3] Tom Crabtree, Tom Hoang, Russell Tom, and Gregg Gildemann. World air cargo forecast, 2016.

[4] Airfrance KLM. May 2017 traffic, June 2017.

[5] Jan Roskam. *Preliminary Configuration Design and Integration of the Propulsion System*. DARcorporation, 1985.

[6] Jan Roskam. *Airplane Design Part V: Component Weight Estimation*. DARcorporation, 1999.

[7] Ir. J.A. Melkert Ir. B.T.C. Zandbergen Dr. ir. R. Vos. Aerospace Design and Systems Engineering Elements I – AE1222-II: The Design of the Fuselage. Lecture Series, 2016. Accessed: 2017-06-11.

[8] Jan Roskam. *Airplane Design Part IV: Layout Design of Landing Gear and Systems*. DARcorporation, 1985.

[9] Australian Government: Civil Aviation Safety Authority. Aircraft electrical load analysis and power source capacity. *Advisory Circular*, March 2015.

[10] Ir. J.A. Melkert Ir. B.T.C. Zandbergen Dr. ir. R. Vos. Aerospace Design and Systems Engineering Elements I – AE1222-II: A/C Preliminary Sizing (class I weight estimation method). Lecture Series, 2016. Accessed: 2017-05-11.

[11] Dr. ir. M. Voskuijl. AE2230-I Flight and Orbital Mechanics Lecture hour 8, 9 - Take-off. Lecture Series, 2015. Accessed: 2017-06-23.

[12] Dr. ir. M. Voskuijl. AE2230-I Flight and Orbital Mechanics Lecture hour 10 - Landing. Lecture Series, 2015. Accessed: 2017-06-23.

[13] Ir. J.A. Melkert Ir. B.T.C. Zandbergen Dr. ir. R. Vos. Aerospace Design and Systems Engineering Elements I – AE1222-II: A/C Preliminary Sizing ($T/W - W/S$ diagram). Lecture Series, 2016. Accessed: 2017-05-11.

[14] S. Bartosch M. Schaefer. Overview on fuel flow correlation methods for the calculation of no_x, co and hc emissions and their implementation into aircraft performance software. Technical report, Deutsches Zentrum für Luft- und Raumfahrt (DLR), 2013.

[15] Aircraft Environmental Support Office. Gaseous emissions from aircraft engines a handbook for the calculation of emission indexes and gaseous emissions from aircraft engines. Technical report, Naval Aviation Depot - North Island - San Diego, California, 1990.

[16] ICAO. Emissions databank (06/2017). Excel Database, 2017. Accessed: 2017-06-22.

[17] H. Youngren M. Drela. Xrotor. Software, Mar 2011. Retrieved From:`http://web.mit.edu/drela/Public/web/xrotor/`.

[18] R. J. Francillon. *Lockheed Aircraft since 1913*. London:Putham, 1982.

[19] FAA. Inm user's guide. PDF, Apr 2007. Retrieved from: `https://www.faa.gov/about/office_org/headquarters_offices/apl/research/models/inm_model/inm7_0c/media/INM_7.0_User_Guide.pdf`.

[20] SAE Committee A-21. Procedure for the calculation of airplane noise in the vicinity of airports (stabilized aug 2012). Technical report, SAE International, Aug 2012.

[21] ICAO. *Environmental Protection. Annex 16 to the convention on International Civil Aviation.*, volume 1. ICAO, 6 edition, July 2011.

[22] Ir. J.A. Melkert. Propulsion and Power – AE2220-II: Real Brayton Cycle. Lecture Series, 2016. Accessed: 2017-06-14.

[23] Ir. J.A. Melkert Ir. Propulsion and Power – AE2220-II: Aero Engines. Lecture Series, 2016. Accessed: 2017-06-14.

[24] Ir. J.A. Melkert Ir. Propulsion and Power – AE2220-II: Exam June 2014. Old Exams, 2016. Accessed: 2017-06-14.

[25] Ir. J.A. Melkert Ir. Propulsion and Power – AE2220-II: Turbomachinery. Lecture Series, 2016. Accessed: 2017-06-14.

[26] n.a. Allison t56/model 501-d data sheet, 2017.

[27] K.D. McCutcheon. Aircraft engine history. Personal Note, n.a.

[28] M. Hepperle. Design of a propeller. Info Sheet, September 2008. Retrieved From: http://www.mh-aerotools.de/airfoils/jp_propeller_design.htm.
[29] D.W. Kurtz J.E. Marte. A review of aerodynamic noise from propellers, rofors, and liff fans. Technical report, NASA.
[30] H.H. Hubbard. Propeller-noise charts for transport airplanes. *N.A.C.A. TN 2968*.
[31] P. Kämpf. What are the advantages of more than 4 propeller blades? Forum, November 2015. Retrieved From: https://aviation.stackexchange.com/questions/23009/what-are-the-advantages-of-more-than-4-propeller-blades.
[32] F.E. Weick. *Aircraft Propeller Design*. McGraw-Hill Book Company, 1930.
[33] Rolls Royce. *The Jet Engine*. Rolls-Royce plc, 1986.
[34] ME Mechanical Team. Differences between centrifugal and axial flow compressors data sheet, 2016. Retrieved from: https://me-mechanicalengineering.com/differences-between-centrifugal-and-axial-flow-compressors/.
[35] Commercial Aviation Safety Team. Introduction to turboprop engine types. http://www.cast-safety.org/pdf/2_engine_types.pdf.
[36] P. Kämpf. Typical rpm values for aircraft turbines. Knowledge Blog, 2016. Accessed: 2017-06-13.
[37] Ir. J.A. Melkert. Propulsion and Power – AE2220-II: Combustion. Lecture Series, 2016. Accessed: 2017-06-14.
[38] R.E. Henderson W.S. Blazowski. *A REVIEW OF TURBOPROPULSION COMBUSTION Pt. II*. NTiS, 1976.
[39] J.D. Mattingly. *Aircraft Engine Design*. AIAA, 2002.
[40] n.a. Performance of Propellers. Thermodynamics Lecture Series, n.a. Accessed: 2017-06-24.
[41] n.a. Comparitive examples of noise levels, 2017.
[42] J.A.Melkert. n.a. Meeting, 2017. Accessed: 2017-06-16.
[43] Dr. A. Elham Ir. D. Steenhuizen. Aerospace design and systems engineering elements ii - ae2111-ii aircraft part - wing design. Lecture Series, 2016. Accessed: 2017-06-23.
[44] D. Scholz M. Nita. Estimating the oswald factor from basic geometrical parameters. 2008.
[45] NUKMAN YUSOFF PRASETYO EDI and AZNIJAR AHMAD YAZID. The design improvement of airfoil for flying wing uav. 2012.
[46] Purdue University. Xflr5 analysis of foils and wings operating at low reynolds numbers, May 2009.
[47] G.A. Crowell Sr. The descriptive geometry of nose cones. 1996.
[48] S.S. Chin. *Missile Configuration Design*. McGraw-Hill Book Company.
[49] P. Sforza. *Commercial Airplane Design Principles*. Butterworth-Heinemann, 2014.
[50] Egbert Torenbeek. *Synthesis of Subsonic Airplane Design*. Delft University Press, 1982.
[51] n.a. Autodesk Flow Design. Software Package, 2017 version. Accessed: 2017-06-12.
[52] Mohammad H. Sadraey. *Aircraft Design Systems Engineering Approach*. John Wiley Sons, Incorporated, 2012.
[53] Dr.ir. Gianfranco La Rocca. Ae3211-i systems engineering and aerospace design requirement analysis and design principles for a/c stability control (part 1). Lecture Series, 2017. Accessed: 2017-06-15.
[54] Dr.ir. Gianfranco La Rocca. Ae3211-i systems engineering and aerospace design requirement analysis and design principles for a/c stability control (part 2). Lecture Series, 2017. Accessed: 2017-06-15.
[55] I. Kroo. *Aircraft Design- Synthesis and Analysis, a digital textbook*. Stanford, 1997.
[56] W.Mutterperl S. Katzoff. The end-plate effect of a horizontal tail surface on a vertical tail surface. Technical report, National Advisory Committee for Aeronautics, February 1941.
[57] M. Drela. Xfoil. Software, Dec 2000. Retrieved from: http://web.mit.edu/drela/Public/web/xfoil/.
[58] Dr. A. Elham. Aerospace design and systems engineering elements ii ae2111-ii aircraft aerodynamic analysis - drag. Lecture Series, 2016. Accessed: 2017-06-09.
[59] A.Deperrois. Xflr5. Software, Nov 2003. Retrieved from: https://sourceforge.net/projects/xflr5/files/.
[60] Dr. A. Elham. Aerospace design and systems engineering elements ii ae2111-ii aircraft part: Aileron design. Lecture Series, 2016. Accessed: 2017-06-14.
[61] J.C. van der Vaart E. de Weerdt C.C. de Visser A.C. in 't Veld E. Mooij J.A. Mulder, W.H.J.J. van Staveren. *AE3202: Flight Dynamics Lecture Notes*. TU Delft, 2013.

[62] A.Deperrois. Xflr5 and stability analysis. PDF, Nov 2010.
[63] Jan Roskam. *Airplane Design Part VI: Preliminary calculation of aerodynamic, thrust and power characteristics*. DARcorporation, 2000.
[64] Jos Sinke. Production of aerospace systems. Reader.
[65] R.J.H. Wanhill N. Eswara Prasad. *Aerospace Materials and Material Technologies*. Springer, 2017.
[66] Chuan Huang. Damping applications of ferrofluids: A review. *Journal of Magnetics*, January 2017.
[67] European Aviation Safety Agency. Rulemaking directorate: Policy statement, airworthiness certification of unmanned aircraft systems (uas). PDF, August 2009. Retrieved from: `https://www.easa.europa.eu/system/files/dfu/E.Y013-01_%20UAS_%20Policy.pdf`.
[68] European Aviation Safety Agency. Technical opinion: Introduction of a regulatory framework for the operation of unmanned aircraft, December 2015.
[69] European Aviation Safety Agency. Airworthiness and environmental certification part-21. PDF, February 2016. Retrieved from: `https://www.easa.europa.eu/system/files/dfu/EasyAccess2Part-21_Feb_2016.pdf`.
[70] European Aviation Safety Agency. Certification specifications for large aeroplanes cs-25, September 2007.
[71] Civil Aeronautics Board. Civil air regulations: Part 18 - maintenance, repair, and alteration of airframes, powerplants, propellers, and appliances. As amended to July, 1956.
[72] Federal Aviation Administration. Cfr part 21 - subpart e - supplemental type certificates, October 1964.
[73] Airtel ATN. Cpdlc mandate, future communication and applications, world atm congress 2016. Presentation, March 2016. Accessed: 2017-06-13.
[74] Olivia Nunez David Bowen Steve Bradford Chip Meserole Didier Delibes Maria A. Di Pasquantonio David Batchelor Florian Guillermet, Edward L. Bolton Jr. Sesar programme 2020, towards global interoperability. Presentation, 2015. Accessed: 2017-06-13.
[75] Juliet Van Wagenen. Why boeing and airbus are pushing for ips. `http://www.aviationtoday.com/2016/06/20/why-boeing-and-airbus-are-pushing-for-ips/`, June 2016. Accessed: 2017-06-14.
[76] Satcom Direct. Jet connex, ultimate connectivity for business and private aviation. PDF, 2016. Retrieved from: https://www.satcomdirect.com/docs/brochures/jet%20connex.pdf.
[77] Inmarsat aviation. Inmarsat cwc update 2017. Slides, 2017. Retrieved from: `http://cwc.satcomdirect.com/wp-content/uploads/Inmarsat_CwC2017_FOR-DISTRIBUTION.pdf`.
[78] SITA. Aircom datalink vdl and atn services. PDF Data sheet. Retrieved from: `https://www.sita.aero/globalassets/docs/brochures/aircom-datalink-vdl-atn-services-data-sheet.pdf`.
[79] Adriana Mattos. Sita aircom service (vhf satellite). Slides, 2009. Retrieved from: `http://www.worldairops.com/FANS/docs/FANS_SITA_AIRCOM_Service.pdf`.
[80] Jun Kitaori. A performance comparison between vdl mode 2 and vhf acars by protocol simulator. *Digital Avionics Systems Conference, 2009. DASC '09. IEEE/AIAA 28th*, Oct 2009.
[81] Ulrich Epple Michael Schnell. Ldacs: future aeronautical communications for air-traffic management. *IEEE Communications Magazine (Volume: 52, Issue: 5, May 2014)*, May 2014.
[82] Fabrice Kunzi. *ADS-B benefits to general aviation and barriers to implementation*. PhD thesis, Massachusetts Institute of Technology, 2011.
[83] European Commission. Commission implementing regulation (eu) no 1207/2011 of 22 november 2011. PDF, 2011. Retrieved from `http://eur-lex.europa.eu/LexUriServ/LexUriServ.do?uri=OJ:L:2011:305:0035:0052:EN:PDF`.
[84] Federal Aviation Administration. Automatic dependent surveillance— broadcast (ads–b) out performance requirements to support air traffic control (atc) service; final rule. PDF, 2010. Retrieved from `https://www.gpo.gov/fdsys/pkg/FR-2010-05-28/pdf/2010-12645.pdf`.
[85] S.C. de Vries. Uavs and control delays. Technical report, TNO Defence, Security and Safety, 2005.
[86] NVIDIA. Nvidia video codec sdk application note - encoder - nvenc_da-06209-001. PDF, Apr 2017. Retrieved from `https://developer.nvidia.com/nvidia-video-codec-sdk#Download`.
[87] Nvidia. Nvidia video codec sdk application note - decoder. PDF, Feb 2017. Retrieved from `https://developer.nvidia.com/designworks/video_codec_sdk/downloads/v8.0`.
[88] A. Hamid Aghvami, Vasilis Friderikos, Magnus Frodigh Adnan Aijaz, Mischa Dohler. Realizing the tactile internet: Haptic communications over next generation 5g cellular networks. *IEEE Wireless Communications*, Oct 2016.

[89] Petar Popovski. Ultra-reliable communication in 5g wireless systems. *1st International Conference on 5G for Ubiquitous Connectivity (5GU)*, 2014.
[90] O3b Networks. What is network latency and why does it matter? White paper PDF. Retrieved from `http://www.o3bnetworks.com/wp-content/uploads/2015/02/white-paper_latency-matters.pdf`.
[91] National Institute of Standards and Technology. Autonomy levels for unmanned systems (alfus) framework volume i: Terminology. PDF, October 2008. Retrieved from: `https://www.nist.gov/sites/default/files/documents/el/isd/ks/NISTSP_1011-I-2-0.pdf`.
[92] Triona Keaveney and Ewa Magnowska. Sesar solutions catalogue. pdf, 2017. Retrieved from: `https://www.sesarju.eu/sites/default/files/solutions/SESAR_Solutions_Catalogue.pdf`.
[93] Kathleen O'Brien William R. Richards and Dean C. Miller. New air traffic surveillance technology, boeing. PDF, 2010. Retrieved from: `http://www.boeing.com/commercial/aeromagazine/articles/qtr_02_10/pdfs/AERO_Q2-10_article02.pdf`.
[94] Federal Aviation Authority. Data communications implementation team tower data link services controller pilot data link communication departure clearance service (cpdlc-dcl) flight deck user guide. pdf, March 2016. Retrieved from: `https://www.faa.gov/about/office_org/headquarters_offices/avs/offices/afs/afs400/afs470/datacomm/media/DCL_FDUG.pdf`.
[95] Ravi Prasanth Jovan D. Boskovic and Raman K. Mehra. A multi-layer control architecture for unmanned aerial vehicles. Technical report, Scientific Systems Company, Inc., Woburn Massachusetts, 2002. Retrieved from: `https://www.researchgate.net/publication/3961048_A_Multi-Layer_control_architecture_for_unmanned_aerial_vehicles`.
[96] Edwin K. P. Chong Christopher M. Eaton and Anthony A. Maciejewski. Multiple-scenario unmanned aerial system control: A systems engineering approach and review of existing control methods. *Aerospace*, Vol. 3, January 2016.
[97] Federal Aviation Authority. Advisory circular, pilots' role in collision avoidance. pdf, April 2016. Retrieved from: `https://www.faa.gov/documentLibrary/media/Advisory_Circular/AC_90-48D.pdf`.
[98] Exelis Inc. Airborne sense avoid radar, skysense-2020htm: Advanced active array 3d radar to enable nas integration. pdf, 2013. Retrieved from: `https://d2cy52pj4xpl74.cloudfront.net/file/502ca1c8-267c-48e8-a770-e085a4083154/58cd8663-b325-4afe-9579-f60e2a93fb89/58cd8663-b325-4afe-9579-f60e2a93fb89.pdf?version=1`.
[99] curtiss Wright. Network centric flight control computer. pdf, 2012. Retrieved from: `https://www.curtisswrightds.com/products/electronic-systems/program-specific-systems/flight-control-computer.html`.
[100] Ravi Prasanth Jovan D. Boskovic and Raman K. Mehra. Mixed integer/lmi programs for low-level path planning. Technical report, Scientific Systems Company, Inc., Woburn Massachusetts, 2015. Retrieved from: `https://www.researchgate.net/publication/3961630_Mixed_integerLMI_programs_for_low-level_path_planning`.
[101] Rexroth Bosch Group. Ball transfer units, year =.
[102] Boeing Authors. *747-8 Airplane Characteristics for Airport Planning*. The Boeing Company, December 2012.
[103] Exxon Mobil Corporation Authors. Exxonmobil jet fuel product data sheet, 2017.
[104] AIRCRAFT COMMERCE. Analysing the 737ng's first base check. article, 2006. Retrieved from: `http://www.aircraft-commerce.com/sample_articles/sample_articles/maintenance_engineering_2_sample.pdf`.
[105] 1.Lt. Bjornar Hoelstad. F-16 environmental control system (ecs), student coursebook. Technical Training Package Reader, 2008. Accessed: 2017-06-09.
[106] Jan Roskam. *Airplane Design Part VIII: Airplane Cost Estimation: Design, Development, Manufacturing and Operating*. DARcorporation, 1997.
[107] AirSatOne. Swiftbroadband features price guide. Retrieved from `https://www.airsatone.com/static-documents/price-guides/inmarsat/AirSatOne_SwiftBroadband_Aircraft_Satcom_Price_Guide_2017_1.24.2017.pdf` on June 20, 2017.
[108] Legal Information Institute. 14 cfr 121.481 - flight time limitations: One or two pilot crews. Retrieved from `https://www.law.cornell.edu/cfr/text/14/121.481` on June 19, 2017.
[109] U.P. Breuer. Commercial aircraft composite technology, 2016. DOI 10.1007/978-3-319-31918-6_2.

Appendix A

Input Variables

Table A.1: Structures input variables

Variable Symbol	Unit	Values		
		ModuLR-100	ModuLR-200	ModuLR-300
$Numberofengines$	[-]	2	2	40
$Ultimateloadingfactor$	[-]	3.03	3.03	3.03
$MTOW$	[kg]	21441	33376	64517
$Wingweight$	[kg]	3240	5800	13229
$Fuelweight$	[kg]	2776	6631	20082
$Fuselageweight$	[kg]	2339	2339	2339
$Payload$	[kg]	1200	6000	12000
$Landinggearweight$	[kg]	2972	2972	2972
$Wingspan$	[m]	25	30	41
$Engineweight$	[kg]	1710	1710	3420
$Cruisedensity$	$[\frac{kg}{m^3}]$	0.6239	0.6597	0.6597
$Cruisevelocity$	$[\frac{m}{s}]$	150	160	155
L/D	[-]	17.3	18.3	19.8
$Fuselagediameter$	[m]	2.9	2.9	2.9
$Tipchord$	[m]	1.14	1.32	1.83
$Rootchord$	[m]	2.84	3.31	4.56
t/c	[-]	0.15	0.12	0.12

Table A.2: Financial analysis input variables

Variable Symbol	Unit	Values		
		ModuLR-100	ModuLR-200	ModuLR-300
Flights per year	[-]	1100	800	400
Pilot salary per year	[€]	87571	87571	87571
Extra reconfigurable wings for 180 A/C	[-]	60	60	60
Extra reconfigurable tails for 180 A/C	[-]	0	60	30
Extra reconfigurable engines for 180 A/C	[-]	0	0	120
MTOW	[kg]	21441	33376	64517
manufacturing labor rate	[$ per hour]	136	136	136
tooling labor rate	[$ per hour]	163	163	163
Number of flight test aircraft	[-]	-	3	-
Fuselage cost fraction	[-]	28	28	28
Wing cost fraction	[-]	27	27	27
Empennage cost fraction	[-]	10	10	10

Table A.3: Performance and propulsion input variables

Variable Symbol	Unit	Values		
		ModuLR-100	**ModuLR-200**	**ModuLR-300**
A	[-]	12	12	12
$\frac{C_{L_{cruise}}}{C_{D_{cruise}}}$	[-]	13.5	15.9	19.1
$C_{L,ground}$	[-]	1.265	0.935	0.605
$C_{L,max,TO}$	[-]	2.1	2.1	1.8
$C_{L,max,TO,roll}$	[-]	1.7	1.7	1.4
$C_{L,max,L}$	[-]	2.3	1.7	1.1
$C_{D0,TO}$	[-]	0.0436	0.0411	0.0380
$C_{D0,L}$	[-]	0.025581	0.019852	0.017855
$C_{D,TO}$	[-]	0.332333	0.201854	0.11856
c_p	$[kg/J]$	$6.81{\cdot}10^{-8}$	$6.81{\cdot}10^{-8}$	$6.81{\cdot}10^{-8}$
e_{TO}	[-]	0.75	0.75	0.75
e_L	[-]	0.85	0.85	0.85
EI_{CO_2}	$[kg/kg]$	3.144437	3.144437	3.144437
η_{prop}	[-]	0.86	0.86	0.86
$\eta_{TO,roll}$	[-]	0.7	0.7	0.7
γ	$[deg]$	3	3	3
g_0	$[m/s^2]$	9.8067	9.8067	9.8067
h_{cruise}	$[m]$	6500	6000	6000
h_{scr}	$[ft]$	50	50	50
μ_{TO}	[-]	0.05	0.05	0.05
μ_L	[-]	0.5	0.5	0.5
$MTOM$	$[kg]$	21441	33376	64517
M_{cruise}	[-]	0.5	0.5	0.5
m_{fres}	[-]	0.1	0.1	0.1
m_{fuel}	$[kg]$	2776	7631	20082
m_{OE}	$[kg]$	17358	20578	32112
m_{PL}	$[kg]$	1200	5000	12000
N_{engine}	[-]	2	2	4
ω_{fuel}	$[kg/s]$	0.195854	0.195854	0.195854
P_a	[W]	5289910	4377100	8444765
ρ_{fuel}	$[kg/m^3]$	804	804	804
ρ_{TO}	$[kg/m^3]$	1.225	1.225	1.225
S	$[m^2]$	53.5	72.6	137.9
T_{rev}^{-}	$[N]$	30000	0	0
$V_{fueltank}$	$[m^3]$	1200	5000	12000
$\frac{W_2}{W_s}$ (engine start-up)	[-]	0.992	0.992	0.992
$\frac{W_3}{W_2}$ (taxi)	[-]	0.996	0.996	0.996
$\frac{W_4}{W_3}$ (take-off)	[-]	0.996	0.996	0.996
$\frac{W_5}{W_4}$ (climb)	[-]	0.990	0.990	0.990
$\frac{W_7}{W_6}$ (descent)	[-]	0.992	0.992	0.992
$\frac{W_e}{W_7}$ (landing, taxi, shutdown)	[-]	0.992	0.992	0.992

Table A.4: Aerodynamics, stability & control input variables

Variable Symbol	Unit	Values		
		ModuLR-100	ModuLR-200	ModuLR-300
A	[-]	12	12	12
$\rho_{landing}$	$[\frac{kg}{m^3}]$	1.225	1.225	1.225
ρ_{cruise}	$[\frac{kg}{m^3}]$	0.6239	0.6597	0.6597
S	$[m^2]$	53.5	72.6	137.9
S_h	$[m^2]$	17.82	27.66	47.58
S_V	$[m^2]$	8.07	9.48	47.18
V_{app}	$[m/s]$	72.8	72.8	72.8
b_w	$[m]$	25.34	29.52	40.68
$C_{L_{\alpha_W}}$	$[rad^-1]$	5.85	6.05	6.08
C_r	$[m]$	2.84	3.31	4.56
λ	$[-]$	0.4	0.4	0.4
I_{xx}	$[kgm^2]$	275278	620916	3006270
$T_{takeoff}$	$[N]$	82497	70923	113755
l_V	$[m]$	10.4	11.0	12.1
$C_{L_{\alpha_V}}$	$[rad^-1]$	2.04	2.04	2.04
$C_{l_{\alpha_h}}$	$[rad^-1]$	6.51	6.51	6.51
$C_{L_{\alpha_h}}$	$[rad^-1]$	5.17	5.17	5.17
S_{net}	$[m^2]$	0.9S	0.9S	0.9S
b_f	$[m]$	2.9	2.9	2.9
h_f	$[m]$	2.9	2.9	2.9
l_f	$[m]$	21.8	21.8	21.8
l_h	$[m]$	11.37	12.10	13.53
l_v	$[m]$	10.35	11.01	12.01
$\bar{c}$	$[m]$	2.11	2.46	3.39
$\bar{x_{ac}}$	[%]	0.25	0.25	0.25
$\bar{x_{cg}}$	[%]	0.43	0.45	0.4
C_{m_α}	$[rad^-1]$	-0.00045	-0.00039	-0.00029
C_{L_h}	[-]	0.053	0.051	0.047
$C_{m0_{wf}}$	[-]	-0.03	-0.03	-0.03
$C_{L_{cr}}$	[-]	0.71	0.65	0.58
α_w	[deg]	0	1	0
α_h	[deg]	0.87	0.85	0.77
C_{X_u}	[-]	-0.0314	-0.0443	-0.0270
C_{m_u}	[-]	-0.0	-0.0	-0.0
C_{X_a}	[-]	0.574	0.545	0.479
C_{m_α}	[-]	-5.5	-5.3	-3.9
C_{X_q}	[-]	-0.372	0.081	0.086
C_{m_q}	[-]	-427.2	-128.9	-59.11
C_{Y_b}	[-]	-0.600	-0.391	-0.348
C_{l_b}	[-]	-0.046	-0.007	0.003
C_{n_b}	[-]	0.268	0.175	0.111
C_{Y_p}	[-]	-0.071	-0.042	0.018
C_{l_p}	[-]	-0.724	-0.601	-0.589
C_{n_p}	[-]	-0.089	-0.111	-0.108
C_{Y_r}	[-]	0.551	0.346	0.218
C_{l_r}	[-]	0.289	0.264	0.205
C_{n_r}	[-]	-0.248	-0.157	-0.070

Appendix B

Detailed Functional Breakdown Structure

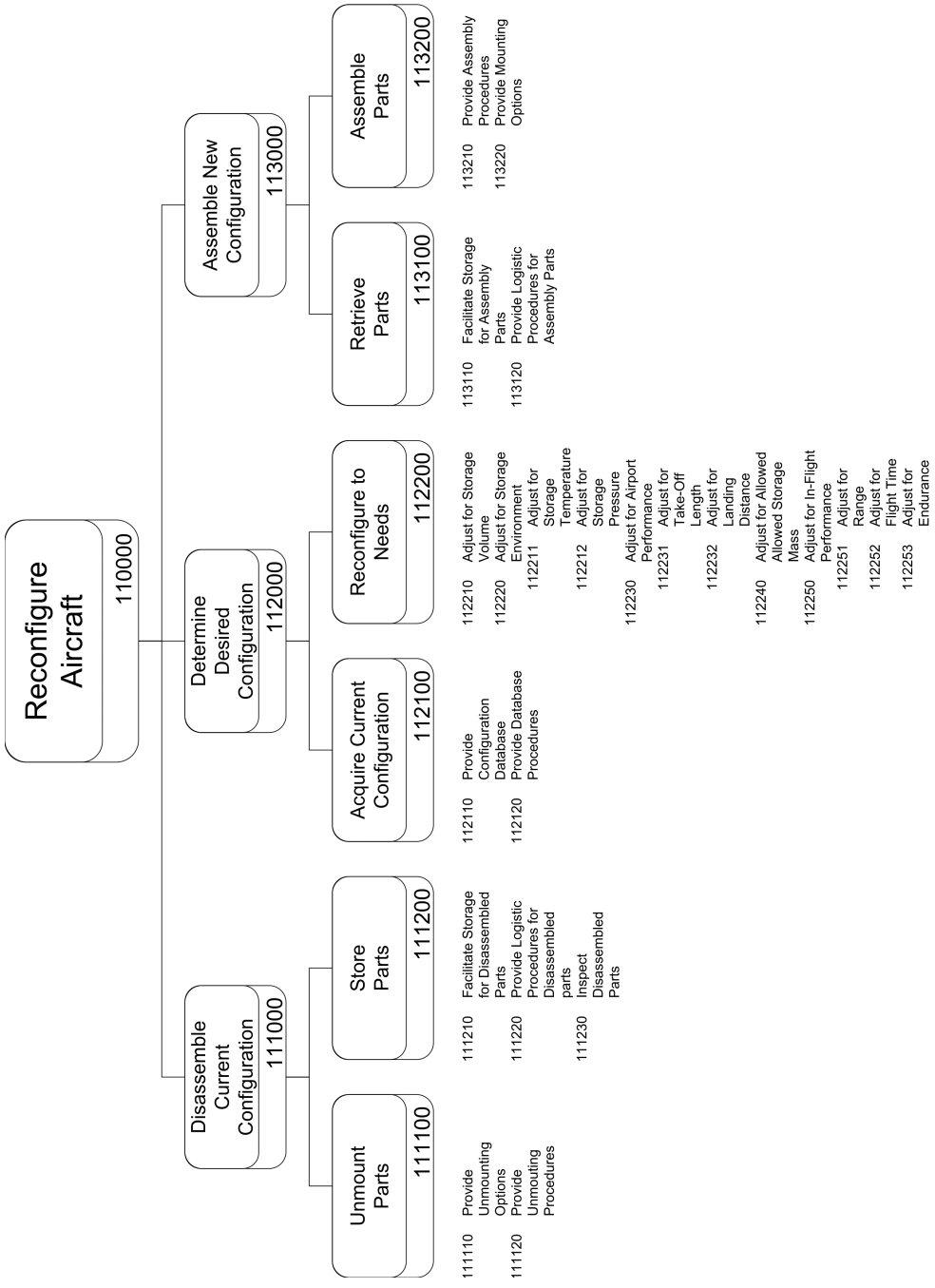

Figure B.1: Functional Breakdown Structure, part 2

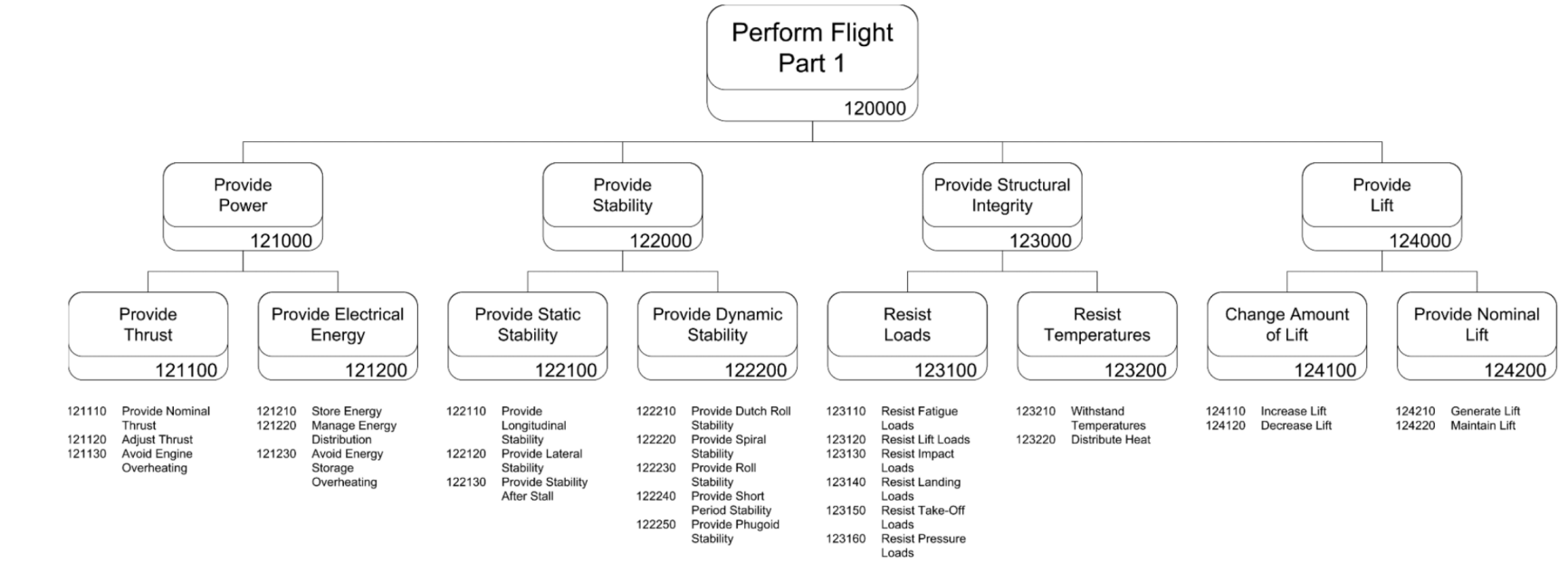

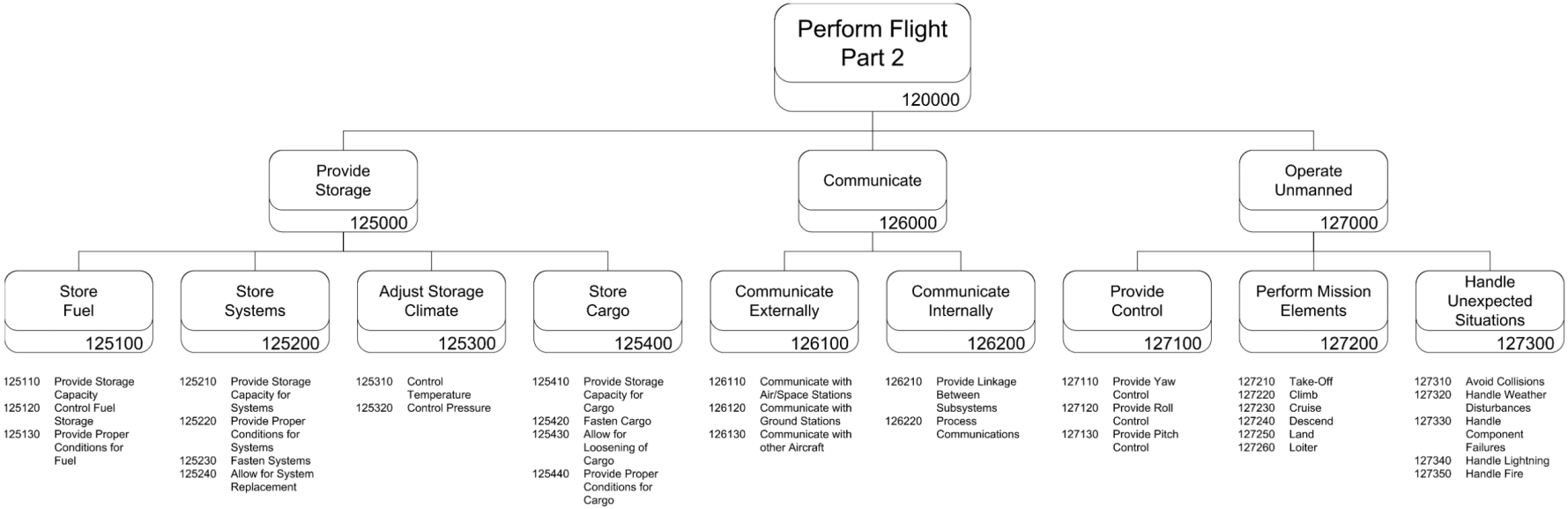

Figure B.2: Functional Breakdown Structure, part 3 and 4

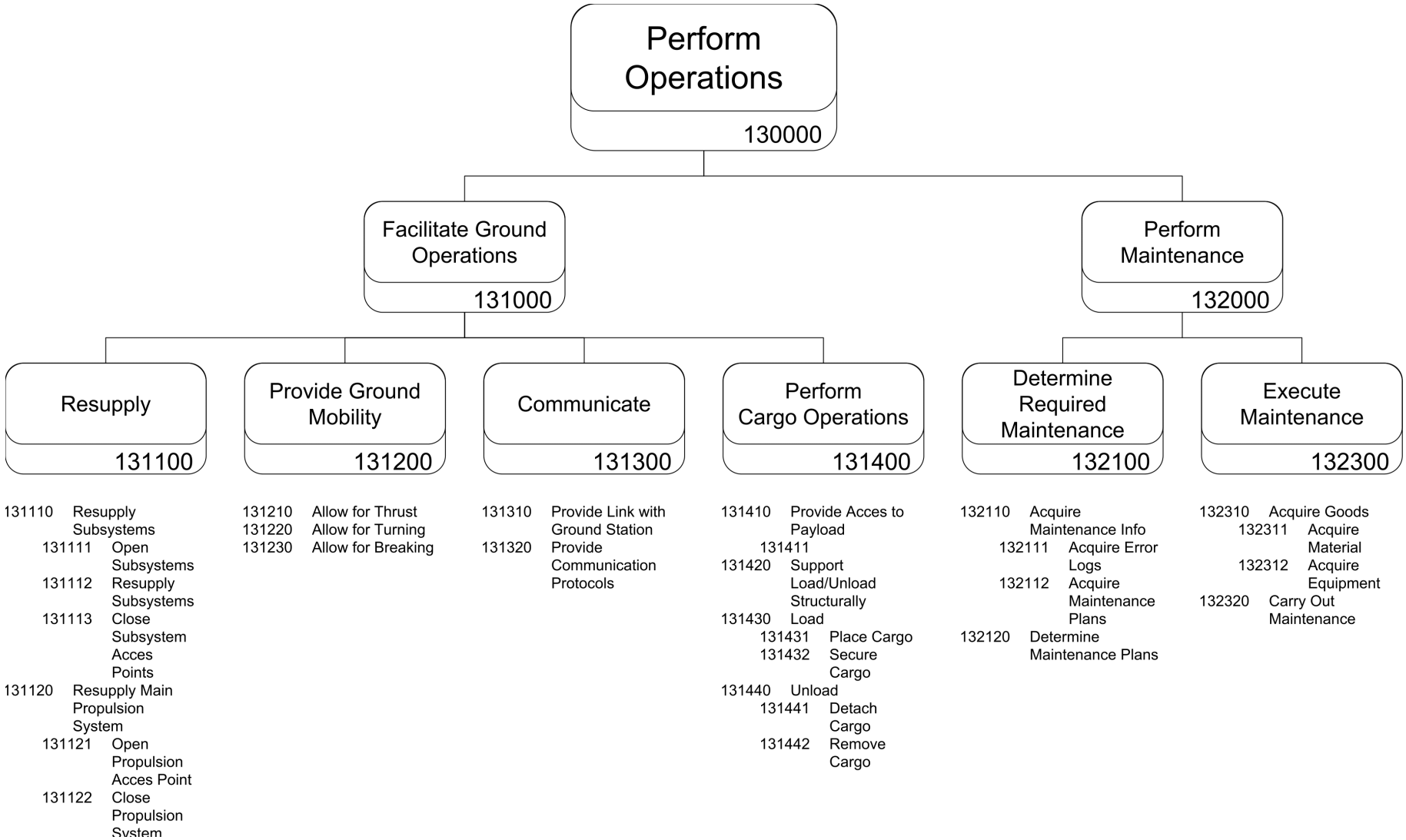

Figure B.3: Functional Breakdown Structure, part 5

Appendix C

Task division

Table C.1: Task division

	Lukas	Leon	Kostas	Joris	Luuk	Mike	Tim	Huy	Bob	Tim v/d W.
Preface		✓								
Executive Summary			✓	✓		✓				
Introduction										✓
Market analysis	✓								✓	
Mission Analysis				✓						
Preliminary Design										
Class I sizing	✓	✓	✓	✓	✓	✓	✓	✓	✓	✓
Class II sizing		✓	✓	✓	✓	✓		✓		✓
Class-I/II sensitivity										✓
Budget allocation				✓						
Performance and Propulsion										
Performance								✓		
Propulsion	✓									
Aero./Stab./Contr.										
Wing design					✓					
Nose design	✓									
Cg determination					✓					
Tail design										✓
Control surfaces			✓							
Dynamic stability										✓
Total drag			✓	✓	✓	✓				
Structures										
Wingbox				✓		✓				
Miscellaneous				✓		✓				

	Lukas	Leon	Kostas	Joris	Luuk	Mike	Tim	Huy	Bob	Tim v/d W.
Air and Ground Operations										
Flight Operational Regulations							✓			
Reconfig. operational certification		✓								
Communications									✓	
Unmanned control system							✓			
Service model									✓	
Ground ops and logistics		✓								
Reconfig. ops		✓								
RAMS							✓		✓	
Manufacturing, assembly, integration									✓	
Sustainability									✓	
Conclusion/Recommendations		✓								
System Characteristics, layout										
Electrical system							✓			
Hydraulic system							✓			
Fuel system							✓			
Environmental control system							✓			
Risk assessment										
Risk analysis						✓				
Mitigation plan						✓				
Financial Analysis										
Cost analysis	✓								✓	
Financial Forecast									✓	
Compliance			✓				✓	✓		✓
Project design development		✓								
Conclusion and Recommendations	✓									
CAD design		✓								